

Weathering of Fe-bearing Minerals Under
Extraterrestrial Conditions, Investigated by
Mössbauer Spectroscopy

Dissertation
zur Erlangung des Grades
"Doktor der Naturwissenschaften"
am Fachbereich Physik, Mathematik und Informatik
der Johannes Gutenberg-Universität
in Mainz

Christian Schröder
geb. in Wiesbaden

Für meine Eltern

”Wer glaubt etwas zu sein, hat aufgehört etwas zu werden!”

Sokrates (469 BC - 399 BC)

”Alles ist Wechselwirkung.”

Alexander von Humboldt (1769 - 1859)

Contents

1	Introduction	7
2	Basic Principles	11
2.1	Mössbauer spectroscopy	11
2.1.1	The Mössbauer effect	11
2.1.2	A basic Mössbauer spectrometer	13
2.1.3	Mössbauer parameters	14
2.2	MIMOS II	18
2.2.1	The drive system	19
2.2.2	Sources, collimator, and detectors	20
2.2.3	Working modes	20
2.2.4	Other applications	21
2.3	Weathering	22
2.3.1	Physical weathering	22
2.3.2	Chemical weathering	23
2.3.3	Biological weathering	24
2.3.4	Space weathering	24
3	Velocity Calibration of the MER Flight Instruments	25
3.1	Determination of maximum velocity	27
3.2	Non-linear velocity	28
3.2.1	Adjusting the fitting routines	28
3.2.2	Folding point	32
3.3	Temperature dependence of v_{max}	34
3.3.1	Experimental determination of the temperature dependence of v_{max}	36
3.4	CCT measurements on Mars	44
3.5	Spatial resolution and cosine smearing	46
3.6	Released velocity scales	49
3.7	Evaluation of MER Mössbauer data	51

4	Martian Meteorites	53
4.1	Dar al Gani 476 and Sayh al Uhaymir 005	54
4.2	Nakhla	59
4.3	ALH84001	62
4.4	Bounce Rock and basaltic shergottites	62
4.4.1	Constraints on the pyroxene composition in Bounce Rock	66
4.5	Conclusions	67
5	Weathering Experiments	69
5.1	Experimental design	70
5.1.1	Reaction kinetics	70
5.1.2	Experimental setup	72
5.1.3	Choice of gases	72
5.1.4	Choice of minerals	74
5.2	Results and discussion	76
5.2.1	Pyrite	76
5.2.2	Olivine and pyroxene	83
5.3	Conclusions	83
6	Weathering on Mars	89
6.1	Data set	93
6.2	Results	96
6.3	Discussion	107
6.3.1	Adirondack class	109
6.3.2	Mazatzal coatings	110
6.3.3	Laguna class soils	112
6.3.4	Clovis class and Pot of Gold subclass	113
6.3.5	Wishstone class and Watchtower class	117
6.4	Conclusions	117
7	Astrobiological Applications	121
7.1	Morphological biosignature samples	122
7.1.1	Microbial filaments	123
7.1.2	Endoliths	128
7.1.3	Relict sedimentary structures	130
7.2	Loihi deep sea mount	133
7.3	Mars	137
7.3.1	Gusev Crater	138
7.3.2	Meridiani Planum	139
7.4	Conclusions	141

<i>CONTENTS</i>	5
8 Summary and Conclusions	143
List of Publications	145
Bibliography	157
A Mars	189
B Mars Exploration Rover	193
Curriculum Vitae	198

Chapter 1

Introduction

Weathering - the interaction between rocks and the atmosphere - is an everyday phenomenon which leaves traces of its actions in the rock record. The study of the relation between weathered material and igneous rock on planetary bodies in the Solar System allows conclusions on the environmental conditions on their surfaces in the past and at present. On Earth, weathering is generally driven by the water cycle; the mediating role of the biosphere is increasingly recognized [e.g., *Schlesinger*, 2003]. The planet Mars (Appendix A) on the other hand, is cold and dry today. However, its surface reveals many features attributed to the actions of liquid water [e.g., *Carr*, 1996] and thus an apparently warmer and wetter past. The surface of the Red Planet may have been hospitable to life back then, whereas it appears hostile today. Understanding why, when, and how the climate on Mars changed so dramatically may also have repercussions for the debate on climate change on Earth. Some answers are hidden in the Martian rocks.

The element Fe is one of the most abundant elements in the universe. Iron is the sixth most abundant element in the Earth's crust and the third most abundant cationic element after Si and Al. There is, therefore, hardly any rock completely free from Fe [*Cornell and Schwertmann*, 1996]. Other than Earth, the Red Planet, in particular, owes its color to ferric oxide pigments [e.g., *Morris et al.*, 1989a, 1993, 1997]. Mars surface materials are enriched in Fe relative to Earth [e.g., *Clark et al.*, 1976; *Toulmin et al.*, 1977; *Rieder et al.*, 1997, 2004; *Gellert et al.*, 2004, 2006]. Mössbauer spectroscopy is a powerful tool to analyze Fe-bearing compounds. Mössbauer spectroscopy provides quantitative information about the distribution of Fe among its oxidation states and crystallographic sites such as octahedral Fe^{3+} , identification of Fe-bearing phases, relative distribution of Fe among those phases, and some information on particle size and crystallinity. Ferrous iron (Fe^{2+}) is present in both primary silicate and oxide minerals such as olivine, py-

roxene, ilmenite, and (titano)magnetite and secondary minerals such as serpentine and sulfates. Although present at significant levels in some primary phases such as augite and (titano)magnetite, ferric iron (Fe^{3+}) is commonly a product of oxidative alteration and weathering of primary minerals and often occurs as oxides and oxyhydroxides. The speciation and distribution of Fe in Martian rock and soil constrain the primary rock type (e.g., olivine-dominated basalt versus pyroxene-dominated basalt), the redox conditions under which primary minerals crystallized (e.g., presence or absence of magnetite), the extent of alteration and weathering (e.g., value of Fe^{3+}/Fe_{Total}), the type of alteration and weathering products (e.g., oxides versus sulfates versus phyllosilicates), and the processes and environmental conditions for alteration and weathering (e.g., neutral versus acid-chloride versus acid-sulfate aqueous process under ambient or hydrothermal conditions) [Morris *et al.*, 2006a]. Morris *et al.* [1989b], Knudsen [1989], Knudsen *et al.* [1990, 1992], and Burns [1993a] have argued in detail for the in situ application of Mössbauer spectroscopy on Mars.

The two NASA¹ Mars Exploration Rovers (MER, Appendix B), Spirit and Opportunity, landed in Gusev Crater and at Meridiani Planum on Mars in January 2004. They each are equipped with the Athena science payload [Squyres *et al.*, 2003], including the Miniaturized Mössbauer Spectrometer MIMOS II [Klingelhöfer *et al.*, 2003]. The primary objective of the Athena science investigation is to explore two sites on the Martian surface where water may once have been present, and to assess past environmental conditions at those sites and their suitability for life [Squyres *et al.*, 2003].

The operation of the MER Mössbauer spectrometers required intense support from the ground. The support included the careful calibration of the Mössbauer instrument (Chapter 3), the evaluation and interpretation of Mössbauer data, the participation in the daily planning cycles for the rovers' workloads, the presentation of results in discussions amongst the rovers' science team, the presentation of results at scientific conferences, and the preparation of results for publication in scientific journals. All raw and calibrated data of the mission had to be made publicly available within six months of acquisition. Success and endurance of the two rovers have exceeded all expectations. The journal 'Science' declared the results from the combined payload the scientific breakthrough of the year 2004 [Kerr, 2004]. At the time of writing this introduction (June 2006) both rovers are still operating.

In preparation for the MER mission several experiments were conducted in the lab. Martian meteorites, a group of achondrites whose origin is believed to be Mars, were analyzed using a laboratory copy of the MIMOS II

¹National Aeronautics and Space Administration

instrument. The rover Opportunity discovered further evidence for a Martian origin of these meteorites. Bounce Rock was the first rock discovered on Mars itself, whose chemical and mineralogical composition matches that of the Martian meteorites (Chapter 4). In another set of experiments, minerals identified in Martian meteorites as well as on the surface of Mars were weathered in simulated Martian atmospheres. Fresh and weathered mineral samples were investigated by Mössbauer spectroscopy (Chapter 5).

In order to determine how surface weathering processes might have changed through Martian history, intact profiles of rocks of similar composition, but with the widest possible range of ages, should be mineralogically analyzed [Gooding *et al.*, 1992]. Such a dataset is now available from Spirit's investigation in Gusev Crater. Correlations between the abundances of primary and secondary Fe-bearing minerals as determined by Mössbauer spectroscopy give insight into weathering processes on Mars (Chapter 6).

The biosphere plays a significant role in mineral weathering and the formation of sedimentary rocks on Earth. If life ever arose on another planet, its signatures may be identified in the rock record. Mössbauer spectroscopy was recommended for the in situ investigation of the Martian surface in an ESA² study on exobiology in the solar system and the search for life on Mars [Westall *et al.*, 2000; Wilson, 1999]. MIMOS II was part of the payload of the ill-fated ESA Mars Express exobiological lander 'Beagle 2' [Sims *et al.*, 1999; Pullan *et al.*, 2003]. In that context, rocks from Mars analogue field sites (e.g., the Ross Desert McMurdo Dry Valleys in Antarctica) exhibiting morphological biosignatures were analyzed with a suite of instruments designed for robotic planetary surface operations, including MIMOS II. In another investigation, Fe oxidation states of basaltic glass samples were determined using Mössbauer spectroscopy. The glass samples had been exposed at a deep sea hydrothermal vent. Iron oxidizing bacteria were cultured from samples previously exposed there. As per the MER mission objectives both rover landing sites were assessed for their potential habitability [Des Marais *et al.*, 2005; Knoll *et al.*, 2005]. The MER Mössbauer results which contributed to these assessments were also summarized in Chapter 7.

The basics of Mössbauer spectroscopy, the build-up of the miniaturized Mössbauer spectrometer MIMOS II, and the concepts of weathering are introduced in the next chapter.

²European Space Agency

Chapter 2

Basic Principles

2.1 Mössbauer spectroscopy

Rudolf Ludwig Mössbauer (Nobel Prize 1961) discovered recoilless absorption and emission of γ -rays by specific nuclei in a solid in 1958 [Mössbauer, 1958a, 1958b, 2000]. There have been numerous reviews of this 'Mössbauer effect' in general [e.g., Wegener, 1965; Greenwood and Gibb, 1971; Gonser, 1975; Gütlich *et al.*, 1978], of its applications in mineralogy and geochemistry [e.g., Bancroft, 1973; Hawthorne, 1988; Mitra, 1992; McCammon, 1995], and in the investigation of planetary surfaces in particular [e.g., Burns, 1993a; Klingelhöfer *et al.*, 1995; Wdowiak *et al.*, 2003]. The following paragraphs provide a brief introduction.

2.1.1 The Mössbauer effect

When a nucleus of a particular isotope in an excited state decays to the ground state, separated by the transition energy E_t , by emitting γ -radiation of the energy E_γ it experiences recoil of energy E_R expressed as

$$E_R = \frac{E_\gamma^2}{2Mc^2}, \quad (2.1)$$

where M is the mass of the nucleus and c is the velocity of light. The isotope ^{57}Fe , for example, occurs with an abundance of 2.14 % in natural iron. Its nuclear spin $I = 3/2$ excited state is separated by $E_t = 14.4$ keV from the $I = 1/2$ ground state (Figure 2.1). Conservation of energy requires that only $E_t - E_R$ is available for E_γ . Likewise, in order to bring a nucleus from the ground state into the excited state, radiation with an energy of $E_\gamma = E_t + E_R$ is necessary. The line width Γ of the emitted γ -radiation can be determined

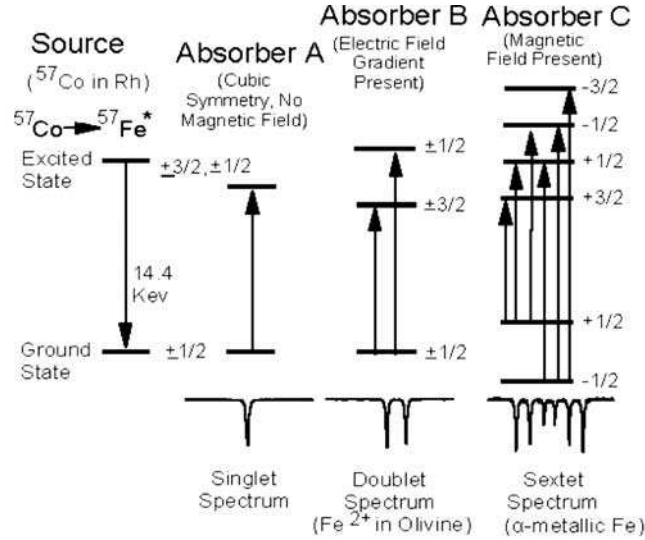


Figure 2.1: Energy level diagram for ^{57}Fe showing singlet emission of 14.4 keV γ -rays from the Mössbauer source and absorption of the γ -rays in three different nuclear environments.

with the lifetime τ of the excited state (10^{-7}s for ^{57}Fe) via Heisenberg's uncertainty principle

$$\Gamma\tau = \hbar, \quad (2.2)$$

where \hbar is Planck's constant divided by 2π . For ^{57}Fe the line width $\Gamma = 4.67 \times 10^{-9}\text{eV}$ and $E_R = 1.9 \times 10^{-3}\text{eV}$. Because $\Gamma \ll E_R$, it is not sufficient to bridge the energy gap of $2E_R$; resonant emission and absorption of γ -rays is not possible in isolated atoms or molecules in the gaseous or liquid state. However, as Mössbauer discovered, when the nucleus is bound rigidly to the crystal lattice of a solid, the crystal as a whole takes up the recoil energy. Recoil energy is thereby transferred to the lattice by exciting phonons (quantum units of lattice vibrations). The energy of excited phonons adds up to E_R on average, but with a certain probability no phonons are excited and emission or absorption processes are recoilless. Conditions for resonant emission and absorption of γ -rays are restored. This probability, the recoil-free fraction f , can be expressed as

$$f = \exp -k^2 \langle x^2 \rangle, \quad (2.3)$$

where k is the wave vector of the γ -ray and $\langle x^2 \rangle$ is the mean vibrational amplitude of the nucleus. This f -factor is also referred to as the Lamb-Mössbauer factor or the Debye-Waller factor. The Mössbauer effect has been observed in specific isotopes of over 40 elements. ^{57}Fe Mössbauer

spectroscopy is the most widely applied because of the relative ease of measurement, and because Fe is one of the most abundant and wide-spread elements.

2.1.2 A basic Mössbauer spectrometer

A simple Mössbauer spectrometer consists of a source emitting the specific γ -rays, a sample or absorber to be investigated, and a γ -ray detector system (Figure 2.2). The isotope ^{57}Co decays by electron capture with a half-life of 270 days to ^{57}Fe . This happens with a certain probability via the $I = 3/2$ excited nuclear spin state of ^{57}Fe , emitting the desired 14.4 keV γ -radiation when finally making the transition to the ground state. Nuclear energy levels are influenced by the chemical environment. If the Mössbauer isotopes in source and absorber reside in different chemical compounds, resonant conditions may be violated. They can be restored by moving the source relative to the absorber with velocity v_s , thereby adding energy E_D to E_γ or subtracting E_D from E_γ via the Doppler effect

$$E_D = \frac{v_s}{c} E_\gamma. \quad (2.4)$$

The x-axis in Mössbauer spectra is therefore labeled in units of velocity (usually mm/s) rather than energy. The detector may be installed in line with

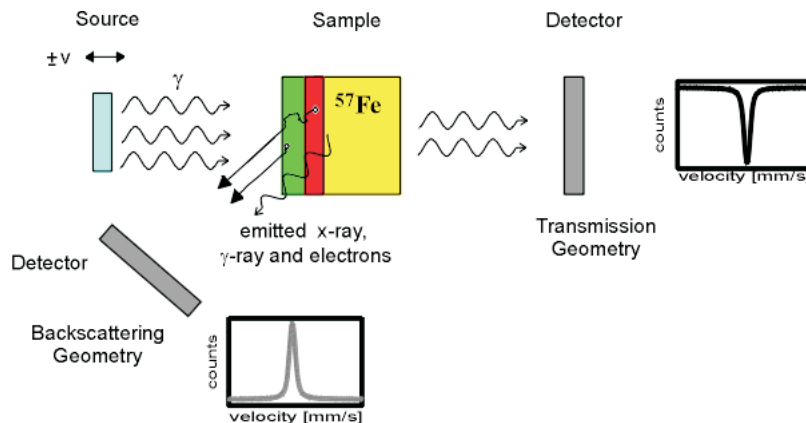


Figure 2.2: The principle of Mössbauer spectroscopy: A source emitting γ -rays is moved relative to an absorber. The absorber resonantly absorbs and re-emits γ -rays. A detector placed behind the absorber measures absorption minima; a detector placed on the same side of the absorber as the source measures reflection maxima of γ -rays or related de-excitation processes.

source and absorber, with the absorber between source and detector (transmission geometry, Figure 2.2). Thin slices or thinly distributed powders of the absorber material have to be especially prepared to let enough radiation pass through to the detector and to keep thickness effects small. Resulting Mössbauer spectra show absorption minima. Alternatively, the detector may be installed on the same side of the absorber as the source (backscattering geometry, Figure 2.2). The detector then records re-emitted γ -rays, or may be tuned to detect competing ways of de-excitation such as conversion electrons, or secondary processes such as X-rays. The resulting Mössbauer spectra show reflection maxima.

2.1.3 Mössbauer parameters

The interaction of a nucleus with its chemical environment affects the nuclear energy levels. Positions of resonant lines in Mössbauer spectra reflect these changes relative to the source material and can thus be used to determine the character of the chemical environment of the absorber. Different kinds of interaction manifest themselves in three important parameters which can be extracted from a Mössbauer spectrum. These hyperfine parameters or Mössbauer parameters are the isomer shift δ , the quadrupole splitting ΔE_Q , and the magnetic hyperfine splitting ΔE_M .

Isomer shift

The isomer shift δ results from electric monopole interaction, i.e., Coulomb interaction of the positive nuclear charge with electrons inside the nucleus. It can be expressed as

$$\delta = \frac{4}{5}\pi Ze^2 R^2 \frac{\delta R}{R} \{|\psi(0)|_A^2 - |\psi(0)|_S^2\}, \quad (2.5)$$

where Ze is the nuclear charge, R is the mean radius of the nucleus in its ground and excited states, δR is the difference between the radii of excited and ground states, and $|\psi(0)|^2$ is the electron density at the nucleus of the source (S) or the absorber (A). Isomer shifts thus also vary according to the source material used (e.g., ^{57}Co in Rh matrix) and have to be cited relative to a common reference material, which in the case of Fe Mössbauer spectroscopy is usually pure metallic Fe foil.

Experimentally one observes the isomer shift plus the second-order Doppler shift (SOD), a small thermal shift due to atomic vibrations. The experimental shift of the centroid of a Mössbauer spectrum from a zero reference point is thus referred to as the center shift. The contribution from the SOD is

similar in most standard materials, so for purposes of comparison the isomer shift is often taken to be equal to the center shift.

The isomer shift δ can be used to determine the oxidation state of iron in a given absorber. The $\delta R/R$ ratio for ^{57}Fe is negative, and thus increasing electron density at the nucleus results in a more negative value of δ . Not considering relativistic effects, only electrons in s-shells have a finite probability of being located at the nucleus. When metallic iron is oxidized to Fe^{2+} , two 4s electrons are removed and δ increases. Further oxidation to Fe^{3+} , however, removes an electron from the 3d shell. The remaining electrons are bound tighter to the nucleus and the electron density at the nucleus increases. As a result, δ values for Fe^{3+} -bearing compounds are more negative than for Fe^{2+} -bearing compounds. The ligand-type (e.g., O versus S bound to Fe) and the coordination symmetry (e.g., Fe in tetrahedrally coordinated sites versus Fe in octahedral sites) also influence the electron density and therefore the isomer shift. For Fe bound to O such as in silicates, sulfates, carbonates, etc., isomer shifts for Fe^{2+} cations typically range from 0.75 - 1.3 mm/s in room temperature Mössbauer spectra; isomer shifts for Fe^{3+} cations range from 0.15 - 0.5 mm/s [e.g., *Burns and Solberg*, 1990; *Burns*, 1993a, 1994].

Quadrupole splitting

Quadrupole splitting ΔE_Q results from electric quadrupole interaction. It is observed only when the nuclear charge is not distributed spherically symmetric (i.e., the nucleus possesses a non-zero quadrupole moment Q) and electron and lattice charges are arranged other than in cubic symmetry, thus producing an electric field gradient at the nucleus which interacts with the quadrupole moment. This interaction partially removes the degeneracy of the $I = 3/2$ excited state of ^{57}Fe , separating it into two levels with magnetic spin quantum numbers of $m_I = \pm 3/2$ and $m_I = \pm 1/2$. The energy difference between these two levels is

$$\Delta E_Q = E_Q(\pm 3/2) - E_Q(\pm 1/2) = eQV_{zz}/2, \quad (2.6)$$

where V_{zz} is the main component of the electric field gradient. Two transitions to the ground state are possible (Figure 2.1), manifesting themselves as two separate resonant lines (a doublet) in a Mössbauer spectrum. The distance between the two line centers is equal to ΔE_Q . In the case of combined electric monopole and quadrupole interaction, the location of the center between the two doublet lines on the x-axis in the Mössbauer spectrum defines the isomer shift δ .

The different electronic configurations of, e.g., Fe^{2+} and Fe^{3+} ions and different coordination environments result in different electric field gradients

at the nucleus. ΔE_Q values are generally larger for compounds containing Fe^{2+} ions than for compounds containing Fe^{3+} . The combination of isomer shift δ and quadrupole splitting ΔE_Q enables one to reliably distinguish between Fe^{2+} and Fe^{3+} ions in mixed-valence compounds [e.g., *Burns and Solberg*, 1990; *Burns*, 1993a, 1994).

Magnetic hyperfine splitting

Magnetic hyperfine splitting ΔE_M results from the interaction of a magnetic field at the nucleus, it may be intrinsic or externally applied, with the magnetic dipole moment μ_N of the nucleus. The degeneracy of nuclear states of spin I is completely removed into $(2I + 1)$ energy levels (nuclear Zeeman effect)

$$E_M = -g_N \mu_N m_I B_{hf}, \quad (2.7)$$

where g_N is the nuclear Landé factor, $m_I = I, I - 1, \dots, -I$, and B_{hf} is the magnetic hyperfine field. The ground state of ^{57}Fe with $I = 1/2$ splits into two, the excited state with $I = 3/2$ into four levels. Selection rules for magnetic dipole transitions ($\Delta I = 1, \Delta m_I = 0, \pm 1$) allow only six transitions, which manifest themselves as six separate resonant lines (a sextet) in the Mössbauer spectrum (Figure 2.1). The parameter ΔE_M is the distance between the outermost line centers of the sextet. In the following chapters the magnetic hyperfine field B_{hf} is often used instead of ΔE_M .

The situation of simultaneous electric monopole interaction, electric quadrupole interaction, and magnetic dipole interaction can be complicated. Fortunately, the magnetic interaction is much stronger in most cases, and the electrical interaction can be treated as a perturbation. Then one can calculate the quadrupole splitting $\Delta E_Q = (1/2)[(v_6 - v_5) - (v_2 - v_1)]$, where enumerated v_6 , for example, corresponds to the center position of line number 6 of a sextet when counted from lower to higher velocity in a Mössbauer spectrum. The isomer shift δ is the distance of the baricenter of the sextet from zero velocity on the x-axis of the Mössbauer spectrum.

The magnetic hyperfine field B_{hf} of magnetically ordered compounds may not be observed in a Mössbauer spectrum when the size of particles of that compound are in the range of magnetically ordered domains. Thermal excitation causes fluctuations of the magnetization direction of such one-domain particles. The fluctuations of the magnetization happen with the relaxation time τ ,

$$\tau = \tau_0 \exp \frac{\kappa V}{kT}, \quad (2.8)$$

where τ_0 is a constant, κ is the magnetic anisotropy energy per unit volume, V is the volume of the particle, and kT is the thermal energy. If the re-

laxation time is smaller than the lifetime of the excited nuclear state, the magnetic field sensed by the nucleus of the Mössbauer isotope is zero on average. The particles become superparamagnetic. At room temperature this effect is observed for particles < 30 nm, i.e., nanocrystalline particles. The magnetic hyperfine splitting ΔE_M may be restored in the Mössbauer spectrum by lowering the temperature of the absorber in the experiment, thereby increasing the relaxation time τ . Nanocrystalline or superparamagnetic iron oxides occur in many environments which are important for the study of weathering under extraterrestrial conditions such as soils [e.g., *Murad*, 1988], the Orgueil carbonaceous chondrite [*Wdowiak and Agresti*, 1984], hydrothermal vent systems [*Agresti et al.*, 1994; *Wade et al.*, 1999], clays at the Cretaceous-Tertiary (KT) boundary [e.g., *Wdowiak et al.*, 2001], or the surface of Mars [e.g., *Morris et al.*, 1989a, 2000, 2001, 2004, 2006a].

Spectral line shape and relative areas

Resonant spectral lines in a Mössbauer spectrum generally have a Lorentzian form

$$I(E) \sim \frac{\Gamma/2\pi}{(E - E_0)^2 + (\Gamma/2)^2}, \quad (2.9)$$

where I is the intensity, E_0 is the resonant energy, and Γ is the natural line width from equation 2.2. In some cases data may be better approximated using Voigt line shapes, i.e. a convolution of Lorentzian and Gaussian line shapes.

Every Fe-bearing compound is characterized by a particular set of the Mössbauer parameters δ , ΔE_Q , and B_{hf} , like a fingerprint. An absorber investigated by Mössbauer spectroscopy may contain several Fe-bearing compounds. Hence, a Mössbauer spectrum may be deconvolved into several single line, doublet, and sextet subspectral components. The relative subspectral area is proportional to the relative amount of Fe in this compound and its Debye-Waller factor. *De Grave and van Alboom* [1991] and *Eeckhout and De Grave* [2003] evaluated Debye-Waller factors for many Fe-bearing minerals. Generally, Fe^{3+} ions have higher Debye-Waller factors than Fe^{2+} ions and an f -factor correction may be applied to account for this difference. If Debye-Waller factors are known at least relative to each other for all components in a Mössbauer spectrum, and if the number of Fe atoms per component molecule is also known or modeled, the weight percentage g for each component k can be calculated as

$$g_k = \frac{A_k S_k}{\sum_i A_i S_i \epsilon_i^k}, \quad (2.10)$$

where A_k is the relative subspectral area of component k , S_k is the stoichiometric factor given by the ratio of the molecular weight of Fe divided by the number of Fe atoms per molecule, ϵ_i^k is the ratio of Debye-Waller factors of components k and i , and g_k is normalized to the sum of g_i of all components [Fegley *et al.*, 1995].

2.2 MIMOS II

The *Miniaturized Mössbauer Spectrometer* MIMOS II (Figure 2.3) was specifically designed for planetary missions. Besides miniaturization this involves low power consumption and a rigid design to withstand high acceleration forces and shocks during launch and landing, large temperature variations typical during, e.g., the Martian diurnal cycle, and cosmic radiation. To avoid complicated sample preparation the instrument is set up in backscattering geometry. The instrument can thus be simply applied to the sample. MIMOS II was chosen as part of the Athena science payload for the NASA Mars Exploration Rovers (MER, see Appendix B) [Squyres *et al.*, 2003] and the payload for the ill-fated ESA Mars Express lander Beagle 2 [Pullan *et al.*, 2003]. The instrument on MER is described in detail by Klingelhöfer *et al.* [2003]. This instrument has two major components: (1) a rover-based

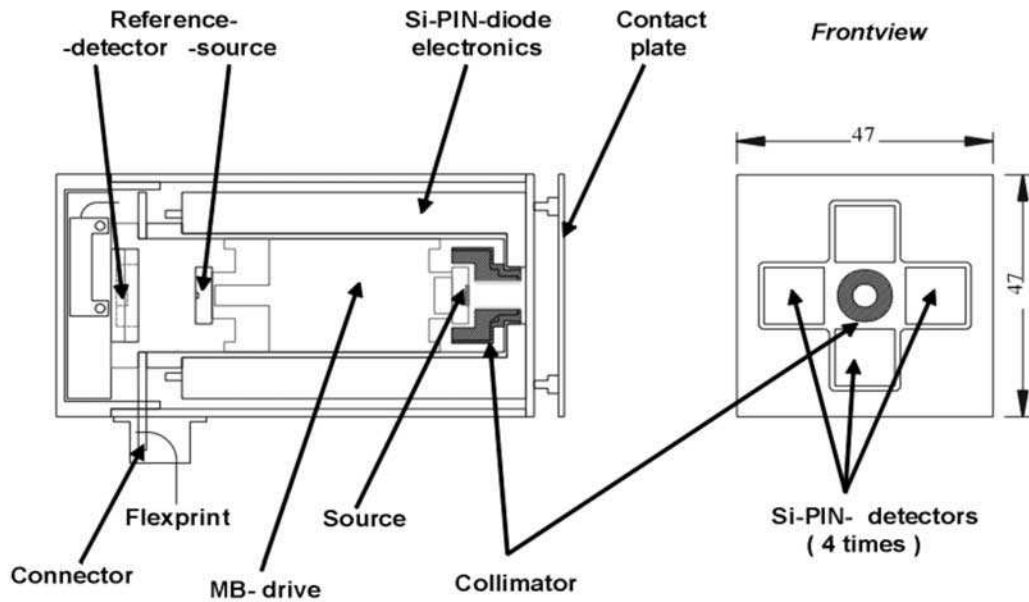


Figure 2.3: Schematic drawing of the main components of the MIMOS II sensorhead.

electronics board that contains power supplies, a dedicated central processing unit, memory, and associated support electronics and is situated inside the Rover's Warm Electronics Box (WEB), and (2) a sensor head that is mounted at the end of the instrument deployment device (IDD) for placement of the instrument in physical contact with soil and rock. A brief description of the instrument parts relevant to this work follows.

2.2.1 The drive system

The MIMOS II miniaturized drive design [Teucher, 1994] is based on a rigid aluminum tube connection between a drive coil and a velocity pick-up coil in the double-loudspeaker arrangement developed by Kankeleit [1964]. The intense main $^{57}\text{Co}/\text{Rh}$ source is mounted at one end of the aluminium tube, and the weaker source for the reference absorber is mounted at the other end. Kapton springs act as membranes of the loudspeaker system. The system is equipped with SmCo permanent magnets and was optimized to give a homogeneous, high magnetic field in the coil gaps (Figure 2.4). The drive operates at a nominal frequency of ~ 24 Hz, which is also its main resonance. A feedback system produces a velocity proportional to a reference signal of triangular waveform. The pickup coil measures the velocity by induction. The error signal (or differential signal) of the feedback system is obtained by connecting the floating pickup coil in series with the reference signal (Figure 2.5). It is possible to read out and store the error signal to check the drive performance.

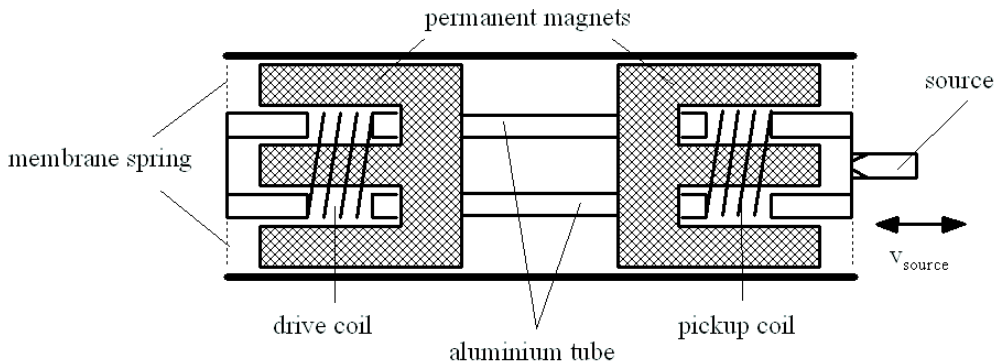


Figure 2.4: Schematic drawing of a double loudspeaker Mössbauer drive system. Source, drive and pickup coil are rigidly connected to an aluminium tube. The tube can move in x-direction while the permanent magnets are fixed in position [figure from Teucher, 1994].

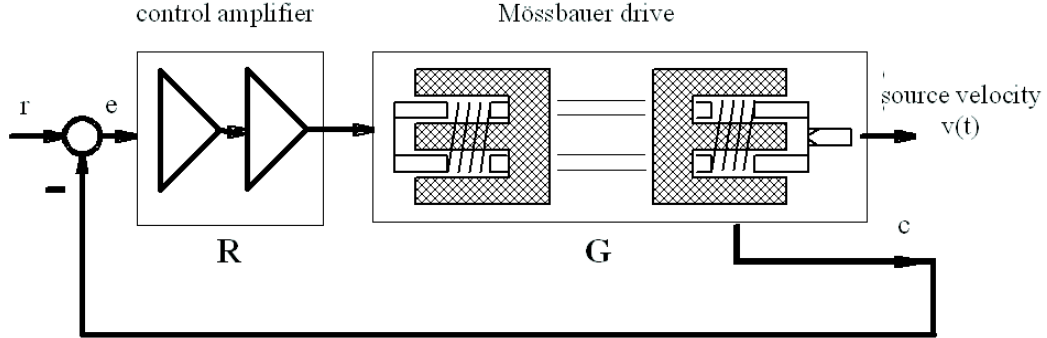


Figure 2.5: Simplified block diagram of the feedback system, where r represents the reference signal, c is the signal from the pickup coil, and $e = r - c$ is the error signal. The letters R and G stand for the transfer functions of the control amplifier and the Mössbauer drive, respectively [figure from *Teucher*, 1994].

2.2.2 Sources, collimator, and detectors

Two ^{57}Co in Rh matrix Mössbauer sources are mounted at opposite ends of the MIMOS II drive (Figure 2.3). The weaker reference source, reference target, and corresponding PIN-diode detector are configured in transmission geometry. This reference setup is internal to the instrument and used for its velocity calibration. The stronger Mössbauer source is used for the analysis of external samples. Very important is an effective shielding of the detector system from direct and cascade radiation from the $^{57}\text{Co}/\text{Rh}$ source. A graded shield consisting of concentric tubes of brass, tantalum, and lead (Figure 3.12) was selected. The thickness and the shape of different parts of the shielding were optimized so that hardly any direct 122 and 136 keV radiation (emitted by the ^{57}Co source) is in line with the detectors. The shielding also acts as the collimator which limits the diameter of the target that is irradiated by γ -rays. This diameter is as large as possible to minimize experiment time within the constraint of acceptable cosine smearing [*Klingelhöfer et al.*, 1992; *Held*, 1997; *Schröder*, 2001]. The backscattered radiation is collected by four PIN-diode detectors [*Imkeller*, 1990; *Weinheimer et al.*, 1992; *Held*, 1993; *Held et al.*, 1993; *Dorn*, 1995; *Bernhardt*, 1997].

2.2.3 Working modes

MIMOS II has four main detectors plus the reference detector. Correspondingly, five digital counters are situated on the electronics board. The reference

detector collects 14.4 keV γ -quanta only, whereas the main detectors can be set to collect either 14.4 keV γ -quanta, or 6.4 keV X-ray quanta resulting from deexcitation by conversion electrons, or 14.4 keV γ -quanta and 6.4 keV X-ray quanta simultaneously (the default mode on the Mars Exploration Rovers). If the latter is the case, in order to be able to bin counts of 6.4 keV and 14.4 keV quanta separately, two of the four counters corresponding to the main detectors store the sum of 14.4 keV quanta collected by two specific detectors each, the other two counters store the sum of 6.4 keV quanta collected by two specific detectors each. The simultaneous collection yields some depth sensitivity within the resulting Mössbauer spectra, because the difference in energy allows the more energetic of the backscattered radiation to come from greater depth of the sample [e.g., *Klingelhöfer et al.*, 2003; *de Souza*, 2004]. However, in the mode of simultaneous collection, faulty detectors cannot be singled out immediately any more. Individual Mössbauer spectra consist of 512 velocity channels.

MIMOS II was designed to work over a wide temperature range. Martian diurnal surface temperatures for example can range from 150 K on a winter night to 293 K during a summer day. Hyperfine parameters of individual minerals, in particular magnetic properties, change with temperature. Certain instrument characteristics are also temperature dependent (Chapter 3.3). Therefore, MIMOS II can work in a temperature independent mode, where a single Mössbauer spectrum is stored for each counter, and a temperature dependent mode, where Mössbauer spectra from each counter are binned into 13 separate memory areas that correspond to 11 temperature intervals that are 10 K wide between 180K and 290 K, plus < 180 K and > 290 K windows. MIMOS II contains three individual temperature sensors: one located on the electronics board in the WEB; one on the contact ring of the sensorhead; and one near the reference target. The binning into different temperature windows is triggered by periodical readouts of the sensor at the contact ring. The Mössbauer spectra stored for the different temperature windows can be evaluated separately or, for example in the case of low statistics in individual windows, summed and subsequently evaluated.

2.2.4 Other applications

The special features of MIMOS II open up a range of terrestrial applications. It has been used in the monitoring of iron ore production [*Klingelhöfer et al.*, 1998], the monitoring of hydromorphic soils in the field [*Klingelhöfer et al.*, 1999; *Feder et al.*, 2005; *Rodionov et al.*, 2006], and in-situ monitoring of corrosion and air pollution studies [*de Souza et al.*, 2001, 2002]. Due to its set-up in backscattering geometry it is a non-destructive method suitable

for the investigation of rare and precious materials, such as archaeological artefacts [Klingelhöfer *et al.*, 2002a, 2002b; de Souza *et al.*, 2003; de Souza, 2004] or Martian meteorites [Schröder, 2001; Schröder *et al.*, 2004; de Souza, 2004].

2.3 Weathering

A rock reaching the surface of a planet through volcanic and/or tectonic processes is out of thermodynamic equilibrium with its new environment which is no longer characterized by high pressures and temperatures. Through physical and chemical reactions the rock breaks down over time, i.e. it weathers. The term 'weathering' stems from 'weather', which is defined as the state of the atmosphere at any given time. At least on Earth one also has to include interactions with the hydrosphere and the biosphere into the concept of weathering.

Erosion is the mass transport of weathered material by water run-off, wind, or ice, ultimately driven by the leveling pull of a planet's gravity. A sediment is material deposited by erosional (physical) agents, chemical agents (precipitation from bodies of water), or biological agents (living or dead organisms). Regolith is a layer of loose heterogeneous material composed of weathered and unweathered fragments of the underlying parent rock, whereas soil is a complex accumulation of weathered materials and organic matter.

Some minerals weather faster than others. *Goldich* [1938] observed that mineral susceptibility to weathering is generally similar to Bowen's sequence of minerals crystallizing from a melt [Bowen, 1928] (Figure 2.6). However, the order of mineral susceptibility to weathering may change under different environmental conditions [e.g., *Wasklewicz*, 1994].

An introduction to the principles of weathering can be found in general textbooks on geology [e.g., *Press and Siever*, 2000] and mineralogy [e.g., *Correns*, 1968; *Matthes*, 2001], as well as dedicated textbooks [e.g., *Carroll*, 1970; *Bland and Rolls*, 1998]. For more detailed insights into particular aspects of weathering, numerous reviews collections are available [e.g., *Colman and Dethier*, 1986; *Hochella and White*, 1990; *White and Brantley*, 1995; *Drever*, 2003; *Schlesinger*, 2003]. According to the different underlying principles, weathering can be divided into several categories.

2.3.1 Physical weathering

Physical weathering processes are mechanical processes involving the disintegration of rock with no chemical alteration. For example, the volumetric



Figure 2.6: Goldich's sequence of mineral susceptibility to weathering. Minerals listed at the top generally weather faster than minerals listed at the bottom.

increase of water in the frozen state or of salts at increasing hydration can result in pressures exceeding the tensile strength of a rock. If water or salt is present within rock fractures and pores, the rock may be shattered during temperature cycles or periodically occurring wet and dry conditions. Physical weathering processes generally increase the rock surface area available to chemical weathering processes.

2.3.2 Chemical weathering

Chemical weathering processes can be divided into three categories [*Bland and Rolls, 1998*]:

- Solution of ions and molecules;
- The production of new materials, e.g. clay minerals, oxides and hydroxides;
- The release of residual unweathered materials, e.g. quartz and gold.

The mechanisms which are components of these categories are hydration, solution, oxidation and reduction, hydrolysis, and complex formation via chelation. In aqueous chemical weathering, the redox potential (Eh), the acidity (pH), and the nature and activity of ions in solution become important variables whose combination determines which products are eventually

precipitated. Chemical weathering weakens a rock and promotes physical weathering processes in return.

2.3.3 Biological weathering

Life has been discovered in all parts of our planet that are within human reach. The important role of biogenic weathering is increasingly recognized [e.g., *Schlesinger*, 2003]. Biological weathering can be seen as a combination of a wide variety of physical weathering processes such as roots penetrating and widening fractures in a rock, and chemical weathering processes such as reactions with humic acids from decaying organisms. The earliest evidence for life on Earth stems from geochemical markers left in the rock record long before the rise of vertebrates [e.g., *Knoll*, 2003]. It is worth looking for such biomarkers on other planets.

2.3.4 Space weathering

Atmosphere-less bodies in the Solar System such as the Moon or asteroids can undergo modification by interaction with the solar wind. Interaction with solar flares and cosmic rays, and impacts of micrometeorites and larger meteorites also fall under the term space weathering.

Chapter 3

Velocity Calibration of the MER Flight Instruments

The Mössbauer spectrometers on board of the Mars Exploration Rovers are the first ever which have been launched into space and successfully returned data from the surface of another planet. All Mössbauer spectra obtained on Mars during the MER mission are released within six months of acquisition to the general public via the world wide web¹. Raw and calibrated data are released. The MER Mössbauer instruments have unique features which require special calibration procedures. Documents describing these calibration procedures are posted alongside Mössbauer spectra. The released calibrated spectra and accompanying documents are the result of the work presented in this chapter.

The interpretation of Mössbauer spectra is impossible without precisely knowing the source velocity relative to an absorber. One can measure the source velocity directly using a Michelson interferometer [e.g., *Fritz and Schulze*, 1968]. However, a simpler and more accurate way is the use of a standard absorber with a well-known magnetic hyperfine splitting such as iron metal ($\alpha\text{-Fe}^0$, Table 3.1).

Mössbauer drive velocity calibration for the MIMOS II flight instruments was done in three different ways to ensure redundancy. Prior to flight the drive system of each instrument, Flight Model 2 (FM2) for the rover Spirit and FM3 for the rover Opportunity², was calibrated as a function of the software velocity settings by measuring an $\alpha\text{-Fe}^0$ foil standard in backscatter mode (Chapter 3.1). During the mission, the CCT (Compositional Cal-

¹Mössbauer data from the Mars Exploration Rover mission are available from the NASA Planetary Data System (PDS) at <http://pds.jpl.nasa.gov/>; Washington University's MER Analyst's Notebook at <http://anserver1.eprsl.wustl.edu/>; homepage of AK-Klingelhöfer at <http://iacgu32.chemie.uni-mainz.de/mer/> [e.g., *Klingelhöfer et al.*, 2005].

²FM1 served as Flight Spare.

Table 3.1: Hyperfine parameters of α -Fe at room temperature [Muir *et al.*, 1967].

Absorber	δ (mm/s)	ΔE_Q (mm/s)	ΔE_M (mm/s)	B_{hf} (T)
$\alpha\text{-Fe}^0$	0^a	0	10.657	33.0^b

^aAll values of the isomer shift δ in this work are quoted relative to α -Fe.

^bFrom [Preston *et al.*, 1962]

ibration Target) was measured in several runs to verify the functionality of MIMOS II (Chapter 3.4). The primary method for velocity calibration are the internal reference target and detector configured in transmission geometry. The Mössbauer spectrum of the internal calibration target is measured simultaneously with each backscatter experiment. That way the actual drive velocity is always well-defined, regardless of the environmental conditions which the instrument is working at.

When Mössbauer experiments are performed at lower or elevated temperatures in the lab, the drive system is usually situated outside the kryostat or furnace and kept at room temperature. The MER instruments, however, are exposed to the Martian environment and the effects of temperature on drive performance have to be considered. When the MER instruments were tested not as stand alone setups in the lab but in a setup resembling the electronic connections on MER, the drive system started 'ringing', i.e. experienced positive feedback at reduced temperatures well within the Martian diurnal range. To avoid that effect, the amplification within the control amplifier had to be reduced to yield additional phase margin³. The reduced amplification resulted in a larger than usual degradation of the velocity linearity and had to be corrected by software (Chapter 3.2). The output of the maximum velocity at a given software velocity setting also depends on temperature. This dependence is evaluated in Chapter 3.3.

Operation time is an important consumable on a spacecraft. One way to minimize the time needed for the acquisition of a Mössbauer spectrum of statistically good quality, is to irradiate as much of the sample as possible with source radiation. This can be achieved through an increase of the opening angle of the γ -ray beam which is controlled by the radius of the collimator. However, increasing the opening angle gives rise to a geometrical effect known as cosine smearing (Chapter 3.5).

³The analysis and adjustment of instrument electronics was performed by Dipl.-Ing. B. Bernhardt.

3.1 Determination of maximum velocity

When an electric current is applied to the drive system, a force F acts on the aluminium tube and the parts rigidly connected to it

$$F_{tube} = F_{drivecoil} + 2F_{spring} = Il_{drivecoil}B_{coilgap} + 2k\Delta x, \quad (3.1)$$

where I corresponds to the current flowing through the drive coil, $l_{drivecoil}$ is the wire length of the drive coil, B is the magnetic flux in the coil gap of the permanent magnets, k is the spring constant of the Kapton springs, and Δx is the deflexion from the equilibrium position of the tube. The force of the springs acts in the opposite direction of the force acting on the drive coil and is multiplied by two because there are two springs in the system. However, because of the soft Kapton springs (i.e., small spring constant k) and in the case of small deflexions, $F_{spring} \ll F_{drivecoil}$ and is neglected in the following. A voltage U_{ind} is induced in the pickup coil, which is proportional to the velocity of the pickup coil and therefore of the tube and the Mössbauer sources rigidly connected to it at opposite ends

$$U_{ind} = v_s l_{pickupcoil} B_{coilgap}, \quad (3.2)$$

where v_s is the velocity of the source, $l_{pickupcoil}$ the wire length of the pickup coil, and $B_{coilgap}$ the magnetic field in the coil gap of the permanent magnet. This induced voltage is compared to a triangular reference signal U_{ref}

$$U_{ref} - U_{ind} = U_{ds}. \quad (3.3)$$

The difference U_{ds} is fed back into the control amplifier with a certain adjustable gain. The feedback loop adjusts the current in the drive coil so that

$$U_{ind} \cong U_{ref}. \quad (3.4)$$

The differential signal (or error signal) $-U_{ds}$ can be read out and used to check the performance of the drive system. The maximum velocity v_{max} is proportional to the amplitude of the reference signal set by the control amplifier

$$v_{max} = \frac{U_{ref,p-n}}{2l_{pickupcoil}B}, \quad (3.5)$$

where $U_{ref,p-n}$ is the difference between positive and negative amplitude of the reference signal. The wire length of the pickup coil and the magnetic field in the coil gap of the permanent magnet may vary between different drives. In addition, the software sets a number, the internal maximum velocity value

$v_{int} \neq v_{max}$ which is also proportional to $U_{ref,p-n}$. The proportionality factor may again differ from drive to drive.

Prior to flight, the drive systems of the flight instruments FM2 and FM3 were calibrated as a function of the software velocity settings. An $\alpha\text{-Fe}^0$ foil standard was measured in backscattering mode for different v_{int} values preset by the firmware. Corresponding values of v_{max} were evaluated from fits of the resulting Mössbauer spectra (Figure 3.1).

3.2 Non-linear velocity

In optimized laboratory drives for the MIMOS II setup the deviation of the real velocity (as measured by the pickup coil) from the nominal velocity given by the triangular reference signal is smaller than 0.1 %. In that case it is not necessary to take the differential signal into account during fitting procedures. Instrument performance tests with the JPL⁴-produced flexprint cable which connects the MIMOS II electronics and the sensorhead on the Mars Exploration Rovers were done late during the Assembly, Test and Launch Operations (ATLO) period. The length of the cable and therefore a large impedance in the grounding wire had unforeseen effects on the instrument performance: The drive system started 'ringing' at low temperatures (~ 200 K). To avoid this problem during Mars surface operations, the amplification in the feedback gain of the drive system was reduced by about a factor of 10 in case of Opportunity and a bit lower on Spirit (unpublished data provided by B. Bernhardt, 2004). This reduction of the amplification resulted in a degradation of the velocity linearity. The differential signal now had to be taken into account in order to enable the fitting of Mössbauer spectra.

3.2.1 Adjusting the fitting routines

The fit routines used in this work assume a linear velocity dependence. They produce a linear triangular velocity scale for each of the 512 channels of MIMOS II. The value v_{max} in mm/s is read in from a parameter file. Then $-v_{max}$ is assigned to channels 0.5 and 512.5, $+v_{max}$ is assigned to channel 256.5, and velocity values are calculated in equal spacings for channels 1 to 256 and 257 to 512, respectively. The parameter v_{max} may be a variable in the case of fitting a calibration target, where for example for $\alpha\text{-Fe}^0$ the magnetic hyperfine splitting is kept as a constraint. After fitting the reference target, the obtained v_{max} value is kept as a constraint for the evaluation of other data.

⁴Jet Propulsion Laboratory, California Institute of Technology, Pasadena/California.

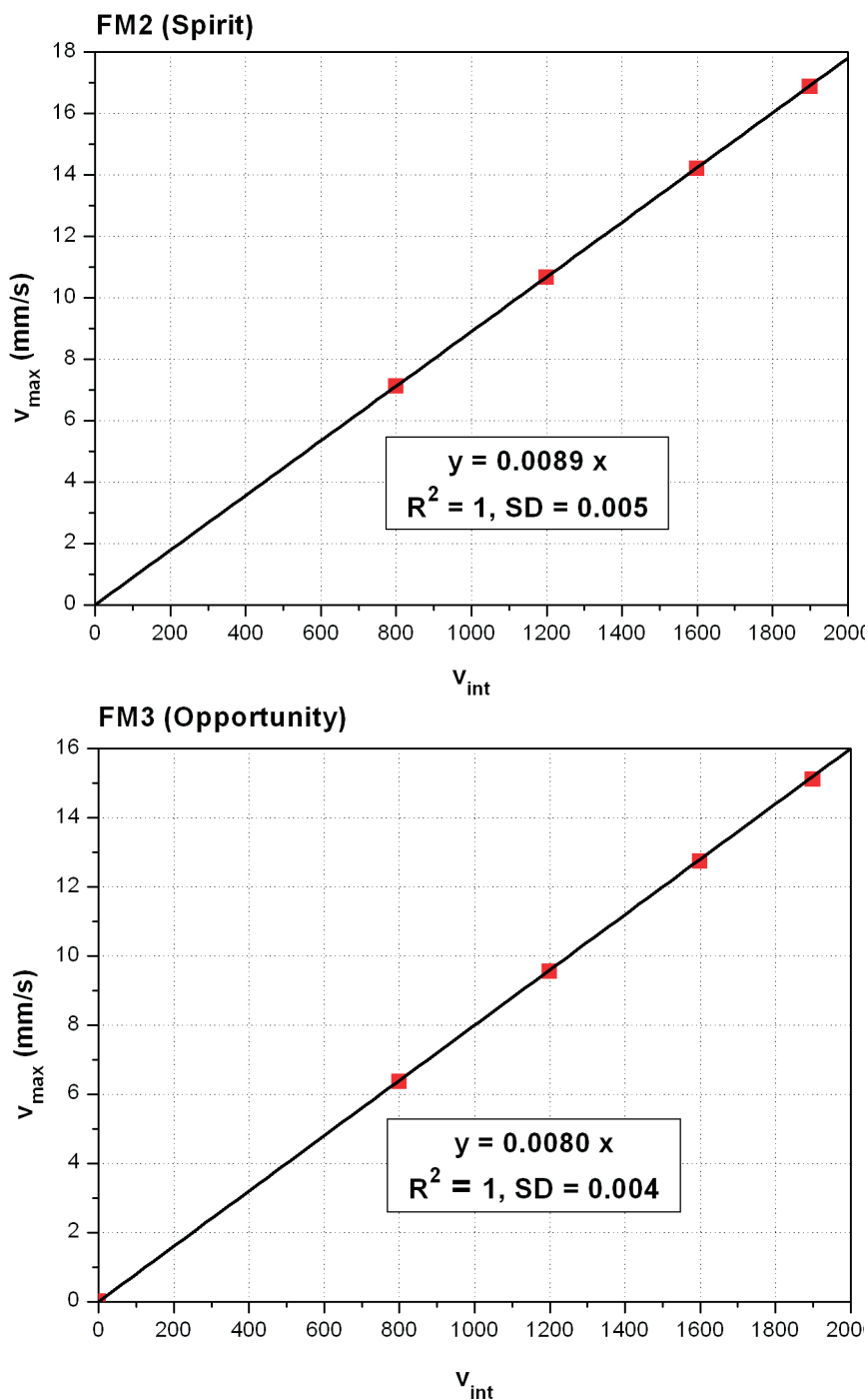


Figure 3.1: Calibration curves of the internal maximum velocity values v_{int} versus the real v_{max} for the FM2 and FM3 sensorheads at room temperature. The proportionality factors are given in the equations. Errors for v_{max} are smaller than the symbols. The coefficients of determination R^2 were determined using the linear fit routine of Microcal Origin. Standard deviations SD are given as a measure of uncertainty.

Figure 3.2 shows the spectrum of an $\alpha\text{-Fe}^0$ reference target measured with FM2 in backscattering geometry. The typical sextet pattern of $\alpha\text{-Fe}^0$ appears twice in the spectrum, the second half of the spectrum being the mirror image of the first half of the spectrum. Differences in the count rate result from the so-called geometry effect - during one half of the velocity sweep the source moves from the equilibrium point of the drive towards the target and back whereby the count rate increases; during the other half the source moves from the equilibrium point away from the target and back. If the two halves of the Mössbauer spectrum taken during one period of the velocity sweep are folded with respect to their mirror image, the geometry effect disappears in first order. In the case of a linear and symmetric velocity signal, folding simply involves summing the counts of channels with corresponding velocity, i.e. channels 1 and 512, 2 and 511, ..., 256 and 257.

If the velocity signal is not sufficiently linear and symmetric any more, folding in this simple manner is not possible. The real velocities in corresponding channels are now different and corresponding spectral lines do not overlap (Figure 3.3). For the evaluation of Mössbauer spectra the knowledge of v_{max} alone does not suffice any more. However, with the knowledge of the differential signal one can calculate the real velocity for each channel: The

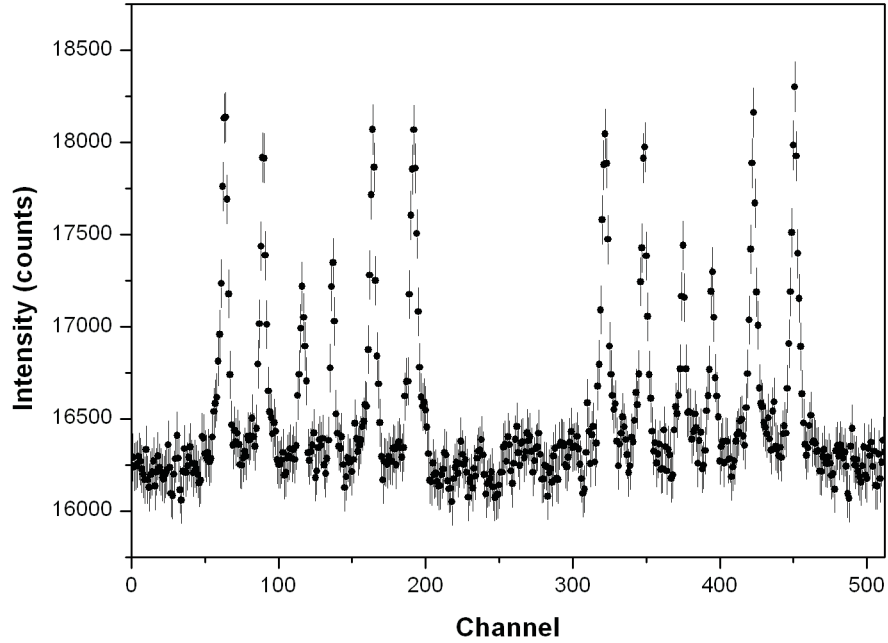


Figure 3.2: Unfolded backscatter spectrum of an $\alpha\text{-Fe}^0$ foil obtained with the FM2 sensorhead.

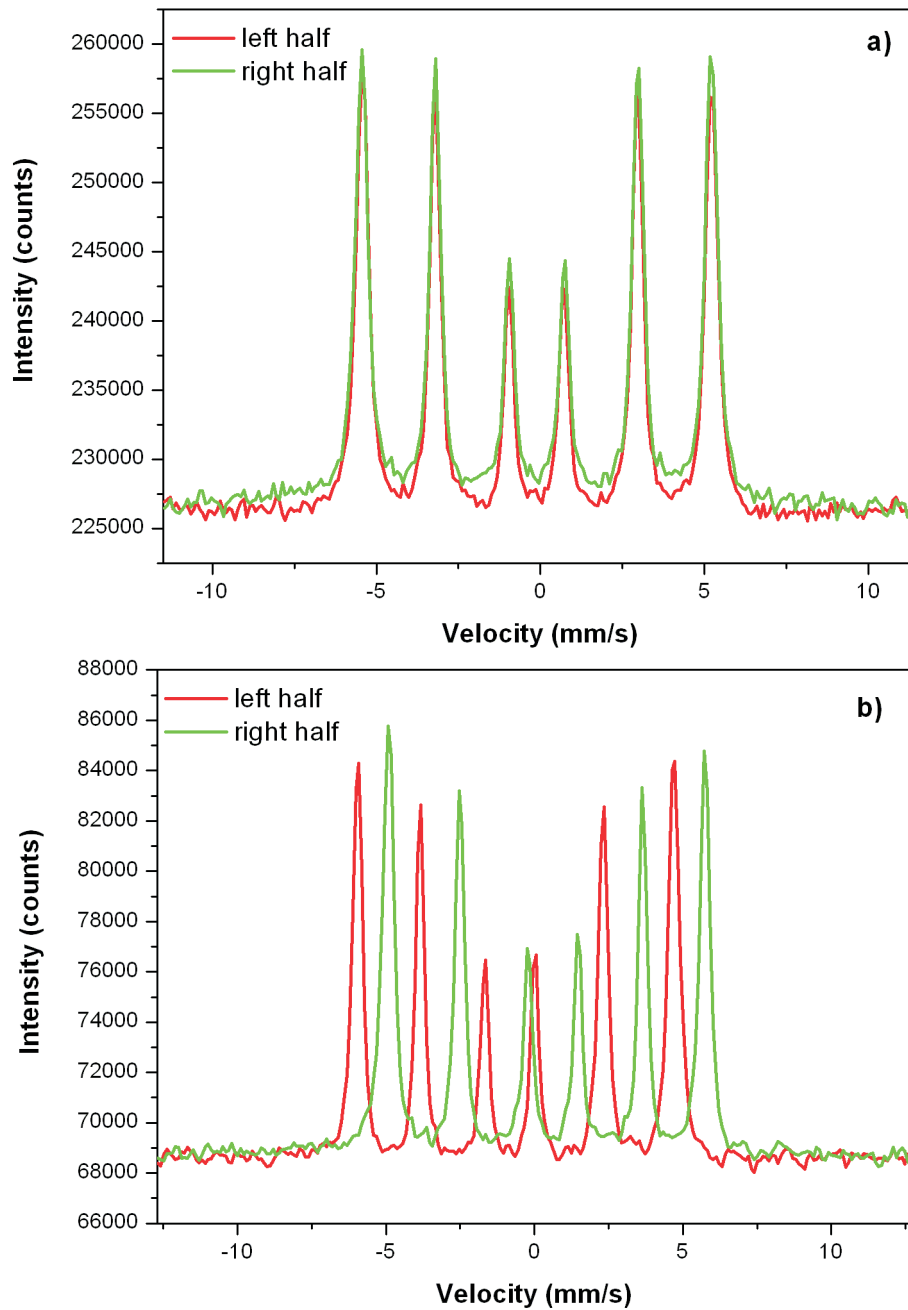


Figure 3.3: Left and right halves of an $\alpha\text{-Fe}^0$ spectrum folded at the center point of an unfolded spectrum assuming linear velocity dependence for a) a laboratory MIMOS II setup, and b) FM3, the Opportunity sensorhead. In b) line positions of left and right halves of the spectrum no longer overlap as a result of a non-linear velocity dependence.

differential signal $U_{ds,i}$ is measured and stored in mV per channel i and can be translated into a velocity $v_{ds,i}$ in mm/s by

$$v_{ds,i} = \frac{2v_{max}U_{ds,i}}{nAU_{ref,p-n}}, \quad (3.6)$$

where n is the number of velocity cycles of the drive (usually 250, the number is adjustable by software) and A is the amplification of U_{ds} in the control amplifier of the feedback circuit. Because $U_{ds} = U_{ref} - U_{ind}$, subtraction of $v_{ds,i}$ from the triangular linear velocity calculated from v_{max} as described above, yields the real, non-linear velocity $v_{real,i}$ (Figure 3.4). Because of the good linear proportionality between v_{max} and v_{int} (Figure 3.1) the ratio $v_{max}/U_{ref,p-n}$ is constant. Thus the conversion factor is independent of v_{max} . Also one does not need to know $U_{ref,p-n}$. Generally only v_{int} is known. Uncertainties of the amplification factor A arise, because only nominal resistance values are known for the electronic parts in the feedback circuit, in particular for the pickup coil. The conversion factors were thus determined experimentally by finding the best overlap of lines from left and right halves in folded reference spectra. For FM2 on Spirit the experimentally determined conversion factor is $0.0079(1) \text{ mm s}^{-1} \text{ mV}^{-1}$, for FM3 on Opportunity $0.0064(1) \text{ mm s}^{-1} \text{ mV}^{-1}$.

On Mars, the differential signal was read out after deployment of the sensorhead to a target prior to every acquisition of a Mössbauer spectrum. The measured differential signal as contained in raw data from the instruments is biased and needs to be centered on a zero line before it can be translated into v_{ds} . The measured offset is completely due to artificial offsets of the ADC system. The mean values of the differential signal and of the real velocity must be exactly zero.

$$U_{ds_centred}(i) = U_{ds}(i) - \frac{\sum_{i=1}^{512} U_{ds}(i)}{512} \quad (3.7)$$

yields a centered differential signal. Here i denotes a particular channel number. The fitting routines used in this work were adjusted to read in the differential signal and to calculate the non-linear, real velocity scales.

3.2.2 Folding point

The nominal velocity is a triangular waveform which starts and ends at negative v_{max} - channel 0.5 and 512.5, respectively - and reaches positive v_{max} nominally at channel 265.5. However, this channel assignment (folding point) is subject to small variations and needs to be determined using a variable parameter in fitting routines. In the fitting routines used in this work the

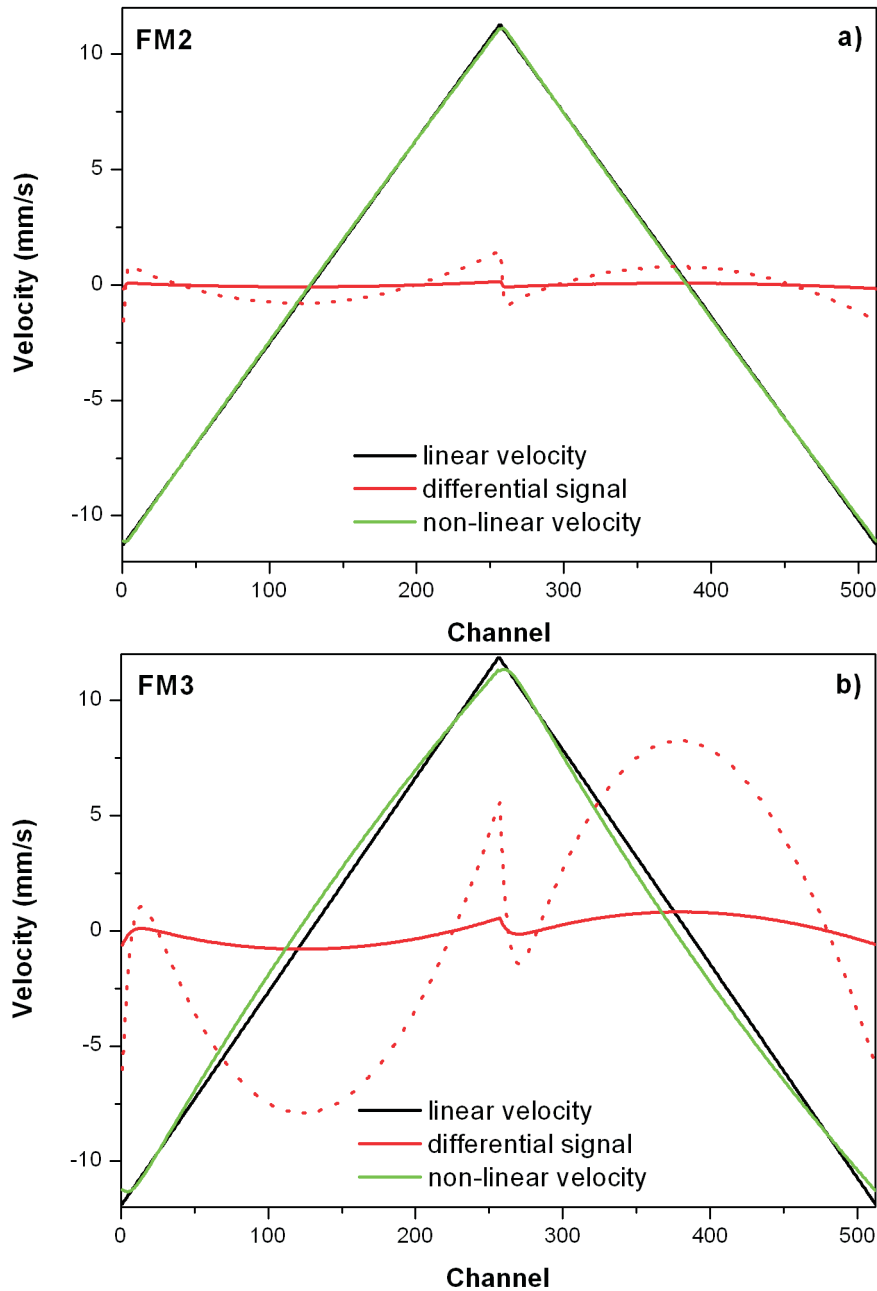


Figure 3.4: Linear velocity signal, differential signal, and resulting non-linear velocity for the a) FM2 sensorhead on Spirit, and the b) FM3 sensorhead on Opportunity. The red dotted lines are the respective differential signals tenfold. Whereas FM2 linear and non-linear velocities are still in reasonable agreement, they differ significantly for FM3.

folding point is entered as a dimensionless fraction of a channel into the parameter file and varied during the fitting procedure. Interpolation between the count rates of two adjacent channels and a subsequent shift by the fraction of a channel as given by the folding point parameter, shifts the spectrum around the center. A positive value shifts the center of the spectrum to higher channels. Alternatively, one can shift the velocity scale.

3.3 Temperature dependence of v_{max}

The drive systems inside the MIMOS II sensorheads on board of the Mars Exploration Rovers are subject to the Martian diurnal temperature range (Figure 3.5). The influence of temperature changes on the performance of the drive system needs to be considered. *Teucher* [1994] investigated three different effects: 1) the influence of temperature changes on the mechanical properties of the Kapton springs, 2) the influence of temperature changes on the resistance of the pickup coil, and 3) the influence of temperature on the magnetic field of the coil gaps in the permanent magnets.

The value of the Kapton spring stiffness and the dampening increases with decreasing temperature. As a result the resonance frequency of the springs shifts to higher values. This does not affect v_{max} , but may have an influence on the velocity linearity of the drive, i.e. the differential signal.

The temperature dependent resistance $R(T)$ of a wire is given by

$$R(T) = \frac{\rho(T)l}{A}, \quad (3.8)$$

whereby $\rho(T)$ is the specific resistance of the wire material, l is the length of the wire, and A is its cross-sectional area. For Cu [*Moeller and Fricke*, 1971]

$$\rho(T) = \rho_{293}(1 + \alpha_{293}(T - 293 K) + \beta_{293}(T - 293 K)^2), \quad (3.9)$$

where T is the temperature in degrees Kelvin, $\rho_{293} = 0.01786 \Omega \text{ mm}^2 \text{ m}^{-1}$, $\alpha_{293} = 3.93 \times 10^{-3} K^{-1}$, $\beta_{293} = 6 \times 10^{-7} K^{-2}$. *Teucher* [1994] concluded that the temperature dependence of the resistance of the copper wire of the coils in the drive has no influence on v_{max} , because it does not influence U_{ref} . However, the resistance of the pickup coil enters into the calculation of the amplification factor of the feedback system and thus the conversion factor for the differential signal (equation 3.6) becomes temperature dependent. The temperature-dependent behavior of other electronic parts in the feedback system is not known.

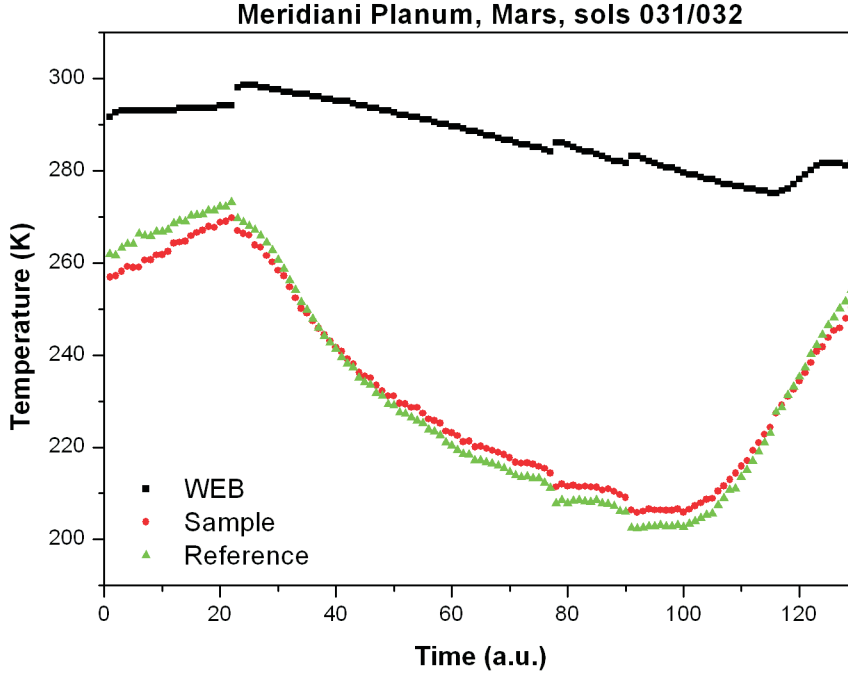


Figure 3.5: Temperature record of a full sol at Meridiani Planum, Mars, as measured by the three temperature sensors of Opportunity's MB sensorhead inside the Warm Electronics Box (WEB); on the MB contact plate; and at the internal reference target. The measurement started at noon Local Solar Time (LST) during sol 31 of Opportunity's mission and ended at noon LST of sol 32. Discontinuities occur when the MB instrument is switched into idle mode during communication passes. While outside temperatures decrease the on-board computer raises the temperature inside the Warm Electronics Box (WEB). The time is given in arbitrary units (a.u.) because information about the duration of the communication passes was not at hand.

The magnetic field B in the coil gaps of the permanent magnets increases with decreasing temperature T

$$B(T) = B_{RT}(1 + \alpha_R(T - 293 \text{ K})), \quad (3.10)$$

where α_R is the temperature coefficient of the remanence. Vakuumschmelze GmbH in Hanau, the company producing the SmCo permanent magnets, provided $\alpha_R = -0.00025 \text{ K}^{-1}$ for temperatures ranging from -100°C to 20°C . According to equation 3.5 $B(T)$ is inversely proportional to v_{max} . At identical v_{int} settings v_{max} thus decreases with decreasing temperature.

3.3.1 Experimental determination of the temperature dependence of v_{max}

Using MIMOS II, a spectrum of the internal reference target is obtained simultaneously with every Mössbauer backscatter spectrum. Reference and backscatter spectra are binned in individual temperature windows (Chapter 2.2.3). For a given v_{int} value the temperature dependence of v_{max} can be determined by fitting the reference spectra in individual temperature bins. The internal reference target⁵ is composed of a metallic iron foil ($\alpha\text{-Fe}^0$, 30 % enriched in ^{57}Fe), and a powder consisting of the minerals hematite ($\alpha\text{-Fe}_2\text{O}_3$, 95 % enriched in ^{57}Fe) and magnetite (Fe_3O_4). The FM3 sensorhead contains more of the hematite/magnetite powder relative to the $\alpha\text{-Fe}^0$ than the FM2 sensorhead, thus preventing a confusion between the two sensorheads (Figure 3.6).

The two components of the MER reference target, the $\alpha\text{-Fe}^0$ foil and the hematite/magnetite powder, were investigated separately using a standard laboratory Mössbauer transmission setup. The components were cooled down in a kryostat. Mössbauer drive and source remained outside the kryostat at room temperature. The drive system was calibrated by measuring the $\alpha\text{-Fe}^0$ foil at room temperature and fitting the spectrum with the values from Table 3.1. The individual components of the MER reference target were then cooled down to and kept at temperatures corresponding to the center of a particular temperature window defined for the MER sensorheads. The temperature difference between source and absorber resulted in changes of the center shift δ which were not observed during MER surface operations where source and sample are usually at the same temperature within 10 K (Figure 3.5). However, the temperature difference between source and absorber does not influence the magnetic splitting. Temperatures, corresponding temperature windows, and the obtained Mössbauer parameters for the individual components are listed in Tables 3.2 and 3.3. The magnetic splitting against temperature of the measured $\alpha\text{-Fe}^0$ foil was compared to values obtained by *Preston et al.* [1962], who used Mössbauer and NMR spectroscopy to determine the magnetic hyperfine field B_{hf} of iron down to a temperature T of 4 K. The temperature-dependent behavior of B_{hf} for a ferromagnetic substance can be approximated by a Brillouin function. Because the temperature range of interest ($\sim 180\text{ K} - 300\text{ K}$) is far away from the Curie temperature (1043 K for Fe), their data were fit using a simpler polynomial

⁵The internal reference targets for the MER Mössbauer spectrometers were assembled by Dr. S. Kane.

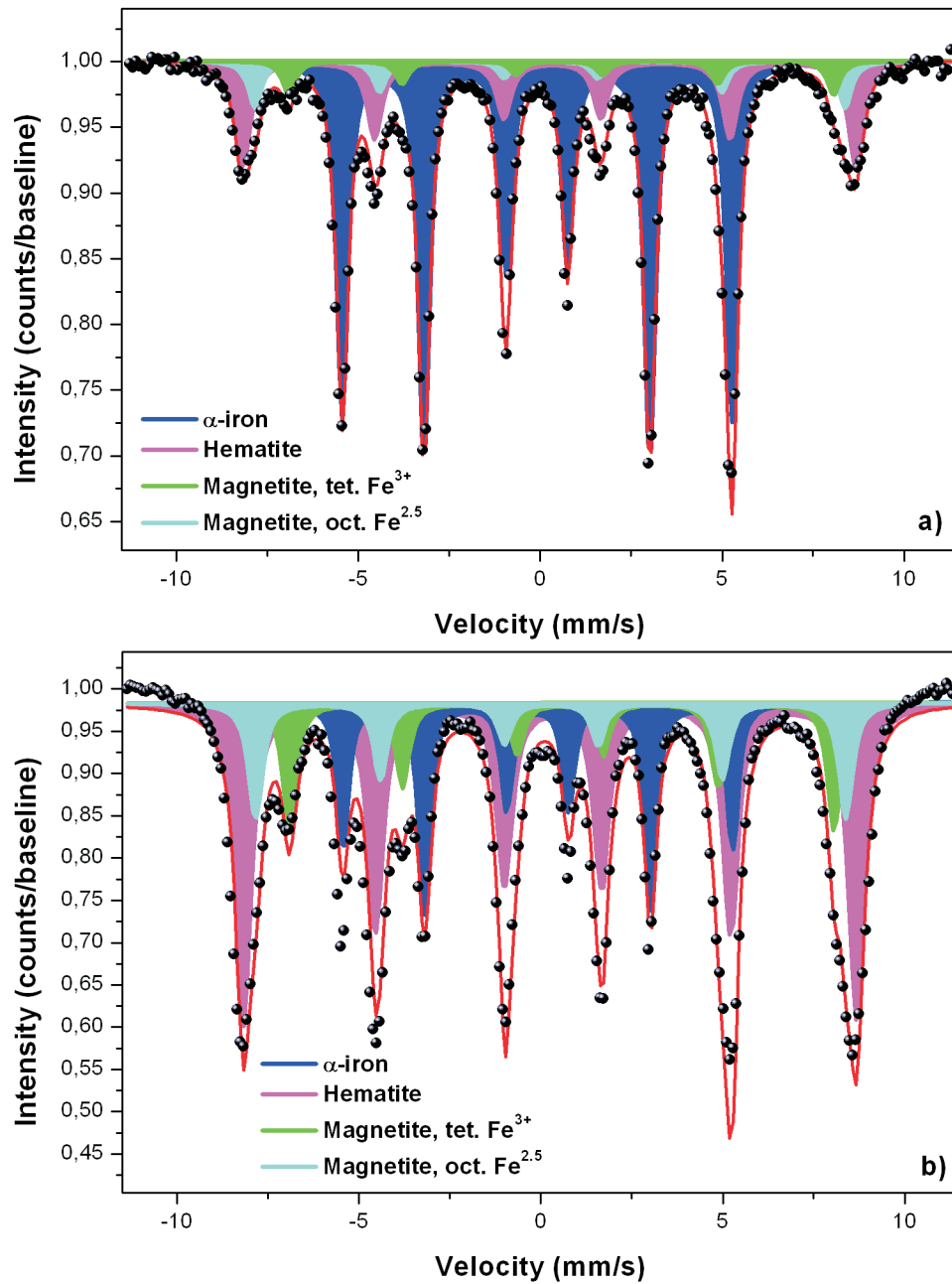


Figure 3.6: Mössbauer transmission spectra of the internal reference target from a) FM2 on Spirit and b) FM3 on Opportunity. Subspectra of individual components are shown. The spectra are from the m9 (250 K - 260 K) temperature window and were obtained on Mars on a) sol 14 of Spirit's mission and b) sol 11 of Opportunity's mission.

function (Figure 3.7)

$$B_{hf}(T) = B_0 + \alpha T + \beta T^2, \quad (3.11)$$

where $B_0 = 33.802(3) T$, $\alpha = -0.00062(6) T/K$, and $\beta = -7.2(2) \times 10^{-6} T/K^2$. This function was used to determine the hyperfine splitting at relevant temperatures. There is a good agreement between the measurement and the data from *Preston et al.* [1962] (Figure 3.8). The polynomial function derived from the fit to the *Preston et al.* [1962] data was used in the following to calculate the hyperfine splitting of Fe for all MIMOS II temperature windows between 180 K and 290 K.

Spectra of the hematite/magnetite powder mixture were obtained at the same set of temperatures (Table 3.3) using the same calibration of the laboratory drive as above. The magnetite in this mixture is non-stoichiometric, i.e. the ratio of subspectral areas of the two sextets resulting from Fe^{2+} and Fe^{3+} in octahedral lattice positions and Fe^{3+} in tetrahedral lattice positions is smaller than the stoichiometric 2:1 ratio. One explanation for this deviation, other than impurities such as Ti and Al, may be the presence of maghemite ($\gamma\text{-}Fe_2O_3$), which is isostructural with magnetite. X-ray diffraction spectra of the magnetite/hematite mixture do not indicate any phase other than hematite and magnetite [*de Souza*, 2004]. However, according to *Vandenberghé et al.* [2000] neither Mössbauer spectroscopy nor XRD can distinguish between non-stoichiometric magnetite or magnetite/maghemite mixtures.

For well-crystalline hematite, the Morin transition where hematite changes

Table 3.2: Measured hyperfine parameters of the $\alpha\text{-}Fe^0$ foil used in the reference absorbers of the FM2 and FM3 sensorheads.

Phase	T (K)	T- window	δ^{ab} (mm/s)	ΔE_Q (mm/s)	ΔE_M (mm/s)	B_{hf} (T)	Γ (mm/s)	Area (%)
$\alpha\text{-}Fe^0$	205	m4	0.05	0.00	10.79	33.4	0.36	100
$\alpha\text{-}Fe^0$	215	m5	0.05	0.00	10.77	33.3	0.36	100
$\alpha\text{-}Fe^0$	225	m6	0.04	0.00	10.76	33.3	0.36	100
$\alpha\text{-}Fe^0$	235	m7	0.04	0.00	10.75	33.3	0.36	100
$\alpha\text{-}Fe^0$	245	m8	0.03	0.01	10.73	33.2	0.36	100
$\alpha\text{-}Fe^0$	255	m9	0.03	0.01	10.72	33.2	0.36	100
$\alpha\text{-}Fe^0$	RT	m13	0.00	0.00	[10.657]	[33.0]	0.35	100

^aRelative to $\alpha\text{-}Fe^0$ at room temperature.

^bTypical errors for the transmission measurement are ± 0.02 mm/s for δ , ΔE_Q , and Γ , ± 0.03 mm/s for ΔE_M , ± 0.1 T for B_{hf} , and $\pm 2\%$ for the area.

Table 3.3: Hyperfine parameters of the hematite/magnetite powder mixture used in the reference absorbers of the FM2 and FM3 sensorheads. Hm: Hematite; Mt 3+: Magnetite, tetrahedral Fe^{3+} ; Mt 2.5+: Magnetite, octahedral Fe^{2+} and Fe^{3+} .

Phase	T (K)	T- window	δ^{ab} (mm/s)	ΔE_Q (mm/s)	ΔE_M (mm/s)	B_{hf} (T)	Γ (mm/s)	Area (%)
Hm			0.43	0.29	17.20	53.3	0.50	70
Mt 3+	205	m4	0.44	0.15	16.36	50.7	[0.44] ^c	16
Mt 2.5+			0.70	0.06	15.16	46.9	[0.45]	14
Hm			0.43	0.28	17.18	53.2	0.49	67
Mt 3+	215	m5	0.43	0.14	16.36	50.7	[0.49]	19
Mt 2.5+			0.69	0.07	15.13	46.9	[0.46]	14
Hm			0.42	0.26	17.14	53.1	0.51	69
Mt 3+	225	m6	0.44	0.11	16.34	50.6	[0.44]	17
Mt 2.5+			0.69	0.06	15.11	46.8	[0.43]	14
Hm			0.42	0.21	17.08	52.9	0.53	71
Mt 3+	235	m7	0.44	0.10	16.25	50.3	[0.44]	16
Mt 2.5+			0.69	0.06	15.05	46.6	[0.44]	13
Hm			0.41	0.09	17.00	52.6	0.57	72
Mt 3+	245	m8	0.42	0.04	16.23	50.3	[0.44]	16
Mt 2.5+			0.69	0.04	15.01	46.5	[0.44]	12
Hm			0.41	-0.08	16.86	52.2	0.51	70
Mt 3+	255	m9	0.39	-0.02	16.23	50.3	[0.44]	16
Mt 2.5+			0.67	0.00	14.97	46.4	[0.43]	14
Hm			0.38	-0.19	16.64	51.5	0.41	65
Mt 3+	RT	m13	0.36	-0.10	15.99	49.5	[0.44]	20
Mt 2.5+			0.64	0.01	14.73	45.6	[0.43]	15

^aRelative to $\alpha\text{-Fe}^0$ at room temperature.

^bTypical errors for the transmission measurement are ± 0.02 mm/s for δ , ΔE_Q , and Γ , ± 0.03 mm/s for ΔE_M , ± 0.1 T for B_{hf} , and $\pm 2\%$ for the area.

^cValues in square brackets were kept constant during the fitting procedure

from a weakly ferromagnetic state into an antiferromagnetic state, happens at 260 K [e.g., *Murad*, 1988, and references therein]. This is manifest in a change of the value of ΔE_Q from a negative to a positive value while crossing the Morin temperature towards lower temperatures. In the reference absorber material the change is observed below 255 K and is gradual rather than sudden. This may be a result of the admixed magnetite or an indication of a distribution of particle sizes and/or different degrees of crystallinity

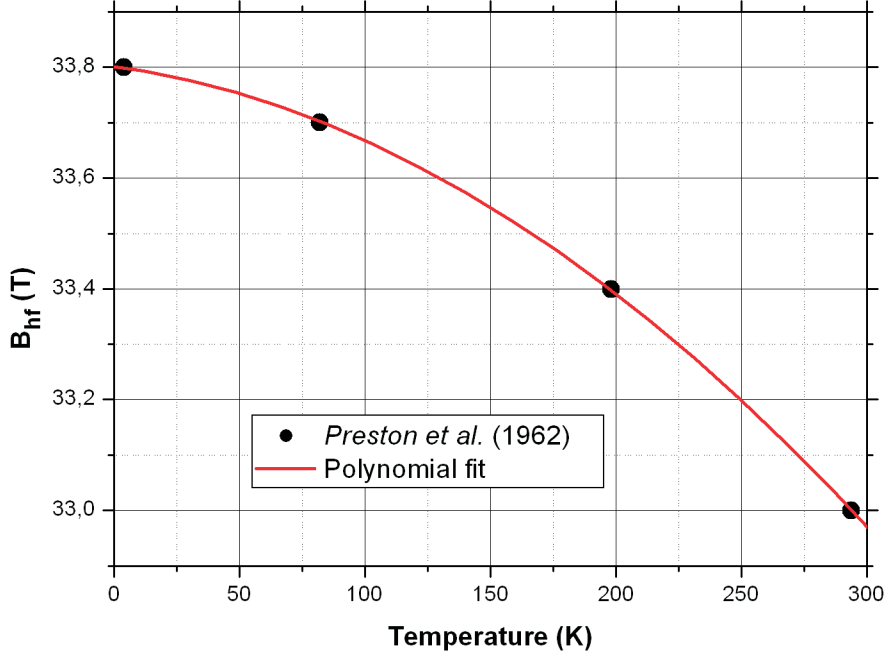


Figure 3.7: The temperature dependence of the splitting of the magnetic hyperfine field B_{hf} of α -iron. Data points are from *Preston et al.* [1962]. The red line is a polynomial fit to the data points.

within the powder.

The hyperfine parameters derived from the kryostat measurements (Tables 3.2 and 3.3) were used as constraints in fits of individual temperature window reference spectra obtained on Mars. For FM2 on Spirit a ~ 14 h measurement from sol 050 of Spirit's mission, spanning a temperature range from ~ 200 K to 280 K, was used to evaluate $v_{max}(T)$ values. For FM3 reference spectra from all measurements between sols 195 and 560 were summed over individual temperature windows. The sum of each temperature window was fitted separately. Only temperature windows for which laboratory data of the single components of the reference absorber are available were evaluated (m4 - m9). In the case of FM2, the m4 reference spectrum contained statistics that were too low to yield a reliable fit.

In Figure 3.9, the experimentally obtained $v_{max}(T)$ values (Table 3.4) for the FM2 and FM3 sensorheads were plotted against temperature. With equations 3.5 and 3.10 the expected temperature dependence of $v_{max}(T)$ for temperatures below room temperature is given by

$$v_{max}(T) = \frac{U_{ref,n-p}}{2lB_{RT}(1 + \alpha_R(T - 293 K))}, \quad (3.12)$$

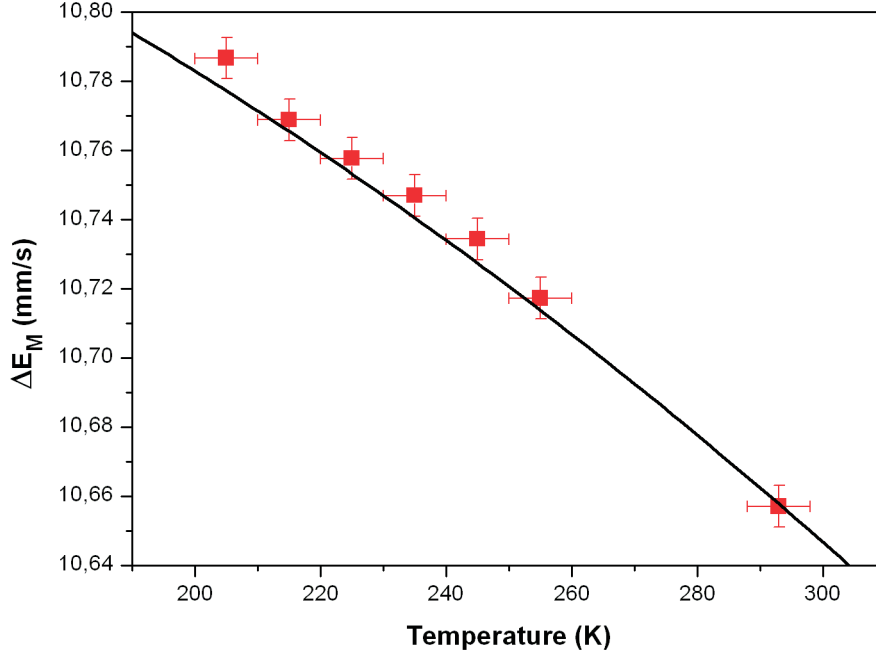


Figure 3.8: Comparison between the hyperfine field ΔE_M of α -iron derived from laboratory measurements (red squares) with the α - Fe^0 foil used in the MER reference absorbers and data determined by *Preston et al.* [1962]. The black line represents the polynomial fit to their data. The error bars result from an assumed uncertainty in temperature of ± 5 K. That the laboratory measurements plot consistently above the polynomial fit line can be explained if room temperature was higher than 293 K during the calibration measurement.

where B_{RT} is the magnetic field of the permanent magnets in the coil gap at room temperature. The proportionality factor $U_{ref,n-p}/(2lB_{RT})$ was derived from the calibration curves in Figure 3.1. At room temperature the proportionality factor equals v_{max} . With the default v_{int} values of 1300 for FM2 and 1500 for FM3, the proportionality factor equals 11.57 mm/s for FM2 and 12.00 mm/s for FM3, respectively. The solid black lines in Figure 3.9 were calculated substituting these proportionality factors into equation 3.12. The experimentally determined data points follow a generally similar pattern as given by equation 3.12, but do not fall on that line. Linear fits through the data points (dashed lines in Figure 3.9) show different inclines. The different inclines may be explained by values of α_R varying slightly between individual magnets used in the sensorheads. Extrapolation of the linear fits through the data points for both sensorheads yield $v_{max}(T)$ values at room temperature

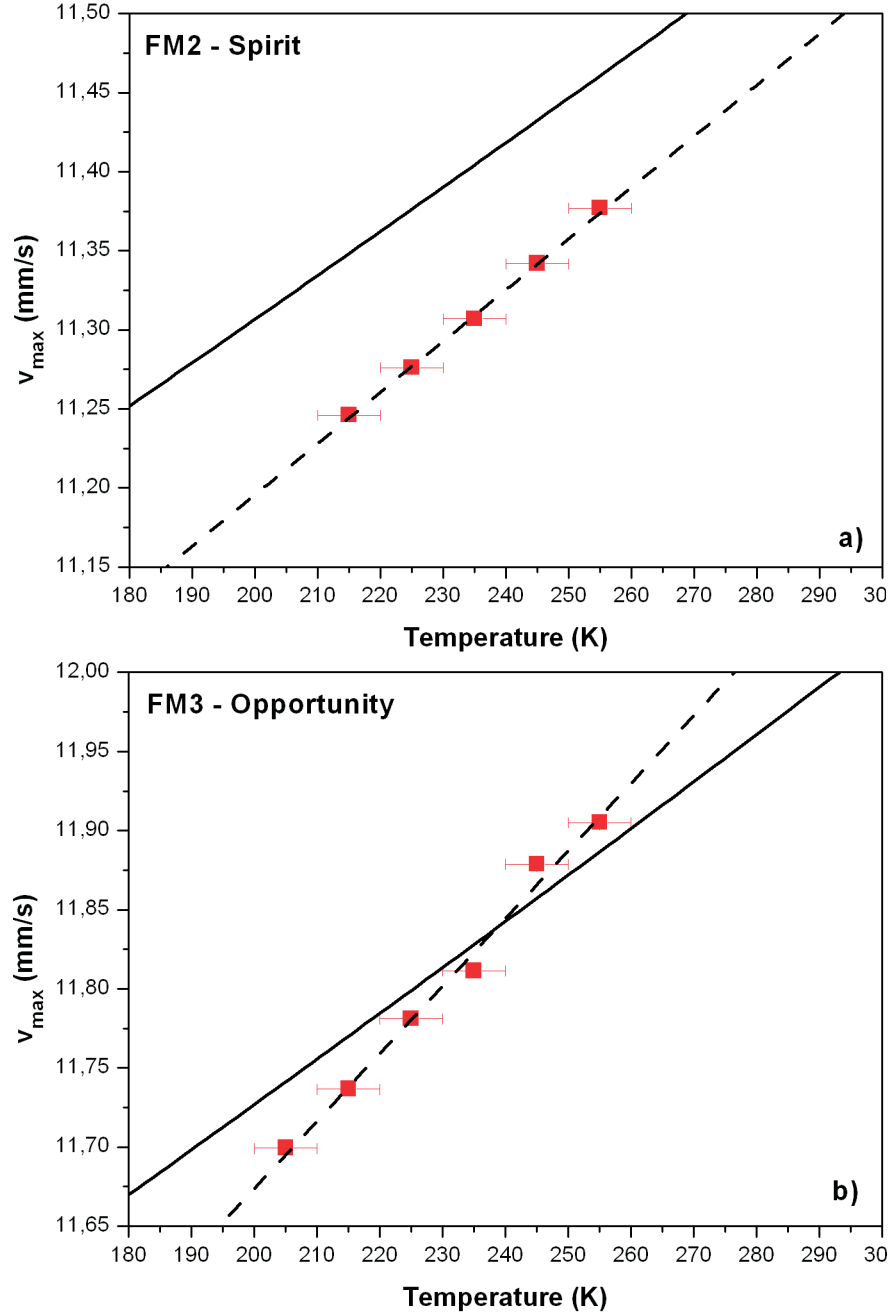


Figure 3.9: The temperature dependence of $v_{max}(T)$ for a) the FM2 sensorhead on Spirit, and b) the FM3 sensorhead on Opportunity. The red squares are $v_{max}(T)$ values obtained by fitting single temperature window reference spectra. Error bars represent the width of the temperature windows. The solid black lines represent the temperature dependence of $v_{max}(T)$ expected from the temperature dependence of the magnetic field in the coil gap. The dashed lines are linear fits to the data points.

Table 3.4: The $v_{max}(T)$ values derived from reference spectra fits and values calculated from equations of linear fits through these data points.

T (K)	T- window	FM2		FM3	
		exp. $v_{max,exp}(T)$ (mm/s)	lin. fit $v_{max}(T)$ (mm/s)	exp. v_{max} (mm/s)	lin. fit $v_{max}(T)$ (mm/s)
185	m2		11.147		11.610
195	m3		11.179		11.652
205	m4		11.212	11.6994(4)	11.695
215	m5	11.246(1) ^a	11.244	11.7367(3)	11.738
225	m6	11.276(1)	11.277	11.7813(3)	11.781
235	m7	11.307(2)	11.309	11.8114(3)	11.823
245	m8	11.342(2)	11.341	11.8788(3)	11.866
255	m9	11.377(2)	11.374	11.9051(3)	11.909
265	m10		11.406		11.951
275	m11		11.439		11.994
285	m12		11.471		12.037
RT	m13		11.498		12.072

^aErrors given are the final step size of variation in the least squares fitting procedure

(11.50 mm/s for FM2, 12.07 for FM3), that differ from values derived from the calibration curves in Figure 3.1. Apparently, the temperature dependence of the magnetic field in the coil gaps is not the only parameter responsible for the temperature dependence of v_{max} . However, the origin of these discrepancies is not known. The calibration curves in Figure 3.1 were obtained in the laboratory on Earth, the data points in Figure 3.9 from measurements on Mars. One might speculate that the stresses of launch and landing or the different conditions on Mars influenced the performance of the instruments. Both instruments showed anomalous behavior during the journey from Earth to Mars.

The derived linear equations

$$v_{max}(T) = a + bT, \quad (3.13)$$

with $a = 10.54769$ mm/s for FM2 and 10.81977 mm/s for FM3, and $b = 0.00324$ mm s^{-1} K^{-1} and 0.00427 mm s^{-1} K^{-1} , respectively, were used to determine v_{max} values for all individual temperature windows. All backscatter spectra were evaluated using these v_{max} values (Table 3.4) as constraints. It has to be noted, that the v_{max} values shown here are virtual values, which

are used to create a linear velocity signal to which the differential signal is added. The real maximum velocities may differ.

3.4 CCT measurements on Mars

During the mission, the magnetite Compositional Calibration Target (CCT) was measured in several runs to verify the functionality and calibration of MIMOS II. Measurements with a MIMOS II laboratory sensorhead were performed on an engineering model of the CCT. The magnetite in the engineering model came from the same piece of rock as the magnetite in the CCT flight models. A spectrum obtained in the lab at room temperature is shown in Figure 3.10, the derived hyperfine parameters are listed in Table 3.5.

The CCT on Spirit was measured on 7 occasions (sols 093, 149, 213, 322, 621, 622, 623) and the CCT on Opportunity on 6 occasions (sols 036, 160, 161, 327, 647, 649). Spectra from individual temperature windows were summed over all measurements for each rover and evaluated. The derived hyperfine parameters are listed in Table 3.6.

Figure 3.11 compares the values of the magnetic splitting B_{hf} of the

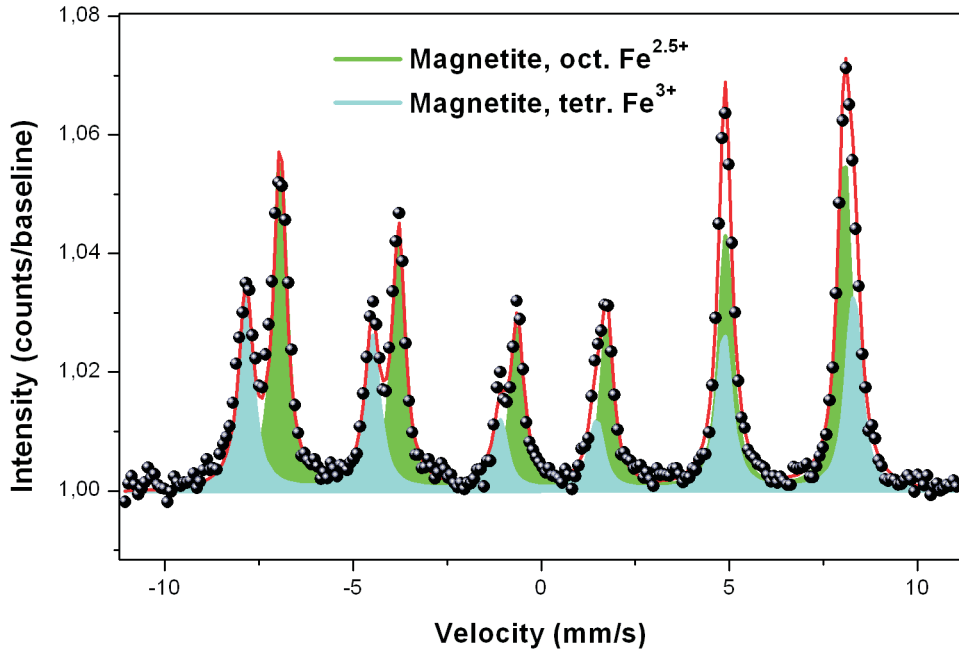


Figure 3.10: Backscatter Mössbauer spectrum of the Compositional Calibration Target (CCT) engineering model.

Table 3.5: Hyperfine parameters of the Compositional Calibration Target (CCT) engineering model obtained with a MIMOS II laboratory sensorhead.

Phase	δ^{ab} (mm/s)	ΔE_Q (mm/s)	ΔE_M (mm/s)	B_{hf} (T)
Magnetite, tet. Fe^{3+}	0.32	0.02	16.1	50.0
Magnetite, oct. $Fe^{2.5+}$	0.67	0.00	15.0	46.4

^aRelative to $\alpha\text{-}Fe^0$ at room temperature.

^bTypical errors for the backscatter measurement are ± 0.02 mm/s for δ and ΔE_Q , ± 0.2 mm/s for ΔE_M , and ± 0.8 T for B_{hf} .

Table 3.6: Hyperfine parameters of the Compositional Calibration Targets (CCT) on Spirit and Opportunity.

Phase	T-window	FM2			FM3		
		δ^{ab} (mm/s)	ΔE_Q (mm/s)	ΔE_M (mm/s)	δ (mm/s)	ΔE_Q (mm/s)	ΔE_M (mm/s)
Mt 3+	m4	0.31	0.03	16.3	0.32	0.00	16.5
Mt 2.5+		0.65	0.00	15.3	0.65	0.02	15.4
Mt 3+	m5	0.31	0.04	16.3	0.33	0.03	16.5
Mt 2.5+		0.66	0.00	15.3	0.66	-0.01	15.4
Mt 3+	m6	0.31	0.04	16.3	0.33	0.02	16.4
Mt 2.5+		0.66	0.00	15.3	0.65	0.00	15.4
Mt 3+	m7	0.31	0.04	16.2	0.33	0.02	16.4
Mt 2.5+		0.66	0.00	15.2	0.65	0.00	15.3
Mt 3+	m8	0.30	0.04	16.2	0.32	0.02	16.4
Mt 2.5+		0.66	0.00	15.2	0.65	0.00	15.2
Mt 3+	m9	0.31	0.02	16.2	0.32	0.02	16.4
Mt 2.5+		0.66	0.00	15.2	0.66	0.00	15.3
Mt 3+	m10	0.31	0.03	16.2	0.31	0.02	16.3
Mt 2.5+		0.66	0.01	15.1	0.67	-0.01	15.2
Mt 3+	m11	0.31	0.02	16.2	0.33	0.03	16.2
Mt 2.5+		0.67	-0.01	15.0	0.67	0.00	15.1
Mt 3+	Extrapol. to RT			16.1			16.2
Mt 2.5+				15.0			15.1

^aRelative to $\alpha\text{-}Fe^0$ at room temperature.

^bTypical errors for the backscatter measurement are ± 0.02 mm/s for δ and ΔE_Q , and ± 0.2 mm/s for ΔE_M .

tetrahedral Fe^{3+} and the octahedral $Fe^{2.5+}$ magnetite sextets derived for the different temperature windows using linear fit $v_{max}(T)$ values listed in Table 3.4. Extrapolating a linear fit through the data points from FM2 in Figure 3.11 to room temperature yields B_{hf} values matching the values from the laboratory room temperature measurement on the CCT engineering model (Table 3.5), thus confirming the temperature dependent calibration for FM2. In comparison, the B_{hf} values of magnetite in the CCT for FM3 show a systematic offset to higher values although they agree within the quoted errors.

It was investigated whether this offset may derive from the different internal calibration targets. The FM2 internal calibration target contains the well-characterized $\alpha-Fe^0$ as the dominant phase in the Mössbauer spectrum (Figure 3.6a), whereas the Mössbauer spectrum of the FM3 internal calibration target is dominated by the less well-characterized hematite/magnetite mixture (Figure 3.6b), which may result in a bias towards higher v_{max} values. The FM3 reference spectra were fitted with only the $\alpha-Fe^0$ fixed; the parameters of the hematite-magnetite mixture were left unconstrained. However, the $v - max$ values did not change significantly and the offset remained.

An alternative explanation for the systematic offset may be small differences in the geometry of the FM2 and FM3 sensorheads. If, for example, during the assembly of the instruments in the lab the drive of FM3 was mounted in such a way that the main source ended up slightly nearer the collimator, the effective opening angle would increase and lead to enhanced cosine smearing effects (see next paragraph or cf. [Schröder, 2001, pp. 46ff]). The sources are assumed to be circular disks with a 4 mm diameter and the central point in one axis with the drive and the center of the collimator opening. If the main source deviates from circular geometry or is slightly off-axis, effects similar to cosine smearing may arise. The sources were delivered in a closed state and their true makeup could not be verified. It is important to note, that both instruments were calibrated using the internal reference target measured in transmission geometry where these geometrical considerations are not effective, contrary to the CCT measurements which were done in backscattering geometry. It must be emphasized here again, that both instruments were subject to the stresses of a rocket launch and an airbag-cushioned landing on the surface of Mars.

3.5 Spatial resolution and cosine smearing

Operation time is a valuable consumable on any spacecraft. Source strength, detector efficiency, energy resolution of the detector, and the irradiated sam-

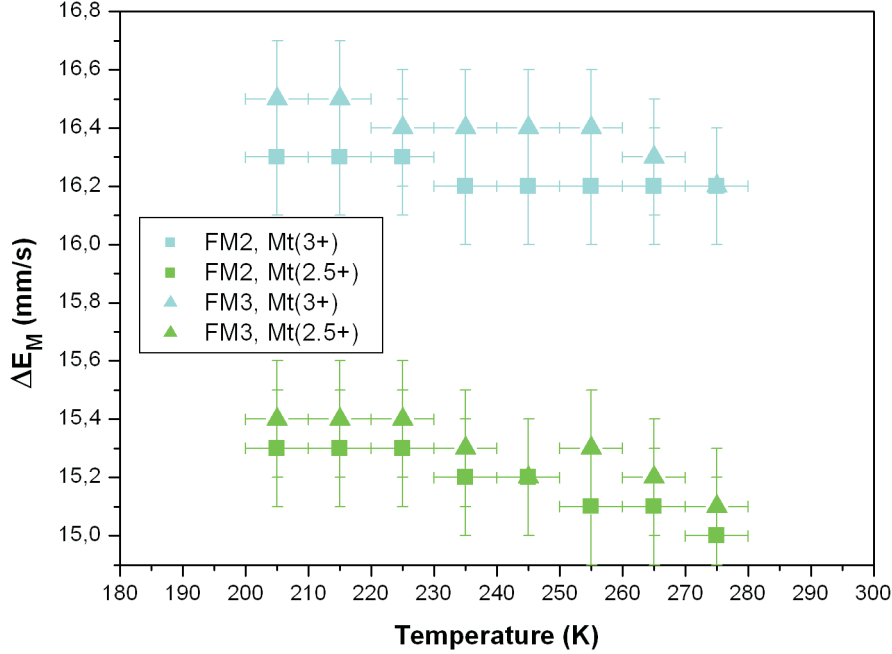


Figure 3.11: Mössbauer spectra of the CCTs on Spirit and Opportunity were evaluated for individual temperature bins, using the respective temperature-dependent velocity calibration. The ΔE_M values for the magnetite sextets of tetrahedral Fe^{3+} and octahedral $Fe^{2.5+}$ show a systematic offset. A possible explanation may be subtle differences in the geometric makeup of the FM2 and FM3 sensorheads.

ple area are parameters which affect the time needed to obtain a good quality Mössbauer spectrum. The irradiated sample area is limited by the diameter of the collimator. When the collimator diameter is increased, the opening angle for emitted γ -photons increases. Photons emitted with an angle θ with respect to the sensorhead axis do not gain the Doppler energy from equation 2.4, but

$$\Delta E = \frac{v_0}{c} E_\gamma \cos\theta, \quad (3.14)$$

where E_γ is the photon energy, and v_0 the relative velocity between source and absorber. This so-called cosine smearing effect leads to an asymmetric broadening and an outward shift of line centers, in particular at higher velocities.

The problem of mathematically accounting for cosine smearing effects has been discussed for coaxial transmission setups, i.e. the centers of source, collimator, sample, and detector, all lining up along the same axis. If the ratio of the collimator radius and the distance between the source and the collimator

is smaller than or equal to 0.1, cosine smearing can be neglected [Aramu and Maxia, 1970]. In case this condition is not fulfilled, Riesenman *et al.* [1969] derived a formula for the line shape for a non-zero source radius. Backscattering geometry introduces another plane. Although the excitation process is still coaxial, the detectors are no longer coaxially positioned. Hence, different parts of the irradiated sample area need to be weighted with respect to the detector geometry. This requires to distinguish between a number of different cases. Held [1997] derived a formula considering these factors, albeit only assuming a point source.

Although the distortion in line shape resulting from cosine smearing can be accounted for mathematically in spectral fitting routines, the reduction in resolution can lead to irretrievable loss of information. The opening angle of the collimator was originally limited to 22° from the central rotational axis to enable the separation of the outer lines of the sextets of hematite ($\alpha\text{-Fe}_2\text{O}_3$) and maghemite ($\gamma\text{-Fe}_2\text{O}_3$) - without any correction for cosine smearing [Held, 1997, p.68]. Experiments by Schröder [2001] showed, that the opening angle can be increased without losing that ability. As part of this work, a new collimator was designed for the MER sensorheads within the weight and place limits of the original, increasing the diameter from 4.5 mm to 5.6 mm (Figure 3.12). This increases the opening angle from 21.1° to 23.6° and the irradiated sample area from 117 mm^2 to 161 mm^2 , respectively [Schröder, 2001]. Much of the background in Mössbauer spectra obtained with a MIMOS II sensorhead comes from scattered radiation within the sensorhead itself. This part of the background stays constant (in fact, it was also diminished through the new collimator design) when increasing the collimator diameter. The result is a significantly increased signal to noise ratio (Figure 3.13).

Figure 3.13 shows Mössbauer spectra obtained from a magnetite CCT engineering model with a MIMOS II setup using 4.5 mm and 5.6 mm diameter collimators. Table 3.7 shows the derived Mössbauer parameters. Integrating both curves in Figure 3.13 shows that the spectral area increases by 46 % using the larger diameter collimator. This effectively reduces the integration time needed to obtain a spectrum of the same statistical quality by over 30 %.

To investigate the effects of cosine smearing a portion of the magnetite rock from which the CCTs were made of was powderized in a ball mill and sieved to a smaller than $45\ \mu\text{m}$ grainsize fraction. This fraction was analyzed with a Mössbauer transmission setup, where the geometry was such that cosine smearing could be neglected. Resulting Mössbauer parameters are listed in Table 3.7. The outward shift of line centers resulting from cosine smearing affects the parameter B_{hf} in particular. The increase is smaller than 1 %

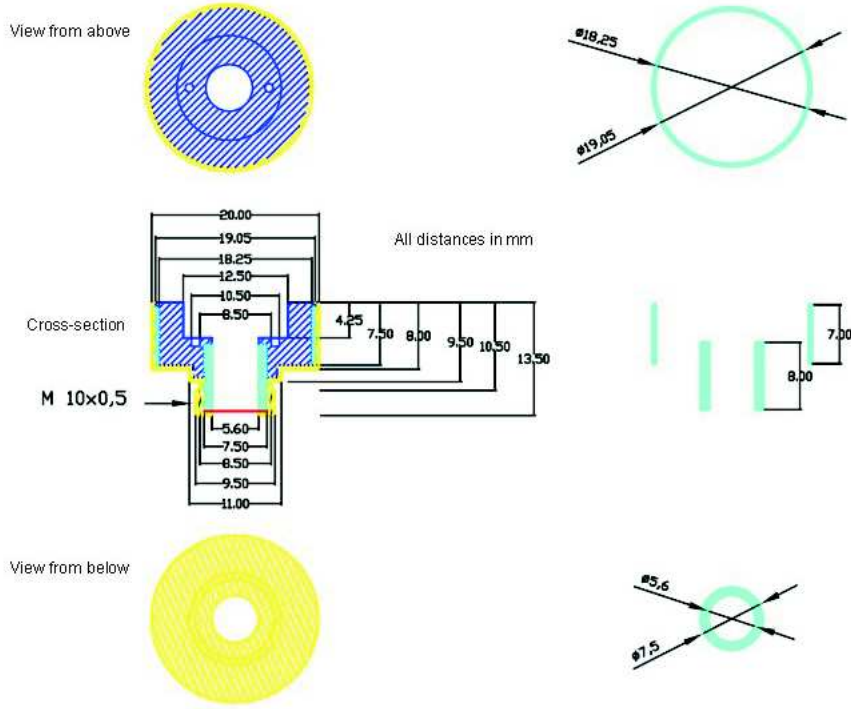


Figure 3.12: Schematic drawings of the new collimator design (blue: Lead; cyan: Tantalum; yellow: Brass; red: Kapton foil). The inner diameter was increased from 4.5 mm to 5.6 mm.

when compared with the previous 4.5 mm diameter collimator design. The B_{hf} values of the tetrahedral Fe^{3+} sextet obtained in transmission geometry and with the 5.6 mm diameter collimator in backscattering geometry agree within the error of ± 0.8 T quoted for B_{hf} in published Mössbauer data [e.g., *Morris et al.*, 2006a].

3.6 Released velocity scales

All MER data are made available to the general scientific community at regular intervals through web-based databases. The released Mössbauer data comprise raw and calibrated data as described in the Mössbauer Experimental Data Record (EDR) and Reduced Data Record Software Interface Specification (RDR-SIS) documents. The released files contain all necessary data which enable interested parties to calibrate and evaluate Martian Mössbauer spectra themselves: Backscatter spectra, reference spectra, and differential signals for each measurement. However, the calibration proce-

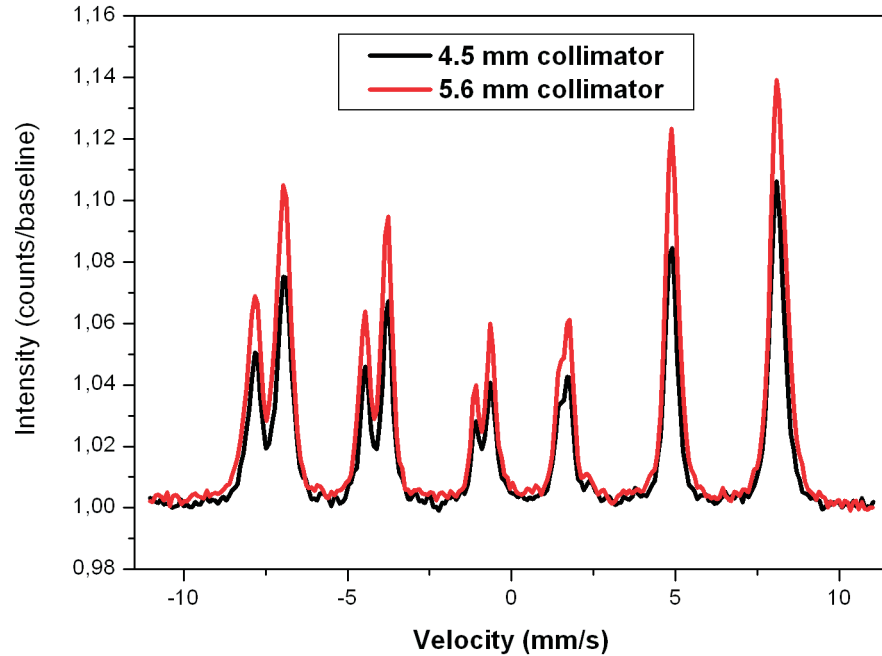


Figure 3.13: Mössbauer spectra of the CCT engineering model obtained using a 4.5 mm diameter collimator and the new 5.6 mm diameter collimator. The spectral area increases by 46 % with the 5.6 mm diameter collimator.

ture as described in the previous paragraphs is unconventional and may be difficult to implement in standard fit routines.

Among the calibrated data are velocity scales for FM2 and FM3 for each temperature window. The velocity scales were created using the temperature dependent $v_{max}(T)$ values in Table 3.4 and an average differential signal for each rover. Because the orientation of the MIMOS sensorheads during CCT measurements is very different to surface measurements, another set of velocity scales was created for CCT measurements with different average differential signals. The velocity scales are provided in their non-linear form in columns of 512 values such that the velocity value in line 1 directly corresponds to the counts in channel 1 of the unfolded raw Mössbauer data file, and so on. That way calibrated Mössbauer spectra are provided without any loss of information from the raw data. The spectra may not be readable by some standard fit routines in that form. One can easily linearize the velocity scales and, by interpolating, manipulate the raw spectral data accordingly in order to make them readable.

The released velocity scales correspond to backscatter spectra. In order to apply them to spectra of the internal reference target which were obtained

Table 3.7: Hyperfine parameters of the Compositional Calibration Targets (CCT) engineering model (obtained in backscattering mode with two different collimators) and a powder derived from the same rock material (obtained in transmission mode).

\emptyset collimator (mm)	Phase	δ^{ab} (mm/s)	ΔE_Q (mm/s)	ΔE_M (mm/s)	B_{hf} (T)	$\Gamma/2$ (mm/s)
Transmission	Mt 3+	0.28	0.00	15.9	49.2	0.14
	Mt 2.5+	0.67	0.00	14.8	45.9	0.18
4.5	Mt 3+	0.30	0.03	16.1	49.7	0.18
	Mt 2.5+	0.67	0.00	15.0	46.3	0.19
5.6	Mt 3+	0.32	0.02	16.1	50.0	0.22
	Mt 2.5+	0.67	0.00	15.0	46.4	0.19

^aRelative to $\alpha\text{-Fe}^0$ at room temperature.

^bTypical errors for the backscatter measurement are ± 0.02 mm/s for δ and ΔE_Q , ± 0.2 mm/s for ΔE_M , ± 0.8 T for B_{hf} , and ± 0.01 mm/s for $\Gamma/2$.

in transmission geometry, the velocity scales need to be multiplied by -1. In some spectra, in particular from the Opportunity MB spectrum (FM3 sensorhead), the lines from left and right halves of reference or backscatter spectra do not overlap when using the provided velocity scales. Here a shift of the folding point needs to be taken into account. This can be achieved by interpolating between velocities corresponding to individual channels and shifting the whole velocity scale along those interpolations by the appropriate fraction of 1.

3.7 Evaluation of MER Mössbauer data

The fitting routines used in this dissertation are not commercially available. They are based on the least squares minimization routine MINUIT [e.g., James, 2004] and were developed and adjusted over time at the Technische Universität in Darmstadt and the Johannes Gutenberg-Universität in Mainz. Members of the MER Mössbauer team at other institutions were using different fit routines. In their fittings they used the released velocity scales described in the previous paragraph.

In laboratory environments, the counting statistics can be made arbitrarily good by long counting times and/or by using strong ^{57}Co sources. On Mars, arbitrarily long counting times are not possible within timely pro-

gression of mission science requirements, and a weak ^{57}Co source cannot be replaced by a stronger one. Therefore the choices for improving counting statistics in MER spectra are either to sum the data for all or a subset of temperature windows for measurements of a single target or to sum data for the same temperature interval (one or more temperature windows) from measurements of multiple targets. If the Mössbauer parameters are strongly dependent on temperature, summing over a wide temperature interval will broaden lines, leading to reduced velocity resolution. Summing spectra over multiple targets for individual temperature windows will not broaden lines if the mineralogical composition is invariant, and the subspectral areas will be the weighted average for the aggregate. Subspectral areas of the individual targets would then be calculated using the information previously obtained (e.g., δ , ΔE_Q , and ΔE_M) as fitting constraints. Both approaches were employed.

All spectra were independently fitted by at least two members of the MER Mössbauer team (always including the author of this dissertation). Two approaches were used to determine line centers during the computations. In one approach, the line centers were fitted and the MB parameters (δ , ΔE_Q , and ΔE_M) calculated from the fitted line positions; in the other approach, the MB parameters were fitted and line positions calculated from the MB parameters. Distribution functions can be used when MB parameters are fitted. The values of the MB parameters reported by *Morris et al.* [2004, 2006a] and *Klingelhöfer et al.* [2004] are averages of the values obtained in these independent fits, and the parameter errors are the larger of the statistical error (not often) or the deviation from the average value of the independent fits. Minimum errors reported are ± 0.02 mm/s for δ and ΔE_Q , ± 0.8 T for B_{hf} and ± 2 % (absolute) for subspectral areas A. *Morris et al.* [2006a] give a detailed account of fitting procedures employed in the evaluation of MER Mössbauer spectra and the identification of Fe-bearing mineralogical phases.

Chapter 4

Martian Meteorites

Martian meteorites [e.g., *McSween, 1994; Treiman et al., 2000*] are a special group of achondrites. Oxygen isotope ratios in these meteorites fall along a fractionation line distinct from Earth rocks. Gas trapped in glass inclusions in the meteorite EETA79001 matches the composition of the Martian atmosphere [*Bogard and Johnson, 1983*]. Martian meteorites are also referred to as SNC meteorites after Shergotty, Nakhla, and Chassigny, three meteorites that are characteristic for individual subgroups of the Martian meteorites. Only 36 Martian meteorites have been identified to date [*Meyer, 2006*]. They have been divided according to their mineralogical composition into clinopyroxenites (or nakhlites), basaltic shergottites, lherzolitic shergottites, olivine-phyric shergottites, dunites (or chassignites), and one orthopyroxenite (ALH84001). The importance of these meteorites lies in the fact that they can be analyzed in great detail in terrestrial laboratories. Therefore, most models of the geochemical evolution of Mars' mantle and crust are based on their mineralogical, geochemical and isotopic studies. In comparison to Earth, the Mars inferred bulk composition has higher abundances of moderately volatile elements (e.g., Mn, Na, etc.) and has higher FeO in the source region of basalts [*Dreibus and Wänke, 1985*]. Isotopic analyses imply early differentiation with the formation of a small core, mantle and crust [*Lugmair and Shukolyukov, 1998; Lee and Halliday, 1997*]. With the exception of ALH84001, these meteorites have relatively young crystallization ages of 1300 million years to as little as 200 million years or less, implying an extant period of volcanism on Mars [*Borg et al., 1997; Nyquist et al., 2001*]. They show only minor signs of alteration. Some of that alteration is of terrestrial origin, whereas some has been shown to be of pre-terrestrial Martian origin [*Bridges et al., 2001*]. Prior to the landing of the Mars Exploration Rovers, rocks specifically matching the composition of Martian meteorites had not been discovered on Mars itself. Martian meteorites are rare and pre-

cious. MIMOS II provides a non-destructive tool for their analysis. Samples of the meteorites Dar al Gani 476, Sayh al Uhaimyr 005, Nakhla, Shergotty, EET79001, and Zagami are from the meteorite collection of the Max-Planck-Institute for Chemistry in Mainz and were kindly provided Dr. Jutta Zipfel. This meteorite collection is now on permanent loan at the Senckenberg Institute in Frankfurt/Main. A sample of the meteorite ALH84001 came from the Carnegie Institution in Washington D.C. and was kindly provided by Dr. Jan Toporski.

4.1 Dar al Gani 476 and Sayh al Uhaymir 005

The olivine-phyric shergottites Dar al Gani 476 and Sayh al Uhaymir 005 were studied using MIMOS II. All spectra were obtained at room temperature under ambient conditions. Samples comprised of one sawn slab each of Dar al Gani 476 (Figure 4.1) and Sayh al Uhaymir 005 (Figure 4.2). *Schröder et al.* [2004] were the first to report Mössbauer spectra from these two meteorites. These spectra are discussed here.

The Martian meteorites Dar al Gani 476 (DaG) and Sayh al Uhaymir 005 (SaU) are thought to be closely related [*Zipfel*, 2000]. DaG is heavily fractured and the fractures and veins are filled with carbonate [*Zipfel et al.*, 2000]. The abundant carbonate is evidence for the percolation of terrestrial CO_2 -rich water in this meteorite. It has not been observed in vein-fillings of unequivocally pre-terrestrial origin in any other Martian meteorite. Veins and vugs observed in rocks during the Mars Exploration Rover mission are associated with enhanced Cl, S, and Br levels, i.e. salts rather than carbonates [e.g., *Gellert et al.*, 2004]. Figure 4.1a shows the front side of the DaG slab, and Figure 4.1b the reverse side. The red circles have a diameter of 15 mm and indicate the field of view of MIMOS II on these spots. The spots on DaG are designated dag002 (center of front side), dag005 (right of dag002), and dag004 (spot on reverse side). The spots on SaU (Figure 4.2) are designated from top left sau004, sau002, and sau003, respectively. Spot dag002 was chosen to be far from the rim and the u-shaped fracture inside the slab to provide a measure of the presumably least-altered part of the meteorite. Spot dag005 covers a domain of calcite veins alongside the u-shaped fracture. Spot dag004 on the reverse side exhibits a large reddish-brown olivine crystal at its center. Spot sau004 at the rim of the SaU slab covers some slightly darker material compared to the bulk matrix. Spot sau002 exhibits a higher abundance of olivine crystals, whereas sau003 shows more of the lighter colored bulk matrix material. Figures 4.3 and 4.4 show Mössbauer spectra taken from these different spots on each meteorite slab of DaG and SaU, respectively.

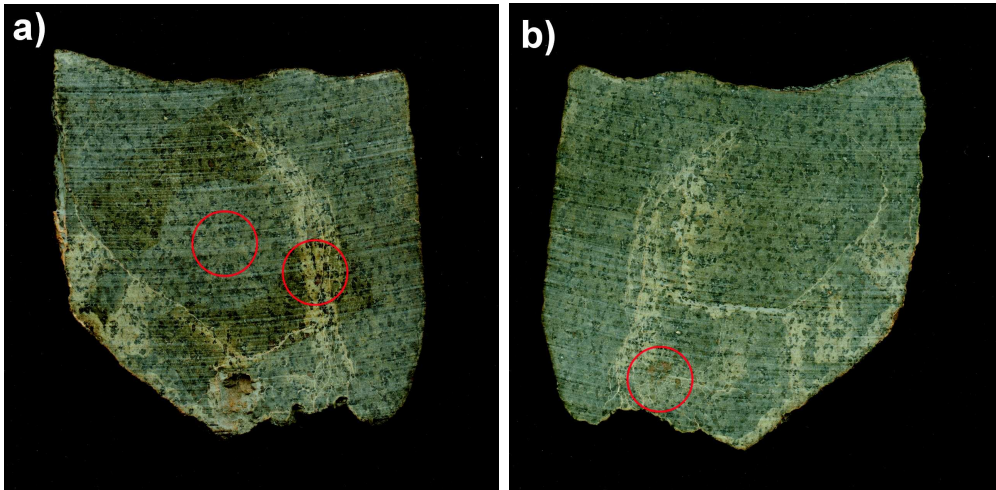


Figure 4.1: Front (a) and reverse side (b) of a slab of the Martian meteorite Dar al Gani 476. Red circles have a diameter of 15 mm and indicate the field of view of MIMOS II during measurements: (a) dag002 (left) and dag005 (right); (b) dag004. The spots were chosen to represent the least weathered interior part distant from the calcite veins (dag002), material intersected by calcite veins (dag005), and a reddish-brown olivine crystal.



Figure 4.2: A slab of the Martian meteorite Sayh al Uhaymir 005. Red circles have a diameter of 15 mm and indicate the field of view of MIMOS II during Mössbauer measurements: sau004, sau002, and sau003 from the top left corner, respectively. The spots were chosen to contain predominantly the light-toned matrix (sau003), predominantly dark-colored olivine crystals (sau002), and a dark-toned matrix at the edge of the meteorite slab (sau005).

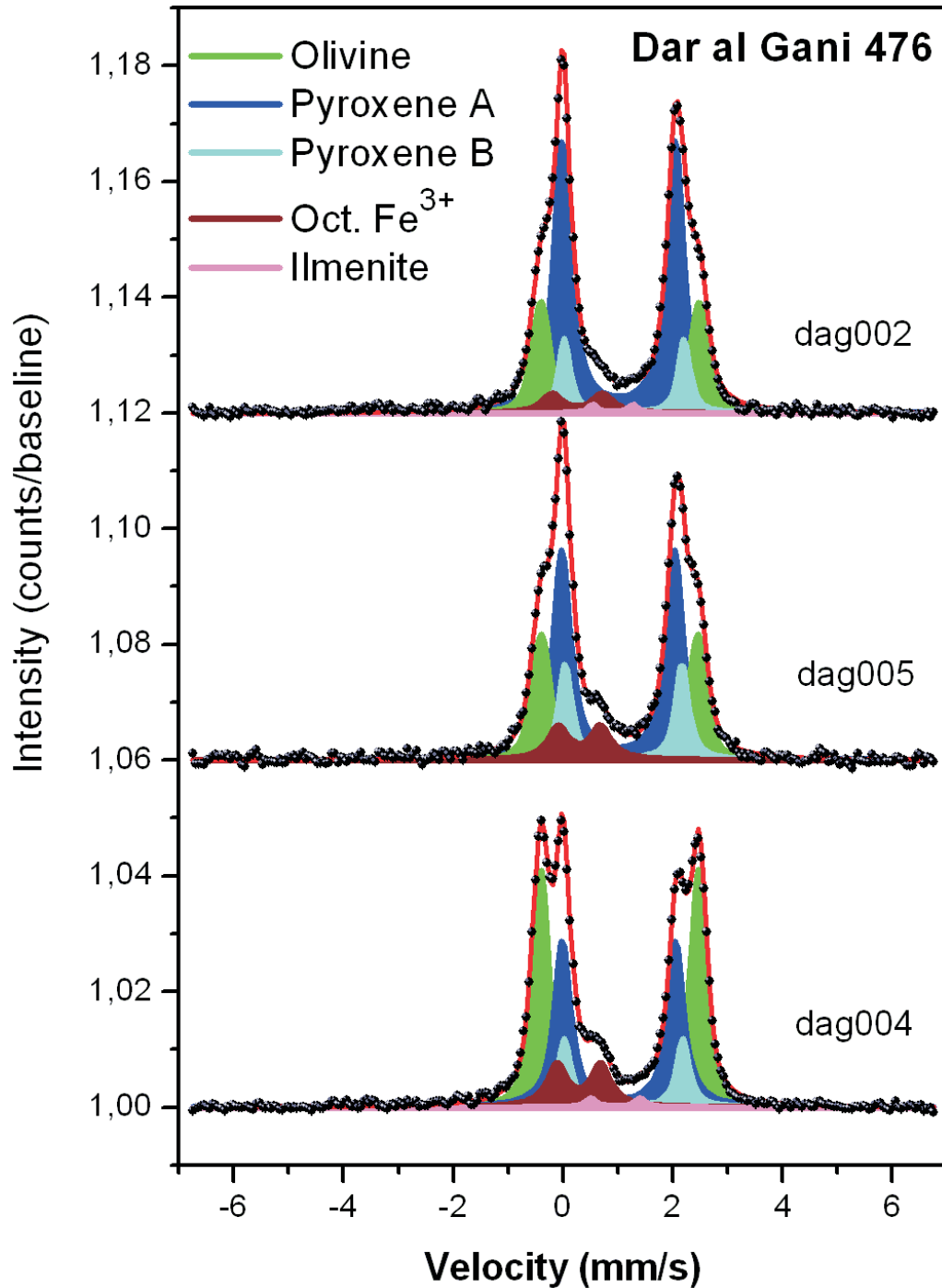


Figure 4.3: Mössbauer spectra from a slab of the Martian meteorite Dar al Gani 476, obtained from different spots on its surface. Spectra are offset along the y-axis for clarity. The spectrum obtained from the interior part which was distant from calcite veins (dag002) contains the least amount of nanophase ferric oxides (np-Ox). The spectrum from calcite veins (dag005) contains almost twice as much np-Ox. The spectrum from the reddish-brown olivine crystal (dag004) contains the most np-Ox which indicates that the red color is a result of oxidative weathering of olivine.

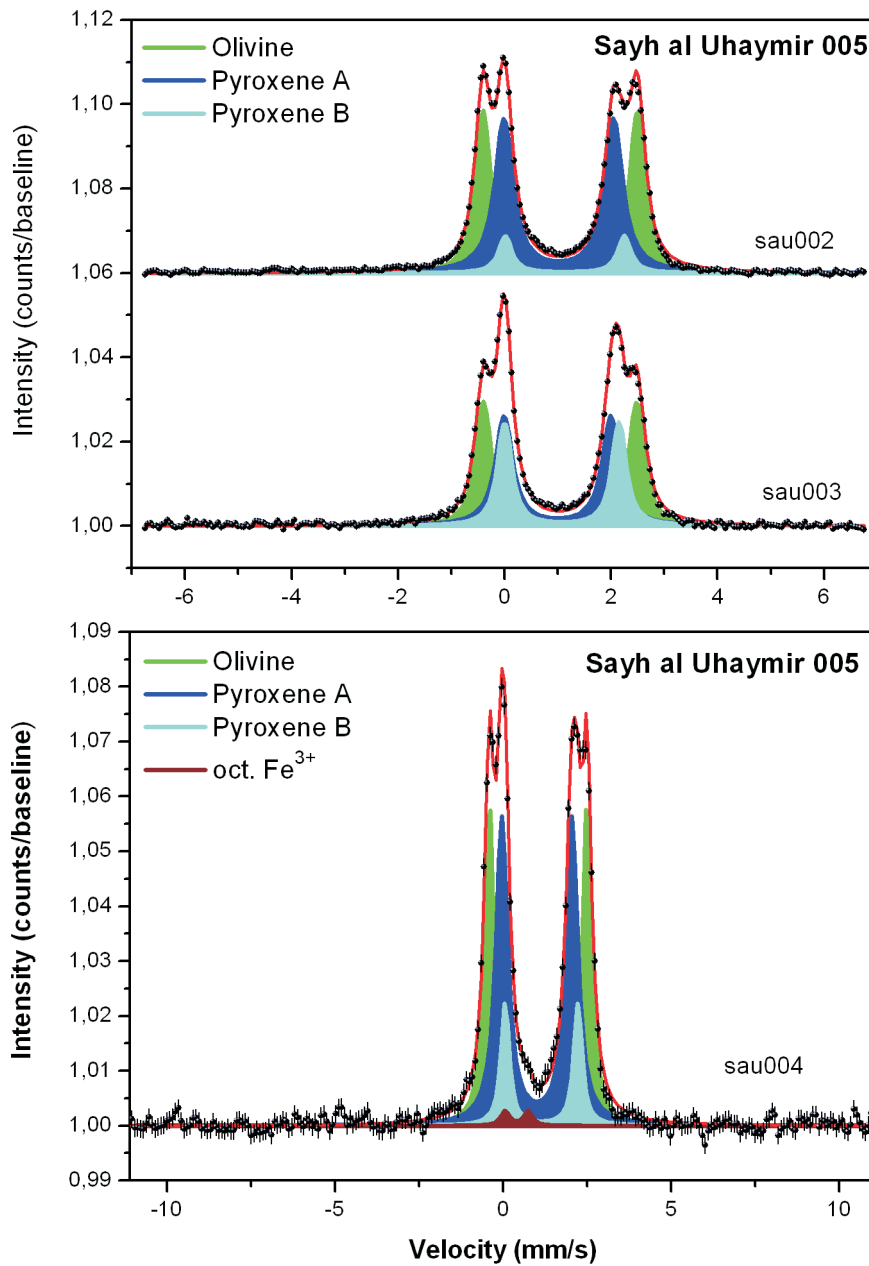


Figure 4.4: Mössbauer spectra from a slab of the Martian meteorite Sayh al Uhaymir 005, obtained from different spots on its surface. Spectra are offset along the y-axis for clarity. The spectrum from dark-colored olivine crystals (sau002) and the spectrum from the predominantly light-toned matrix (sau003) can be distinguished by their olivine/pyroxene ratio. Only the spectrum from the dark-toned matrix at the edge of the meteorite slab (sau004) contains small amounts of octahedral Fe^{3+} .

Table 4.1: Hyperfine parameters from Mössbauer spectra of the Martian meteorite Dar al Gani 476.

Mineral phase	Fe ox. and coord.	δ^{ab} (mm/s)	ΔE_Q (mm/s)	Area (%)
<i>dag002</i>				
Olivine	Oct. Fe^{2+}	1.15	2.89	22
Pyroxene A	Oct. Fe^{2+}	1.13	2.06	61
Pyroxene B	Oct. Fe^{2+}	1.23	2.18	11
Ilmenite	Fe^{2+}	1.02	0.74	1
Fe^{3+} phase(s)	Oct. Fe^{3+}	0.38	0.92	5
<i>dag004</i>				
Olivine	Oct. Fe^{2+}	1.14	2.89	43
Pyroxene A	Oct. Fe^{2+}	1.14	2.06	34
Pyroxene B	Oct. Fe^{2+}	1.22	2.16	11
Ilmenite	Fe^{2+}	1.08	0.90	1
Fe^{3+} phase(s)	Oct. Fe^{3+}	0.40	0.80	11
<i>dag005</i>				
Olivine	Oct. Fe^{2+}	1.14	2.86	26
Pyroxene A	Oct. Fe^{2+}	1.21	2.05	48
Pyroxene B	Oct. Fe^{2+}	1.22	2.13	17
Fe^{3+} phase(s)	Oct. Fe^{3+}	0.41	0.77	9

^aRelative to α -Fe.

^bTypical uncertainties are ± 0.02 mm/s for δ and ΔE_Q , and ± 2 % for the area.

Hyperfine parameters are listed in Tables 4.1 and 4.2. Typical uncertainties are 0.02 mm/s for δ and ΔE_Q . Both meteorites contain olivine and pyroxene in variable amounts. The relative intensity of olivine lines increases with the presence of large, dark-colored olivine crystals in the analyzed spots. DaG also contains minor amounts of ilmenite. DaG is strongly altered as indicated by a - compared to other SNC meteorites [e.g., *Dyar, 2003*] - very high content of ferric iron present in all spectra shown here. As expected, the ferric iron content is particularly high on spots along the calcite veins. However, large amounts in comparison to SaU are also found in the center far away from these veins (dag002). Apparently water penetrated DaG deeper than the visible carbonate veins suggest. SaU shows measurable amounts of ferric iron only along the rim (sau004). Assuming a close relationship between the two meteorites [*Zipfel, 2000*] and considering the fractures in DaG, the high ferric iron contents in DaG can be attributed to alteration by terrestrial fluids from which the carbonate precipitated. Some olivine crystals in DaG show a brownish-red color, in particular in the center of the analyzed spots

Table 4.2: Hyperfine parameters from Mössbauer spectra of the Martian meteorite Sayh al Uhaymir 005.

Mineral phase	Fe ox. and coord.	δ^{ab} (mm/s)	ΔE_Q (mm/s)	Area (%)
<i>sau002</i>				
Olivine	Oct. Fe^{2+}	1.16	2.90	42
Pyroxene A	Oct. Fe^{2+}	1.13	2.06	49
Pyroxene B	Oct. Fe^{2+}	1.24	2.24	9
<i>sau003</i>				
Olivine	Oct. Fe^{2+}	1.16	2.88	36
Pyroxene A	Oct. Fe^{2+}	1.11	2.01	36
Pyroxene B	Oct. Fe^{2+}	1.19	2.15	28
<i>sau004</i>				
Olivine	Oct. Fe^{2+}	1.15	2.92	38
Pyroxene A	Oct. Fe^{2+}	1.11	2.08	47
Pyroxene B	Oct. Fe^{2+}	1.26	2.17	13
Fe^{3+} phase(s)	Oct. Fe^{3+}	0.51	0.68	2

^aRelative to α -Fe.

^bTypical uncertainties are ± 0.02 mm/s for δ and ΔE_Q , and ± 2 % for the area.

dag004 and dag005 (Figure 4.1). The Mössbauer spectra suggest that this color results from ferric alteration products of olivine.

4.2 Nakhla

An irregular-shaped piece of the clinopyroxenite Nakhla was also investigated with MIMOS II. The results shown here were initially published by *Schröder et al.* [2004]. The piece of Nakhla shows remnants of the fusion crust on one side (Figure 4.5).

Figure 4.6 shows the Mössbauer spectrum of the interior of the Nakhla sample and Table 4.3 contains the respective hyperfine parameters. Typical uncertainties are 0.02 mm/s for δ and ΔE_Q . The Fe-bearing phases in Nakhla are reported as 78 % modal pyroxene and 15 % olivine, respectively [*Meyer, 2006*]. *Harvey and McSween* [1991] describe the composition of olivine in Nakhla as fayalitic (fa65-75). The ΔE_Q values of olivine decrease with increasing Fe content [e.g., *Morris et al., 2004*]. Although *Solberg and Burns* [1989] report a ΔE_Q value as low as 2.78 mm/s for olivine in Nakhla, the value obtained from the MIMOS II measurement of the interior of Nakhla, ΔE_Q of 2.71 mm/s (Table 4.6), was considered too low to be attributed to

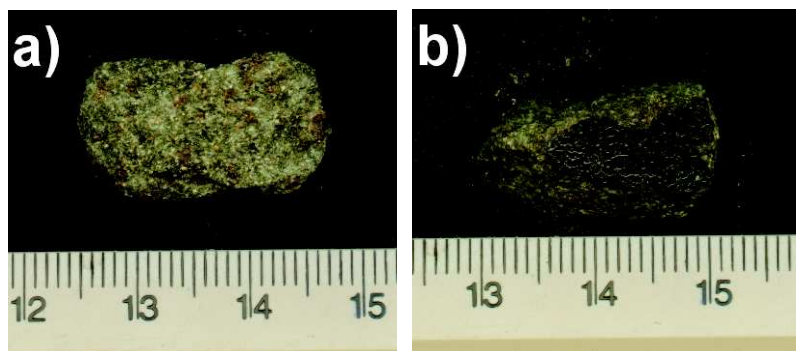


Figure 4.5: A piece of the Martian meteorite Nakhla (scale bar in cm) showing the interior (a) and part of the dark fusion crust (b).

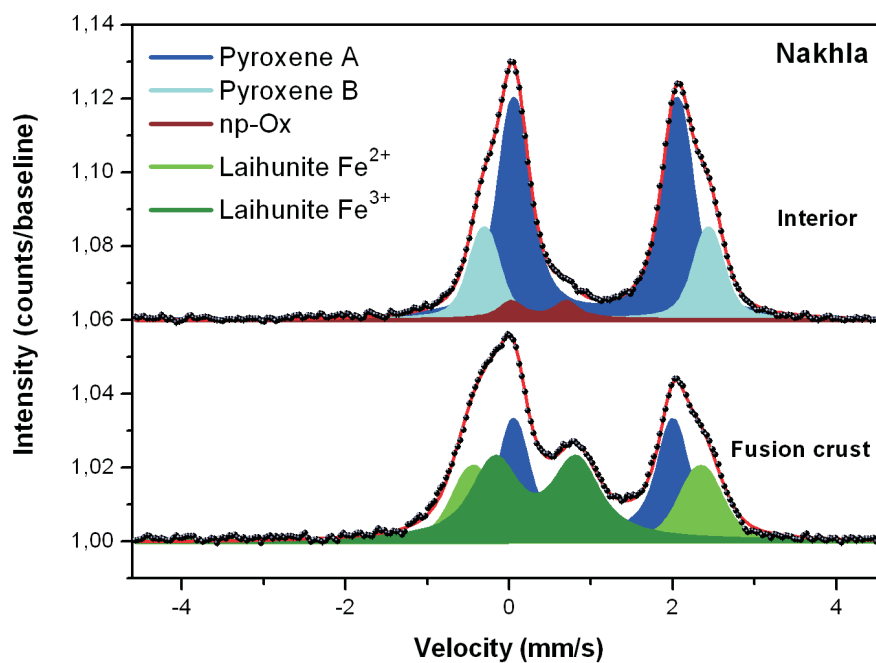


Figure 4.6: Mössbauer spectra of the Martian meteorite Nakhla. Spectra are offset along the y-axis for clarity. The fusion crust is highly oxidized compared to the interior of the the meteorite.

Table 4.3: Hyperfine parameters from Mössbauer spectra of the Martian meteorite Nakhla.

Mineral phase	Fe ox. and coord.	δ^{ab} (mm/s)	ΔE_Q (mm/s)	Area (%)
<i>Interior</i>				
Pyroxene A	Oct. Fe^{2+}	1.16	1.97	70
Pyroxene B	Oct. Fe^{2+}	1.17	2.71	25
Fe^{3+} phase(s)	Oct. Fe^{3+}	0.47	0.66	5
<i>Fusion crust</i>				
Pyroxene A	Oct. Fe^{2+}	1.13	1.92	39
Laihunite	Oct. Fe^{2+}	1.06	2.75	25
	Oct. Fe^{3+}	0.43	0.99	36

^aRelative to α -Fe.

^bTypical uncertainties are ± 0.02 mm/s for δ and ΔE_Q , and ± 2 % for the area.

olivine. Mössbauer spectra and hyperfine parameters in Figure 4.6 and Table 4.3 match the spectrum and hyperfine parameters *Dyar* [2003] obtained from a pyroxene separate of Nakhla. Therefore the doublet with $\Delta E_Q = 2.71$ mm/s was assigned to an Fe^{2+} pyroxene phase. The other two Fe-bearing phases identified are a second Fe^{2+} pyroxene phase and an Fe^{3+} phase, whose assignment is uncertain. It has previously been assigned to Fe^{3+} in pyroxene [*Vieira et al.*, 1986; *Vistisen et al.*, 1990], and also to a hydrated alteration phase resembling iddingsite [*Burns and Martinez*, 1990; *Burns*, 1991], a common weathering product of olivine. The iddingsite is thought to be an alteration phase of Martian origin [*Reid and Bunch*, 1975]. The absence of olivine in the analyzed spot of the interior is unusual and shows the inhomogeneity of Nakhla on the scale of the field of view of MIMOS II.

The Mössbauer spectrum of the fusion crust shows a strong increase in Fe^{3+} (Figure 4.6 and Table 4.3). The fusion crust is a thin alteration rind which formed by frictional heating during the meteorite's descent through Earth's atmosphere. In this case the Fe^{3+} cannot be simply assigned to pyroxene or iddingsite. In fact, the hyperfine parameters obtained from the spectrum of the fusion crust for the Fe^{2+} phase with ΔE_Q equal to 2.75 and the Fe^{3+} phase are in the range of hyperfine parameters reported for the mineral laihunite ($Fe^{2+}Fe_2^{3+}(SiO_4)_2$, also referred to as ferrifayalite) [*Schaefer*, 1983; *Kan and Coey*, 1985]. The visual appearance of the fusion crust supports this assignment. Laihunite is described as an opaque, dark brown or black mineral. *Kondoh et al.*, [1985] obtained laihunite by heating synthetic fayalite crystals in air at 400, 600, and 700°C. The fusion crust formed at similar conditions.

4.3 ALH84001

The orthopyroxenite ALH84001 gained notoriety after *McKay et al.* [1996] announced to have found evidence for possible Martian relic biogenic activity in it. His claims were partly linked to the presence of Fe-rich carbonate globules, typically 50 μm in diameter. A mm-sized piece of ALH84001 was investigated with MIMOS II.

Electron microscopy and energy-dispersive X-ray (EDX) analyses confirmed the presence of at least one carbonate globule on the surface of this piece. However, the abundance of carbonate globules was too low within the MIMOS II field of view. Spectral features of the carbonate could not be resolved in the Mössbauer spectrum against the overwhelming pyroxene background, although the measurement was running for several weeks (Figure 4.7). Mössbauer parameters are listed in Table 4.4.

4.4 Bounce Rock and basaltic shergottites

The Mars Exploration Rover Opportunity landed in 22 m diameter Eagle crater on Meridiani Planum. After leaving Eagle crater, the rover approached

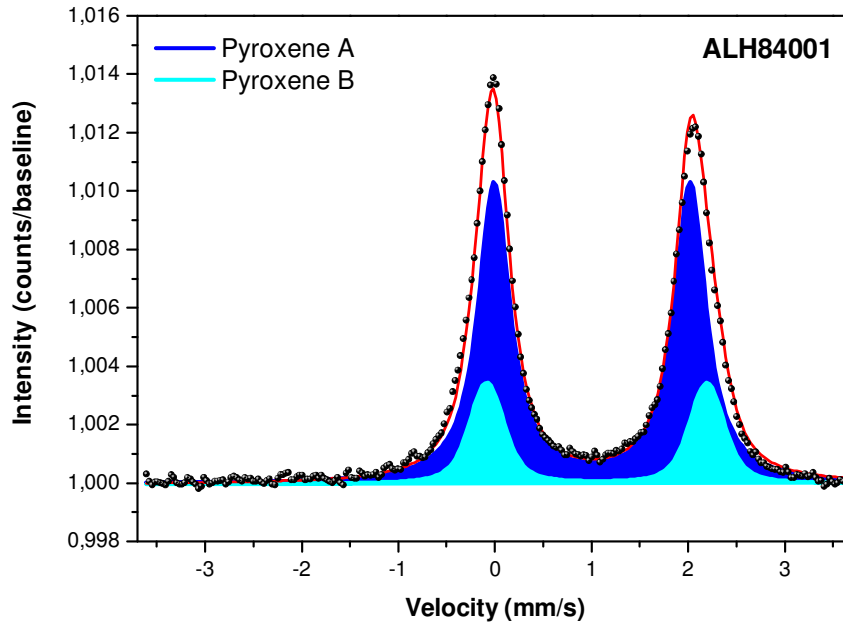


Figure 4.7: Mössbauer spectrum of the Martian meteorite ALH84001, an orthopyroxenite.

Table 4.4: Hyperfine parameters from a Mössbauer spectrum of the Martian meteorite ALH84001.

Mineral phase	Fe ox. and coord.	$\delta^{a,b}$ (mm/s)	ΔE_Q (mm/s)	Area (%)
Pyroxene A	Oct. Fe^{2+}	1.12	2.03	77
Pyroxene B	Oct. Fe^{2+}	1.17	2.28	23

^aRelative to α -Fe.

^bTypical uncertainties are ± 0.02 mm/s for δ and ΔE_Q , and ± 2 % for the area.

an isolated rock, approximately 40 cm by 20 cm in size. Since it was close to a bounce mark from the airbag shell and may have been hit during the landing, the rock was dubbed Bounce Rock (Figure 4.8). No other rock this large was found in the vicinity of Bounce Rock. It lies on top of the fine-grained soil.

Opportunity’s Mössbauer spectrometer was the first in situ instrument applied to Bounce Rock. Spectra were taken from a RAT-ground target and from eight different target spots of the undisturbed, dust-covered, and potentially coated surface of the rock. All but one spectrum were acquired using the standard maximum drive velocity of about 12 mm/s, because Bounce Rock was initially characterized by remote sensing instruments as hematite-rich. The absence of the typical sextet feature in these Mössbauer spectra excludes the presence of hematite and other magnetically split Fe oxide phases in Bounce Rock. One spectrum from an undisturbed rock target was acquired with a reduced drive velocity range of about 4 mm/s to allow for a better resolution of the doublet lines.

Bounce Rock appears remarkably homogeneous in the Mössbauer spectra. Spectra of undisturbed and abraded surfaces show no marked differences, implying that surface dust and any potential coatings are absent or too thin to contribute to spectra. Fe is exclusively distributed between pyroxene phases, represented by two doublets in the Mössbauer spectra (Figure 4.9). Bounce Rock shows no signs of chemical alteration as indicated by the lack of Fe^{3+} , and is thus distinguished from the surrounding soil and the sulfate-rich outcrop rocks. There is no evidence for the presence of olivine, which further distinguishes Bounce Rock from basaltic soils at Meridiani Planum [Klingelhöfer *et al.*, 2004] and from basaltic rocks and soils investigated by the rover Spirit in Gusev crater [Morris *et al.*, 2004, 2006a]. In addition, the Mössbauer parameters of pyroxene phases in Bounce Rock differ from those of basaltic soils at Meridiani Planum [Klingelhöfer *et al.*, 2004] and of basaltic rocks and soils in Gusev crater. Although spectra from Bounce Rock are unique among Martian surface samples to date, they are similar to spectra from Martian meteorites. Data from the whole instrument suite onboard



Figure 4.8: False color image of Bounce Rock after grinding with the Rock Abrasion Tool (RAT). Mössbauer spectra were obtained prior to and after RAT-grinding. The photo is an enhanced color composite generated from Pancam's 600, 530, and 480 nm filters (NASA/JPL/Cornell).

the rover confirm that Bounce Rock is closely related to basaltic shergottites [Christensen *et al.*, 2004; Klingelhöfer *et al.*, 2004; Rieder *et al.*, 2004; Squyres *et al.*, 2004b], a subgroup of the Martian meteorites. Figure 4.9 compares a Mössbauer spectrum of Bounce Rock to Mössbauer spectra of other basaltic shergottites, EETA79001 B, Shergotty, and Zagami, which were obtained with a laboratory MIMOS II setup. The intensity of the Mössbauer signal decreases from Bounce to EETA79001 B to Shergotty to Zagami. The decrease correlates with the decrease in the total Fe content of these meteorites. Table 4.5 lists the respective Mössbauer parameters.

Because the composition of Bounce Rock is different from the underlying soil and the sedimentary outcrop rocks at Meridiani Planum, the rock must have been transported from elsewhere on Mars to its current location. An impact-related origin is likely. A relatively fresh 25-km crater located 75 km southwest of Eagle crater has been identified as a possible source region [Squyres *et al.*, 2004b]. A detailed integration of the observations from all

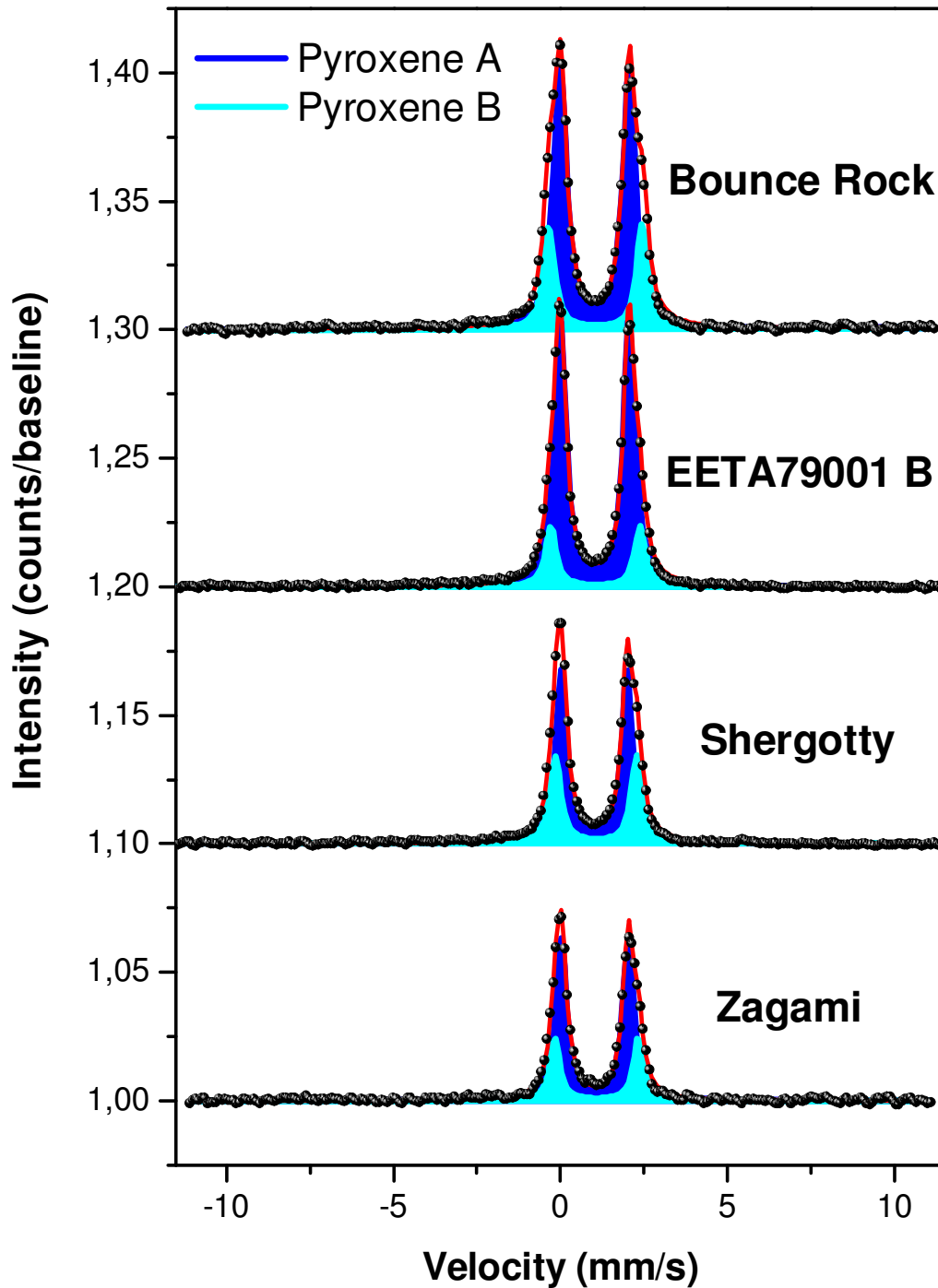


Figure 4.9: Mössbauer spectra of Bounce Rock (after RAT-grinding, target Case) and other basaltic shergottites. The spectrum of Bounce Rock was obtained over a temperature range from 201-255 K, the spectra of the other basaltic shergottites were obtained at room temperature. Spectra are offset along the y-axis for clarity.

Table 4.5: Pyroxene Mössbauer parameters from whole rock analyses of Bounce Rock and selected Martian meteorites.

Name	Pyroxene A			Pyroxene B			Ref.
	δ^a (mm/s)	ΔE_Q (mm/s)	A ^b (%)	δ (mm/s)	ΔE_Q (mm/s)	A (%)	
Bounce Rock ^c <i>Basaltic shergottites</i> ^d	1.17	2.01	74	1.20	2.63	26	[1]
QUE94201	1.14	2.01	52	1.16	2.64	24.1	[2]
EETA79001 B	1.14	2.03	73	1.17	2.52	27	[3]
Shergotty	1.13	1.97	66	1.19	2.44	34	[3]
Zagami	1.15	2.00	73	1.20	2.50	27	[3]
Los Angeles	1.14	1.96	42.7	1.17	2.54	43.3	[2]

[1]: *Klingelhöfer et al.* [2004]; [2]: *Dyar* [2003]; [3]: This work.

^aAll δ values relative to α -Fe

^bIf sum of areas <100 %, other Fe-bearing were present.

^cMössbauer parameter values extrapolated to room temperature

^dMössbauer spectra acquired at room temperature

instruments on the rover is in preparation (Zipfel, Schröder, et al., manuscript in preparation).

4.4.1 Constraints on the pyroxene composition in Bounce Rock

Pyroxenes are single-chain silicates with either orthorhombic (orthopyroxenes) or monoclinic (clinopyroxenes) structure. Orthopyroxenes range compositionally between the endmembers $Mg_2Si_2O_6$ (enstatite) to $Fe_2Si_2O_6$ (ferrosilite). Clinopyroxenes range between the four-component endmember system $CaMgSi_2O_6$ (diopside) - $CaFeSi_2O_6$ (Hedenbergite) - $Mg_2Si_2O_6$ - $Fe_2Si_2O_6$ and are divided into low-Ca pyroxenes and high-Ca pyroxenes. Pigeonite [e.g., $Ca_x(Mg, Fe)_{2-x}Si_2O_6$] is common in Martian meteorites. Augite [e.g., $(Ca, Na)(Mg, Fe, Al)(Si, Al)_2O_6$] is another pyroxene found in Martian meteorites, which contains additional cations such as Na.

The generic formula of pyroxene can be written as $M1M2T_2O_6$, where M1 and M2 represent two distinct octahedrally coordinated crystallographic sites, and T represents tetrahedrally coordinated crystallographic sites. The larger M2 octahedra accommodate Ca, whereby Mg and Fe^{2+} cations occupy M1 and M2 sites. The Fe^{3+} cation may be present in the tetrahedral as well

as the octahedral sites. Mössbauer spectra of pyroxenes may thus be resolved into two doublets resulting from Fe^{2+} in M1 and M2 sites, respectively, or more doublets resulting from next nearest neighbor effects [e.g., *Dyar et al.*, 1989], and distinct doublets for Fe^{3+} in either octahedral or tetrahedral sites (doublets resulting from Fe^{3+} in distinct octahedrally coordinated sites overlap strongly and can generally not be resolved). In Mössbauer spectra M1 and M2 sites are distinguished on the base of their ΔE_Q values. M1 sites are generally attributed to larger ΔE_Q values than the M2 sites. However, the range of ΔE_Q values reported for M1 sites overlaps the entire range of ΔE_Q values reported for M2 sites. Distinguishing between ortho- and clinopyroxenes, or high-Ca and low-Ca clinopyroxenes, is difficult based on Mössbauer parameters alone [compare *Bancroft*, 1973, p. 169; *Mitra*, 1992, p. 158]. A natural rock may contain a mixture of several chemically distinct pyroxene crystals. Hence, Mössbauer spectra may be resolved into distinct doublets attributable to pyroxene phases, but it cannot be inferred, whether the different doublets represent different crystallographical sites in one pyroxene, the same crystallographic site in different pyroxenes, or any combination of those possibilities. Therefore, no attempt was made here or in previous paragraphs to assign individual doublets corresponding to pyroxene to either M1 or M2 sites. Rather, distinct pyroxene doublets were simply labeled 'pyroxene A' and 'pyroxene B'.

Nevertheless, to put some constraints on the pyroxene composition in Bounce Rock, one may compare it to the basaltic shergottites which are well-characterized by many different techniques. The best match for the pyroxene Mössbauer parameters in Bounce Rock (Table 4.5) comes from pyroxene parameters reported for the meteorite QUE94201 by *Dyar*, [2003]. QUE94201 contains complex zoned pyroxenes with Mg-rich pigeonite cores mantled by Mg-rich augite followed by Fe-rich pigeonite [*Mikouchi et al.*, 1998]. Pyroxenes in lithology B of EETA79001 show similar compositional zoning [*Mikouchi et al.*, 1998]. Thus, one feasible interpretation of the two doublets used in the fitting model for Bounce Rock is that the larger split doublet ($\Delta E_Q = 2.63$ mm/s) may be a combination of Fe^{2+} in M1 sites of augite and pigeonite. The lower split doublet ($\Delta E_Q = 2.01$ mm/s) may be a combination of Fe^{2+} in M1 and M2 sites in augite and pigeonite.

4.5 Conclusions

The Martian meteorites are the only rocks believed to be from Mars which are available for detailed analyses in terrestrial laboratories. Bounce Rock adds evidence for their origin. Bounce Rock was discovered by the Mars

Exploration Rover on Meridiani Planum and is similar in chemical and mineralogical composition to basaltic shergottites, a subgroup of the Martian meteorites.

MIMOS II allows non-destructive analysis of these meteorites. Mössbauer spectra show that the olivine-phyric shergottite Dar al Gani 476 contains Fe^{3+} throughout its interior structure, whereas the closely related meteorite Sayh al Uhaymir 005 has no Fe^{3+} in its interior and only small amounts close to the rim. The Fe^{3+} in Dar al Gani 476 stems from the oxidative alteration of olivine by terrestrial water, which percolated the whole rock along fractures and veins.

Mössbauer spectra from the clinopyroxenite Nakhla revealed an inhomogeneous composition on the scale of the MIMOS II field of view (1.4 cm). Whereas olivine was not identified in a spectrum obtained from the interior of Nakhla, Mössbauer parameters derived for components in the fusion crust are consistent with laihunite, an oxidized form of olivine.

Chapter 5

Weathering Experiments

Natural weathering processes are slow and often yield measurable effects only over many years. The challenge for the study of weathering processes in the lab is to reduce these long timescales to a suitable experimental time frame. Because liquid water is directly involved in almost all chemical weathering processes on Earth, most laboratory studies have been performed in aqueous solutions [e.g., *Colman and Dethier*, 1986; *White and Brantley*, 1995]. To speed up reactions, solutions are often high or low in pH compared to the near-neutral conditions found in most natural environments.

Liquid water may not have been present or was only intermittently present in small quantities on most parts of the surface of Mars for millions or even billions of years. Nevertheless, weathering experiments under Martian conditions were also done under aqueous conditions [e.g., *Burns*, 1993b; *Banin et al.*, 1997; *Baker et al.*, 2000; *Tosca et al.*, 2004; *Golden et al.*, 2005], because chemical weathering processes in solutions happen magnitudes faster than gas-solid reactions. However, over the long timescales available on Mars, gas-solid reactions may have been effective. *Gooding* [1978] investigated chemical weathering on Mars theoretically from the standpoint of heterogeneous equilibrium between solid mineral phases and the Martian atmosphere. Based on his theory, experiments were carried out to investigate the interactions between individual minerals and components of the Martian atmosphere. Some of the results presented in this chapter were initially published by *Schröder et al.* [2004].

5.1 Experimental design

5.1.1 Reaction kinetics

The challenge for laboratory weathering studies lies in adjusting reaction kinetics to a suitable time frame (days to weeks rather than multitudes of years) in such a way that one can still compare them to natural environments. In a system involving solid reagents, reactions can only proceed at the surface of the solid compound. To increase the surface available to reactions, fine-grained powders of the solid reagents can be used. In reactions involving gaseous reagents, collision theory becomes important. Effective collisions between reagent molecules need to overcome an energetic barrier. This activation energy E_a must be provided in the form of kinetic energy by the collision. The ratio of effective collisions and hence the reaction rate can be increased by raising the temperature according to the Arrhenius equation

$$k = A \exp \frac{-E_a}{RT}, \quad (5.1)$$

where k is the rate constant, A is the frequency factor, R is the gas constant, and T is the absolute temperature. The upper limit for the temperature in the experiment is the melting point of the solid reagent. Reagents should remain stable at elevated temperatures; solids must not change into different structures, gases should not dissociate.

Thermodynamic calculations can tell us, whether a reaction occurring at elevated temperatures in the experiment will also occur at the low temperature prevailing on the Martian surface and vice versa. Spontaneous Reactions are generally exothermic. According to Le Chatelier's principle, a rise in temperature results in a lower yield of reaction products in an exothermic reaction. Note that Le Chatelier's principle assumes equilibrium conditions, but does not make any assumptions on how fast that equilibrium is reached. Thus, by raising the temperature one trades in some yield of reaction products for reaching equilibrium faster. This trade pays off especially for reactions with large equilibrium constants K , i.e. when the equilibrium lies to a large degree on the side of the products.

Spontaneous reactions occur when the change in Gibbs free energy ΔG is negative. According to the equation

$$\Delta G = \Delta H - T\Delta S, \quad (5.2)$$

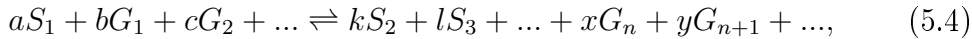
where T is the absolute temperature and ΔS is the change in entropy, this requires a negative value for ΔH (exothermic reaction) and a positive value for ΔS (increase of entropy), or an appropriate combination of the two. If,

for example, the exothermic reaction between two gases produces a liquid or a solid, entropy would decrease ($\Delta S < 0$). If the temperature is chosen too high ΔG may become positive and the reaction, which would occur at lower temperatures, does not proceed any more. Gibbs free energies depend on temperature. Gibbs free energies of formation ΔG_f at different temperatures are available from compilations of thermodynamic data [e.g., *Robie et al.*, 1978]. Values of ΔG_f at different temperatures for compounds appearing in this chapter are listed in Table 5.1.

The equilibrium constant K for a reaction is linked to the Gibbs free energy by the equation

$$\Delta G = -RT \ln(K), \quad (5.3)$$

where R is the gas constant, and T is the absolute temperature. In gas-solid reactions such as



one solid mineral S_1 reacts with one or more gases G_1, G_2, \dots , to form solid alteration products S_2, S_3, \dots , and residual gases G_n, G_{n+1}, \dots . The equilibrium constant can be evaluated from equation 5.4 as

$$K = \frac{[P_{G_n}]^x [P_{G_{n+1}}]^y \dots}{[P_{G_1}]^b [P_{G_2}]^c \dots}, \quad (5.5)$$

where $[P_{G_n}]$, for example, is the partial pressure per pressure unit of gas n . The activities of solids are taken as unity, as are the activities of gases at

Table 5.1: Gibbs free energies of formation ΔG_f from the elements at different temperatures for selected compounds [*Robie et al.*, 1978]).

Compound	ΔG_f (kJ mol ⁻¹)		
	298 K	600 K	1100 K
<i>FeS</i> _{2(s)}	-160.229	-143.551	n.a.
<i>Fe</i> ₂ <i>SiO</i> _{4(s)}	-1379.375	-1279.627	-1118.527
<i>Fe</i> ₃ <i>O</i> _{4(s)}	-1012.566	-911.679	-759.427
<i>Fe</i> ₂ <i>O</i> _{3(s)}	-742.683	-661.886	-536.201
<i>SiO</i> _{2(s)} ^a	-850.559	-797.063	-710.402
<i>H</i> ₂ <i>O</i> _(l)	-237.141	-213.987	-186.985
<i>H</i> ₂ <i>O</i> _(g)	-228.569	-213.981	-186.989
<i>CO</i> _{2(g)}	-394.375	-395.149	-395.936
<i>CO</i> _(g)	-137.171	-164.473	-209.024

^aSilica glass

low pressures such as in the atmospheres of Earth and Mars. Substituting (5.5) into (5.3), boundaries for reaction (5.4) can be calculated and shown in a partial pressure stability diagram [e.g., *Garrels and Christ*, 1965, pp. 144-171].

The boundaries calculated for experiments at elevated temperatures have to be compared to the boundaries calculated for the low temperatures prevailing on Mars. *Gooding* [1978] chose a temperature of 240 K for his calculations. This temperature is close to the average temperature encountered by the Mars Exploration Rovers. Values of ΔG_f for temperatures below room temperature are not as readily available. However, *Gooding* [1978] argues that changes in ΔG over the temperature range from 240 K to 298 K are negligible. Therefore, equilibrium constants K can be calculated with equation 5.3 using room temperature values for ΔG and substituting the temperature T accordingly.

5.1.2 Experimental setup

Powders of minerals occurring on Mars were exposed to gases which are components of the Martian atmosphere. Figure 5.1 shows a sketch of the experimental setup. A mineral powder in a corundum crucible was placed into a glass tube which was situated inside a Carbolite MTF tube furnace. The mineral powder was heated to a specific temperature. Gas release from a bottle was controlled by a pressure reducer. After passing through a wash bottle which was optionally filled with deionized water or left empty, the gas flow was split. Each of the two new lines of the gas flow was led through a glass tube within a tube furnace. The gas could be directed through both furnaces in parallel or just through one furnace at a time. Behind the furnaces the gas flow was reunited and entered two subsequent wash bottles. The first wash bottle was left empty to catch any accidental back flow from the second wash bottle which was filled with water. Finally the gas flow was released to the waste air system.

5.1.3 Choice of gases

The major constituents of the Martian atmosphere are CO_2 (95.32 %), N_2 (2.7 %), ^{40}Ar (1.6 %), O_2 (0.13 %), CO (0.07 %), and H_2O (0.03 %) [*Owen*, 1992]. The mean pressure of the atmosphere at the Martian surface is 6 mbar. CO_2 is rather inert. On Earth, carbonates form from CO_2 dissolved in water which produces carbonic acid (H_2CO_3), not from reactions with CO_2 in the atmosphere. On Mars, photo-dissociation of CO_2 in the atmosphere

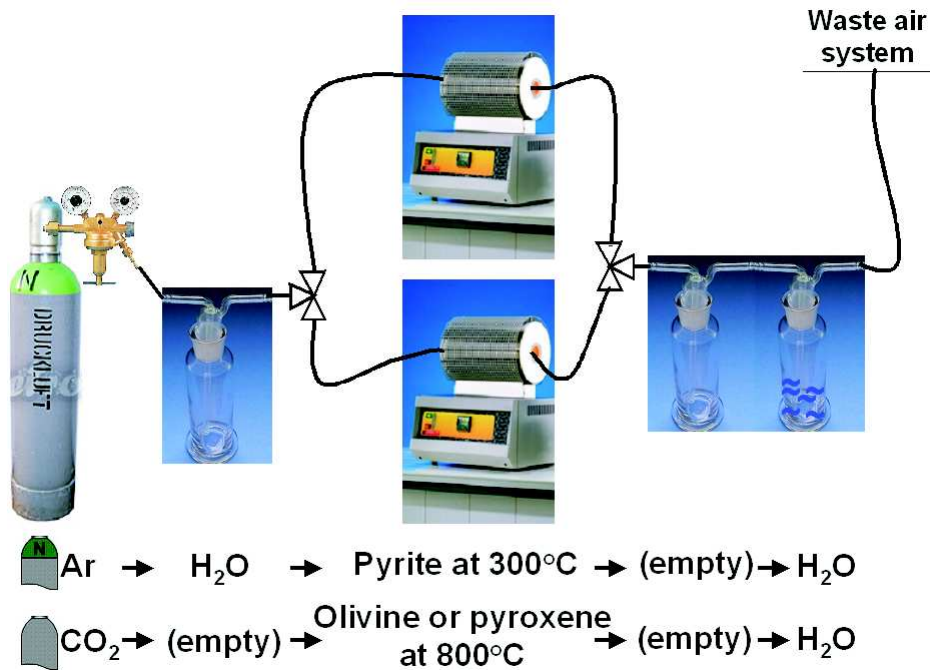


Figure 5.1: This collage shows the arrangement of the weathering experiment. Mineral powders in corundum crucibles were placed inside a glass tube which is situated in a tube furnace. In one set of experiments argon was bubbled through deionized water and then led past pyrite powder at 300°C. In another set of experiments CO_2 was led past olivine or pyroxene powders at 800°C.

results in the more reactive species CO and O_2 . Partial pressures for selected components of the Martian atmosphere are listed in Table 5.2.

Reactions between minerals and water vapor in the Martian atmosphere were investigated in a first set of experiments. Ar gas was bubbled through deionized water to take up water vapor. The gas mixture was then led

Table 5.2: Partial pressures of selected components of the Martian atmosphere.

Component	Abundance (%)	log P ^a
CO_2	95.32	-2.2
O_2	0.13	-5.1
CO	0.07	-5.4
H_2O	0.03	-5.7

^aP is given in partial pressure per millibar

through the tube furnaces to react with the mineral powders. Reactions between minerals and CO_2 were investigated in a second set of experiments. CO_2 was led through the tube furnace without prior contact with water.

5.1.4 Choice of minerals

The weathering experiments were performed with three different minerals: Pyrite, olivine, and pyroxene. Pyrite (FeS_2) is by far the most common sulfide mineral on Earth. Pyrite has not been identified on Mars to date, but levels of S are generally enhanced in Martian soils [e.g., *Clark et al.*, 1976; *Toulmin et al.*, 1977; *Rieder et al.*, 1997, 2004; *Gellert et al.*, 2004, 2006], inferring the presence of sulfide ore bodies. The Tinto river, an acidic mine drainage system, has its source region in the Iberian pyrite belt. From the oxidation of pyrite ore bodies it produces sediments rich in Fe-sulfates and Fe-oxyhydroxides, which provide an Earth analogue for the sulfate-rich outcrop rocks identified by the Mars Exploration Rover Opportunity at Meridiani Planum on Mars [*Fernández-Remolar et al.*, 2004, 2005; *Klingelhöfer et al.*, 2004].

Pyrite was synthesized by adding stoichiometric amounts of Fe and S into a quartz glass ampulla. The ampulla was subsequently evacuated, sealed, and heated to 370°C. The reaction products had a flaky appearance. Mössbauer spectroscopy (Figure 5.2) and X-ray diffraction (XRD) confirmed the formation of pyrite. No other compounds were identified, albeit Mössbauer spectra revealed relatively large line widths for the pyrite doublet (Figure 5.2, Table 5.3). The broad lines indicate a low level of crystallinity. Figure 5.2 compares MB spectra of synthetic and natural pyrite. The natural pyrite was obtained from Ward's (now Sargent Welch) and originally collected at Zacatecas, Mex-

Table 5.3: Mössbauer parameters of synthetic and natural pyrite.

Sample	δ^{ab} (mm/s)	ΔE_Q (mm/s)	Lorentz ^c (mm/s)	Gauss ^d (mm/s)	Area (%)
Synthetic pyrite	0.31	0.63	0.18	0.15	100
Natural pyrite	0.31	0.62	0.16	0.01	100

^aRelative to α -Fe.

^bTypical uncertainties are ± 0.02 mm/s for δ and ΔE_Q , ± 0.01 mm/s for Lorentz and Gauss, and ± 2 % for the area.

^cHalf width at half maximum. Spectra were fitted with Voigt line shapes, a convolution of Lorentzian and Gaussian line shapes. Gauss = 0 results in pure Lorentzians, Lorentz = 0 in pure Gaussians.

^dSee footnote b.

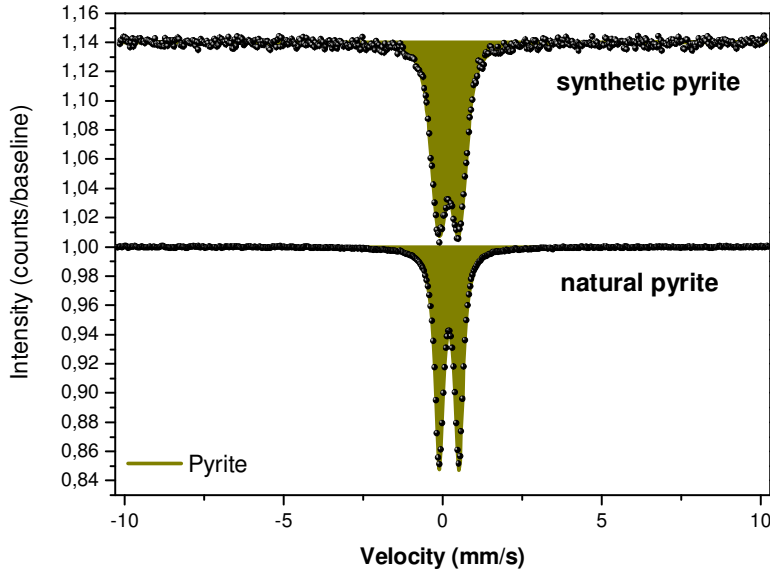


Figure 5.2: Mössbauer spectra of synthetic and natural pyrite samples. The pyrite doublet of the synthetic sample shows a broader line width which implies a lower crystallinity than in the natural pyrite. Spectra are offset along the y-axis for clarity.

ico. The chemical composition of the natural pyrite was investigated by ion microprobe analysis. Ten spots each on four different centimeter-sized mineral specimen were investigated. The averaged results are listed in Table 5.4. They show negligible amounts of impurities.

The nesosilicate olivine $[(Mg, Fe)_2SiO_4]$ with its Mg-rich and Fe-rich end-members forsterite (Mg_2SiO_4) and fayalite (Fe_2SiO_4), respectively, occurs in many of the Martian meteorites. It has been identified on Mars from orbit [e.g., *Bandfield, 2002; Hoefen et al., 2003; Bibring et al., 2005; Mustard et al., 2005*], and in situ in many Martian rocks and soils by the Mössbauer spectrometers on the Mars Exploration Rovers [*Klingelhöfer et al., 2004; Morris et al., 2004, 2006a*]. Natural forsteritic olivine, originally collected at Twin Sisters Range, Washington, USA, was obtained from Ward’s (now Sargent-Welch). Its chemical composition was investigated by ion microprobe analyses, analogous to the natural pyrite samples described above. The averaged composition is given in Table 5.5. The Mg/(Mg+Fe) elemental ratio is 0.93, i.e. the composition of the olivine is Fo93. The analysis revealed Ni and Mn impurities, which are common in natural olivines.

Pyroxenes (see discussion on pyroxenes in Chapter 4.4.1) were identified on Mars from orbit [e.g., *Bandfield, 2002; Hoefen et al., 2003; Bibring et al.,*

Table 5.4: Average elemental composition in wt% of natural pyrite samples from ion microprobe analyses.

	Minimum	Maximum	Average ^a	Sigma
As	0.00	0.34	0.06	0.09
S	52.50	53.51	52.92	0.22
Cu	0.00	0.07	0.02	0.02
Fe	45.71	46.61	46.24	0.28
Si	0.01	0.05	0.03	0.01
Ni	0.00	0.06	0.02	0.02
Zn	0.00	0.03	0.00	0.01
Co	0.00	0.00	0.00	0.00
Total	98.39	100.09	99.29	0.46

^aFrom 40 data sets.

2005; *Mustard et al.*, 2005], and in situ in many Martian rocks and soils by the Mössbauer spectrometers on the Mars Exploration Rovers [*Klingelhöfer et al.*, 2004; *Morris et al.*, 2004, 2006a]. They have not been constrained to a particular composition. Augite originally collected at Harcourt Township, Ontario, Canada, was obtained from Ward's (now Sargent-Welch). Augite has been identified in Martian meteorites. Pigeonite is more common in Martian meteorites but was not commercially available. The chemical composition of the augite was investigated by ion microprobe analyses, analogous to the natural pyrite samples described above. The averaged composition is given in Table 5.6. From stoichiometric considerations Al^{3+} must be in tetrahedral positions substituting for Si^{4+} , whereas Fe^{3+} resides in octahedral positions as suggested by the corresponding Mössbauer parameters (Table 5.10). Because the sum of Ca and Na fill all available M2 sites, all Fe must reside in M1 sites and one can only observe one Fe^{2+} doublet (Figure 5.6).

5.2 Results and discussion

5.2.1 Pyrite

In a first set of experiments the synthetic pyrite flakes were crushed in a mortar. The resulting powder was then filled into corundum crucibles which in turn were placed inside the tube furnaces. Argon was bubbled through deionized water before flowing past the pyrite. Fresh pyrite powder was exposed for three days at 150°C, three days at 250°C, and 12 days at 300°C,

Table 5.5: Average elemental composition in oxide wt% of olivine samples from ion microprobe analyses.

	Minimum	Maximum	Average^a	Sigma
<i>Al₂O₃</i>	0.00	0.02	0.01	0.01
<i>SiO₂</i>	40.95	41.99	41.33	0.22
<i>CaO</i>	0.00	0.01	0.01	0.00
<i>FeO</i>	5.98	7.85	7.11	0.63
<i>NiO</i>	0.34	0.44	0.38	0.03
<i>MgO</i>	51.23	53.44	52.24	0.67
<i>Cr₂O₃</i>	0.01	0.03	0.02	0.01
<i>MnO</i>	0.08	0.16	0.11	0.02
<i>Na₂O</i>	0.00	0.00	0.00	0.00
<i>K₂O</i>	0.00	0.00	0.00	0.00
<i>TiO₂</i>	0.00	0.00	0.00	0.00
Total	100.12	102.37	101.20	0.49

^afrom 40 data sets.

Table 5.6: Average elemental composition in oxide wt% of augite samples from ion microprobe analyses.

	Minimum	Maximum	Average	Sigma
<i>Al₂O₃</i>	0.63	1.05	0.85	0.13
<i>SiO₂</i>	51.42	52.95	52.42	0.38
<i>CaO</i>	23.27	24.20	23.73	0.23
<i>FeO</i>	9.68	10.48	10.02	0.16
<i>NiO</i>	0.00	0.00	0.00	0.00
<i>MgO</i>	11.80	12.44	12.12	0.18
<i>Cr₂O₃</i>	0.00	0.17	0.06	0.05
<i>MnO</i>	0.20	0.38	0.28	0.04
<i>Na₂O</i>	0.43	0.76	0.59	0.09
<i>K₂O</i>	0.00	0.03	0.00	0.01
<i>TiO₂</i>	0.00	0.09	0.02	0.03
Total	100.12	102.37	101.20	0.49

respectively. Temperatures were chosen to be above the boiling point of water to avoid water condensation on the pyrite powder, and below the temperature which the pyrite was synthesized at. Changes were only observed in the third run. Mössbauer spectroscopy identified magnetite and hematite as the alteration products (Figure 5.3). Table 5.7 lists the reactions used to calculate a partial pressure stability diagram (Figure 5.4). According to that stability diagram pyrite would eventually decompose to hematite at 240 K and $\log P_{O_2} = -5.1$, approximating the present conditions on Mars. Both magnetite and hematite were observed in Mössbauer spectra from the experimentally weathered material. Equilibrium constants for the production of magnetite and hematite (Table 5.7) are of similar magnitude, but eventually the magnetite should also be oxidized to hematite.

The altered material was unstable with respect to the oxygen-rich atmosphere encountered when stored in the office. Water vapor apparently condensed from moisture in the office air onto the stored pyrite powder. Figure 5.3 shows Mössbauer spectra obtained from the experimentally altered sample after storage for 4 days, one month, and two months in the office. During storage time magnetite was further oxidized which is suggested by a change in area ratios for the two sextets due to Fe^{3+} in tetrahedral sites, and mixed Fe^{3+} and Fe^{2+} in octahedral sites (Table 5.8). The crystallinity of hematite increased which was indicated by its decreasing line width. An Fe^{2+} -sulfate, szomolnokite ($FeSO_4 \cdot H_2O$), appeared alongside a sulfide with higher stoichiometric Fe/S ratio than pyrite. The Mössbauer parameters of that sulfide are consistent with pentlandite (Fe_9S_8). The pyrite line widths decreased which suggests that less well-crystalline pyrite was preferably altered.

The successful alteration experiment was repeated with the natural pyrite. The natural pyrite was crushed into a powder with the help of a ball mill. The crushed pyrite was then sieved into several grain-size fractions: $< 45 \mu m$, $45-63 \mu m$, $63-250 \mu m$, and $> 250 \mu m$. Pyrite powder with a grain size

Table 5.7: Pyrite weathering reactions and logarithms of equilibrium constants at different temperatures.

Reaction	log K (600 K)	log K (298 K)	log K (240 K)
$H_2O_{(l)} \rightleftharpoons H_{2(g)} + \frac{1}{2}O_{2(g)}$	-18.6	-40.1	-49.7
$3FeS_{2(s)} + 2O_{2(g)} \rightleftharpoons Fe_3O_{4(s)} + 3S_{2(g)}$	41.9	93.2	115.7
$2FeS_{2(s)} + \frac{3}{2}O_{2(g)} \rightleftharpoons Fe_2O_{3(s)} + 2S_{2(g)}$	32.6	74.0	91.9
$2Fe_3O_{4(s)} + \frac{1}{2}O_{2(g)} \rightleftharpoons 3Fe_2O_{3(s)}$	14.1	35.6	44.2

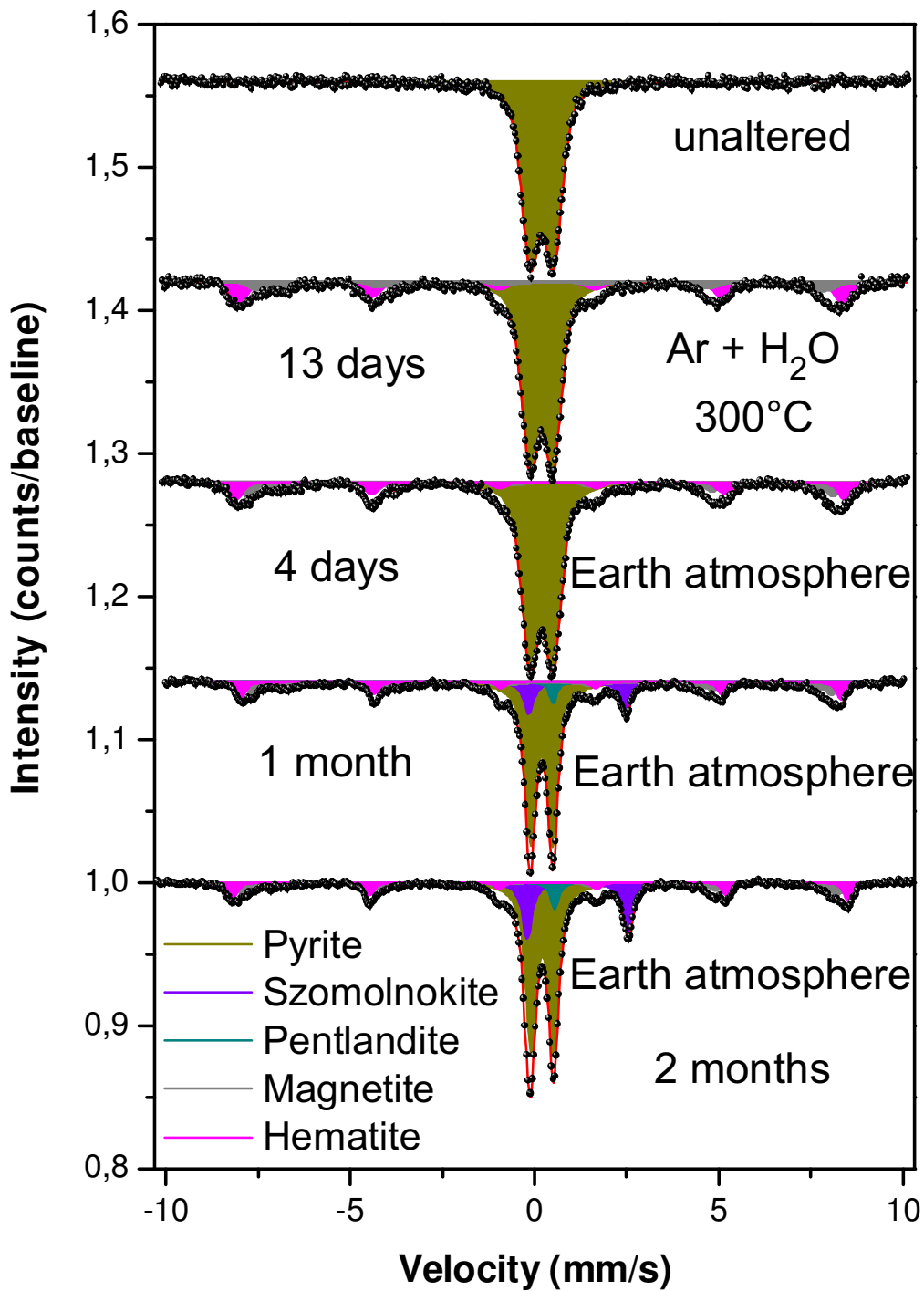


Figure 5.3: Mössbauer spectra of synthetic pyrite before and after alteration experiments. Iron oxides were produced during the experiment in which elevated temperatures prevented water from condensing. Szomolnokite, a hydrous ferrous sulfate, formed during subsequent storage of the altered samples in the apparently moist office atmosphere. Spectra are offset along the y-axis for clarity.

Table 5.8: Mössbauer parameters of fresh and weathered synthetic pyrite samples.

Mineral	Fe ox. and coord.	δ^{ab} (mm/s)	ΔE_Q (mm/s)	B_{hf} (T)	Lorentz ^c (mm/s)	Gauss ^d (mm/s)	Area (%)
Synthetic pyrite, unaltered							
Pyrite	Fe^{2+}	0.31	0.63	-	0.18	0.15	100
Synthetic pyrite, $Ar + H_2O$, 300°C							
Pyrite	Fe^{2+}	0.30	0.62	-	0.16	0.15	66
Magnetite	Tet. Fe^{3+}	0.34	0.00	48.1	0.11	0.17	6
	$Fe^{2.5+}$	0.58	-0.01	45.4	0.37	0.00	11
Hematite	Oct. Fe^{3+}	0.37	-0.17	50.9	0.11	0.19	17
Synthetic pyrite, Earth atmosphere, 4 days							
Pyrite	Fe^{2+}	0.30	0.62	-	0.17	0.15	66
Magnetite	Tet. Fe^{3+}	0.32	-0.05	49.1	0.11	0.16	9
	$Fe^{2.5+}$	0.61	-0.06	45.7	0.37	0.20	13
Hematite	Oct. Fe^{3+}	0.38	-0.21	51.3	0.11	0.14	12
Synthetic pyrite, Earth atmosphere, 1 month							
Pyrite	Fe^{2+}	0.31	0.61	-	0.17	0.02	54
Szomolnokite	Fe^{2+}	1.27	2.64	-	0.16	0.00	11
Pentlandite	Tet. Fe^{2+}	0.62	0.00	-	0.11	0.00	2
Magnetite	Tet. Fe^{3+}	0.34	-0.07	48.7	0.12	0.12	10
	$Fe^{2.5+}$	0.56	0.06	44.8	0.40	0.00	13
Hematite	Fe^{3+}	0.38	-0.20	50.5	0.11	0.06	10
Synthetic pyrite, Earth atmosphere, 2 months							
Pyrite	Fe^{2+}	0.32	0.61	-	0.16	0.02	52
Szomolnokite	Fe^{2+}	1.28	2.73	-	0.16	0.01	17
Pentlandite	Tet. Fe^{2+}	0.65	0.00	-	0.13	0.01	3
Magnetite	Tet. Fe^{3+}	0.35	-0.07	49.7	0.13	0.18	12
	$Fe^{2.5+}$	0.59	-0.03	45.6	0.11	0.20	5
Hematite	Oct. Fe^{3+}	0.37	-0.22	51.8	0.12	0.06	11

^aRelative to α -Fe.

^bTypical uncertainties are ± 0.02 mm/s for δ and ΔE_Q , ± 0.1 T for B_{hf} , ± 0.01 mm/s for Lorentz and Gauss, and ± 2 % for the area.

^cHalf width at half maximum. Spectra were fitted with Voigt line shapes, a convolution of Lorentzian and Gaussian line shapes. Gauss = 0 results in pure Lorentzians, Lorentz = 0 in pure Gaussians.

^dSee footnote b.

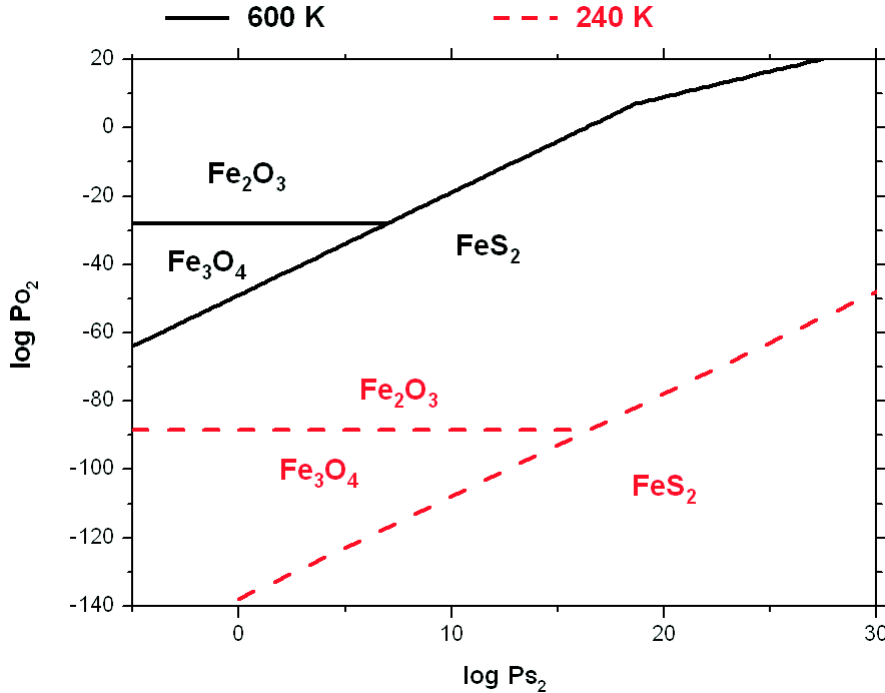


Figure 5.4: Partial pressure diagram for an $\text{FeS}_2(\text{s})\text{-O}_2(\text{g})\text{-S}_2(\text{g})$ system calculated from values given in Table 5.1. On Mars ($\log \text{PO}_2 = -5.1$) pyrite should decompose to hematite.

below $45 \mu\text{m}$ was used in the experiment. Fresh powders were exposed to the $\text{Ar} + \text{H}_2\text{O}$ vapor at 300°C for 1 day, 3, 4, 9, and 16 days. No alteration was observed by Mössbauer spectroscopy in the natural pyrite powders. One sample, however, when investigated by Mössbauer spectroscopy after storage in the office for more than one month, had developed small amounts of the Fe^{2+} -sulfate szomolnokite again (Figure 5.5, Table 5.9).

Taking the results from the synthetic and the natural pyrite together, the susceptibility to alteration under the conditions described above increases with decreasing crystallinity. The water-bearing iron sulfate szomolnokite only formed after temperatures were low enough to allow the condensation of water. Adsorption of atmospheric water on pyrite crystal surfaces is a possible scenario on Mars under the current environmental conditions. However, ferrous sulfates have not been observed on Mars to date. Conditions on Mars are thus more oxidizing and/or sulfate ions preferentially combine with other doubly-charged cations such as Mg, whereas iron is altered into oxides. Mg-sulfates such as kieserite were observed from orbit [Bibring *et al.*, 2005] and inferred from APXS results on MER [e.g., Ming *et al.*, 2006]. In

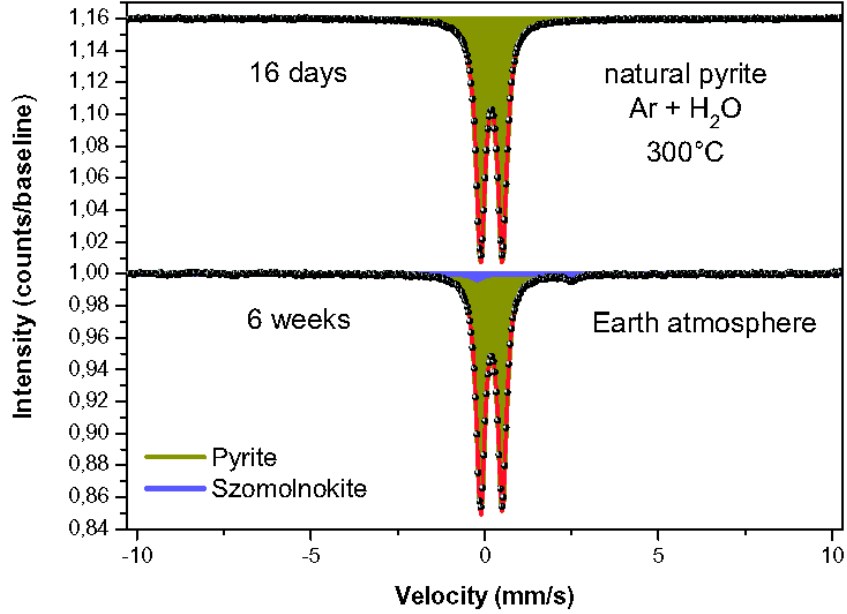


Figure 5.5: Mössbauer spectra of natural pyrite before and after alteration experiments. The well-crystalline natural pyrite was not altered during the experiments in which liquid water was prevented from condensing through elevated temperatures. However, szomolnokite, a hydrous ferrous sulfate, formed during storage of the sample in the apparently moist office atmosphere. Spectra are offset along the y-axis for clarity.

Table 5.9: Mössbauer parameters of fresh and weathered natural pyrite samples.

Mineral	Fe ox. and coord.	$\delta^{a,b}$ (mm/s)	ΔE_Q (mm/s)	B_{hf} (T)	Lorentz ^c (mm/s)	Gauss ^d (mm/s)	Area (%)
Natural pyrite, $Ar + H_2O$, 300°C							
Pyrite	Fe^{2+}	0.31	0.62	-	0.16	0.01	100
Natural pyrite, Earth atmosphere							
Pyrite	Fe^{2+}	0.31	0.62	-	0.14	0.03	97
Szomolnokite	Fe^{2+}	1.27	2.73	-	0.17	0.00	3

^aRelative to α -Fe.

^bTypical uncertainties are ± 0.02 mm/s for δ and ΔE_Q , ± 0.01 mm/s for Lorentz and Gauss, and ± 2 % for the area.

^cHalf width at half maximum. Spectra were fitted with Voigt line shapes, a convolution of Lorentzian and Gaussian line shapes. Gauss = 0 results in pure Lorentzians, Lorentz = 0 in pure Gaussians.

^dSee footnote b.

experiments by *Tosca et al.* [2004] the formation of ferrous sulfates was only observed at low pH (< 4), whereas Mg sulfates and Fe oxides formed at pH levels between 4 and 7.

5.2.2 Olivine and pyroxene

Olivine and pyroxene powder samples were exposed to an Ar gas flow bubbled through water in the same way as described above. No alteration was observed in either mineral. In another experiment, the minerals olivine and pyroxene were exposed to a dry CO_2 gas flow. The wash bottle between gas bottle and tube furnaces remained empty. The experiments were carried out at a temperature of $800^\circ C$. This temperature is high considering that it approaches the temperature of some alkaline melts. The melting points of mafic minerals, such as olivines and pyroxenes, however, are considerably larger. Melting points for olivine range from $1205^\circ C$ (fayalite) to $1890^\circ C$ (forsterite), melting points for pyroxenes are $> 1543^\circ C$ [Matthes, 2001].

Mössbauer spectra of the powders were taken at room temperature prior to and after these weathering experiments. Standard Mössbauer transmission setups were used for these analyses. The spectra are shown in Figures 5.6 (augite) and 5.7 (olivine). Hyperfine parameters are listed in Tables 5.10 and 5.11. While pyroxene developed no Fe-bearing alteration other than an increase in ferric iron, olivine was altered significantly. Olivine was oxidized to hematite of varying degrees of crystallinity. Next to the changes determined by Mössbauer spectroscopy a color change was observed in the weathered samples. Augite powder changed slightly from light greyish green into a greenish yellow, olivine powder changed from light grey to rusty red.

A sextet was attributed to poorly-crystalline hematite in the Mössbauer spectrum of altered olivine powder (grainsize $< 45 \mu m$). Its Mössbauer parameters could also be reconciled with maghemite. Maghemite is isostructural to magnetite, but has all Fe as Fe^{3+} . However, maghemite restructures to hematite at temperatures above $600^\circ C$. Olivine is given as fayalite here because the Mössbauer results allow only conclusions on the iron-bearing alteration reactions. At the $\sim 1100 K$ of the experiment fayalite is altered to magnetite at $\log P_{O_2} = -14.3$ (-99.2 at $240 K$, respectively) and to hematite at $\log P_{O_2} = -12.4$ (-95.6 at $240 K$, respectively).

5.3 Conclusions

The experimental results highlight the increasing susceptibility to weathering with decreasing crystallinity and particle size. An important component

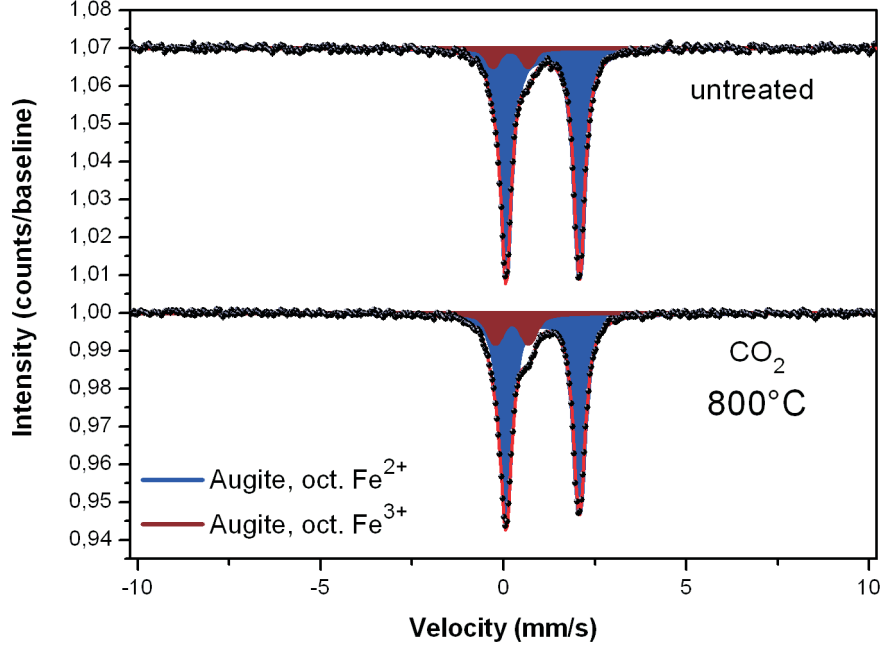


Figure 5.6: Mössbauer spectra of augite before and after alteration experiments. The experiment resulted in an increase of the octahedral Fe^{3+} component. Spectra are offset along the y-axis for clarity.

Table 5.10: Mössbauer parameters of fresh and weathered augite samples.

Mineral	Fe ox. and coord.	δ^{ab} (mm/s)	ΔE_Q (mm/s)	B_{hf} (T)	Lorentz ^c (mm/s)	Gauss ^d (mm/s)	Area (%)
<i>Fresh augite</i>							
Augite	Oct. Fe^{2+}	1.19	2.01	-	0.18	0.02	93
	Oct. Fe^{3+}	0.30	0.96	-	0.11	0.11	7
<i>Weathered augite, CO_2 at $800^\circ C$</i>							
Augite	Oct. Fe^{2+}	1.19	2.00	-	0.18	0.04	85
	Oct. Fe^{3+}	0.35	0.91	-	0.16	0.12	15

^aRelative to α -Fe.

^bTypical uncertainties are ± 0.02 mm/s for δ and ΔE_Q , ± 0.01 mm/s for Lorentz and Gauss, and $\pm 2\%$ for the area.

^cHalf width at half maximum. Spectra were fitted with Voigt line shapes, a convolution of Lorentzian and Gaussian line shapes. Gauss = 0 results in pure Lorentzians, Lorentz = 0 in pure Gaussians.

^dSee footnote b.

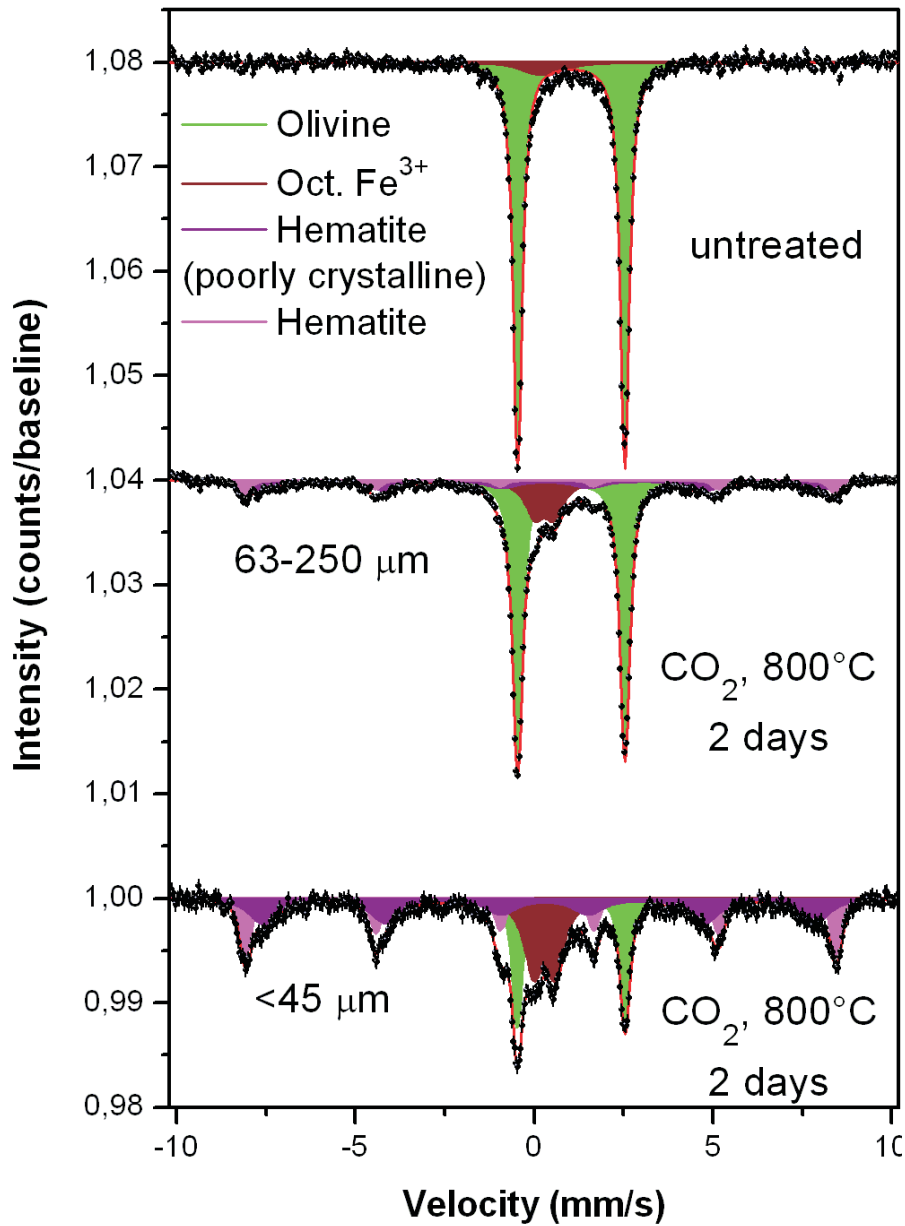


Figure 5.7: Mössbauer spectra of olivine before and after alteration experiments. The experiment resulted in the formation of hematite with varying degrees of crystallinity. The amount of alteration increased with decreasing particle size. Spectra are offset along the y-axis for clarity.

Table 5.11: Mössbauer parameters of fresh and weathered olivine samples.

Mineral	Fe ox. and coord.	δ^{ab} (mm/s)	ΔE_Q (mm/s)	B_{hf} (T)	Lorentz ^c (mm/s)	Gauss ^d (mm/s)	Area (%)
Fresh olivine							
Olivine	Oct. Fe^{2+}	1.15	3.00	-	0.14	0.03	94
	Oct. Fe^{3+}	[0.39] ^e	[0.59]	-	0.40	0.20	6
Weathered olivine, CO_2 at 800°C, 63-250 μm grainsize							
Olivine	Oct. Fe^{2+}	1.15	3.00	-	0.14	0.05	61
	Oct. Fe^{3+}	0.40	0.55	-	0.32	0.00	14
p.c. Hem. ^f	Oct. Fe^{3+}	0.36	-0.14	47.7	0.40	0.20	18
Hematite	Oct. Fe^{3+}	0.37	-0.19	51.2	0.11	0.12	7
Weathered olivine, CO_2 at 800°C, <45 μm grainsize							
Olivine	Oct. Fe^{2+}	1.14	3.02	-	0.12	0.07	21
	Oct. Fe^{3+}	0.39	0.59	-	0.31	0.00	23
p.c. Hem.	Oct. Fe^{3+}	0.33	-0.16	47.5	0.40	0.19	34
Hematite	Oct. Fe^{3+}	0.39	-0.17	51.2	0.11	0.10	22

^aRelative to α -Fe.

^bTypical uncertainties are ± 0.02 mm/s for δ and ΔE_Q , ± 0.1 T for B_{hf} , ± 0.01 mm/s for Lorentz and Gauss, and ± 2 % for the area.

^cHalf width at half maximum. Spectra were fitted with Voigt line shapes, a convolution of Lorentzian and Gaussian line shapes. Gauss = 0 results in pure Lorentzians, Lorentz = 0 in pure Gaussians.

^dSee footnote b.

^eValues in square brackets were fixed during the fitting procedure.

^fPoorly crystallized hematite

Table 5.12: Olivine weathering reactions and logarithms of equilibrium constants at different temperatures.

Reaction	log K (1100 K)	log K (298 K)	log K (240 K)
$CO_{2(g)} \rightleftharpoons CO_{(g)} + \frac{1}{2}O_{2(g)}$	-8.9	-45.1	-56.0
$3Fe_2SiO_{4(s)} + O_{2(g)} \rightleftharpoons 2Fe_3O_{4(s)} + 3SiO_{2(s)}$	14.3	79.9	99.2
$Fe_2SiO_{4(s)} + \frac{1}{2}O_{2(g)} \rightleftharpoons Fe_2O_{3(s)} + SiO_{2(s)}$	6.2	38.5	47.8
$2Fe_3O_{4(s)} + \frac{1}{2}O_{2(g)} \rightleftharpoons 3Fe_2O_{3(s)}$	4.3	35.6	44.2

of the Martian surface and atmosphere is fine-grained dust. From atmospheric observations during the Mars Exploration Rover mission, *Lemmon et al.* [2004] estimated a mean grain size of $1.5 \mu\text{m}$ for dust particles suspended in the Martian atmosphere. The powders used in the experiments had grain-sizes $< 45 \mu\text{m}$. Aeolian dust is a global component of the Martian soil. It has accumulated as bright layers in favorable locations on the surface [*Yen et al.*, 2005a] so that a Mössbauer spectrum could be obtained. This component of the soil is generally more oxidized [*Morris et al.*, 2004, 2006a; *Klingelhöfer et al.*, 2004] than darker-toned soil material. Mössbauer spectra obtained from atmospheric dust collected by magnets on the Mars Exploration Rovers confirm this observation [*Goetz et al.*, 2005]. The experimental results described in this chapter suggest that the oxidation of Martian fine-grained dust is to a large degree the result of oxidative alteration of olivine by the atmosphere.

Well-crystalline pyrite appeared to be stable in the experiments as long as liquid water was prevented from condensing on mineral surfaces through elevated temperatures. In the case of poorly-crystallized pyrite ferric oxides formed as reaction products in the absence of liquid water. A ferrous sulfate, szomolnokite, formed from both poorly-crystallized and well-crystallized pyrite when liquid water was allowed to condensate. Basaltic soil has been identified at both Mars Exploration Rover landing sites. It is very similar in elemental and mineralogical composition at both landing sites and may thus be a global unit [*Yen et al.*, 2005a; *Morris et al.*, 2006a]. Ferrous sulfates have not been identified in this unit, but iron oxides were observed [*Klingelhöfer et al.*, 2004; *Morris et al.*, 2006a]. If one assumes pyrite ore bodies as a source of the elevated sulfur levels in Martian basaltic soils, the experimental results suggest mainly dry conditions on Mars since the formation of the global basaltic soil unit.

Chapter 6

Weathering on Mars

All chemical weathering processes on Earth are driven by the water cycle. On Mars, however, the role of liquid water is not yet well understood. While there are many signatures attributable to the actions of liquid water on the surface of Mars [e.g., *Carr, 1996*], the environmental conditions today, i.e., cold temperatures and low atmospheric pressures, do not allow for the existence of liquid water on its surface. Hence, Mars apparently experienced a period of a warmer and wetter climate in the past and conditions were more Earth-like. When the climate on Mars changed, water may have remained in the subsurface largely in the form of ice [*Squyres et al., 1992*]. Some water may have been lost to space [e.g., *Luhmann et al., 1992*].

Water ice is abundant in the Martian polar caps, as observed, e.g., by the NASA Mars Global Surveyor (MGS) orbiter's Thermal Emission Imaging System (THEMIS) [*Titus et al., 2003*] or the ESA Mars Express orbiter's Observatoire pour la Minéralogie, l'Eau, les Glaces, et l'Activité (OMEGA) [*Bibring et al., 2005; Langevin et al., 2005*]. Recent glacial activity has also been observed at lower latitudes by Mars Express' High Resolution Stereo Camera (HRSC) [*Neukum et al., 2004*]. The distribution of hydrogen in the near surface as evidence for subsurface ice deposits has been mapped by the NASA Mars Odyssey orbiter's Gamma-ray Spectrometer (GRS) [*Boynton et al., 2002*], and evidence for subsurface ice deposits have been discovered in a buried crater by Mars Express' Mars Advanced Radar for Subsurface and Ionospheric Sounding (MARSIS) [*Picardi et al., 2005*]. The atmosphere is composed of 95 % CO_2 , but contains amounts of water vapor which are sufficient to produce frost veneers on the surface as observed on cold mornings during the Viking and MER missions. Whether these ice deposits together with undiscovered deposits mount up to Mars original water inventory or whether they are just fractional remnants is not known.

Mars lacks the extensive plate tectonism known on Earth. Effective burial

mechanisms for rocks are reduced to fresh lava flows and sand and dust sheets moved around by aeolian activity. Seasonal dust storms frequently engulf the entire planet. Thus, rocks whose weathering patterns recorded the ancient wetter period, and younger rocks whose weathering patterns record more modern climates, are all accessible on the Martian surface. The in situ study of such diverse rocks will add important pieces to the Martian climate puzzle. *Gooding et al.* [1992] summarized possible weathering scenarios for the surface of Mars (Table 6.1). As they noted, intact profiles of rocks of similar composition, but with the widest possible range of ages, should be mineralogically analyzed to determine how surface weathering processes might have changed through Martian history. Comparable analyses would be desirable for soil profiles so that pedogenic weathering could be compared with surface weathering. Such a dataset is now available from the Mars Exploration Rover Spirit's investigation in Gusev Crater.

Table 6.1: Possible attributes of weathering on Mars [*Gooding et al.*, 1992].

<p>Physical weathering processes</p> <ul style="list-style-type: none"> • Frost riving • Secondary mineral(oid) riving • Wind abrasion (dust or ice projectiles)
<p>Chemical weathering processes</p> <ul style="list-style-type: none"> • Oxidation: uptake of oxygen to form oxides or more highly oxidized silicates • Hydration: uptake of water to form minerals with structural OH^- or H_2O • Carbonation: uptake of CO_2 to form carbonate minerals • Solution: dissolving of mineral in water
<p>Styles that vary with environmental conditions</p> <ul style="list-style-type: none"> • Surface weathering (controlled by mineral surfaces exposed to atmosphere) <ul style="list-style-type: none"> ◦ Gas-solid (present climate, +/- UV photocatalysis) ◦ Liquid-solid (ancient climates with liquid water) • Pedogenic weathering (within soil profile below free surface) <ul style="list-style-type: none"> ◦ Liquid-like films of unfrozen water ◦ Pore-gas pressures higher than atmospheric pressure ◦ Brines • Hydrothermal alteration (groundwater circulation driven by transient heat source) <ul style="list-style-type: none"> ◦ Meteorite impact crater ◦ Volcanic eruption

The Mars Exploration Rovers (Figure B.1) are equipped with the Athena Science Payload [*Squyres et al.*, 2003]. In situ instruments on the rovers' robotic arm (IDD - Instrument Deployment Device) other than the Mössbauer spectrometer MIMOS II include the Alpha Particle X-ray Spectrometer (APXS) [*Rieder et al.*, 2003] providing information on elemental chemistry, the Microscopic Imager (MI) [*Herkenhoff et al.*, 2003] providing small-scale visual context, and the Rock Abrasion Tool (RAT) [*Gorevan et al.*, 2003] providing access to dust-free and fresh rock surfaces through brushing and grinding actions. Trenching with the rovers' wheels provides access to sub-surface soils¹ and soil profiles. Remote sensing instruments mounted on top of the Pancam Mast Assembly (PMA) include a multispectral Panorama Camera (Pancam) [*Bell et al.*, 2003] and a Miniaturized Thermal Emission Spectrometer (Mini-TES) [*Christensen et al.*, 2003], providing mineralogical information and macroscopic context. Further insight into weathering phenomena can be gained by the analysis of aeolian dust collected by magnet arrays on the rovers [*Madsen et al.*, 2003].

The primary MER objective is to explore two sites on the Martian surface where water may once have been present, and to assess past environmental conditions at those sites and their suitability for life [*Squyres et al.*, 2003]. Spirit landed in Gusev crater on 4 January 2004 UTC. Located at the outlet of Ma'adim Vallis and 250 km south of the volcano Apollinaris Patera, the crater could have collected sediments from a variety of sources during its 3.9 Ga history, including fluvial, lacustrine, volcanic, glacial, impact, regional and local aeolian, and global air falls [*Cabrol et al.*, 2003]. Results from Spirit's primary 90 sol mission were summarized by *Squyres et al.* [2004a]. *Arvidson et al.* [2006] give an overview of the extended mission up until sol 512. Spirit found little evidence for aqueous alteration of rocks and soils during its traverse from the landing site across the Gusev plains towards the Columbia Hills [e.g., *Morris et al.*, 2004; *Haskin et al.*, 2005; *Wang et al.*, 2006]. The Columbia Hills are embayed by and therefore older than the Hesperian age Gusev plains basalt flow (Figure 6.1) [*Golombek et al.*, 2006]. They contain morphological [*Cabrol et al.*, 2006] as well as substantial geochemical and mineralogical indicators for aqueous processes [*Ming et al.*, 2006] such as the identification of the iron oxyhydroxide goethite (α -FeOOH) [*Morris et al.*, 2006a].

Rocks investigated until sol 512 (Figure 6.2) have been divided into six rock classes [*Squyres et al.*, 2006] based on their chemical composition [*Gellert*

¹The term 'Martian soil' is used here to denote any loose unconsolidated materials that can be distinguished from rocks, bedrock, or strongly cohesive sediments. No implication of the presence or absence of organic materials or living matter is intended. For a discussion of 'soil' versus 'regolith' on Mars see *Banin et al.* [1992] or *Banin* [2005].

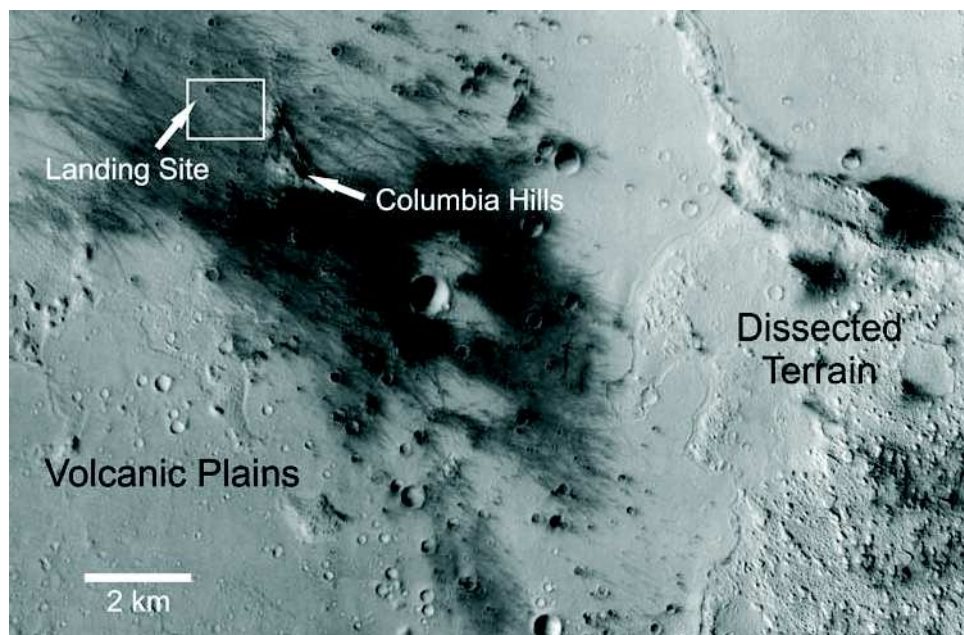


Figure 6.1: THEMIS-based mosaic showing the Spirit landing site in cratered plains in Gusev Crater. The Columbia Hills to the east of the landing site and the dissected terrain to the southeast are older deposits embayed by the plains materials. Dark streaks extending from plains craters are interpreted to be tracks of dust devils, where high winds eroded surface dust and exposed underlying materials.

et al., 2006; *Ming et al.*, 2006], and several subclasses based on their Fe-bearing mineralogy from MB spectroscopy (Figure 6.3) [*Morris et al.*, 2006a].

Rock classes range from weakly altered olivine basalt on the plains to pervasively altered basalt in the Columbia Hills. Varying degrees of alteration are also apparent among different rocks within individual rock classes. Here we take a detailed look at the relationship between primary and secondary Fe-bearing minerals within individual rock classes and subclasses as reported by *Morris et al.* [2006a], and how they relate to different hypothesized weathering scenarios such as gas-solid weathering [*Gooding*, 1978; *Gooding et al.*, 1992], the acid-fog model [*Banin et al.*, 1997; *Tosca et al.*, 2004], or weathering in acidic solutions [e.g., *Burns*, 1993b].

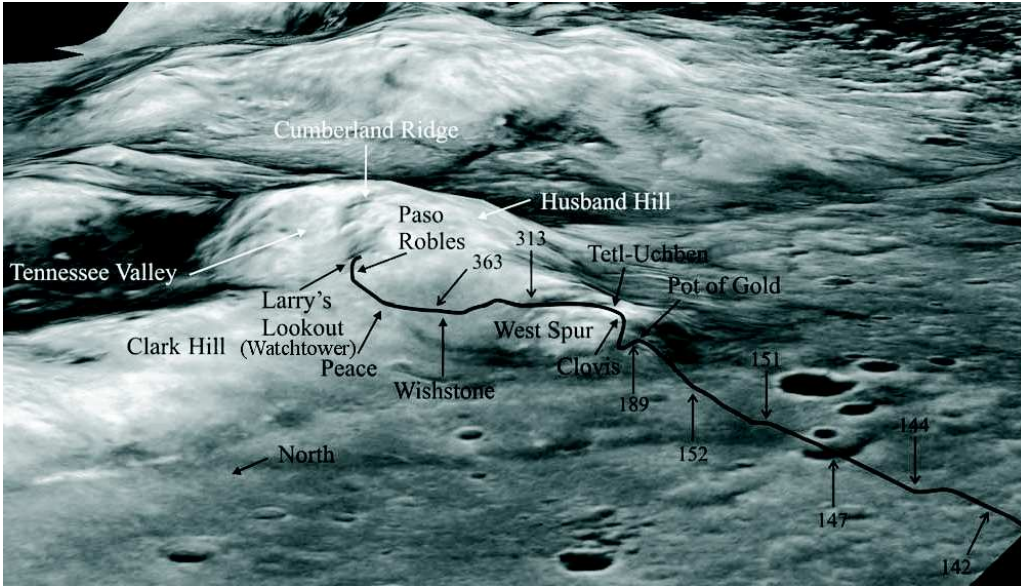


Figure 6.2: Perspective view of Columbia Hills looking to the southeast with Spirit’s traverses from the plains to the Hills shown. Key features, measurement campaigns, and the ground track of the rover are identified. Numbers show rover locations on specific sols. Generated from stereogrammetric reduction of MOC (Mars Orbital Camera) NA frames R0200357 and E0300012.

6.1 Data set

Rocks in Gusev crater encountered by Spirit until sol 512 of its mission have been divided into six different rock classes: Adirondack class in the Gusev crater plains [McSween *et al.*, 2004, 2006]; Clovis class, Wishstone class, Peace class, Watchtower class, and Backstay class in the Columbia Hills [Squyres *et al.*, 2006]. The rock classes are named after individual rock targets representative to that class, usually the first rock of its class encountered by Spirit. The classification is based on the chemical composition of RAT-ground rock surfaces, i.e., rock surfaces ideally representing the fresh, unweathered interior of the particular rock [Ming *et al.*, 2006]. Based on significant differences in the Fe-bearing mineralogy, Morris *et al.* [2006a] divided two of the rock classes into several subclasses (Figure 6.3): Clovis class into Woolly Patch subclass and Clovis subclass; Watchtower class into Watchtower subclass, Keystone subclass, and Keel subclass. Several rocks had distinct chemical and mineralogical signatures, but were not classified because no clean RAT-ground surfaces had been investigated. Morris *et al.* [2006a] put these rocks down under Other Rock classes, divided into Joshua

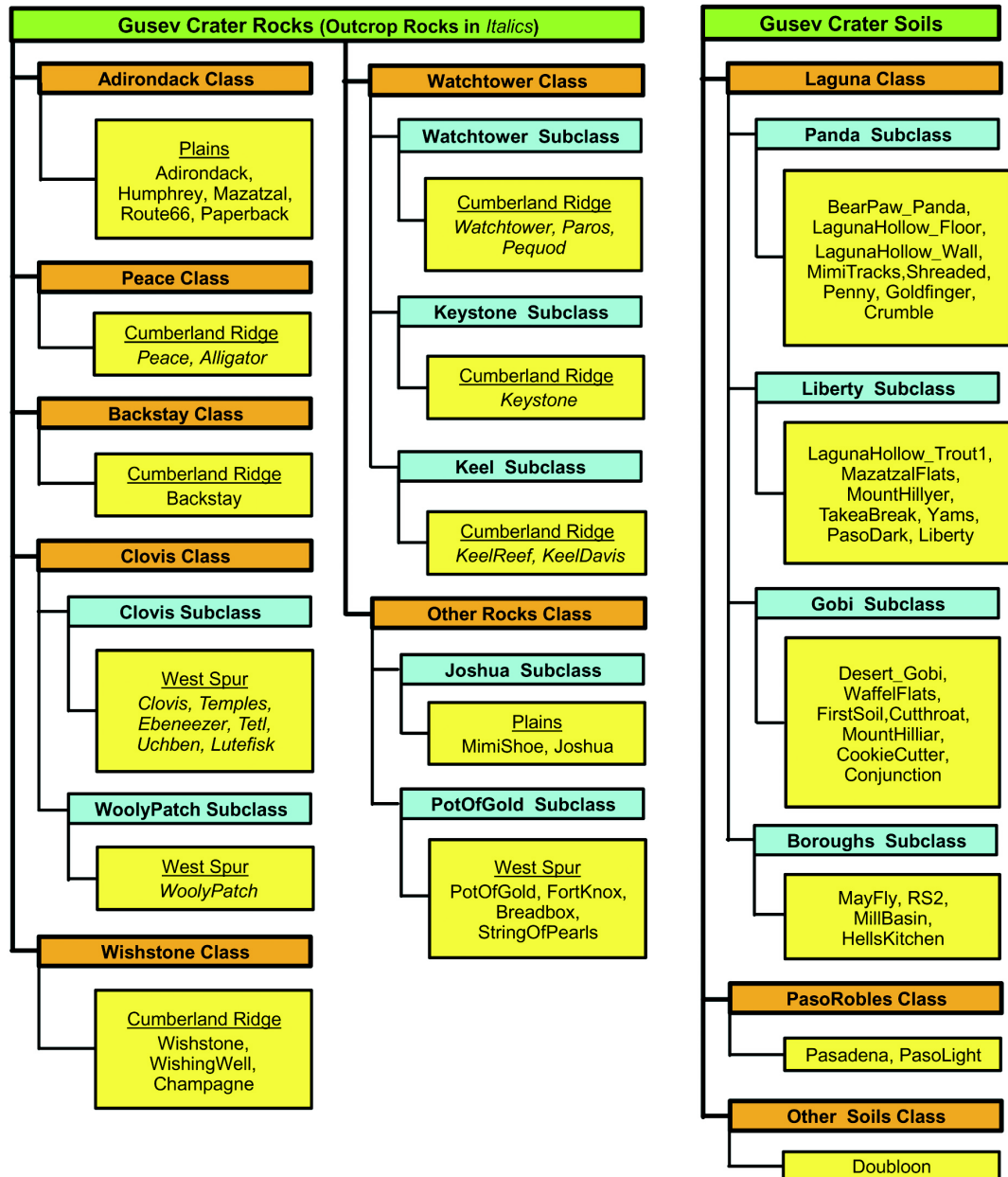


Figure 6.3: Classification scheme for Gusev crater rocks and soils through sol 510 of Spirit's mission. Classes for rocks [after *Squyres et al.*, 2006] and soils were formed on the basis of elemental composition, and subclasses were formed on the basis of mineralogical composition. Location names are underlined, and outcrop rocks are in italics.

subclass and Pot of Gold subclass. Joshua subclass rocks were encountered on the Gusev plains. Pot of Gold subclass rocks were encountered on the base of the West Spur of the Columbia Hills, close to the Clovis class rocks. Their elemental composition is similar to Clovis class rocks [Ming *et al.*, 2006]. Morris *et al.* [2006a] also divide soils into Laguna class, Paso Robles class, and Other Soils classes. Rock and soil classes and subclasses can be grouped according to the locations they were encountered at: Adirondack class and Other Rock classes (Joshua subclass) in the Gusev plains; Other Rock classes (Pot of Gold subclass) and Clovis class (Watchtower subclass and Clovis subclass) on the West Spur of the Columbia Hills; Wishstone class, Peace class, Watchtower class (Watchtower subclass, Keystone subclass, and Keel subclass), and Backstay class on Husband Hill in the Columbia Hills (Figure 6.2). Laguna class soils are found throughout Gusev Crater, Paso Robles class soils were encountered only on Husband Hill, and Other Soils class soil only adjacent to a Watchtower class (Watchtower subclass) rock. Clovis class, Peace class, and Watchtower class contain outcrop rocks which show layering and bedding [Squyres *et al.*, 2006], whereas all other rock classes contain float rocks.

Primary iron-bearing minerals, i.e. minerals crystallized from a parent melt, which were identified in Gusev rocks and soils are the ferrous mafic silicates olivine ($(Mg, Fe)_2SiO_4$) and pyroxene ($(Mg, Fe, Ca)SiO_3$), the ferrous iron titanium oxide ilmenite ($FeTiO_3$), and the mixed-valence iron oxide magnetite (Fe_3O_4). Secondary iron-bearing minerals, i.e. minerals formed from primary minerals via alteration processes, which were identified in Gusev rocks and soils are the ferric iron oxide hematite ($\alpha-Fe_2O_3$), the ferric iron oxyhydroxide goethite ($\alpha-FeOOH$), a ferric iron sulfate, and nanophase ferric oxide (np-Ox), which is generally a poorly-crystalline product of oxidative weathering that contains nanometer-sized particles of Fe^{3+} -bearing material. Nanophase ferric oxides on Mars could result, either singly or in combination, from a number of phases, including superparamagnetic hematite and goethite, lepidocrocite ($\gamma-FeOOH$), akaganeite ($\beta-FeOOH$), schwertmannite ($\sim Fe_8O_8(OH)_6SO_4 \cdot nH_2O$), iddingsite, ferrihydrite, and palagonite (altered basaltic glass) [Morris *et al.*, 1989a, 1993, 2000, 2001, 2004; Bishop and Murad, 1996]. For an in depth discussion of the properties of np-Ox, see Morris *et al.* [2006a, p. 15ff].

This assignment of primary and secondary mineral phases may be ambiguous in some cases. Magnetite is also known to form as an alteration product, e.g., during the serpentinization of olivine. However, primary magnetite has been recently identified by MB spectroscopy in the Martian meteorite MIL03346 in amounts comparable to the magnetite abundance in Adirondack class rocks [Morris *et al.*, 2006b]. Pyroxene can accommodate Fe^{3+}

in its structure to variable extents [e.g., *Rossmann*, 1980], which cannot be distinguished from np-Ox as described above in Mössbauer spectra. There is, however, a negative trend between the abundance of pyroxene and np-Ox in the MB data from Gusev rocks and soils (Figure 6.7a and [*Morris et al.*, 2006a, Figure 6c]). A MB study of pyroxene separates of Martian meteorites found only minute amounts of Fe³⁺ associated with pyroxene [*Dyar*, 2003]. Hence, counting all magnetite as primary and all np-Ox as secondary, *Morris et al.* [2006a] calculated a Mineral Alteration Index (MAI) as the sum of all secondary mineral phases. The higher the MAI the more weathered is a particular rock or soil target.

The aim of the work presented in this chapter is to look at the relationships between individual primary and secondary iron-bearing minerals. Based on many indications such as the red color of the Martian surface, weathering processes on Mars are generally oxidizing. Therefore the Fe^{3+}/Fe_{Total} ratio is adopted here as a measure for the degree of weathering.

Morris et al. [2006a] evaluated Mössbauer spectra acquired from rock and soil targets until sol 511 as described in Chapter 3.7. They list mineral subspectral areas (A) for all targets. These areas are proportional to the distribution of Fe among oxidation and coordination states and among iron-bearing phases in the target (Chapter 2.1.3). $A_{Olivine}$ for example is the relative amount of Fe in olivine. Subspectral areas do not provide information about the proportion of the iron-bearing phases themselves, unless the concentration of Fe (e.g., relative to Mg in olivine, or relative to Mg and Ca in pyroxene) in those phases is independently known or modeled. For olivine with its endmembers forsterite (Fo, Mg_2SiO_4) and fayalite (Fa, Fe_2SiO_4) this concentration has been estimated to Fo60 based on olivine MB parameters [*Morris et al.*, 2004], Fo45-52 based on normative calculations [*McSween et al.*, 2006], and Fo35-60 based on Mini-TES spectral analyses [*Christensen et al.*, 2004]. Comparable estimates for other iron-bearing minerals are not available.

6.2 Results

To understand which of the iron-bearing minerals listed in the previous paragraph undergo weathering and which minerals are more resistant, relative abundances of Fe in the primary minerals were plotted against Fe^{3+}/Fe_{Total} ratios in Figure 6.5. Rocks and soils are labeled according to their classes, subclasses, and locations. A good correlation between the decreasing abundance of a certain mineral and increasing Fe^{3+}/Fe_{Total} ratios, overall or

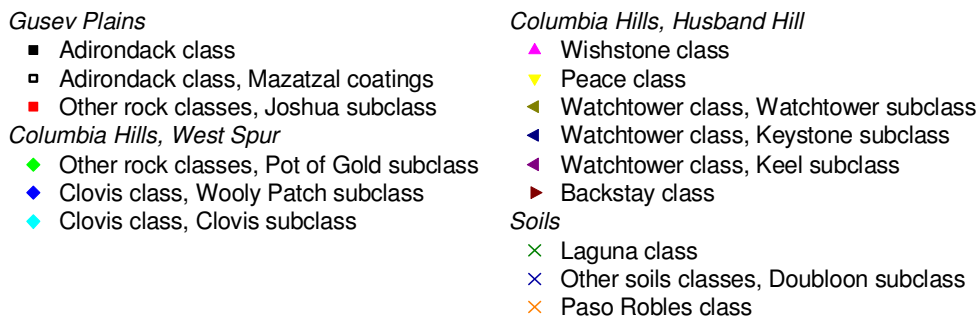


Figure 6.4: Legend to Figures 6.5 to 6.9

within a certain rock class, indicates that the respective mineral underwent some form of oxidative weathering. Mineral abundances which remain stable or scatter randomly suggest that the mineral is obviously not affected by weathering processes. A correlation between increasing abundance of a certain mineral and increasing Fe^{3+}/Fe_{Total} ratios indicates mineral formation as an alteration product, or alternatively, such as in the case of magnetite, changes in oxygen fugacity fO_2 during crystallization of the primary melt. The minerals olivine and magnetite, in particular, can be linked by either weathering processes such as serpentinization or changes in fO_2 in the vicinity of the Quartz-Fayalite-Magnetite (QFM) buffer.

In order to find out which secondary phases are forming by the alteration of particular primary minerals, abundances of olivine, pyroxene, and magnetite were each plotted against abundances of np-Ox, hematite, and goethite, respectively (Figures 6.6 - 6.8). Ilmenite was not investigated further, because it shows no apparent alteration (Figure 6.5c). Olivine and Pyroxene were also plotted against magnetite (Figures 2d and 3d, respectively). An Fe^{3+} sulfate occurred only in two Paso Robles class soil targets. It was not investigated further.

Secondary phases may evolve with time. Nanophase ferric oxides may increase in particle size and/or crystallinity, such as changing from superparamagnetic hematite into well-crystalline hematite. Goethite may de-hydroxylate and transfer into hematite with time. To investigate these options np-Ox was plotted against hematite and goethite; goethite was plotted against hematite (Figure 6.9).

Linear regressions were fit to the data points of each rock and soil class or subclass in Figures 6.5-6.9. The resulting correlation coefficients R, standard deviations SD, probabilities P that R is zero, and slopes S are listed in Tables 6.2 and 6.3. Some rock or soil classes or subclasses contain only one target, and thus neither slopes nor correlation coefficients can be calculated.

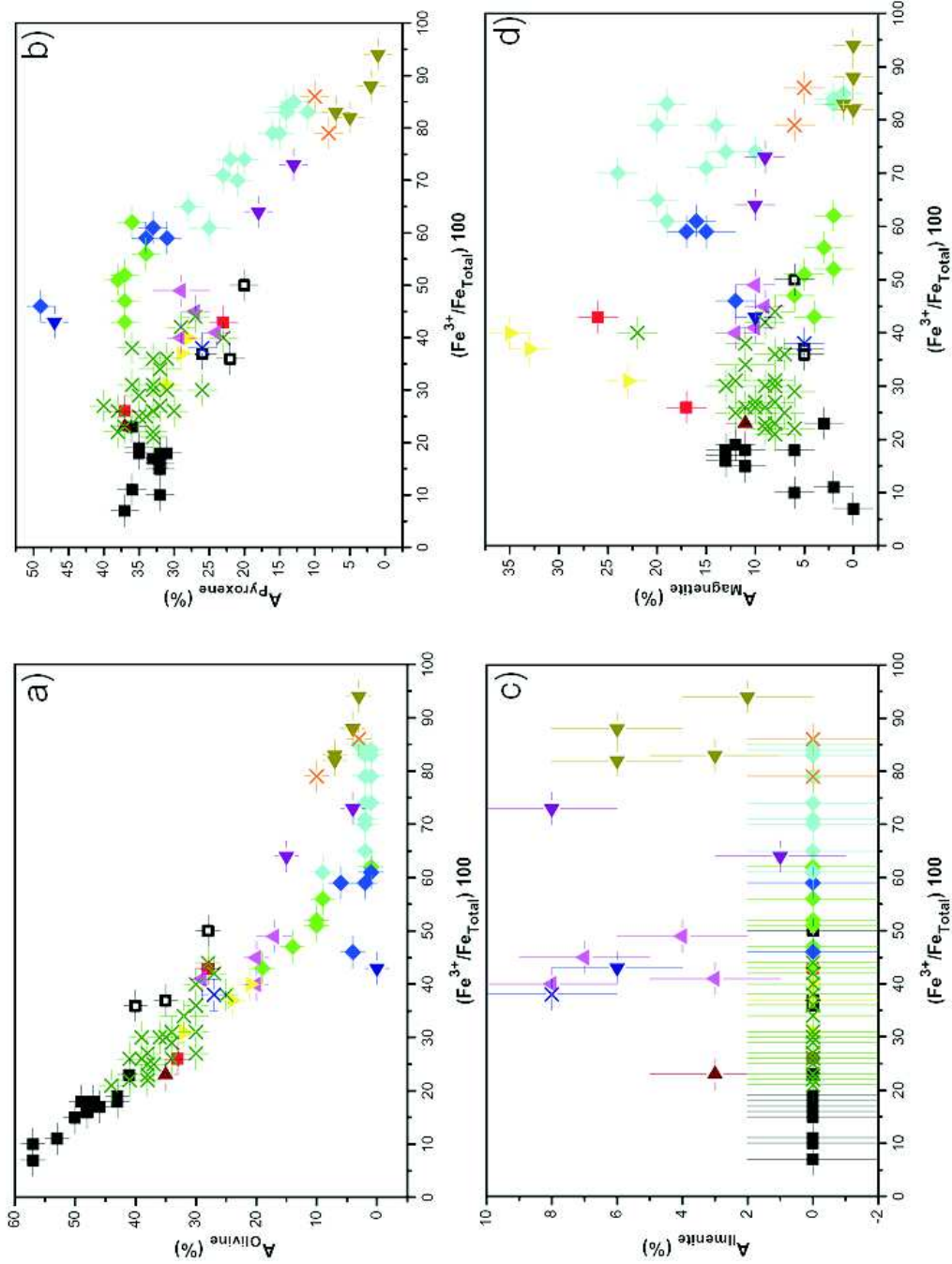


Figure 6.5: The plots show the relationships between primary minerals olivine (a), pyroxene (b), ilmenite (c), and magnetite (d) and the Fe^{3+}/Fe_{Total} ratio in different rock and soil classes. The good correlation between olivine and the Fe^{3+}/Fe_{Total} ratio suggests alteration of that mineral. Pyroxene is only altered in rocks with large Fe^{3+}/Fe_{Total} ratios. Ilmenite does not appear to be altered. Alteration of magnetite is not apparent. The legend is shown in Figure 6.4. Errors are as reported by *Morris et al.*, [2006a].

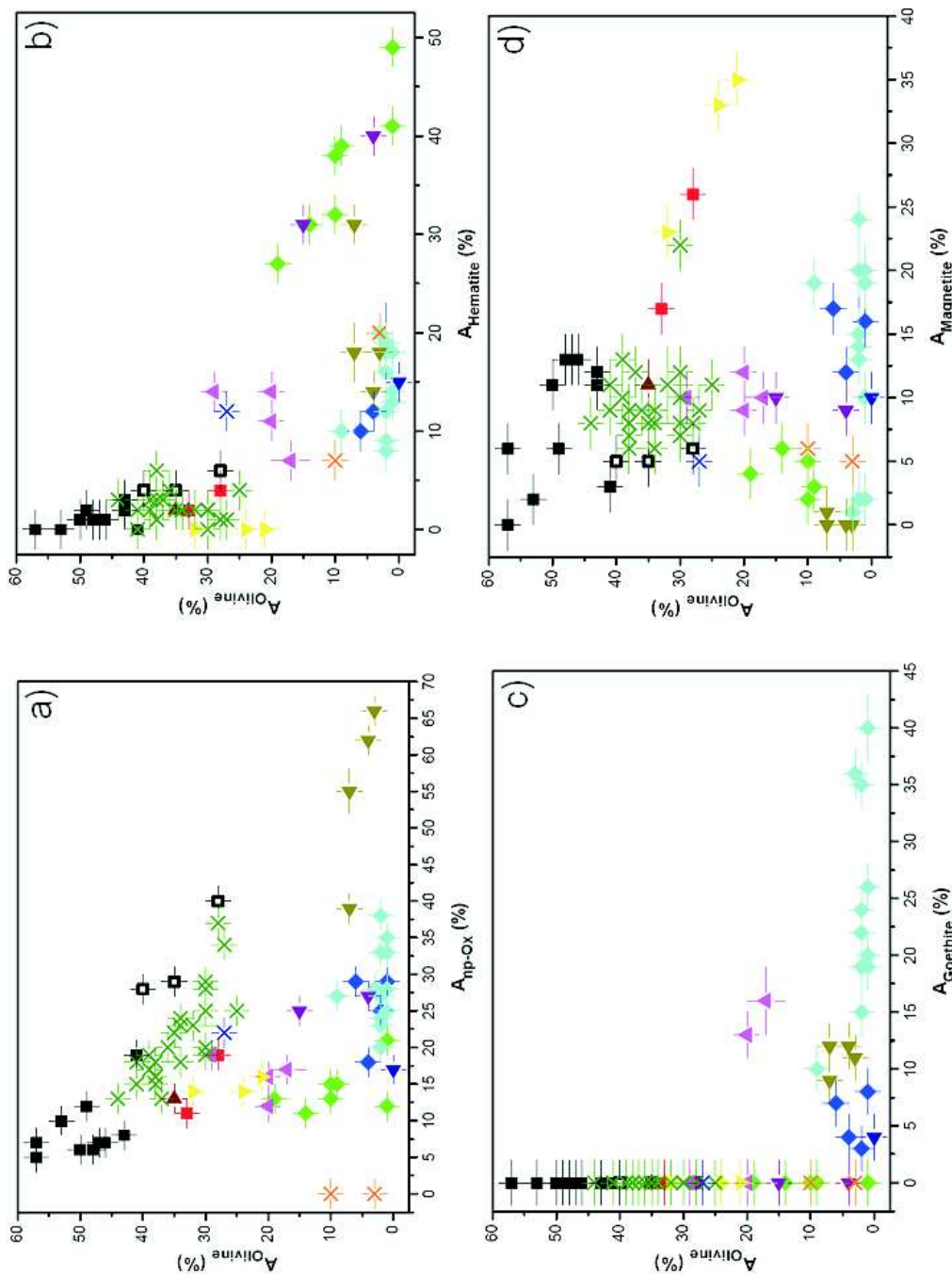


Figure 6.6: The plots show relationships between olivine and the secondary minerals a) nanophase ferric oxides (np-Ox), b) hematite, c) goethite, and d) magnetite in different rock and soil classes. Good correlations exist between olivine and np-Ox in Laguna class soils (a) and for olivine and hematite in Pot of Gold class rocks (b). The legend is shown in Figure 6.4. Errors are as reported by *Morris et al.*, [2006a].

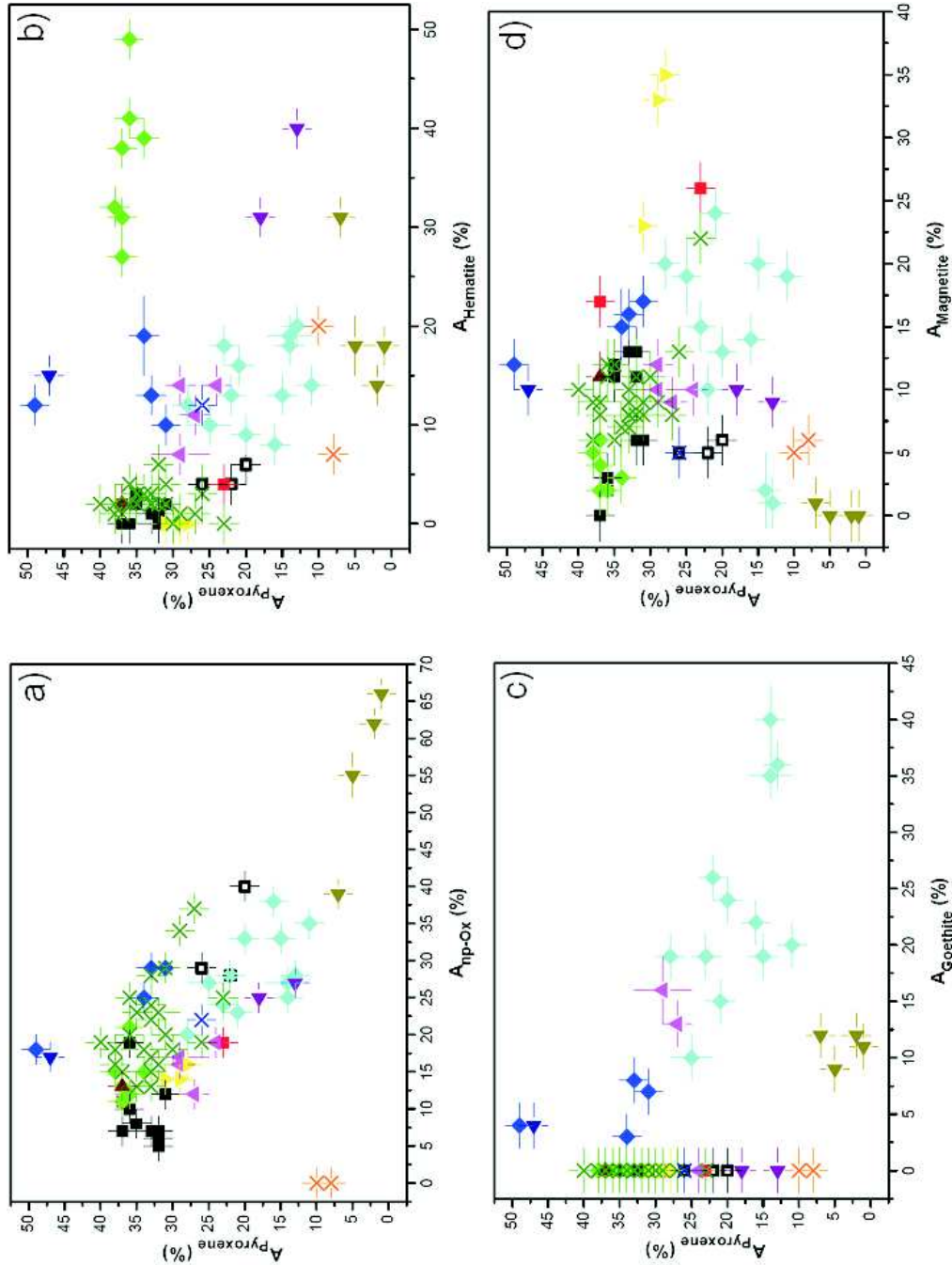


Figure 6.7: The plots show relationships between pyroxene and the secondary minerals a) nanophase ferric oxides (np-Ox), b) hematite, c) goethite, and d) magnetite in different rock and soil classes. Good correlations exist between pyroxene and np-Ox in Woolly Patch subclass, Clovis subclass and Watchtower subclass rocks (a). The legend is shown in Figure 6.4. Errors are as reported by *Morris et al.*, [2006a].

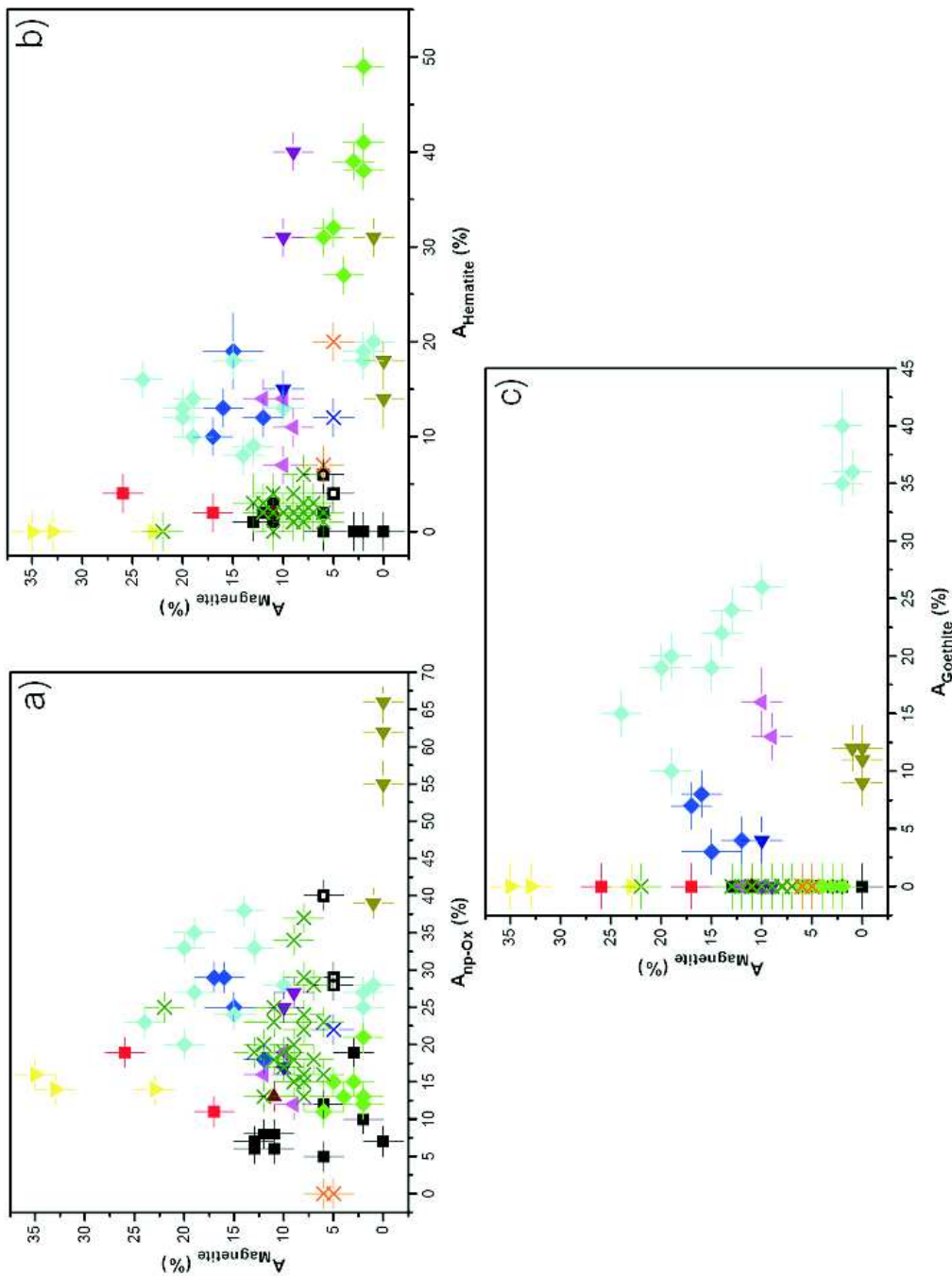


Figure 6.8: The plots show relationships between magnetite and the secondary minerals a) nanophasic ferric oxides (np-Ox), b) hematite, and c) goethite in different rock and soil classes. Good correlations exist between magnetite and goethite in Clovis subclass rocks (c). The legend is shown in Figure 6.4. Errors are as reported by *Morris et al.*, [2006a].

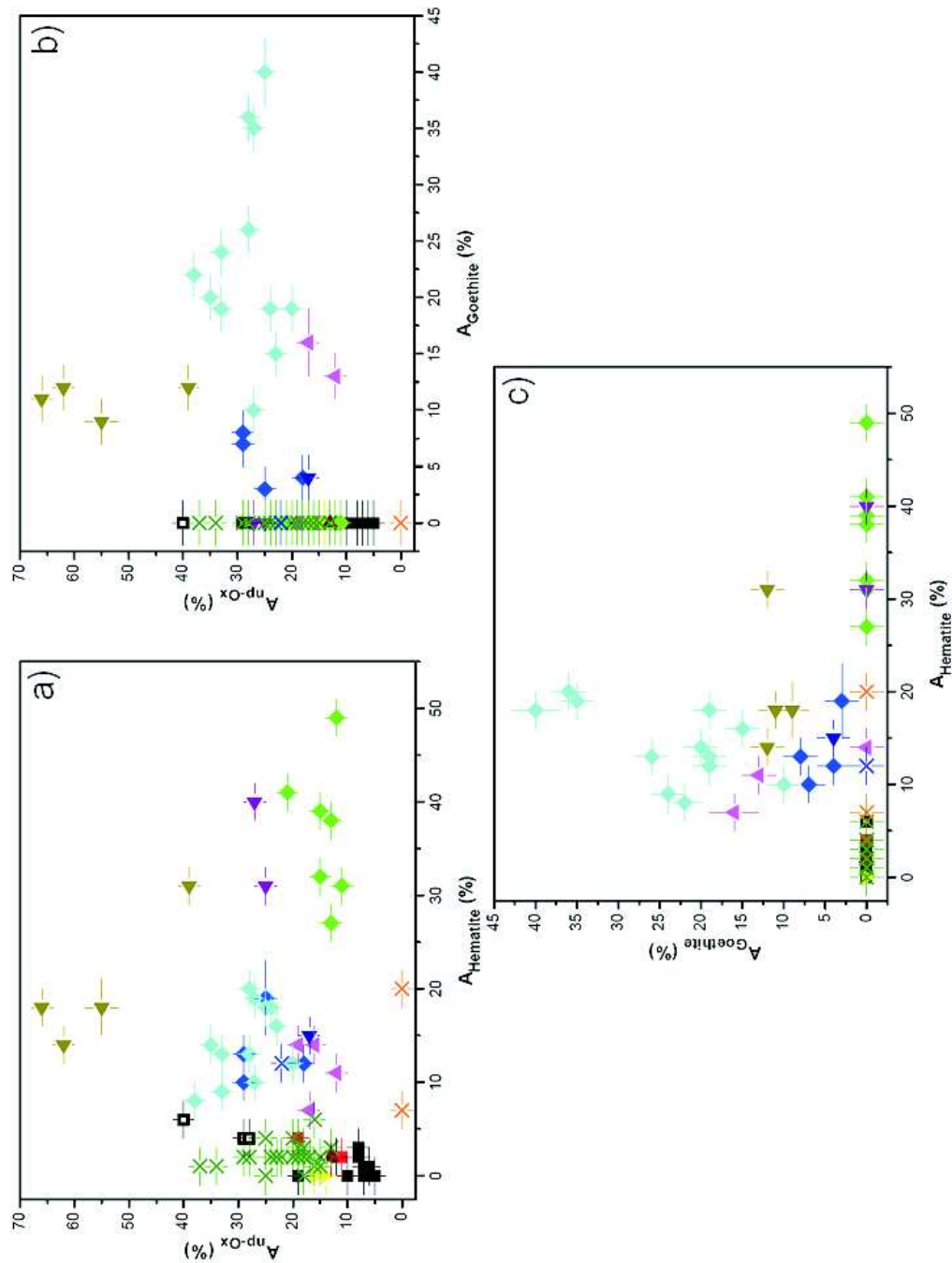


Figure 6.9: The plots show relationships between secondary minerals and their possible evolution products: (a) nanophase ferric oxides (np-Ox) versus hematite, b) np-Ox versus goethite, and c) goethite versus hematite. The lack of good correlations suggests that such evolution did not take place. The legend is shown in Figure 6.4. Errors are as reported by *Morris et al.*, [2006a].

Table 6.2: Correlation coefficients R, standard deviations SD, probabilities P that R is zero, and slopes S between primary and secondary minerals in Gusev Crater rock classes encountered in the plains and at the West Spur of the Columbia Hills. The number N of targets in each class or subclass is given. Ad: Adirondack class; Mz: Mazatzal coatings; Jo: Other Rocks class, Joshua subclass; Pg: Other Rocks class, Pot of Gold subclass; Wp: Clovis class, Woolly Patch subclass; Cl: Clovis class, Clovis subclass.

		Ad	Mz	Jo	Pg	Wp	Cl
	N	11	3	2	7	4	12
Ol/ Fe^{3+}	R	-0.94541	-0.93462	-1	-0.98424	-0.31055	-0.58709
	SD	0.92928	1.51585	0	0.63131	1.29071	0.92889
	P	<0.0001	0.23148	<0.0001	<0.0001	0.68945	0.04476
	S	-1.1(1)	-0.7(2)	-0.29	-0.9(1)	-0.1(2)	-0.16(8)
Px/ Fe^{3+}	R	-0.16605	-0.71247	-1	-0.50647	-0.97536	-0.94686
	SD	1.09244	1.51585	0	0.60094	1.11607	0.85732
	P	0.62559	0.49515	<0.0001	0.24608	0.02464	<0.0001
	S	-0.1(1)	-0.3(2)	-0.82	-0.1(1)	-1.2(2)	-0.70(9)
Mt/ Fe^{3+}	R	0.46653	0.99795	1	-0.71269	0.93322	-0.64917
	SD	2.29155	0.02614	0	0.62179	0.47532	3.15977
	P	0.14803	0.04078	<0.0001	0.07228	0.06678	0.02236
	S	0.5(1)	0.1(2)	0.53	-0.2(1)	0.3(2)	-0.66(8)
Ol/np-Ox	R	-0.48498	-0.93851	-1	-0.50558	-0.09417	-0.13762
	SD	2.49375	1.47153	0	3.07989	1.35181	1.13654
	P	0.13054	0.22441	<0.0001	0.24706	0.90583	0.66974
	S	-0.7(2)	-0.8(2)	-0.63	-1.0(2)	-0.0(2)	-0.1(1)
Ol/Hm	R	-0.55448	-0.90993	-1	-0.90876	-0.64044	-0.25358
	SD	2.37304	1.76777	0	1.48968	1.04283	1.10996
	P	0.07669	0.27226	<0.0001	0.0046	0.35956	0.42646
	S	-3.0(6)	-5(1)	-2.5	-0.8(1)	-0.4(3)	-0.1(1)
Ol/Gt	R	-	-	-	-	0.03158	-0.43266
	SD	-	-	-	-	1.35717	1.0345
	P	-	-	-	-	0.96842	0.16008
	S	-	-	-	-	0.0(5)	-0.10(7)
Ol/Mt	R	-0.49666	-0.90993	-1	0.6569	0.06959	0.15734
	SD	2.47498	1.76777	0	2.69148	1.35456	1.13317
	P	0.12017	0.27226	<0.0001	0.10893	0.93041	0.62529
	S	-0.5(1)	-10(2)	-0.56	2.6(5)	0.1(5)	0.04(8)

Table 6.2: Continued

		Ad	Mz	Jo	Pg	Wp	Cl
	N	11	3	2	7	4	12
Px/np-Ox	R	0.35963	-0.70463	-1	-0.23233	-0.96241	-0.60859
	SD	1.0337	1.53285	0	0.67786	1.37396	2.11491
	P	0.27734	0.50222	<0.0001	0.61615	0.03759	0.03573
	S	0.2(2)	-0.3(2)	-1.75	-0.1(2)	-1.5(2)	-0.6(1)
Px/Hm	R	-0.23787	-0.75593	-1	-0.50054	-0.11981	-0.28834
	SD	1.07602	1.41421	0	0.60335	5.02259	2.55215
	P	0.48122	0.45437	<0.0001	0.25258	0.88019	0.36342
	S	-0.5(6)	-2(1)	-7	-0.1(1)	-0.3(3)	-0.4(2)
Px/Gt	R	-	-	-	-	-0.50002	-0.51614
	SD	-	-	-	-	4.38119	2.28289
	P	-	-	-	-	0.49998	0.08582
	S	-	-	-	-	-1.7(5)	-0.32(7)
Px/Mt	R	-0.57542	-0.75593	-1	0.4625	-0.97124	0.47843
	SD	0.90605	1.41421	0	0.61791	1.20453	2.47983
	P	0.064	0.45437	<0.0001	0.29605	0.02876	0.11563
	S	-0.2(1)	-4(2)	-1.56	0.4(5)	-3.7(5)	-0.33(8)
Mt/np-Ox	R	-0.45386	0.99718	1	-0.40097	0.98172	0.01022
	SD	2.30857	0.03066	0	0.81203	0.25179	4.15385
	P	0.16085	0.04785	<0.0001	0.37267	0.01828	0.97485
	S	-0.6(2)	0.1(2)	1.125	-0.2(2)	-0.4(2)	0.0(1)
Mt/Hm	R	0.58995	1	1	-0.75712	-0.15883	-0.53811
	SD	2.09189	0	0	0.57906	1.30608	3.50135
	P	0.05607	<0.0001	<0.0001	0.04875	0.84117	0.07111
	S	2.9(6)	0.5	4.5	-0.2(1)	-0.1(4)	-1.1(1)
Mt/Gt	R	-	-	-	-	0.74217	-0.9348
	SD	-	-	-	-	0.88661	1.47545
	P	-	-	-	-	0.25783	<0.0001
	S	-	-	-	-	0.8(6)	-0.82(7)
np-Ox/Hm	R	-0.12637	0.99718	1	0.1958	-0.09124	-0.48009
	SD	2.06858	0.35355	0	1.7737	3.16381	2.45354
	P	0.7112	0.04785	<0.0001	0.67393	0.90876	0.11419
	S	-0.5(6)	6(1)	4	0.1(1)	-0.1(3)	-0.6(1)
np-Ox/Gt	R	-	-	-	-	0.71524	-0.02219
	SD	-	-	-	-	2.22039	2.79626
	P	-	-	-	-	0.28476	0.94543
	S	-	-	-	-	1.6(5)	-0.01(7)
Gt/Hm	R	-	-	-	-	-0.65079	0.55613
	SD	-	-	-	-	1.1068	3.58055
	P	-	-	-	-	0.34921	0.06043
	S	-	-	-	-	-0.4(3)	1.2(2)

Table 6.3: Correlation coefficients R, standard deviations SD, probabilities P that R is zero, and slopes S between primary and secondary minerals in Gusev Crater rock classes encountered on the northwest flank and at Columbia Ridge of Husband Hill in the Columbia Hills, and Laguna class soils encountered throughout Gusev Crater. The number N of targets in each class or subclass is given. Ws: Wishstone class; Pc: Peace class; Wt: Watchtower class, Watchtower subclass; Kl: Watchtower class, Keel subclass; Lg: Laguna class soils; Pr: Paso Robles class soils.

		Ws	Pc	Wt	Kl	Lg	Pr
	N	4	3	4	2	25	2
Ol/ Fe^{3+}	R	-0.53371	-0.99779	-0.96279	-1	-0.84781	-1
	SD	2.46435	0.26726	0.34116	0	1.32733	0
	P	0.46629	0.04235	0.03721	<0.0001	<0.0001	<0.0001
	S	-0.8(3)	-1.2(3)	-0.4(2)	-1.22	-0.64(6)	-1
Px/Fe^{3+}	R	0.14752	-1	-0.88583	-1	-0.58022	1
	SD	1.3048	0	0.78247	0	1.64966	0
	P	0.85248	<0.0001	0.11417	<0.0001	0.00236	<0.0001
	S	0.1(4)	-0.33	-0.4(2)	-0.56	-0.35(6)	0.29
Ilm/ Fe^{3+}	R	-0.28939	-	-0.52182	1	-	-
	SD	1.39537	-	1.07693	0	-	-
	P	0.71061	-	0.47818	<0.0001	-	-
	S	-0.2(3)	-	-0.2(2)	0.78	-	-
Mt/ Fe^{3+}	R	-0.56356	0.98432	-0.45455	-1	0.30438	-1
	SD	0.63653	0.80178	0.27273	0	1.54165	0
	P	0.43644	0.11287	0.54545	<0.0001	0.13905	<0.0001
	S	-0.2(3)	1.4(3)	-0.0(2)	-0.11	0.15(6)	-0.14
Ol/np-Ox	R	0.64822	-0.71074	-0.83546	-1	-0.7989	-
	SD	2.21893	2.82843	0.69377	0	1.50545	-
	P	0.35178	0.49672	0.16454	<0.0001	<0.0001	-
	S	1.1(4)	-4(1)	-0.1(1)	-5.5	-0.63(7)	-
Ol/Hm	R	0.62323	-	0.60547	-1	0.11001	-1
	SD	2.27894	-	1.00473	0	2.48779	0
	P	0.37677	-	0.39453	<0.0001	0.60063	<0.0001
	S	1.2(4)	-	0.2(2)	-1.22	0.4(3)	-0.54
Ol/Gt	R	-0.62362	-	-0.343	-	-	-
	SD	2.27802	-	1.18585	-	-	-
	P	0.37638	-	0.657	-	-	-
	S	-0.4(2)	-	-0.5(8)	-	-	-
Ol/Mt	R	-0.12444	-0.99387	0.56592	1	-0.18536	1
	SD	2.89144	0.4445	1.04083	0	2.4596	0
	P	0.87556	0.07052	0.43408	<0.0001	0.37504	<0.0001
	S	-0.5(9)	-0.9(2)	2(2)	11	-0.3(1)	7

Table 6.3: Continued

		Ws	Pc	Wt	Kl	Lg	Pr
	N	4	3	4	2	25	2
Px/np-Ox	R	-0.46107	-0.75593	-0.96105	-1	-0.47885	-
	SD	1.17064	0.70711	0.46605	0	1.77815	-
	P	0.53893	0.45437	0.03895	<0.0001	0.01545	-
	S	-0.3(4)	-1(1)	-0.2(1)	-2.5	-0.31(7)	-
Px/Hm	R	-0.29976	-	0.80446	-1	0.13673	1
	SD	1.25857	-	1.00171	0	2.00645	0
	P	0.70024	-	0.19554	<0.0001	0.51459	<0.0001
	S	-0.3(5)	-	0.3(2)	-0.56	-0.4(3)	0.15
Px/Gt	R	0.23701	-	-0.08559	-	-	-
	SD	1.28165	-	1.68015	-	-	-
	P	0.76299	-	0.91441	-	-	-
	S	0.1(2)	-	-0.2(8)	-	-	-
Px/Mt	R	0.51391	-0.98432	0.7868	1	-0.51455	-1
	SD	1.1317	0.1905	1.04083	0	1.73676	0
	P	0.48609	0.11287	0.2132	<0.0001	0.0085	<0.0001
	S	0.9(9)	-0.2(2)	4(2)	5	-0.6(1)	-2
Mt/np-Ox	R	0.35994	0.62862	-0.92418	-1	0.01896	-
	SD	0.71891	3.53553	0.11695	0	1.61816	-
	P	0.64006	0.56724	0.07582	<0.0001	0.92834	-
	S	0.2(4)	4(1)	-0.0(1)	-0.5	-0.01(7)	-
Mt/Hm	R	0.4393	-	0.96709	-1	-0.22821	-1
	SD	0.69222	-	0.07791	0	1.57574	0
	P	0.5607	-	0.03291	<0.0001	0.27256	<0.0001
	S	0.2(3)	-	0.1(2)	-11	-0.6(3)	-0.08
Mt/Gt	R	-0.63403	-	0.4714	-	-	-
	SD	0.59587	-	0.27003	-	-	-
	P	0.36597	-	0.5286	-	-	-
	S	-0.1(1)	-	0.2(8)	-	-	-
np-Ox/Hm	R	0.1707	-	-0.92097	1	-0.25065	-
	SD	1.77632	-	2.83932	0	3.07236	-
	P	0.8293	-	0.07903	<0.0001	0.22686	-
	S	0.2(3)	-	-1.5(2)	0.22	-1.2(3)	-
np-Ox/Gt	R	-0.48178	-	-0.25306	-	-	-
	SD	1.57976	-	7.05011	-	-	-
	P	0.51822	-	0.74694	-	-	-
	S	-0.2(1)	-	-3(1)	-	-	-
Gt/Hm	R	-0.9248	-	0.28626	-	-	-
	SD	1.72971	-	0.82979	-	-	-
	P	0.0752	-	0.71374	-	-	-
	S	-2.7(4)	-	0.1(2)	-	-	-

Some rock or soil classes or subclasses contain only two targets. Correlation coefficients are then equal to 1 by default and meaningless. The calculated slopes on the other hand may retain some meaning. Tables 6.2 and 6.3 therefore contain also the number of samples, N.

Areas of primary minerals were plotted along the y-axis and areas of secondary minerals were plotted along the x-axis. A slope value of -1 means, that the loss of Fe in the primary mineral matches the gain of Fe in the secondary mineral. This suggests a direct transformation from one mineral into another albeit caution is necessary, because several secondary phases may result from the alteration of one mineral. Likewise, the alteration of different primary minerals may add to the abundance of one secondary mineral.

6.3 Discussion

At first glance, Figure 6.5 resembles the classic observation by *Goldich* [1938] that mineral susceptibility to weathering is generally similar to Bowen's sequence of minerals crystallizing from a melt [*Bowen*, 1928]. Even the least altered rocks of the Adirondack class show evidence that olivine has weathered (Figure 6.5a), whereas only the most altered rocks of the Clovis and Watchtower classes show evidence for the alteration of pyroxene (Figure 6.5b). There is no evidence of any alteration of ilmenite (Figure 6.5c), and evidence of alteration of magnetite is not immediately apparent (Figure 6.5d). When put in order of decreasing stability towards weathering, the sequence ilmenite - magnetite - pyroxene - olivine also agrees with a sequence of mineral persistence based on mineral frequency in sedimentary rocks of increasing age [*Pettijohn*, 1941]. The adherence to Goldich's sequence points towards acidic conditions [*Wasklewicz*, 1994], which agrees with evidence for acid weathering inferred from the presence of Cl and S in Martian fines at all sites of successful landings, i.e. Viking [*Clark et al.*, 1976; *Toulmin et al.*, 1977], Pathfinder [*Rieder et al.*, 1997], and MER [*Gellert et al.*, 2004, 2006; *Rieder et al.*, 2004].

The secondary Fe-bearing mineralogy lacks carbonates and clay minerals [*Morris et al.*, 2006c], although small amounts of clay minerals may be present in iddingsite-like assemblages among the np-Ox. Ferric Sulfates may also be present among the np-Ox phases [*Morris et al.*, 2005]. They have been unequivocally identified in Paso Robles class soils. However, the evidence of well-crystalline secondary minerals identified in rocks suggests that the np-Ox phase is mainly made up of iron oxides. The observed Fe-bearing secondary mineralogy points to pH values between 4 and 7 when compared to weathering experiments conducted by *Tosca et al.* [2004]. *Tosca et al.*

[2004] observed the dissolution of ilmenite only at lower pH levels. At such low pH levels ferrous sulfates formed rather than oxides, because of slower oxidation rates of dissolved Fe^{2+} .

Olivine has been identified by MB spectroscopy in targets from all rock and soil classes in variable amounts [Morris *et al.*, 2004, 2006a]. Individual rock and soil targets which contain little or no olivine generally plot to the right of the interception of the overall trend with the x-axis in Figure 6.5a. That suggests that olivine was present in the unweathered precursor rocks. Oxidative weathering continued after all olivine was consumed. Normative calculations assuming isochemical weathering yielded olivine in Clovis class and Watchtower class rocks. Amounts of olivine for Clovis class rocks range up to values comparable to the high-olivine Adirondack class rocks [Ming *et al.*, 2006]. Olivine has been identified by Mössbauer spectra in basaltic (dark) soils at both MER landing sites, Gusev crater [Morris *et al.*, 2004, 2006a] and Meridiani Planum [Klingelhöfer *et al.*, 2004]. The dark soils at Gusev and Meridiani are similar in composition and may represent a distinct global unit, or given the apparent uniformity of basaltic terrains mapped from orbit, the connection between these dark soils may be a result of the general similarity in the rocks from which they originated [Yen *et al.*, 2005a]. The earliest evidence for olivine on the Martian surface [Adams, 1968], although not conclusive, was derived from Earth-based spectroscopic measurements [Tull, 1966]. It has been unequivocally identified as a major mineral phase in the so-called Martian meteorites, particularly in the subgroups (in order of decreasing olivine abundance) dunites, lherzolithic shergottites, olivine-phyric shergottites and the clinopyroxenites [e.g., Meyer, 2006, and references therein]. Occurrences of olivine on Mars have been identified by orbiting spacecraft using visible/near-infrared spectroscopy through Mars Global Surveyor's (MGS) Thermal Emission Spectrometer (TES) [e.g., Bandfield, 2002; Hoefen *et al.*, 2003], and Mars Express' Observatoire pour la Minéralogie, l'Eau, les Glaces, et l'Activité (OMEGA) [Bibring *et al.*, 2005; Mustard *et al.*, 2005].

The distribution of secondary minerals derived from olivine, based on calculated correlation coefficients and slopes (Tables 6.2 and 6.3), varies between different rock and soil classes (Figure 6.6) which suggests different weathering scenarios. The same is true for the distribution of secondary minerals derived from pyroxene and magnetite (Figures 6.7 and 6.8, respectively). Therefore individual rock and soil classes are discussed in more detail in the following paragraphs.

6.3.1 Adirondack class

Adirondack class rocks are the least oxidized rocks in Gusev crater, They are the least altered rocks based on MAI [Morris *et al.* 2006a] and combined S, Cl, and Br content [Ming *et al.*, 2006]. Nevertheless, they plot along the general trend for oxidative olivine alteration (Figure 6.5a) with good negative correlation (-0.95) and a slope of -1.1. Pyroxene in Adirondack class rocks is not affected by oxidative weathering ($R = -0.2$; slope = -0.1). There is a positive slope between magnetite and the Fe^{3+}/Fe_{Total} ratio. In fact, Fe^{3+} in magnetite accounts for up to $\sim 50\%$ of the total Fe^{3+} in Adirondack class rocks. At the same time, a negative slope exists between Olivine and magnetite (Figure 6.6d). Based on comparison with comparable amounts of magnetite found in the Martian meteorite MIL03346, this may result from variation in the oxidation state of the lavas from which the rocks crystallized [Morris *et al.*, 2006b].

There appears to be evidence for the formation of np-Ox (Figure 6.6a) and hematite (Figure 6.6b) from olivine, though correlations are only weak. Iddingsite, a badly constrained mixture of iron oxides and clay minerals, is a common terrestrial weathering product of olivine. It is also present in a number of Martian meteorites, including MIL03346 [Dyar *et al.*, 2005]. Iddingsite in Martian meteorites has been shown to be of pre-terrestrial origin and formed within the last one billion years [e.g., Bridges *et al.*, 2001]. Morris *et al.* [2006a] listed iddingsite as one of the possible phases for np-Ox. McSween *et al.* [2006] noted patches of light-colored material in abraded surfaces of Adirondack class rocks, which may be an alteration product of olivine. Two Adirondack class rocks (Adirondack and Humphrey) have been investigated on 'as is', brushed and RAT-ground surfaces, whereby np-Ox and the Fe^{3+}/Fe_{Total} ratio are lowest per individual rock in the abraded surface where olivine abundances are highest. A third rock (Mazatzal) investigated in the same way revealed several layers of a coating, which will be the topic of the next paragraph. It is important to note that Adirondack class rock targets associated with the highest abundances of np-Ox in Figure 6.6a (and Figures 6.7a, 6.8a, and 6.9a and b) may have had additional external sources of np-Ox: A076RU0 Paperback_Appendix² (19 % np-Ox) was an 'as is' target on a low-lying, light-toned (i.e. dust-covered) rock, and the same is true for the target A094RU0 Route66_Candidate7 (10 %); A082RR0

²Target naming convention: Awwwxyz Feature-name_Target-name. A = MER-A (Gusev crater); www = Gusev crater sol number; x = R (rock) or S (soil); y = U (undisturbed), D (disturbed), T (trench), B (RAT-brushed surface), R (RAT-ground surface), or G (RAT grindings); z = 0 by default; z = 1, 2, 3. . . for multiple analyses of the same target on the same sol. See Morris *et al.* [2006a] for details.

Mazatzal_NewYork (12 %) was a RAT-ground target, where the RAT operation left a considerable area of a dark smooth coating associated with high np-Ox untouched.

The observations presented above are consistent with a weathering scenario at low pH and low water/rock ratios derived by *Hurowitz et al.* [2006] from reduced Fe and Mg abundances in brushed as opposed to RAT-ground surfaces. In a scenario proposed by *Yen et al.* [2005a, 2005b] and derived from the distribution of bromine in soils, frost deposited at night may rapidly sublime in the morning and condense in cold traps. Condensation in excess of a single molecular monolayer allows the H_2O molecules to behave as a liquid. Diurnal, or perhaps seasonal, cycling of these thin films of water over geologic timescales may be sufficient to account for the observed alteration of olivine.

Adirondack class rocks represent the Hesperian age Gusev plains lava flow [Golombek *et al.*, 2006], which engulfs and hence postdates the formation of the Columbia Hills. Alteration observed in Adirondack class rocks are thus representative of the more recent and probably currently active weathering phenomena in Gusev crater.

6.3.2 Mazatzal coatings

Mazatzal has a complex multilayer surface coating [Haskin *et al.*, 2005]. Materials encountered as brushing and abrasion proceeded were: (1) loose dust cover, (2) an outer light-toned soft coating (removed by brushing), (3) a dark-toned hard coating (partially removed by abrasion), (4) an inner light-toned coating, and (5) the basaltic interior matrix with filled vugs and veins. The coatings are associated with high S, Cl and Br levels as well as high Fe^{3+}/Fe_{Total} ratios.

Data derived from 'as is' surfaces and brushed surfaces of Mazatzal are indicated separately in Figures 6.5-6.9. They do not follow the trends apparent for other Adirondack class rocks. The coatings contain more Fe^{3+} than other targets with comparable amounts of olivine (Figures 6.5a and 6.6a). Figures 6.5b and 6.7a suggest, that pyroxene abundances are reduced accordingly to yield the necessary levels of Fe^{3+} . This would, however, imply that for the formation of the Mazatzal coatings olivine and pyroxene weathered at approximately the same rates, contrary to the observations for all other rock and soil targets. The results can be explained alternatively with the MB sampling depth (see Chapter 2.2.3). The sampling depth of the 14.4 keV radiation likely exceeds the thickness of the coatings. The simultaneous sampling of coating and subsurface is indicated in Figure 6.10. In the 14.4 KeV spectra, olivine and pyroxene decrease while np-Ox increases in spectra

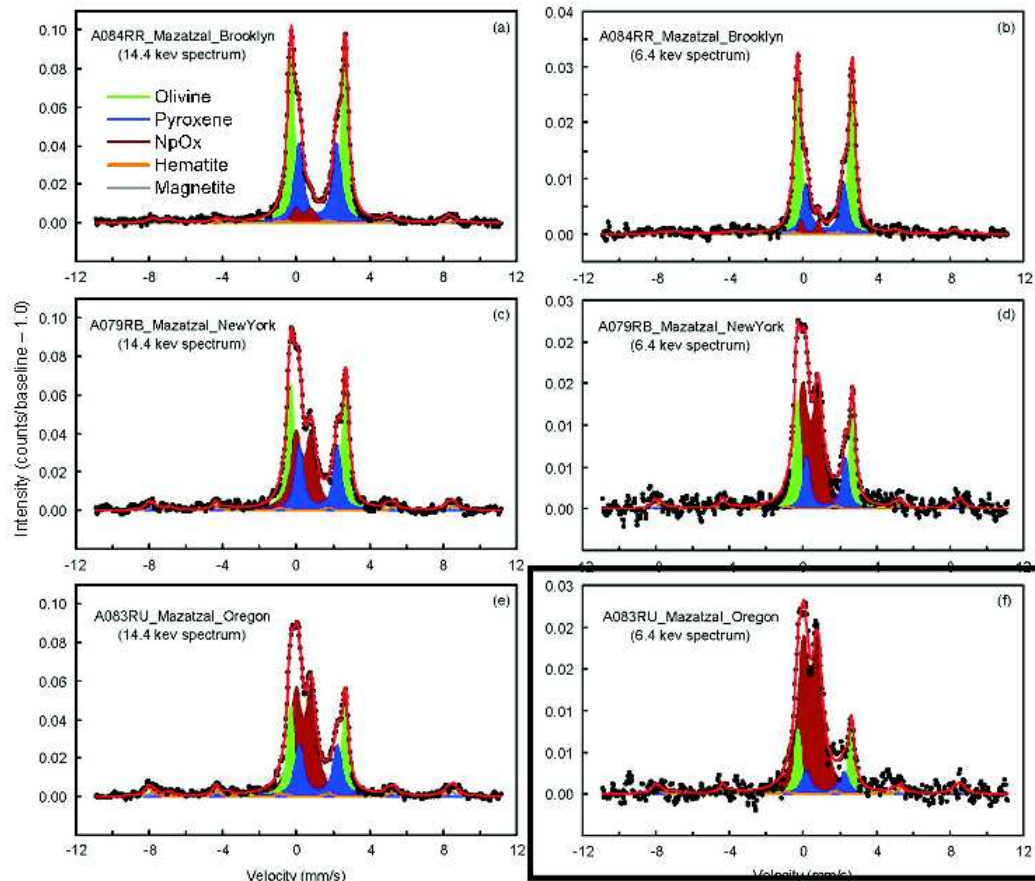


Figure 6.10: The plots show 14.4 keV (left column) and 6.4 keV (right column) Mössbauer spectra of different targets on the rock Mazatzal. Mazatzal has a multilayer coating. Spectra of the undisturbed (e and f) and brushed surface (c and d) are enriched in nanophase ferric oxides (np-Ox) compared to the abraded surface. The 14.4 keV radiation has a larger sampling depth than the 6.4 keV radiation. The amount of np-Ox in undisturbed and brushed surfaces is higher in the 6.4 keV spectra compared to the 14.4 keV spectra. The sampling depths of both energies may exceed the thickness of the coating.

of the brushed and 'as is' surfaces (Figures 6.10c and e, respectively) relative to the spectrum of the abraded surface (Figure 6.10a). The ratio of olivine to pyroxene stays approximately the same in all three spectra. The 6.4 keV spectra where the ratio of sampled coating to subsurface increases, were also evaluated. The np-Ox phases become yet more abundant in spectra of the brushed and as is surfaces (Figures 6.10d and f) while olivine and pyroxene become less abundant. The olivine to pyroxene ratio remains approximately the same. Hence the coatings alone are more oxidized than indicated in Figures 6.5 to 6.9. It can be inferred from Figure 6.10, that Fe in the coatings occurs to a large extent in the form of np-Ox with possible minor contributions from hematite and magnetite. Olivine and pyroxene in the spectra are mostly a contribution from the underlying rock.

Weathering mechanisms described in the previous paragraph for Adirondack class rocks may be enhanced in the near-subsurface to produce the coatings observed on Mazatzal [Yen *et al.*, 2005a, 2005b]. Enhanced np-Ox abundances combined with high S, Cl and Br have also been observed in subsurface soils which were revealed by trenches into mature regolith in the inter-crater plains [Haskin *et al.*, 2005; Wang *et al.*, 2006].

Another low-lying, light-toned rock target in the vicinity of Mazatzal, but not investigated by brushing and grinding, is Paperback-Appendix [Arvidson *et al.*, 2006]. Its np-Ox abundance (19 %) is highest among Adirondack class rocks and it plots generally close to the Mazatzal coatings (Figures 6.5a and d, 6.6a and d, and 6.8a).

6.3.3 Laguna class soils

Laguna class soils [Morris *et al.*, 2006a] are present in the Gusev plains as well as the Columbia Hills, and soils of similar composition have also been observed at Meridiani Planum [Klingelhöfer *et al.*, 2004]. They are thus important on a global scale [Yen *et al.*, 2005a]. The ubiquitous presence of olivine in these soils suggests that physical rather than chemical weathering processes currently dominate at Gusev crater [Morris *et al.*, 2004] and beyond.

Olivine is the only primary Fe-bearing mineral in Laguna class soils whose alteration is of significance (Figure 6.5). Olivine oxidation results mainly in the formation of np-Ox (Figure 6.6a). The concentration of iron associated with this phase has a positive correlation with S (slope = $\text{Fe}/\text{S} = 0.57$), implying a sulfate or formation in direct proportion to sulfates [Morris *et al.*, 2005; Yen *et al.*, 2005a]. Normative calculations done for subsurface regolith exposed in trenches and enriched in both np-Ox and S, suggest mainly Mg and Ca sulfates and only minor contributions from Fe sulfate [Haskin *et al.*,

2005; Wang *et al.*, 2006]. Hence, np-Ox may be Fe oxides associated with Mg sulfates.

The observed alteration trends of laguna class soils are consistent with weathering scenarios described in previous paragraphs for Adirondack class rocks and the Mazatzal coatings. Endmembers of Laguna class soils are bright dust and dark soil [Yen *et al.*, 2005a]. The bright dust contains higher amounts of np-Ox compared to the dark soil, when the dark soil is not associated with the enhanced S, Cl and Br levels as encountered in the inter-crater plains trenches. Experiments by Schröder *et al.* [2004] (Chapter 5) with fine-grained olivine showed, that interaction with the Martian atmosphere can alter olivine to np-Ox and hematite without invoking transient or thin films of water. MB investigation of fine-grained aeolian dust adhering to the capture magnet showed higher Fe^{3+}/Fe_{Total} than for average Martian soil [Goetz *et al.*, 2005].

6.3.4 Clovis class and Pot of Gold subclass

Clovis class rocks (Wooly patch subclass and Clovis subclass) and the associated Pot of Gold subclass rocks range from intermediate degrees of alteration to pervasively altered rocks. Amongst this subset of rock targets Pot of Gold subclass contains the least altered rocks. In many ways they continue the trends which Adirondack class rocks followed. Olivine is the primary mineral undergoing weathering, whereas pyroxene levels remain constant (Figures 6.5a and b). Pot of Gold rocks were encountered at the base of the West Spur, i.e. at the boundary between the Gusev plains and the Columbia Hills [Arvidson *et al.*, 2006]. They show visible signs of alteration in the form of cavernous weathering and case-hardening [Cabrol *et al.*, 2006; Arvidson *et al.*, 2006], implying higher water/rock ratios or water available over longer timespans than required for the weathering observed in Adirondack class rocks. Water must have been available long enough or in sufficient amounts to allow well-crystalline hematite rather than np-Ox to form from olivine (Figure 6.6b). However, water availability was not as high as to also affect pyroxene. There is no evidence that the hematite evolved from intermediate np-Ox over time (Figure 6.9a). Wooly Patch subclass rock targets link Pot of Gold subclass rocks in several ways to Clovis subclass rocks. The physical location of the outcrop rock Wooly Patch is above Pot of Gold subclass rocks and below Clovis subclass rocks on the West Spur of the Columbia Hills [Arvidson *et al.*, 2006]. The Fe^{3+}/Fe_{Total} ratio of Wooly patch targets matches the most oxidized Pot of Gold subclass rock targets and the least oxidized Clovis subclass rock targets. Wooly Patch targets plot at the intersection of the olivine trend in Figure 6.5a with the x-axis, i.e. where all

olivine has been transformed into Fe^{3+} -bearing phases. The Clovis subclass targets start to trail off from that point. Wooly Patch targets plot also at the intersection of the constant pyroxene trend of Pot of Gold class rock targets and the pyroxene weathering trend defined by Clovis subclass targets in Figure 6.5b. On a first glance Mössbauer spectra obtained from Wooly Patch targets look like the end product of Pot of Gold subclass weathering [Schröder *et al.*, 2005]: They have the same abundance of pyroxene and no olivine. However, hematite abundances in Wooly Patch targets are lower than in Pot of Gold targets (Figures 6.6b and 6.11). In a similar manner it could be at the beginning of the Clovis subclass weathering trends (Figure 6.12) which begin with a high abundance of pyroxene and little goethite. The magnetite abundance in Wooly Patch targets is lower compared to the least oxidized Clovis subclass targets, though (Figures 6.5d and 6.8c).

Pot of Gold subclass targets and Wooly patch subclass targets fall along an elemental abundance mixing line between Adirondack class rocks and The Boroughs trench data (Laguna class soil) [Arvidson *et al.*, 2006, Figure 12a]. This suggests that the rocks at the base of the West Spur have compositions matched by combining Adirondack class rocks and alteration phases, but they have rather different modification histories than Adirondack class rocks, given the distinctive mineralogy. Clovis class rocks have compositions similar to basaltic soils (Laguna class) on the Gusev plains with the exception of higher Mg, Cl, and Br and lower Ca and Zn [Ming *et al.*, 2006].

Clovis subclass rock targets contain little or no olivine. Figure 6.5a and normative calculations indicate that all olivine from the proposed protolith has been consumed by oxidative weathering. Since olivine is absent, no trends are available to show which secondary phases formed from the alteration of olivine, however, based on the Wooly Patch mineralogy and the bad correlation between pyroxene and hematite (Figure 6.7b), hematite was probably derived from olivine together with some np-Ox and goethite. The alteration of pyroxene added more np-Ox and goethite. The bulk amount of goethite however seems to come from the oxidation and hydroxylation of magnetite (Figure 6.8c), judging by the good correlation ($R = -0.93$) and a slope close to -1 (-0.82). There is no evidence for any further evolution of goethite such as dehydroxylation and the subsequent formation of hematite (Figure 6.9c). The obvious alteration of pyroxene and magnetite in addition to olivine increases the necessary amounts of water and the timespan of availability of water relative to Pot of Gold subclass rocks.

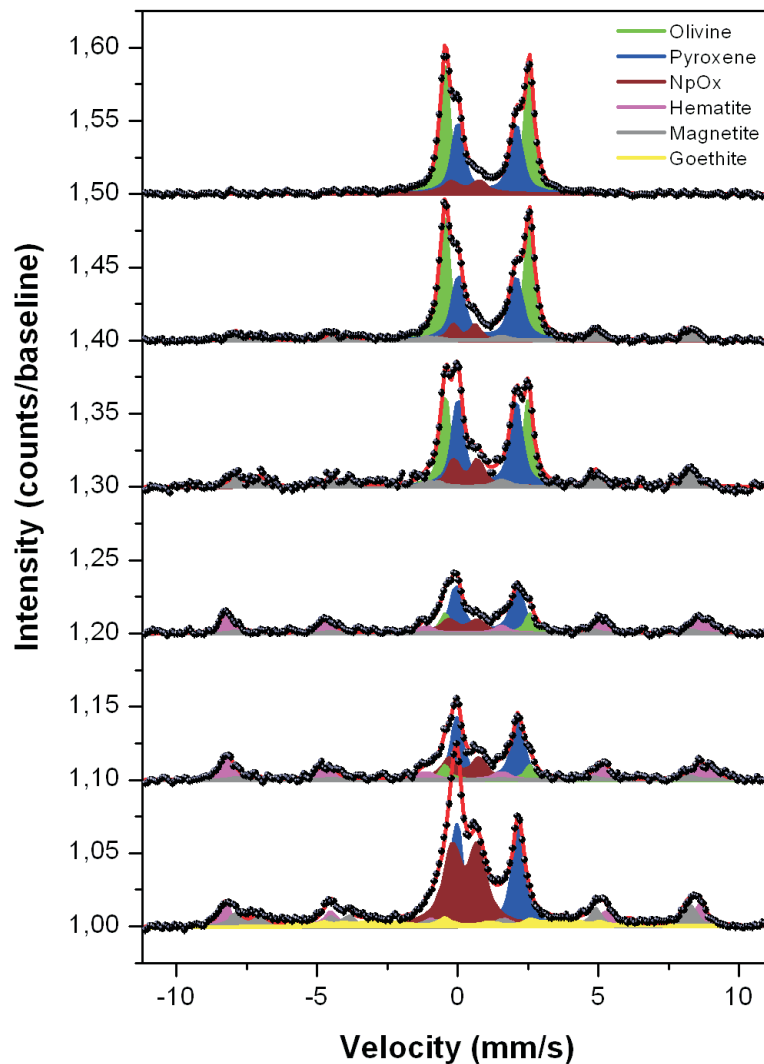


Figure 6.11: The plot shows Mössbauer spectra obtained from rock targets in the Gusev Crater plains and on the foot of the West Spur of the Columbia Hills. The spectra are arranged in the order of increasing Fe^{3+}/Fe_{Total} ratios, starting from the top: A100RB0 Route66_SoHo; A060RR0 Humphrey_Heyworth2; A150RU0 Mojave_Joshua; A176RU0 Breadbox_Sourdough; A171RR0 PotOfGold_FoolsGold; A200RR0 WoolyPatch_Mastadon. The targets A100RB0, A060RR0 (both Adirondack class), and A150RU0 (Other Rock class, Joshua subclass) were encountered in the Gusev plains; targets A176RU0, A171RR0 (both Other Rock class, Pot of Gold subclass), and A200RR0 (Clovis class, Wooly Patch subclass) were encountered on the foot of the West Spur of the Columbia Hills. This stack of Mössbauer spectra exemplifies the general olivine weathering trend apparent in Figure 6.5a. Spectra are offset along the y-axis for clarity.

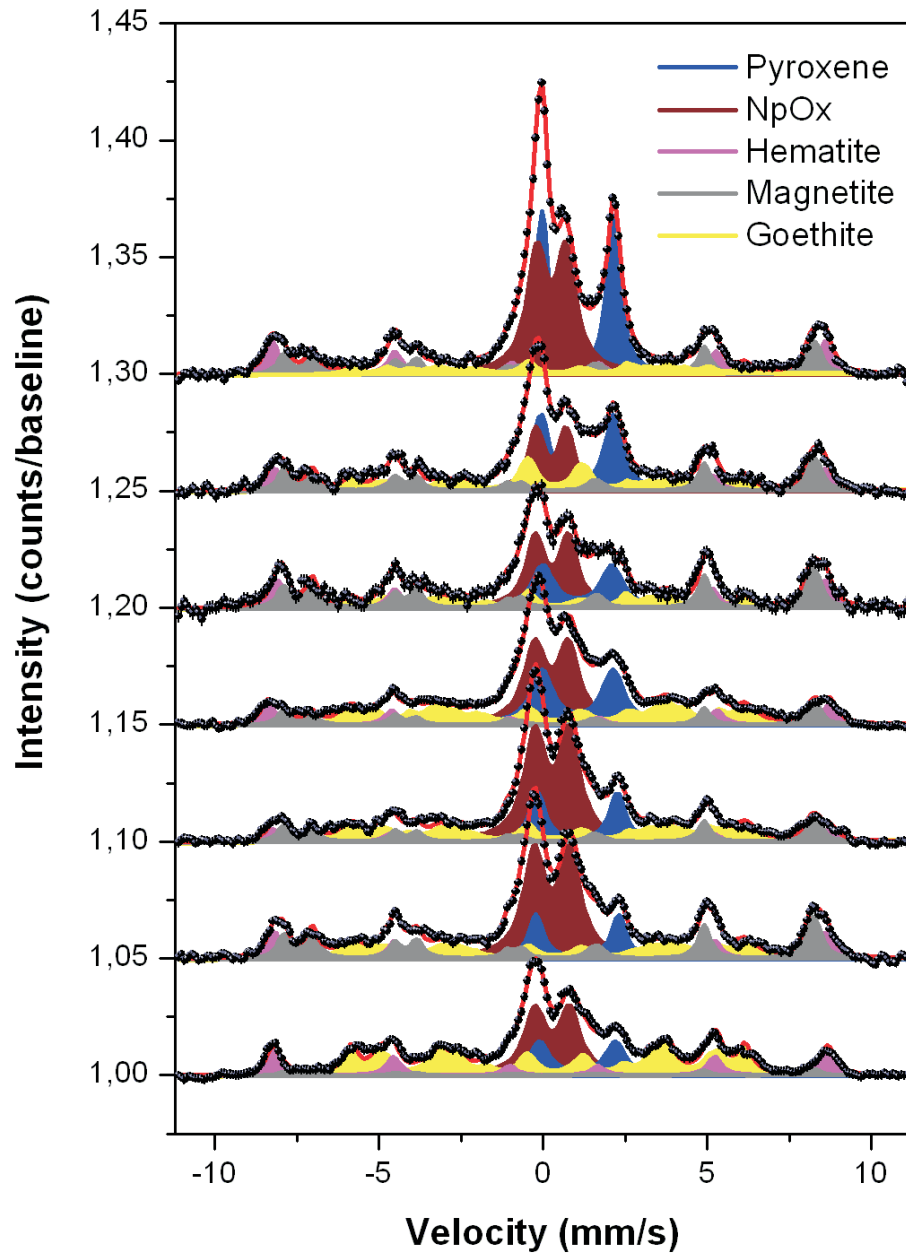


Figure 6.12: The plot shows Mössbauer spectra of Clovis class rock targets encountered at the West Spur of the Columbia Hills. The spectra are arranged in the order of increasing Fe^{3+}/Fe_{Total} ratios, starting from the top: A200RR0 WoolyPatch_Mastadon; A303RB0 Lutefisk_Roe; A275RU0 Tetl_Clump; A269RU0 Temples_Dwarf; A288RR0 Uchben_Koolik; A233RR0 Ebenezer_Ratchit2; A218RR0 Clovis_Plano. This stack of Mössbauer spectra exemplifies the pyroxene weathering trend in Clovis class rocks apparent in Figure 6.5b. Spectra are offset along the y-axis for clarity.

6.3.5 Wishstone class and Watchtower class

Watchtower class rocks have been found on Husband Hill in the Columbia Hills. These rocks are diverse in their alteration state based on Fe^{3+}/Fe_{Total} ratios and Fe-bearing mineralogy. On that basis *Morris et al.* [2006a] divided Watchtower class rocks into Watchtower subclass, Keystone subclass, and Keel subclass. This division also reflects morphological differences [*Squyres et al.*, 2006]. Wishstone class rocks are geochemically similar to Watchtower class rocks [*Ming et al.*, 2006]. The major element compositional variability evident for Watchtower Class rocks is consistent with mixing between two end-member rocks in varying relative proportions. A Wishstone-like end-member dominates the mix, while the other endmember is richer in ferromagnesian elements than Wishstone class rocks (*Hurowitz et al.*, Mixing relationships among Husband Hill lithologies, manuscript submitted to JGR).

Keystone subclass is the least oxidized and Watchtower subclass the most oxidized, with the target A493RB0 LarrysLookout_Paros having the highest Fe^{3+}/Fe_{Total} (0.94) of all rock and soil targets in the data set investigated in this chapter. Keystone contains pyroxene, magnetite, and ilmenite as primary minerals (in order of abundance), but no olivine. Wishstone class rocks show a similar degree of oxidation as Keystone subclass. They contain pyroxene, olivine, ilmenite, and magnetite as primary minerals. All three Watchtower class subclasses plot distinct from each other in Figures 6.5-6.9. The only apparent trend followed by all three subclasses is the oxidation of pyroxene (Figure 6.5b). Keel subclass rock targets as well as Watchtower subclass rock targets contain varying levels of olivine, whereas Keystone subclass contains no olivine. Wishstone class rock targets therefore often appear to combine for a better trend with Keel subclass and Watchtower subclass targets (Figure 6.13b) than Keystone subclass (Figure 6.13a). This is evident for the oxidation of olivine (Figure 6.5a) and the formation of np-Ox from olivine and pyroxene (Figures 6.6a and 6.7a). The similarity between the Wishstone MB spectrum and Keel subclass MB spectra is striking. The absence of a clear alteration trend suggests that alteration processes varied over short spatial scales or may alternatively be a consequence of the compositional differences.

6.4 Conclusions

The mineral mainly undergoing weathering processes in Gusev rocks and soils is olivine. Olivine is generally the most susceptible to weathering among the common rock forming minerals [e.g., *Goldich*, 1938; *Pettijohn*, 1941]. Because

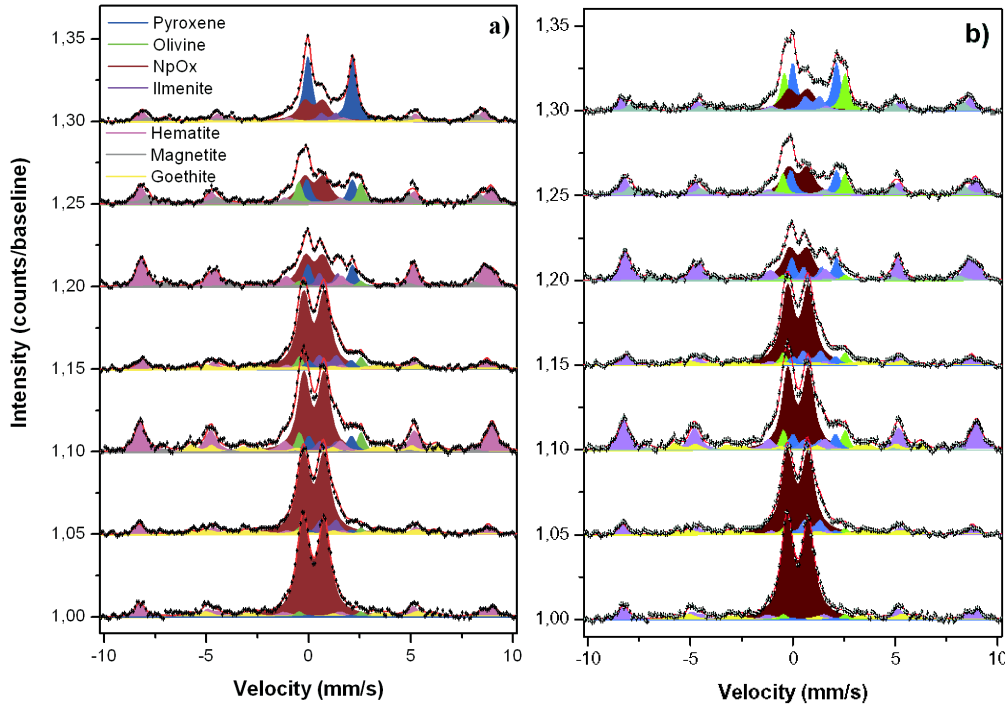


Figure 6.13: The plot shows Mössbauer spectra of Watchtower class rock targets encountered at Cumberland Ridge in the Columbia Hills. The spectra are arranged in the order of increasing Fe^{3+}/Fe_{Total} ratios, starting from the top: A472RB0 Keystone_Haunch in (a) or A336RR0 Wishstone_Chisel in (b); A483RU0 Keel_Reef; A486RB0 Keel_Davis; A501RU0 Pequod_MobyDick; A418RR0 Watchtower_Joker; A498RU0 Pequod_Ahab; A493RB0 LarrysLookout_Paros. Wishstone class rocks are geochemically similar to Watchtower class rocks. Spectra are offset along the y-axis for clarity.

of its wide-spread occurrence on Mars, the study of the relation between olivine and secondary iron-bearing minerals in Gusev crater has implications on a planet-wide scale.

The limited alteration of minerals other than olivine argues for a reduced availability of water. The adherence to Goldich's sequence of mineral susceptibility to weathering suggests generally acidic conditions. The observed secondary mineralogy, i.e., ferric oxides rather than ferrous sulfates, and the stability of ilmenite suggest pH levels between 4-6. Differences in alteration patterns seem to result mainly from varying availability of liquid water both in abundance and in time. The variation of alteration patterns over short spatial scales supports volcanic or impact origin of Columbia Hills. Water

may have been present as hydrothermal springs or ice melted by volcanic activity or impact. These sources would make for a transient availability of water.

The low degree of alteration of Adirondack class rocks are representative of the sparsity of water under the present climatic conditions on Mars.

Chapter 7

Astrobiological Applications

The field of astrobiology includes the study of the origin, evolution and distribution of life in the universe [*Des Marais and Walter, 1999*]. Research in the Solar System concentrates on the planet Mars, followed by Europa and Titan, moons of Jupiter and Saturn, respectively. On Earth much of the research concentrates on the study of so-called extreme environments that can serve as analogues for possible habitats on the planets and moons mentioned above, and on extremophiles - mostly microbial life-forms that thrive in these environments [e.g., *Rothschild and Mancinelli, 2001*]. Introductory texts to the field of astrobiology are available by, e.g., *Des Marais and Walter [1999]*, *Brack et al. [2001]*, *Gee et al. [2001]*, *Gilmour and Sephton [2003]*, and *Knoll [2003]*.

The element Fe and Fe-bearing minerals occur ubiquitously throughout the field of astrobiology. The formation of pyrite at hydrothermal vents, for example, may have played a crucial role at the origin of life, providing energy for the fixation of carbon as well as mineral binding surfaces for organic constituents [*Wächtershäuser, 1988, 1992*]. Banded iron formations (BIFs) are among the oldest rocks on Earth. Layers of ferric iron in BIFs may record the evolution of oxygenic photosynthesis [*Walker, 1979*]. Fe-rich carbonate globules and magnetite particles resembling those found in terrestrial magnetotactic bacteria in the Martian meteorite ALH84001 were interpreted to great controversy as evidence for possible relic biogenic activity by *McKay et al. [1996]*. This re-energized the discussion about life on Mars. Environments on the young Earth as well as present day Mars, Saturnian Titan, or Jovian Europa have a lack of free oxygen in common. In anaerobic environments iron can act as both an electron donor in its ferrous form and a terminal electron acceptor in its ferric form to support metabolism [e.g., *Megonigal et al., 2003*, and references therein]. Furthermore, Fe oxide and hydroxide minerals have the potential to preserve microfossils and physical biomarkers

[e.g., *Allen et al.*, 2004].

The following paragraphs summarize Mössbauer results with respect to astrobiology. Samples exhibiting morphological biosignatures as well as basaltic glass samples exposed at the Loihi deep sea hydrothermal vent system were investigated. The MER Mössbauer results were evaluated from an astrobiological perspective. The results from the basaltic glass samples and the MER results were published by *Schröder et al.* [2006].

7.1 Morphological biosignature samples

The interaction of living organisms with their environment leaves biosignatures behind such as [*Des Marais and Walker*, 1999]: Cellular remains; textural fabrics in sediments that record structure and/or function of biological communities (e.g. stromatolites); biogenic organic matter, including hydrocarbons; minerals whose deposition has been affected by biological processes; stable isotopic patterns that reflect biological activity; atmospheric constituents whose concentrations require a biological source. Biosignatures are not necessarily conclusive evidence for biologic activity. They must pass the Knoll criterium (Knoll, 2006, private communication): "While we can't be certain that life elsewhere in the universe will have the same features as the life we know on Earth, physics and chemistry will be the same. Thus, as a practical guide to exploration, we should become interested in observations as being potentially biological if we can't understand them in terms of purely physical/chemical processes".

A set of rock samples exhibiting morphological features related to or potentially mediated by biology was analyzed with a suite of instruments designed for robotic planetary surface operations. The aim of this study was to investigate if and how such biosignatures and associated sedimentary structures can be identified during remote robotic exploration. This work forms part of a wider programme of integrated and multi-disciplinary studies that address the practicalities of in situ measurements at planetary surfaces (PAFS-net¹). Selected results obtained with MIMOS II are reported here.

All samples were obtained from planetary (Martian) analogue field sites on Earth, including modern high latitude extreme environments, Tertiary (10-39 Ma) crater lake/hydrothermal deposits and Archaean (3.45 Ga) volcanoclastic sediments. Samples broadly fall into three morphological categories: fossilized microbial filaments, endolithic microbial communities and

¹The Planetary Analogue Field Studies Network (PAFS-net) is a multi-disciplinary group of scientists and engineers with a generic interest in planetary exploration and thematic studies incorporating terrestrial analogues in the lab and in the field.

ancient relict sedimentary structures containing microbial fossils. The samples are archived in the Geological Specimen Archive (GSPARC²). Mössbauer parameters from selected samples are summarized in Table 7.1 and discussed below.

Table 7.1: Mössbauer parameters from samples exhibiting morphological biosignatures.

Sample ^c	Fp.	Mineral phase	δ^{ab} (mm/s)	ΔE_Q (mm/s)	B_{hf} (T)	A (%)	Fe^{3+}/Fe_T
140	A	Oct. Fe^{3+}	0.35	0.55	-	100	1.00
	B	Oct. Fe^{3+}	0.36	0.56	-	100	1.00
45	A	Hematite	0.39	-0.24	50.6	25	1.00
		Goethite	[0.37] ^d	[-0.26]	7.3-36.6	75	
	B	Hematite	0.40	-0.26	50.3	31	1.00
		Goethite	[0.37]	[-0.26]	7.9-36.6	69	
179	A	Goethite	[0.37]	[-0.26]	17.1-28.9	80	1.00
		Oct. Fe^{3+}	0.38	0.59	-	20	
	B	Goethite	[0.37]	[-0.26]	17.0-33.8	64	1.00
		Oct. Fe^{3+}	0.38	0.58	-	36	
114	A	Oct. Fe^{3+}	0.33	0.89	-	100	1.00
	B	<i>Signal too low - no reasonable fit possible</i>					
159	A	<i>Signal too low - no reasonable fit possible</i>					
	B	Oct. Fe^{3+}	0.33	0.53	-	100	1.00
163	A	Hematite	[0.37]	[-0.20]	51.5	26	1.00
		Goethite	[0.37]	[-0.26]	26.0-35.9	74	
	B	Goethite	[0.37]	[-0.26]	13.3-38.0	100	1.00

^aRelative to α -Fe.

^bTypical uncertainties are ± 0.02 mm/s for δ and ΔE_Q , ± 0.8 T for B_{hf} , ± 2 % for the area, and ± 0.02 for Fe^{3+}/Fe_T .

^cGSPARC ID.

^dValues in square brackets were used as constraints during fitting procedures.

7.1.1 Microbial filaments

Specimens containing fossilized microbial filaments all exhibit microscopic morphology (isolated individuals) and/or macroscopic morphology (commu-

²The Geological Specimen Archive (GSPARC) is an expanding repository of physical specimens (including planetary analogues) and associated on-line database of experimental results accumulated from PAFS-net topic studies. All samples referred to here are identified by a GSPARC ID (for more details visit www.gsparc.com).

nities/assemblages). Three modes of preservation are represented: calcification (freshwater limestone), silicification (opaline sinter and chalcedony), and heavy metal precipitation (goethite).

Freshwater limestone, Hainsfarth, Ries Crater, Germany (GSPARC 140)

The Ries and Steinheim craters of the Jurassic Alb plateau in Southern Germany represent well-studied examples of terrestrial impact structures [Pohl *et al.*, 1977; Pache *et al.*, 2001]. Near-shore crater lake carbonates are well exposed at Büschelberg near Hainsfarth (48° 57.15' N, 10° 38.1' E), 2.5 km east of Öttingen and have been extensively studied [Arp, 1995]. The site (a former quarry) is the highest elevation above the eroded flat plains of the inner basin which lies 60 m below. The carbonate sequence is thick (>8 m) and consists of extensive bioherms of cladophorites (green algae) with minor stromatolites and carbonate sands composed of gastropods and ostracods. The carbonates lie directly on basal suevite.

The specimens represent a combination of well-preserved (fresh) and weathered calcified remnants of cladophorites cemented in a dolomite matrix. The tubular morphology is due to an accumulation of carbonate veneers around the original cladophorites threads, completely oxidizing the remains and leaving a void. Although the visible calcified tubes are abiogenic, their morphology which results from mineralization over a cladophorites substrate, classifies these features as a biosignature.

Figure 7.1 shows the sample and Mössbauer spectra acquired from two different positions. Orange-colored areas suggest the presence of Fe-oxide, and Mössbauer spectra show a doublet resulting from octahedral Fe^{3+} . Iron oxides also partook in the preservation of the filaments. The iron oxide may be superparamagnetic or contain substantial impurities. The signal in the Mössbauer spectra increases when looking down into the exposed tubes (footprint B). A greater volume of the iron oxide is within the instrument's field of view. The Fe oxide may be nanophase or superparamagnetic material or exhibit low crystallinity. The Mössbauer spectrum does not add much to the understanding of this rock while it is available for detailed investigations in a terrestrial laboratory. However, if the spectra shown in Figure 7.1 were obtained remotely from an otherwise uncharacterized rock on Mars, they would initiate a detailed investigation of that rock. The low bulk iron content indicated by the low signal to noise ratios together with the pure Fe^{3+} signature show that this rock was chemically altered to a large extent, most likely in the presence of water.

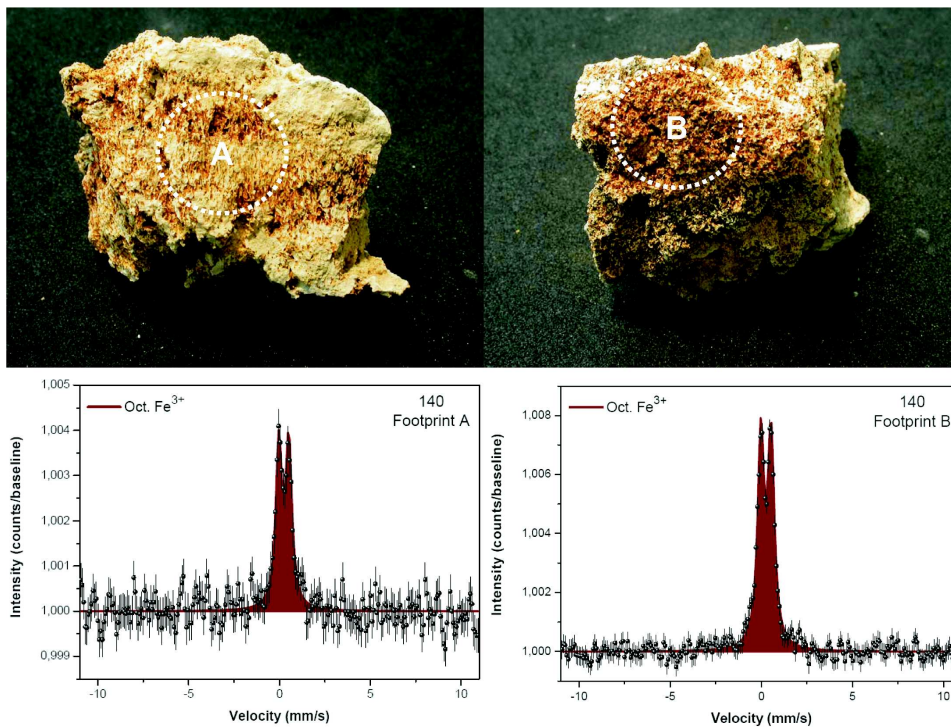


Figure 7.1: A freshwater limestone from Hainsfarth, Nördlinger Ries, Germany. The sample contains microbial filaments. Mössbauer spectra were obtained from two different positions labeled footprint A and B. The footprints shown are approximately 1.4 cm in diameter.

Chalcedony, Cady Mountains, California, USA (GSPARC 45)

The Lower Miocene volcanic and sedimentary sequence of the Sleeping Beauty Ridge region of the Cady Mountains (34° 46' N, 116° 17' W) has been extensively studied [Glazner, 1988]. Veining within the dacites and basalts extends to over 2 km and is up to 50 cm thick. Veins containing subsurface filamentous fabric (SFF) are mainly composed of chalcedony, Fe-hydroxides and calcite and are strongly enriched in trace elements Sb, As, Mo, Pb, Be and Ag. The study specimens were collected from a well preserved silica-rich vein within weathered volcanic country rock [Hofmann and Farmer, 2000].

The filaments were formed within a hydrothermal regime a few hundred meters below the palaeosurface. The filament bearing zones were originally porous and served by nutrient-rich fluids providing a suitable subterranean habitat. Late stage infilling of these voids with chalcedony and calcite preserved the filaments. The oldest filamentous fabric is heavily Fe-encrusted and macroscopically preserved but no individual filament details are dis-

cernible [Hofmann *et al.*, 2002]. Subsequent generations of filaments exhibit less Fe-cementation and show preserved individual morphology including visible cores.

Mössbauer spectra of an irregular sample surface (footprint A) and a sawn sample surface (footprint B) identify hematite and goethite (Figure 7.2). The well resolved goethite sextet suggests a high degree of crystallinity and/or only minor impurities in the goethite phase. The hematite to goethite ratio in footprint B is higher than in footprint A (Table 7.1) which correlates with a higher ratio of red to yellow area in the field of view. On Mars, for example, the simultaneous occurrence of hematite and goethite would be unequivocal evidence for the alteration of that rock by water and merit a full investigation with the available instrument payload. The color/mineral correlation can be used to track mineralogical changes in photos of the vicinity of the rock.

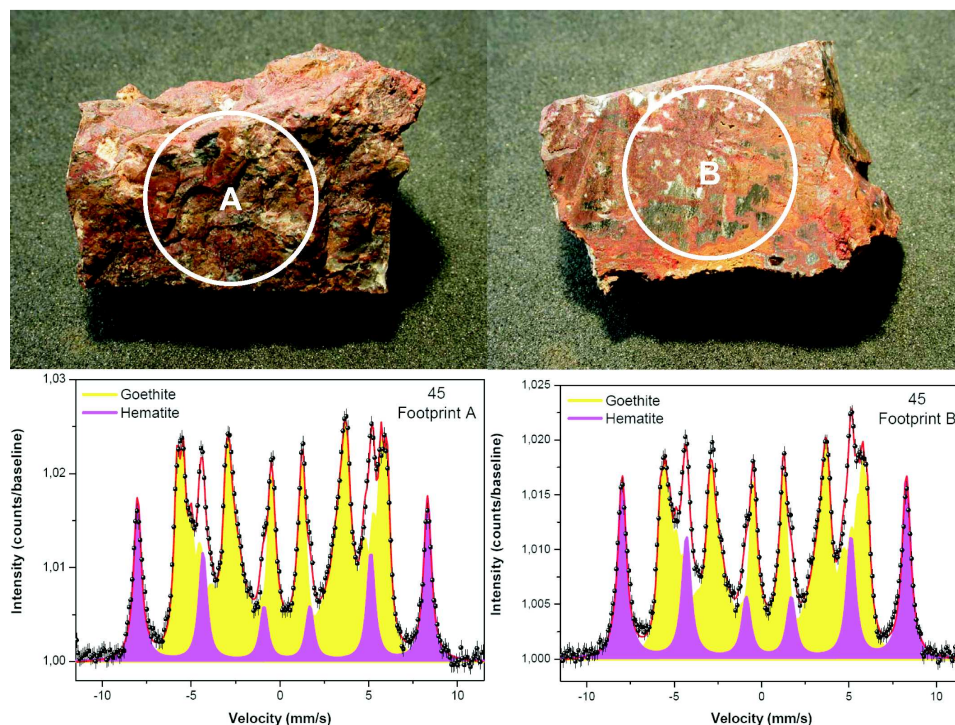


Figure 7.2: A chalcidony vein from Cady Mountains, Mojave Desert, California. The sample contains microbial filaments. Mössbauer spectra were obtained from two different positions. Dotted circles indicate the 1.4 cm diameter field of view of the MIMOS II instrument.

Goethite, Cerro de Pasco, Peru (GSPARC 179)

The Matagente orebody is part of the magmatic-hydrothermal Zn-Pb-Ag-Bi-(Cu) ore complex of Cerro de Pasco situated 170 km NNE of Lima ($10^{\circ} 38.5' S$, $76^{\circ} 10.5' W$). Prior to exploitation the maximum lateral extent of the orebody was $480 \text{ m} \times 200 \text{ m}$. Mining of the Pb-Ag deposit took place predominantly within the oxidation zone [*Sangameshwar and Barnes, 1983*] which reached approximately 100 m depth.

Oxidation zones of sulphide ore bodies commonly contain filamentous fabrics originally formed below a palaeosurface [*Hofmann and Farmer, 2000*]. Such an environment provides an energy source (usually from pyrite) for chemosynthetic organisms [*Melchiorre and Williams, 2001*]. These Fe-hydroxide filamentous fabrics potentially act as substrates for subsequent growth of oxidation zone minerals.

The study specimens exhibit externally linear texture similar in appearance to "fossilized wood" (Figure 7.3) and have a high porosity ($> 50 \%$).

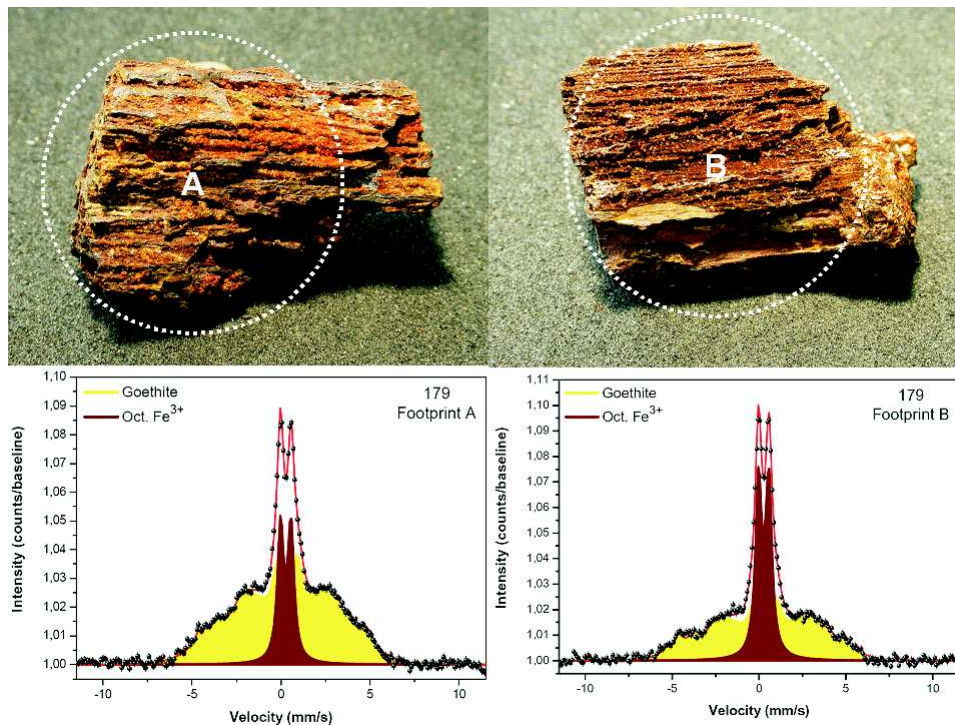


Figure 7.3: In this sample from Cerro de Pasco, Peru, goethite was preserving filamentous fabric. Mössbauer spectra were obtained from two different positions. Dotted circles indicate the 1.4 cm diameter field of view of the MIMOS II instrument.

Fe-hydroxides drape the surface in curtain-like laminae approximately 1-3 mm thick. The surface is festooned with macroscopic filamentous assemblages. Individual filaments are also preserved with core diameters of about $0.3 \mu\text{m}$ when observed by SEM.

Mössbauer spectra of the goethite (Figure 7.3, Table 7.1) show a large distribution of sextets overlapping to form a lump and an octahedral Fe^{3+} doublet. Both features can be attributed to poorly crystallized goethite. Because of the large size of the goethite particles impurities are favored as the reason rather than superparamagnetism. As for the previous two rock samples, if discovered on Mars, the identification of goethite and the high ferric iron content would be strong evidence of chemical alteration by water and single this rock out for detailed investigation.

7.1.2 Endoliths

Specimens containing endolithic microbial colonies were sourced from the extreme environments of two high latitude sites on Earth (McMurdo dry valleys, Antarctica [*Friedmann*, 1982] and Haughton Crater, Devon Island, Canada [*Cockell et al.*, 2002]). Only an orthoquartzite sample from McMurdo was analyzed by Mössbauer spectroscopy.

Orthoquartzite, McMurdo, Victoria Land, Antarctica (GSPARC 114)

The dry valleys of Southern Victoria Land, Antarctica, extend across an area of 5000 km² and lie between 76° 30' S and 78° 30' S and 160° E and 164° E. Geomorphologically they are a system of gouged glacial valleys with a predominant east-west trend. During the summer air temperatures range between -15°C and 0°C and can fall to almost -60° C in the winter. Less than 10 mm water equivalent of precipitation occurs annually. The Upper Devonian orthoquartzites of the Beacon Sandstone Formation outcrop throughout the dry valleys and contain well-studied examples of cryptoendolithic lichens and micro-algal communities [*Friedmann*, 1982; *Friedmann et al.*, 1988].

Specimens of exfoliated orthoquartzite containing cryptoendoliths were collected by the British Antarctic Survey (BAS) in 1995 from the Ross Desert McMurdo Dry Valleys at Linnaeus Terrace (77° 36' S, 161° 05' E, elevation 1600 m). Much research has already been done on these and other rocks of the region [*Friedmann*, 1982; *Edwards et al.*, 1997, 2004; *Wierzchos et al.*, 2003; *Blackhurst et al.*, 2005]. As such these specimens provide an appropriate benchmark from which to draw comparison with other types of endolithic biosignatures.

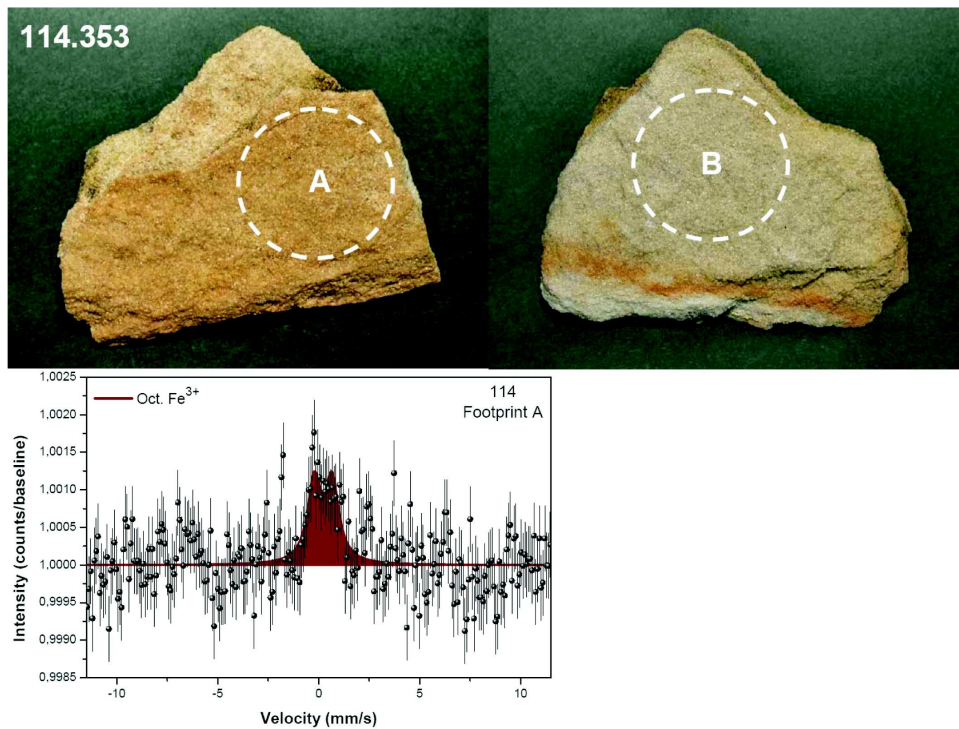


Figure 7.4: This orthoquartzite from McMurdo, Victoria Land, Antarctica, contains cryptoendolithic lichens and micro-algal communities. Mössbauer spectra were obtained from two different positions. Dotted circles indicate the 1.4 cm diameter field of view of the MIMOS II instrument. The spectrum obtained from footprint B showed only a baseline and is not shown here.

The rocks are colonized by photosynthesizing cryptoendolithic lichens that form by symbiotic association between unicellular green algae (phycobionts) and filamentous fungi (mycobionts). The physical makeup of the fresh orthoquartzite (translucency and porosity) provides a favorable protective environment for these organisms. The outer surface is case hardened and oxidized. Over time, oxalic acid secretions from the lichens dissolve the intergranular cement of the host rock leading to bioweathering and exfoliation of the rock surface [Sun and Friedmann, 1999]. The lichens have mobilized iron compounds and leached the rock of iron bearing minerals in a zone between 1 mm and 4 mm thick [Sun and Friedmann, 1999], concentrating them in a red zone at the base of the white zone.

Mössbauer spectroscopy shows a low signal attributed to octahedral Fe^{3+} correlating with the orange color in footprint A (Figure 7.4). As expected, no discernible signal was detected from the white surface in footprint B. X-ray

diffraction (XRD) analyses on the same sample picked up quartz and calcite, but no iron oxide. The iron oxide is present as a thin veneer on quartz grains and highlights the difference between surface and volume sampling. Visible wavelength do not penetrate the orange surface to any depth, while the Mössbauer γ -radiation samples a volume of the magnitude of 100 μm depth [Klingelhöfer *et al.*, 2003]. The low bulk Fe content in contrast with the orange coloration provides valuable surface to volume information from a remote sensing point of view. Low bulk Fe exclusively present as Fe^{3+} again suggest extensive chemical alteration and trigger detailed examination if discovered on Mars.

7.1.3 Relict sedimentary structures

The Early-Mid Archaean samples (3.45 Ga volcanoclastic sediments from the Pilbara, Western Australia and a 3.2 Ga Banded Iron Formation (BIF) from the Barberton Greenstone Belt, South Africa) represent an epoch when Earth and Mars possibly experienced similar conditions [Westall, 2005]. These low grade metamorphosed rocks (prehnite-pumpellyite to lower greenschist), although highly silicified, exhibit well-preserved sedimentary structures, such as laminations, cross-bedding, flaser-linsen bedding and load structures. They also contain traces of microbial life and activity in the form of microfossils, stromatolites and chemical signatures [Westall and Southam, 2006], although there is some debate concerning the biogenic interpretations of these signatures.

Stromatolitic chert, North Pole Dome, Pilbara, Australia (GSPARC 159)

Well-preserved coniform and columnar stromatolites in silicified carbonate Panorama Formation sediments (3.446 Ga) occur in the North Pole Dome area [Hofmann *et al.*, 1999]. Allwood *et al.* [2005a,b] suggest microbial mediation in their formation and Westall (unpublished data) has observed microfossils in these rocks. Specimens of domical stromatolites were acquired from the Panorama Formation near North Pole Dome (undisclosed coordinates) in 2000. The sample displays stromatolitic texture in cross section on both natural and sawn surfaces (Figure 7.5).

There is no discernible signal in Mössbauer spectra from the sawn surface (footprint A, Figure 7.5) and only a very weak signal from the orange-colored natural surface (footprint B). Its Mössbauer parameters suggest an octahedral Fe^{3+} phase of possible nanophase/superparamagnetic material. XRD analyses picked up quartz in both footprints but failed to detect any iron

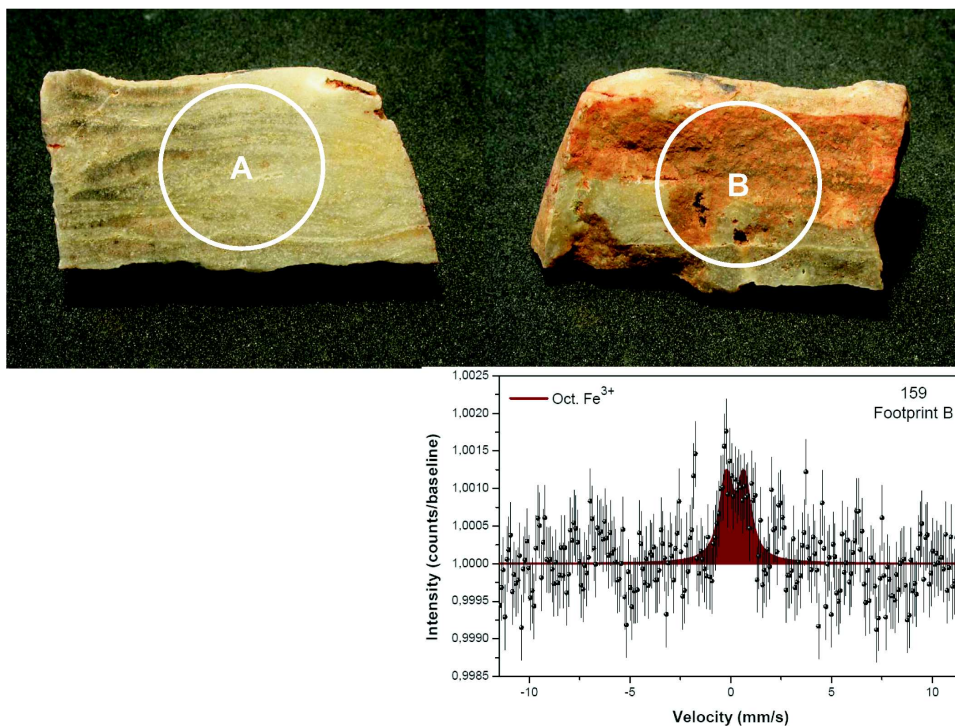


Figure 7.5: The pictures show a stromatolitic chert from North Pole Dome, Pilbara, Australia. Mössbauer spectra were obtained from two different positions. Dotted circles indicate the 1.4 cm diameter field of view of the MIMOS II instrument. The spectrum obtained from footprint A showed only a baseline and is not shown here.

oxide in either of them. Again there is a discrepancy between optical wavelength sampling the very surface and the Mössbauer γ -radiation sampling to a depth of $\sim 100 \mu\text{m}$. The low Mössbauer signal indicates a thickness of the orange-colored veneer of not more than several micrometers. On Mars, the low bulk iron content present exclusively as Fe^{3+} would once more indicate extensive chemical alteration. The presence of a coating can be inferred from the discrepancy between optical and Mössbauer data alone and would demand a grinding or drilling action.

Banded Iron Formation (BIF), Barberton, South Africa (GSPARC 163)

The Barberton Greenstone Belt (BGB) is a remnant of an Early Archaean orogenic belt [*de Wit et al.*, 1982; *de Ronde et al.*, 1994] located near the Transvaal-Swaziland border ($25^{\circ} 30'$ to $26^{\circ} 15'$ S, $30^{\circ} 30'$ to $31^{\circ} 30'$ E). The

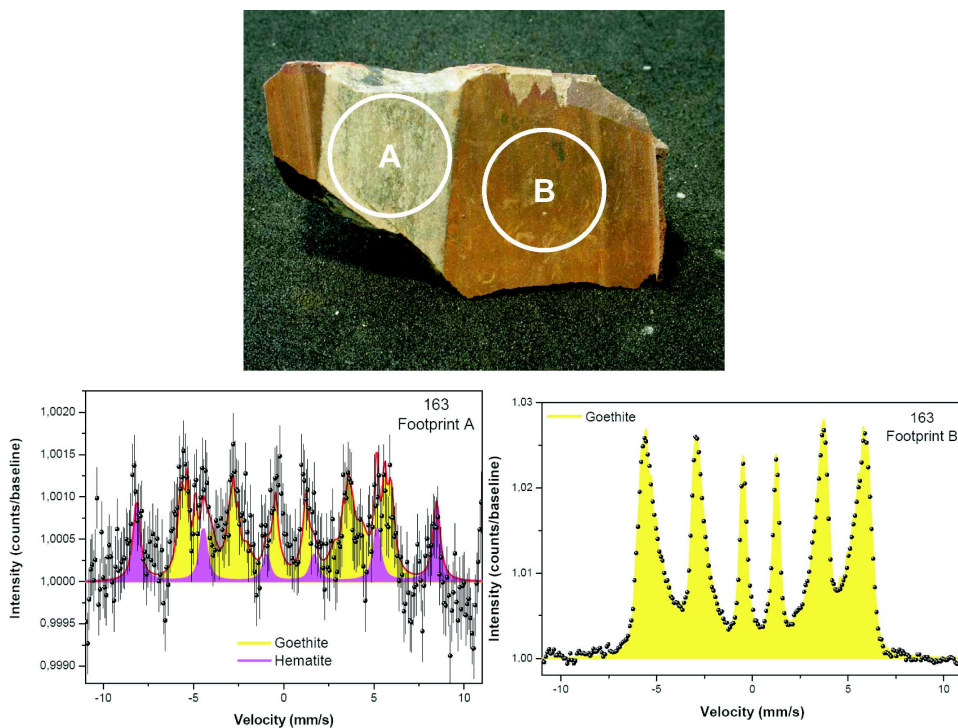


Figure 7.6: The picture shows a piece from a Banded Iron Formation (BIF) from the Fig Tree Group, Barberton Greenstone Belt, South Africa. Mössbauer spectra were obtained from two different positions. Dotted circles indicate the 1.4 cm diameter field of view of the MIMOS II instrument.

Swaziland Supergroup sequence in the BGB consists of mainly mafic and ultramafic rocks of the Onerwacht Group (3.45 Ga), overlain by pyroclastic and epiclastic sediments of the Fig Tree Group (3.2 Ga) followed by conglomerates and siltstones of the Moodies Group (3.22 Ga to 3.1 Ga). Low grade regional metamorphism (lower greenschist facies) has had no effect on the preserved textures, especially within the older units of the sequence (Onerwacht and Fig Tree Groups) where preservation is exceptional. This has led to much interest in the search for evidence of endogenous early life within these rocks [Byerly *et al.*, 1986; Walsh, 1992, 2004; Westall *et al.*, 2001; Tice and Lowe, 2004].

Specimens of Banded Iron Formation (BIF) from the Fig Tree Group were collected in 1999 from the Msauli River. The sample investigated here has a particularly prominent siliceous band exhibiting a well-defined linear contact with a massive Fe-oxide layer (Figure 7.6).

Mössbauer spectra show that the Fe-oxide layer consists of well-crystalline goethite. Although XRD analyses identified only quartz in the siliceous band,

it is not totally free of iron oxides as the Mössbauer spectrum reveals. A low signal from footprint A shows the spectral signatures of goethite and hematite. The hematite is not seen in the oxide layer and the goethite identified in the siliceous band has different B_{hf} values (Table 7.1). Hence, neither hematite nor goethite identified in the siliceous band are a result from a misplaced footprint overlapping the oxide layer. Naturally, on Mars the Mössbauer spectra would again attract considerable attention to the rock they were acquired from.

7.2 Loihi deep sea mount

Deep sea hydrothermal vents and the surrounding oceanic basaltic crust have been hypothesized as the possible origin of life on the prebiotic Earth and provide Earth-bound analogues to possible subsurface biospheres on Mars and Europa. The pressure, temperature, temperature gradients, lack of sunlight and oligotrophic nature of these surroundings are extreme in nature and force life to incorporate alternate methods of metabolism for survival. It is thermodynamically possible for chemolithotrophs and chemolithoautotrophs to utilize the large energy potential found in the form of Fe^{2+} to Fe^{3+} transitions within the basaltic glass found in oceanic crust and seamount pillow basalts. Iron is the leading nutrient candidate in the basaltic glass as an electron donor due to its relative abundance (~ 12 wt% Fe_{Total}), high degree of reduced iron (~ 90 % Fe^{2+}) and energy yield per reaction. Thus, the use of Mössbauer spectroscopy as a tool to measure this potential yield can ultimately lead to an upper limit on energy available for biomass production in a particular environment.

Weathering rates of basaltic glass in seawater have been an ongoing study with early work done by *Moore* [1966] describing the palagonitization of pillow basalts taken offshore near Hawaii. However, continued laboratory studies of the weathering rinds on both natural and synthetic basalts have produced a wide array of rates of palagonitization varying from 10^{-4} to $70 \mu\text{m}/1000$ years [*Techer et al.*, 2001]. Numerous experiments [e.g., *Advocat et al.*, 1991] have shown that dissolution of natural and synthetic glasses depends on three main factors: 1) temperature and pH of the surrounding solution, 2) hydrolysis of the glass matrix, and 3) the secondary mineral phases generated by the weathering eventually sealing the fresh glass off from further weathering. One can argue that over the past several decades, a fourth method of dissolution/alteration has been discovered in the form of microbiology [e.g., *Ross and Fisher*, 1986; *Thorseth et al.*, 1992, 1995; *Furnes et al.*, 1996, 2001; *Giovannoni et al.*, 1996; *Torsvik et al.*, 1998; *Furnes and Staudigel*, 1999].

Daughney et al. (2004) report microbiota enhanced removal of Mn and Fe from natural basalt when compared to abiotic controls, furthering the theory that microbes play an important role in chemical cycling between the oceanic basalt crust and seawater [*Staudigel and Hart*, 1983]. *Agresti et al.* [1994], using Mössbauer spectroscopy, identified superparamagnetic Fe oxide material at deep sea smoker vents, which is correlated with anaerobic bacteria found to thrive there. *Bailey et al.* [2004] have cultured several strains of Fe-oxidizing bacteria from various basalt surfaces with SEM data showing significant colonization of fresh basalt after a one year exposure to hydrothermal vent water in Hawaii.

Biotic alteration of basaltic glass competes with abiotic alteration in the deep biosphere as bottom seawater interacts with the glass to form palagonite, an oxidized, hydrated form of basaltic glass [*Thorseth et al.*, 1991]. Numerous researchers have shown that photomicrographs of pillow basalt thin sections allow for quantification and identification of various types of alteration [e.g., *Torsvik et al.*, 1998; *Furnes and Staudigel*, 1999; *Fisk et al.*, 1998]. *Furnes and Staudigel* [1999] took several samples from DSDP/ODP drill holes and quantified the amount of abiotic vs biotic alteration in glass margins from pillow basalts. Their results show that 60-85 % of total alteration in the upper 250 m of oceanic crust can be attributed to biological alteration. This trend gradually decreases to approximately 10 % biological alteration at 550 m depth where temperature, oxygen availability and porosity limit biological growth and effects.

To study the effects of iron in basaltic glass on microbial communities, several synthetic basalt glasses of varying composition and oxidation states were created in platinum crucibles in a molybdenum heating element furnace. The raw starting material for the synthetic glasses was quenched tholeiitic basalt glass taken from an active lava flow from the Pu'u O'o vent, Kilauea Volcano, Hawaii, USA. The raw material was then powdered in a disc mill and remelted at 1450°C to achieve homogeneity and lack of crystal structure. Some glass samples were also amended with other nutrients necessary for survival such as apatite (a phosphate rich mineral) and reduced manganese, another potential electron donor, but these fall outside the realm of this study. The iron oxidation state of each glass substrate was either unaltered from its natural state or oxidized by firing at sub-solidus temperatures (700°C) for four hours prior to remelting, yielding samples containing primarily reduced and oxidized iron, respectively.

The substrates were again powdered and sewn into sachets with 50 μm mesh and housed in open 4" PVC tubes. Each different type of glass was exposed for one year on Loihi Seamount, Hawaii in a diffuse hydrothermal vent field at the base of the Tower Vents inside Pele's Pit (water temp 10°C,

ambient 3°C). The PVC tubes were placed into active hydrothermal vents using the Pisces V submersibles operated by the Hawaii Undersea Research Laboratory (HURL). The samples were collected in the following year after a 13 month deployment. Upon retrieval, fine grained sediment in the sample, predominately composed of starting material but enriched in secondary mineral phases (iron oxyhydroxides and clays) and altered glass (palagonite) created in the weathering process of the fresh glass, was separated from the bulk sample by immersion in distilled, deionized (DDI) water, sonicated to separate secondary mineral phases from nucleation sites on the glass and suspending the fines in DDI water followed by suction filtration through $0.22\ \mu\text{m}$ Teflon filters.

The iron oxidation state of the fine fraction of glass was analyzed via Mössbauer spectroscopy using a common laboratory transmission setup, and compared to the bulk oxidation state of the coarse remaining material, which is believed to have negligible amounts of weathering due to large grain size to gauge reaction rates and weathering over a one year time period. The Mössbauer spectra were evaluated fitting ferric and ferrous-bearing phases with Voigt line shapes. In accordance with *De Grave and van Alboom* [1991] and *Morris et al.* [1995] the ratio $f(\text{Fe}^{3+})/f(\text{Fe}^{2+}) = 1.21$ was used. Figure 7.7 and Table 7.2 show an initial $\text{Fe}^{3+}/\text{Fe}_{\text{Total}}$ ratio of 0.13 (Sample 2) and 0.70 (Sample 4) percent in the bulk natural and oxidized glasses, respectively.

The fine fraction, representing a higher degree of alteration/weathering, shows an increase of the $\text{Fe}^{3+}/\text{Fe}_{\text{Total}}$ ratio to 0.17 in the natural glass (Sample 1) and 0.72 in the oxidized glass (Sample 3). The increase of Fe^{3+} by 4 % over one year in the bulk natural sample is in good agreement with theoretical estimates (see below), but the change is low in comparison to the errors for relative line areas, usually quoted as $\pm 2\%$ absolute. The observed increase of Fe^{3+} in the oxidized glass (2 %) is smaller than in the natural glass, which is as expected from the reduced availability of Fe^{2+} to start with. Repeated measurements with different velocity settings on the same samples confirm the observed trends.

Calculating potential biomass yields from chemolithoautotrophic growth is an extremely difficult and complex problem. Several papers aimed at quantifying this type of biomass production have been generated [e.g., *Battley*, 1998]. *Bach and Edwards* [2003] used results from *Heijnen and Van Dijken* [1992] to estimate that up to $48 \pm 21 \times 10^{10}$ g cellular C per year are created through aerobic and anaerobic iron and sulphur oxidation. Building upon this previous work, initial estimates of the rate of iron oxidation on Loihi within our crushed synthetic basaltic glasses have been shown to be about 3 % per year. Using this oxidation rate and the aerobic Fe oxidation values set forth by *Bach and Edwards* [2003] (292 ± 117 kJ/g C produced, ΔG of 66.2

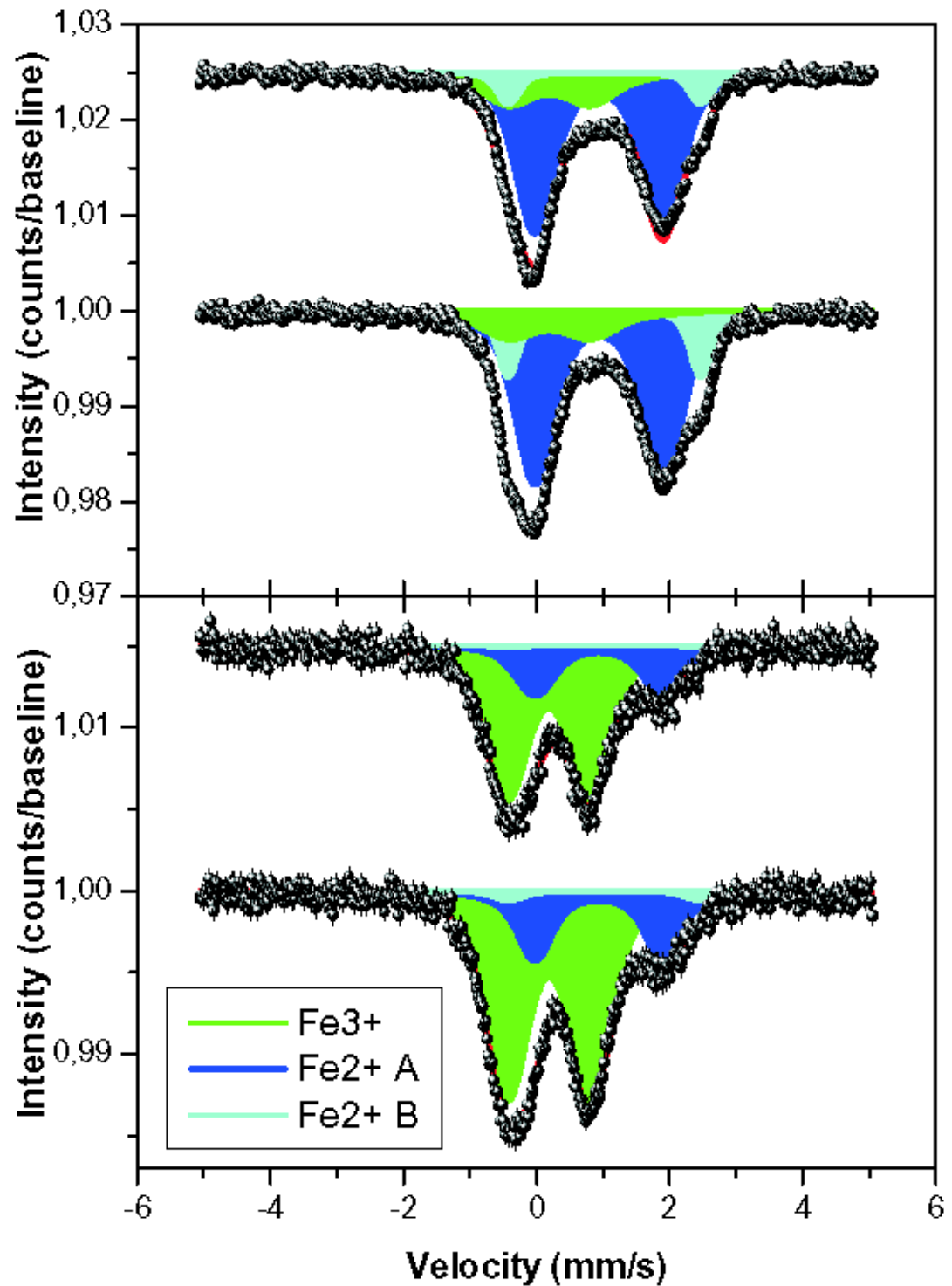


Figure 7.7: The graph shows Mössbauer spectra of basaltic glass samples exposed for 1 year at the Loihi seamount. From the top: Sample 1, natural glass, fine fraction; sample 2, natural glass, coarse fraction; sample 3, oxidized glass, fine fraction; sample 4, oxidized glass, coarse fraction. Spectra are offset for clarity.

Table 7.2: Mössbauer parameters from basaltic glass samples at the Loihi deep sea hydrothermal vent. Sample 1: Natural glass, fine fraction; 2: Natural glass, coarse fraction; 3: Oxidized glass, fine fraction; 4: Oxidized glass, coarse fraction.

Phase	MB parameter	1	2	3	4
Fe^{3+}	δ^{ab} (mm/s)	[0.31] ^c	[0.31]	0.30	0.31
	ΔE_Q (mm/s)	[1.23]	[1.23]	1.25	1.25
	Area ^d (%)	17	13	72	70
Fe^{2+} A	δ (mm/s)	[1.05]	1.05	[1.05]	[1.05]
	ΔE_Q (mm/s)	[1.92]	1.92	[1.92]	[1.92]
	Area (%)	74	71	28	27
Fe^{2+} B	δ (mm/s)	[1.13]	1.13	[1.13]	[1.13]
	ΔE_Q (mm/s)	[2.89]	2.89	[2.89]	[2.89]
	Area (%)	8	15	1	3
Fe^{3+}/Fe_{Total}		0.17	0.13	0.72	0.70

^aRelative to α -Fe.

^bTypical uncertainties are ± 0.02 mm/s for δ and ΔE_Q , ± 2 % for the area.

^cValues in square brackets were kept as constraints during fitting procedures.

^dArea ratios are f-factor corrected using $f(Fe^{3+})/f(Fe^{2+}) = 1.21$.

kJ/mole Fe oxidized, a factor of 1:2.2 in g C biomass:g dry weight of cells), a total of approximately $3 \pm 1 \times 10^{-2}$ g cellular weight/kg fresh basalt glass can be produced per year. Approximately 2.5 km² of new oceanic crust/year are generated at spreading ridges and if the upper 5 m of this new crust is about 10 % basalt glass, the total potential biomass production per year over the spreading ridges alone is about 3×10^7 g cellular weight! This is only the maximum upper bound on biomass production, however, from an astrobiology perspective, it shows that there indeed exists energy available from iron oxidation wherever water and Fe-rich rock interact that life can harness for growth and proliferation.

7.3 Mars

According to the objectives of the Mars Exploration Rover mission, the landing sites of both Spirit and Opportunity have been assessed for their past environmental conditions and their suitability for life. The contributions in-

ferred from the Mössbauer results to the assessments of Gusev Crater [Des Marais *et al.*, 2005] and Meridiani Planum [Knoll *et al.*, 2005] are summarized below.

7.3.1 Gusev Crater

Gusev Crater was selected as the landing site for the Mars Exploration Rover (MER) Spirit mission, because the crater could have collected sediments from a variety of sources during its 3.9 Ga history, including fluvial, lacustrine, volcanic, glacial, impact, regional and local aeolian, and global air falls. It may thus be a unique site to investigate the past history of water on Mars, climate and geological changes, and the potential habitability of the planet [Cabrol *et al.*, 2003].

During its primary mission Spirit found no evidence for lacustrine sedimentation in the plains surrounding its landing site [Squyres *et al.*, 2004a]. Instead Spirit's Mössbauer spectrometer identified olivine, pyroxene, non-stoichiometric magnetite, and unspecified nanophase iron oxide in rocks and soils. Olivine is usually the first mineral to weather away in aqueous environments [e.g., Eggleton, 1986]. The ubiquitous presence of olivine in soil suggests that physical rather than chemical weathering processes currently dominate at Gusev crater [Morris *et al.*, 2004]. However, water probably has been involved to a limited degree in the formation of veins, filled vugs, and surface coatings that are associated with rocks at the Spirit landing site [Squyres *et al.*, 2004a; Haskin *et al.*, 2005]. Spirit's Mössbauer spectrometer identified crystalline hematite and elevated Fe^{3+}/Fe_{Total} ratios associated with a multilayered coating on a basaltic olivine-bearing rock dubbed Mazatzal (compare chapter 6.3.2) and provided part of the evidence. In that coating, Fe^{2+} in olivine is negatively correlated with Fe^{3+} in nanophase ferric oxides, requiring alteration of adhering soil or the underlying rock itself [Haskin *et al.*, 2005]. Effects of aqueous activity are also seen in subsurface soils exposed in trenches dug using the rover wheels in the intercrater plains. These effects include the oxidation of Fe^{2+} as indicated by elevated Fe^{3+}/Fe_{Total} ratios measured in the subsurface soils compared to the topmost soil layer [Haskin *et al.*, 2005; Wang *et al.*, 2006]. The combined evidence implicates interaction with liquid water, but not pools of surface or ground water, nor hydrothermal conditions [Haskin *et al.*, 2005]. Possible sources of water include precipitation and condensation from the atmosphere (e.g., acid fog) or melting of ground ice during episodes of higher obliquity [Arvidson *et al.*, 2004].

Des Marais et al. [2005] assessed the availability of nutrient elements, energy and liquid water on the Gusev plains. Energy and reducing power

to sustain microbial synthesis can be provided by reduced minerals such as olivine, when altered by water. Serpentinization of ultramafic rocks at temperatures $< 300^{\circ}\text{C}$ would end in the production of magnetite and H_2 [Sleep *et al.*, 2004]. Molecular hydrogen acts as a near-universal source of energy and reducing power for microorganisms. *Chapelle et al.* [2002] describe a subsurface hydrogen-based methanogenic microbial community in deeply buried igneous rocks on Earth. The Fe-bearing mineralogy of dark soils derived from Mössbauer spectra from both MER landing sites, Gusev Crater and Meridiani Planum, is essentially identical and contains olivine, pyroxene, nanophase iron oxide and non-stoichiometric magnetite as described above. From that evidence *Yen et al.* [2005a] conclude that olivine-bearing precursor rocks may be wide-spread on the surface of Mars. Magnetite forms also by solely igneous processes and its presence alongside olivine does not necessarily infer that it was formed by serpentinization processes as described above [Schröder *et al.*, 2005]. *Des Marais et al.* [2005] conclude, that, despite the current sparsity of water at the surface, because of the potential of mafic and ultramafic terrains to sustain chemosynthetic microorganisms in subsurface environments, the Gusev Crater plains and related terrains merit closer scrutiny in future orbiter and lander missions.

On sol 156 after landing at Gusev Crater MER Spirit left the plains and started ascending into the Columbia Hills, rising about 90 m above the surrounding plains [Arvidson *et al.*, 2006]. The Columbia Hills are composed of older material than the surrounding plains. Rocks in the Columbia Hills are diverse in composition, some outcrop rocks exhibit layered structures [Squyres *et al.*, 2006]. Iron oxidation ratios $\text{Fe}^{3+}/\text{Fe}_{\text{Total}}$ of rocks in the Columbia Hills range from 0.2 to 0.9, i.e. from little alteration comparable to rocks encountered in the plains, to highly altered. Well-crystalline hematite and goethite were identified by Mössbauer spectroscopy in pervasively altered rocks, providing evidence for aqueous processes. Goethite in particular provides unequivocal mineralogical evidence for aqueous processes because it has structural hydroxide and is formed under aqueous conditions [Morris *et al.*, 2006a]. However, Columbia Hills outcrops and rocks do not represent lacustrine sediments [Squyres *et al.*, 2006]. They may have formed by the aqueous alteration of basaltic rocks, volcaniclastic materials, and/or impact ejecta by solutions that were rich in acid-volatile elements [Ming *et al.*, 2006].

7.3.2 Meridiani Planum

Meridiani Planum was selected as the landing site for the MER Opportunity mission because of the detection of hematite from orbital observations by

the Mars Global Surveyor TES [Christensen *et al.*, 2000; Christensen *et al.*, 2001]. Hematite formation in most cases involves aqueous processes.

At its landing site in 22 m diameter Eagle crater, Opportunity discovered flat-lying, finely laminated sedimentary rocks which contained abundant sulfate salts [Squyres *et al.*, 2004b]. These rocks provide in situ evidence for an ancient aqueous environment at Meridiani Planum, where conditions were suitable for biological activity for some time in Martian history [Squyres *et al.*, 2004c]. A key to these findings is the identification of jarosite within the sedimentary rocks by Opportunity's Mössbauer spectrometer [Klingelhöfer *et al.*, 2004]. Jarosite is an iron hydroxide sulfate mineral, whose general formula can be written $(K, Na, H_3O)(Fe_{3-x}Al_x)(SO_4)_2(OH)_6$, where $x < 1$. Other cations such as Pb are possible. Jarosite provides mineralogical in situ evidence for the presence of water on Mars and for aqueous acid sulfate processes under oxidizing conditions. The average outcrop matrix contains 2 wt% H_2O within the jarosite alone [Klingelhöfer *et al.*, 2004]. Jarosite forms only under low pH conditions (5 or less) [e.g., Catling, 2004] and puts thus strong constraints on the chemistry and mineralogy of sedimentary outcrop material at Meridiani Planum [Clark *et al.*, 2005], the diagenesis of the sedimentary outcrop formations [McLennan *et al.*, 2005], and the geochemical modeling of evaporation processes on Mars [Tosca *et al.*, 2005]. Knoll *et al.* [2005] give an astrobiological perspective on Meridiani Planum. Although the high levels of acidity inferred from the presence of jarosite would have challenged prebiotic chemical reactions thought to have played a role in the origin of life on Earth, microbial populations on Earth have adapted to low pH levels and episodic water limitation. Fe^{2+} is soluble under low pH and thus would have been available as an electron donor for microbial metabolism. Hence, the Meridiani plain may have been habitable during the time that the deposition of the outcrop material took place.

Dispersed throughout the sedimentary rocks are mm-sized spherules, which are interpreted to be concretions formed by post-depositional diagenesis, again involving liquid water [Squyres *et al.*, 2004c]. The spherules are eroded from the rocks and cover large parts of the Meridiani plains [Soderblom *et al.*, 2004]. Measurements with Opportunity's Mössbauer spectrometer showed that the spherules are hematite-rich [Klingelhöfer *et al.*, 2004] and are thus the source for the hematite observed from orbit. The occurrence of sulfates and iron oxides, both of which can preserve chemical, textural and microfossil signatures [e.g., Allen *et al.*, 2004; Fernández-Remolar *et al.*, 2005], make Meridiani Planum a prime candidate for a Mars sample return mission [Knoll *et al.*, 2005].

Based on mineralogy and jarosite occurrence, the Tinto river system in Spain, an extreme acidic environment under the control of iron, provides an

analogous habitat for Meridiani Planum on Earth [*Fernández-Remolar et al.*, 2004]. The site may facilitate the understanding of Meridiani mineral precipitation and diagenesis. At Rio Tinto a microbial ecosystem is sustained by the iron cycle [*González-Toril et al.*, 2003]. Biosignature and microfossils are preserved in iron oxides in the sedimentary rocks. The site has been extensively studied by Mössbauer spectroscopy to allow for comparison with data obtained from Meridiani Planum [*Fernández-Remolar et al.*, 2005]. Jarosite also forms during acid-sulfate alteration of volcanic rocks. Jarositic tephra on Mauna Kea, Hawaii, are also well-studied by Mössbauer spectroscopy [*Morris et al.*, 1996].

The composition of Bounce Rock (Chapter 4.4) adds further evidence to the origin of Martian meteorites. The Martian meteorites show that exchange of matter - and possibly life or prebiotic chemical compounds - between Mars and Earth occurred.

The recent findings from MER and the European orbiter Mars Express [e.g., *Formisano et al.*, 2004] combined, prompted one commentator to say: "Given what we now know about Mars, planetary protection considerations require the assumption that Martian life exists, until we learn otherwise" [*Kargel et al.*, 2004].

7.4 Conclusions

Samples collected from Mars analogue field sites on Earth which contain morphological biosignatures were investigated with MIMOS II as part of a suite of instruments designed for robotic planetary surface operations. The Mössbauer results indicated, for example, impurities in the goethite in sample GSPARC 179 and detected hematite and goethite in the siliceous layer of a BIF sample, which were not picked up by XRD analyses. The results could not add much to the understanding of the biosignatures in those samples which had been already well-studied in terrestrial laboratories. From the viewpoint of robotic planetary operations, however, the Mössbauer spectra from each rock indicated a high degree of chemical alteration in the presence of liquid water. Based on the experience from MER, each spectrum would have led to the investigation of that rock with the full rover payload. Correlations between color and mineral abundance from Mössbauer spectra can be used to track changes in mineral composition in color photographs. Discrepancies between orange surfaces indicating abundant iron oxides and low bulk iron contents inferred from Mössbauer spectra help to identify rock coatings and veneers.

Results from Mössbauer spectroscopy confirm estimates of biomass yield

from the utilization of the Fe^{2+}/Fe^{3+} redox potential in basaltic glass by chemolithoautotrophs at deep sea hydrothermal vent systems. While not all aqueous oxidation of iron within basaltic glass is evidence for life, the iron does present an energy source for chemolithoautotrophic growth and relative proportions of Fe^{2+}/Fe^{3+} allow for a measure of potential energy for use by a microbial community. Such measurements are just one example of how the technique can help to understand habitats, which are possibly analogous to sub-ice environments on Europa and Jupiter's other icy moons Ganymede and Callisto.

The Mössbauer spectrometers on the Mars Exploration Rovers identified aqueous minerals such as jarosite and hematite [*Klingelhöfer et al.*, 2004]. The identification of jarosite was crucial to evaluate the habitability of Opportunity's landing site at Meridiani Planum during the formation of the sedimentary outcrop rocks, because jarosite puts strong constraints on pH levels [*Knoll et al.*, 2005]. Its identification is also crucial for the evaluation of analogous habitats that can be studied on Earth such as the Rio Tinto system in Spain [*Fernández-Remolar et al.*, 2004 2005]. Fe oxidation states and Fe^{3+}/Fe_{Total} ratios provide further evidence for aqueous processes on Mars [*Haskin et al.*, 2005]. In contrast, the identification of olivine in rocks and soils on the Gusev crater plains provide evidence for the long term sparsity of water in that area on Mars [*Morris et al.*, 2004]. Aqueous alteration of olivine may provide an energy source for microbial metabolism, however [*Des Marais et al.*, 2005].

Mössbauer spectroscopy supported the identification of the first rock on Mars, which is actually similar in elemental and mineralogical composition to Martian meteorites discovered on Earth (Zipfel, Schröder et al., manuscript in preparation).

Although Mössbauer spectroscopy cannot detect life directly, the identification of Fe-bearing minerals can aid the search. Iron oxides such as hematite and Fe-bearing sulfates can preserve microfossils [e.g., *Allen et al.*, 2004; *Fernández-Remolar et al.*, 2005]. So-called biominerals comprise Fe oxides such as magnetite, as well as sulfides, carbonates, and phosphates of iron [*Cornell and Schwertmann*, 1996]. Mössbauer spectroscopy thus remains an important contact instrument to choose rocks in situ that merit further analysis in sophisticated laboratories inside future rovers or on Earth after a Mars Sample Return mission.

Chapter 8

Summary and Conclusions

The weathering of Fe-bearing minerals under extraterrestrial conditions was investigated by Mössbauer spectroscopy to gain insights into weathering processes and the role of water on the planet Mars. The NASA Mars Exploration Rovers Spirit and Opportunity each carry a miniaturized Mössbauer spectrometer MIMOS II for the in situ investigation of Martian soils and rocks as part of their payload.

The MER flight instruments had to be especially modified in order to work over the Martian diurnal temperature range (180 K - 290K) and within the unique electronic environment of the rovers. As a result, a decrease in the velocity linearity of the drive system had to be compensated for by software. Fit routines were adjusted to calculate velocity scales taking the differential signal (drive error signal) into account. Velocity calibration of the MIMOS II flight instruments was more difficult than anticipated, because the velocity output of the drive systems also depended on their temperature. Calibrated, temperature-dependent velocity scales were produced and released to the international scientific community. The integration time necessary to obtain a good quality Mössbauer spectrum with the MIMOS II flight instruments was reduced by 30 % through the design of a new collimator.

The in situ investigation of rocks along the Rover Spirit's traverse in Gusev crater revealed weakly altered olivine basalt on the plains and pervasively altered basalt in the Columbia Hills. Olivine is the mineral which is primarily involved in weathering reactions. This argues for a reduced availability of water. The obvious adherence to Goldich's sequence of mineral susceptibility to weathering suggests generally acidic conditions. The observed secondary mineralogy, i.e., ferric oxides rather than ferrous sulfates, and the stability of ilmenite suggest pH levels between 4-6. Goethite is proof for the involvement of liquid water in the weathering of rocks in the Columbia Hills. Differences in alteration patterns seem to result mainly from varying availability of liquid

water, both in abundance and in time. The variation of alteration patterns over short spatial scales supports a volcanic or impact origin of Columbia Hills. Water may have been present as hydrothermal springs or ice melted by volcanic activity or impact. These sources would make for a transient availability of water.

The Columbia Hills are older than the embaying plains. The weak alteration of olivine basalt in the plains is evidence that the presence of liquid water is severely limited under current conditions. Although there is evidence for the action of thin films of liquid water, the observed alteration may in large part result from gas-solid reactions with the atmosphere, in particular for the fine-grained soil component. Experiments in which mineral powders were exposed to components of the Martian atmosphere showed that interaction with the atmosphere alone, in the absence of liquid water, is sufficient to oxidize Martian surface materials. The fine-grained dust suspended in the Martian atmosphere may have been altered solely by gas-solid reactions.

Fresh and altered specimens of Martian meteorites were investigated with MIMOS II. The study of Martian meteorites in the lab helped to identify in Bounce Rock the first rock on Mars which is similar in composition to basaltic shergottites, a subgroup of the Martian meteorites.

The field of astrobiology includes the study of the origin, evolution and distribution of life in the universe. Water is a prerequisite for life. The MER Mössbauer spectrometers identified aqueous minerals such as jarosite and goethite. The identification of jarosite was crucial to evaluate the habitability of Opportunity's landing site at Meridiani Planum during the formation of the sedimentary outcrop rocks, because jarosite puts strong constraints on pH levels. The identification of olivine in rocks and soils on the Gusev crater plains provide evidence for the long term sparsity of water in that area on Mars. However, subsurface aqueous alteration of olivine may provide an energy source for microbial metabolism. Indeed, in a related study Fe^{2+}/Fe^{3+} ratios were obtained with Mössbauer spectroscopy from basaltic glass samples which were exposed at a deep sea hydrothermal vent. The ratios were used as a measure of potential energy for use by a microbial community. Although Mössbauer spectroscopy does not detect biosignatures, it was able to identify chemically altered rocks as a first step towards their detection.

The MER Mössbauer spectrometers provided evidence for weathering under aqueous conditions in the past and at dry conditions in the current climate. Mössbauer spectroscopy can be a valuable tool in future missions to Mars with an astrobiological emphasis.

List of Publications

Articles in peer-reviewed journals

1. Klingelhöfer, G., B. Bernhardt, J. Foh, U. Bonnes, D. Rodionov, P.A. de Souza Jr., C. Schröder, R. Gellert, S. Kane, P. Gütlich and E. Kankeleit (2002), The Miniaturized Mössbauer Spectrometer MIMOS II for Extraterrestrial and Outdoor Terrestrial Applications: A Status Report, *Hyperfine Interactions*, 144/145, 371-379.
2. Klingelhöfer, G., R.V. Morris, B. Bernhardt, D. Rodionov, P.A. de Souza Jr., S.W. Squyres, J. Foh, E. Kankeleit, U. Bonnes, R. Gellert, C. Schröder, S. Linkin, E. Evlanov, B. Zubkov, and O. Prilutski (2003), Athena MIMOS II Mössbauer spectrometer investigation, *Journal of Geophysical Research*, 108(E12), 8067, doi:10.1029/2003JE002138.
3. Morris, R.V., G. Klingelhöfer, B. Bernhardt, C. Schröder, D.S. Rodionov, P.A. de Souza Jr., A. Yen, R. Gellert, E.N. Evlanov, J. Foh, E. Kankeleit, P. Gütlich, D.W. Ming, F. Renz, T. Wdowiak, S.W. Squyres, and R.E. Arvidson (2004), Mineralogy at Gusev Crater from the Mössbauer Spectrometer on the Spirit Rover, *Science*, 305, 833-836.
4. Schröder, C., G. Klingelhöfer, and W. Tremel (2004), Weathering of Fe-bearing minerals under Martian conditions, investigated by Mössbauer spectroscopy, *Planetary and Space Science*, 52(11), 997-1010, doi:10.016/j.pss.2004.07.018.
5. Soderblom, L.A., R.C. Anderson, R.E. Arvidson, J.F. Bell III, N.A. Cabrol, W. Calvin, P.R. Christensen, B.C. Clark, T. Economou, B.L. Ehlmann, W.H. Farrand, D. Fike, R. Gellert, T.D. Glotch, M.P. Gombek, R. Greeley, J.P. Grotzinger, K.E. Herkenhoff, D.J. Jerolmack, J.R. Johnson, B. Joliff, G. Klingelhöfer, A.H. Knoll, Z.A. Learner, R. Li, M.C. Malin, S.M. McLennan, H.Y. McSween, D.W. Ming, R.V. Morris, J.W. Rice Jr., L. Richter, R. Rieder, D. Rodionov, C. Schröder, F.P. Seelos IV, J.M. Soderblom, S.W. Squyres, R. Sullivan, W.A. Waters, C.M. Weitz, M.B. Wyatt, A. Yen, and J. Zipfel (2004), Soils of Eagle Crater and Meridiani Planum at the Opportunity Rover Landing Site, *Science*, 306, 1723-1726.
6. Klingelhöfer, G., R.V. Morris, B. Bernhardt, C. Schröder, D.S. Rodionov, P.A. de Souza Jr., A. Yen, R. Gellert, E.N. Evlanov, B. Zubkov, J. Foh, U. Bonnes, E. Kankeleit, P. Gütlich, D.W. Ming, F. Renz, T. Wdowiak, S.W. Squyres, and R.E. Arvidson (2004), Jarosite and

Hematite at Meridiani Planum from Opportunity's Mössbauer Spectrometer, *Science*, *306*, 1740-1745.

7. Yen, A.S., R. Gellert, C. Schröder, R.V. Morris, J.F. Bell III, A.T. Knudson, B.C. Clark, D.W. Ming, J.A. Crisp, R.E. Arvidson, D. Blaney, J. Brückner, P.R. Christensen, D.J. DesMarais, P.A. de Souza Jr., T.E. Economou, A. Ghosh, B.C. Hahn, K.E. Herkenhoff, L.A. Haskin, J.A. Hurowitz, B.L. Joliff, J.R. Johnson, G. Klingelhöfer, M.B. Madsen, S.M. McLennan, H.Y. McSween, L. Richter, R. Rieder, D. Rodionov, L. Soderblom, S.W. Squyres, N.J. Tosca, A. Wang, M. Wyatt, and J. Zipfel (2005), An integrated view of the chemistry and mineralogy of Martian soils, *Nature*, *436*, 49-54, doi:10.1038/nature03637.
8. Goetz, W., P. Bertelsen, C.S. Binou, H.P. Gunnlaugsson, S.F. Hviid, K.M. Kinch, D.E. Madsen, M.B. Madsen, M. Olsen, R. Gellert, G. Klingelhöfer, D.W. Ming, R.V. Morris, R. Rieder, D.S. Rodionov, P.A. de Souza Jr., C. Schröder, S.W. Squyres, T. Wdowiak, and A. Yen (2005), Indication of drier periods on Mars from the chemistry and mineralogy of atmospheric dust, *Nature*, *436*, 62-65, doi:10.1038/nature03807.
9. Haskin, L.A., A. Wang, B.L. Joliff, H.Y. McSween, B.C. Clark, D.J. Des Marais, S.M. McLennan, N.J. Tosca, J.A. Hurowitz, J.D. Farmer, A. Yen, S.W. Squyres, R.E. Arvidson, G. Klingelhöfer, C. Schröder, P.A. de Souza Jr., D.W. Ming, R. Gellert, J. Zipfel, J. Brückner, J.F. Bell III, K. Herkenhoff, P.R. Christensen, S. Ruff, D. Blaney, S. Gorevan, N.A. Cabrol, L. Crumpler, J. Grant, and L. Soderblom (2005), Water alteration of rocks and soils on Mars at the Spirit rover site in Gusev crater, *Nature*, *436*, 66-69, doi:10.1038/nature03640.
10. Tosca, N.J., S.M. McLennan, B.C. Clark, J.P. Grotzinger, J.A. Hurowitz, A.H. Knoll, C. Schröder, and S.W. Squyres (2005), Geochemical modeling of evaporation processes on Mars: Insight from the sedimentary record at Meridiani Planum, *Earth and Planetary Science Letters*, *240*, 122-148, doi:10.1016/j.epsl.2005.09.042.
11. Knoll, A.H., M. Carr, B. Clark, D.J. DesMarais, J.D. Farmer, W.W. Fischer, J.P. Grotzinger, S.M. McLennan, M. Malin, C. Schröder, S. Squyres, N.J. Tosca, and T. Wdowiak (2005), An astrobiological perspective on Meridiani Planum, *Earth and Planetary Science Letters*, *240*, 179-189, doi:10.1016/j.epsl.2005.09.045.
12. Arvidson, R.E., S.W. Squyres, R.C. Anderson, J.F. Bell III, D. Blaney, J. Brückner, N.A. Cabrol, W.M. Calvin, M.H. Carr, P.R. Christensen,

- B.C. Clark, L. Crumpler, D.J. Des Marais, P.A. de Souza Jr., C. d'Uston, T. Economou, J. Farmer, W.H. Farrand, W. Folkner, M. Golombek, S. Gorevan, J.A. Grant, R. Greeley, J. Grotzinger, E. Guinness, B.C. Hahn, L. Haskin, K.E. Herkenhoff, J.A. Hurowitz, S. Hviid, J.R. Johnson, G. Klingelhöfer, A.H. Knoll, G. Landis, C. Leff, M. Lemmon, R. Li, M.B. Madsen, M.C. Malin, S.M. McLennan, H.Y. McSween, D.W. Ming, J. Moersch, R.V. Morris, T. Parker, J.W. Rice Jr., L. Richter, R. Rieder, D.S. Rodionov, C. Schröder, M. Sims, M. Smith, P. Smith, L.A. Soderblom, R. Sullivan, S.D. Thompson, N.J. Tosca, A. Wang, H. Wänke, J. Ward, T. Wdowiak, M. Wolff, and A. Yen (2006), Overview of the Spirit Mars Exploration Rover Mission to Gusev Crater: Landing site to Backstay Rock in the Columbia Hills, *Journal of Geophysical Research*, *111*, E02S01, doi:10.1029/2005JE002499.
13. Hurowitz, J.A., S.M. McLennan, N.J. Tosca, R.E. Arvidson, J.R. Michalski, D.W. Ming, C. Schröder, and S.W. Squyres (2006), In situ and experimental evidence for acidic weathering of rocks and soils on Mars, *Journal of Geophysical Research*, *111*, E02S19, doi:10.1029/2005JE002515.
 14. McSween, H.Y., M.B. Wyatt, R. Gellert, J.F. Bell III, R.V. Morris, K.E. Herkenhoff, L.S. Crumpler, K.A. Milam, K.R. Stockstill, L.L. Tornabene, R.E. Arvidson, P. Bartlett, D. Blaney, N.A. Cabrol, P.R. Christensen, B.C. Clark, J.A. Crisp, D.J. Des Marais, T. Economou, J.D. Farmer, W. Farrand, A. Ghosh, M. Golombek, S. Gorevan, R. Greeley, V.E. Hamilton, J.R. Johnson, B.L. Joliff, G. Klingelhöfer, A.T. Knudson, S. McLennan, D. Ming, J.E. Moersch, R. Rieder, S.W. Ruff, C. Schröder, P.A. de Souza Jr., S.W. Squyres, H. Wänke, A. Wang, A. Yen, and J. Zipfel (2006), Characterization and petrologic interpretation of olivine-rich basalts at Gusev Crater, Mars, *Journal of Geophysical Research*, *111*, E02S10, doi:10.1029/2005JE002477.
 15. Ming, D.W., D.W. Mittlefehldt, R.V. Morris, D.C. Golden, R. Gellert, A. Yen, B.C. Clark, S.W. Squyres, W.H. Farrand, S.W. Ruff, R.E. Arvidson, G. Klingelhöfer, H.Y. McSween, D.S. Rodionov, C. Schröder, P.A. de Souza Jr., and A. Wang (2006), Geochemical and mineralogical indicators for aqueous processes in the Columbia Hills of Gusev crater, Mars, *Journal of Geophysical Research*, *111*, E02S12, doi:10.1029/2005JE002560.
 16. Wang, A., L.A. Haskin, S.W. Squyres, B.L. Joliff, L. Crumpler, R. Gellert, C. Schröder, K. Herkenhoff, J. Hurowitz, N.J. Tosca, W.H. Farrand, R. Anderson, and A.T. Knudson (2006), Sulfate deposition

in subsurface regolith in Gusev crater, Mars, *Journal of Geophysical Research*, 111, E02S17, doi:10.1029/2005JE002513.

17. R.V. Morris, G. Klingelhöfer, C. Schröder, D.S. Rodionov, A. Yen, D.W. Ming, P.A. de Souza Jr., I. Fleischer, T. Wdowiak, R. Gellert, B. Bernhardt, E.N. Evlanov, B. Zubkov, J. Foh, U. Bonnes, E. Kankeleit, P. Gütlich, F. Renz, S.W. Squyres, and R.E. Arvidson (2006), Mössbauer mineralogy of rock, soil, and dust at Gusev crater, Mars: Spirit's journey through weakly altered olivine basalt on the plains and pervasively altered basalt in the Columbia Hills, *Journal of Geophysical Research*, 111, E02S13, doi:10.1029/2005JE002584.
18. Schröder, C., B. Bailey, G. Klingelhöfer, H. Staudigel, Fe Mössbauer spectroscopy as a tool in astrobiology, *Planetary and Space Science*, in press.

Articles in submission

1. Rodionov, D.S., G. Klingelhöfer, B. Bernhardt, C. Schröder, M. Blumers, S. Kane, F. Trolard, G. Bourrie, and J.-M. Genin, Automated Mössbauer spectroscopy in the field and monitoring of fougérite, accepted for publication in *Hyperfine Interactions* (Conference Proceedings of the International Conference on the Applications of the Mössbauer Effect (ICAME), September 5-9, 2005, Montpellier, France).
2. Schröder, C., G. Klingelhöfer, B.E. Bailey, and H. Staudigel, Mössbauer Spectroscopy as a Tool in Astrobiology, accepted for publication in *Hyperfine Interactions* (Conference Proceedings of the International Conference on the Applications of the Mössbauer Effect (ICAME), September 5-9, 2005, Montpellier, France).
3. Clark, B.C., R.E. Arvidson, R. Gellert, R.V. Morris, D.W. Ming, L. Richter, S.W. Ruff, J.R. Michalski, W.H. Farrand, A. Yen, K.E. Herkenhoff, R. Li, S.W. Squyres, C. Schröder, G. Klingelhöfer, and J.F. Bell III, Evidence for Montmorillonite or its Compositional Equivalent in Columbia Hills, Mars, submitted to *Journal of Geophysical Research* (in review).
4. Squyres, S.W., R.E. Arvidson, D. Bollen, J.F. Bell III, J. Brückner, N.A. Cabrol, W.M. Calvin, M.H. Carr, P.R. Christensen, B.C. Clark, L. Crumpler, D.J. Des Marais, C. d'Uston, T. Economou, J. Farmer, W.H. Farrand, W. Folkner, R. Gellert, T.D. Glotch, M. Golombek, S. Gorevan, J.A. Grant, R. Greeley, J. Grotzinger, K.E. Herkenhoff,

- S. Hviid, J.R. Johnson, G. Klingelhöfer, A.H. Knoll, G. Landis, M. Lemmon, R. Li, M.B. Madsen, M.C. Malin, S.M. McLennan, H.Y. McSween, D.W. Ming, J. Moersch, R.V. Morris, T. Parker, J.W. Rice Jr., L. Richter, R. Rieder, C. Schröder, M. Sims, M. Smith, P. Smith, L.A. Soderblom, R. Sullivan, N.J. Tosca, H. Wänke, T. Wdowiak, M. Wolff, and A. Yen, Overview of the Opportunity Mars Exploration Rover Mission to Meridiani Planum: Eagle Crater to Purgatory Ripple, submitted to *Journal of Geophysical Research* (in review).
5. Morris, R.V., G. Klingelhöfer, C. Schröder, D.S. Rodionov, A. Yen, D.W. Ming, P.A. de Souza Jr., T. Wdowiak, I. Fleischer, R. Gellert, B. Bernhardt, U. Bonnes, B.A. Cohen, E.N. Evlanov, J. Foh, P. Gütlich, E. Kankeleit, T. McCoy, D.W. Mittlefehldt, F. Renz, M.E. Schmidt, B. Zubkov, S.W. Squyres, and R.E. Arvidson, Mössbauer mineralogy of rock, soil, and dust at Meridiani Planum, Mars: Opportunity's journey across sulfate-rich outcrop, basaltic sand and dust, and hematite lag deposits, submitted to *Journal of Geophysical Research*.
 6. Zipfel, J., C. Schröder, B.L. Jolliff, R. Anderson, J.F. Bell III, J. Brückner, J.A. Crisp, P.R. Christensen, B.C. Clark, P.A. de Souza Jr., G. Dreibus, C. d'Uston, T. Economou, R. Gellert, S.P. Gorevan, B.C. Hahn, K.E. Herkenhoff, G. Klingelhöfer, G.W. Lugmair, H.Y. McSween Jr., D.W. Ming, R.V. Morris, R. Rieder, D.S. Rodionov, S.W. Squyres, H. Wänke, M.B. Wyatt, and A.S. Yen, Bounce Rock at Meridiani Planum - a rock similar to Martian Meteorites, to be submitted.

Oral and poster presentations

1. Schröder, C., G. Klingelhöfer, and Wolfgang Tremel (2002), Weathering of iron-bearing minerals under extraterrestrial conditions, investigated by Mössbauer spectroscopy, XRD, and other methods, Fifth Seeheim Workshop on Mössbauer Spectroscopy, May 21-25, P-52, Seeheim, Germany (Poster).
2. Klingelhöfer, G., C. Schröder, and W. Tremel (2003), Weathering of iron-bearing minerals on Mars investigated by Mössbauer spectroscopy, 2nd Colloquium SPP 1115 "Mars and the Terrestrial Planets", Aug. 20-21, Münster, Germany (Oral).
3. Schröder, C., G. Klingelhöfer, and W. Tremel (2003), Weathering scenarios on Mars, First Workshop of the Subgroup "Atmosphere and Surface Processes" of the DFG Priority Programme "Mars and the Terrestrial Planets", 10-11 March 2003, Darmstadt, Germany (Oral).

4. Schröder, C., G. Klingelhöfer, and W. Tremel (2003), Weathering of Fe-bearing minerals in Martian conditions investigated by Mössbauer spectroscopy, 3rd European Mars Conference, 26-28 September, Bremen, Germany (Oral).
5. Schröder, C., G. Klingelhöfer, and W. Tremel (2003), Weathering of Fe-bearing minerals in Mars-like environments, investigated by Mössbauer spectroscopy, Student's Abstracts, European Student Participation Programme to the 54th International Astronautical Federation Congress, 29 September - 3 October 2003, Bremen, Germany, p. 32 (Poster).
6. Schröder, C., G. Klingelhöfer, R.V. Morris, B. Bernhardt, D. Rodionov, P.A. de Souza Jr., and F. Renz (2004), Mössbauer spectroscopy on Mars and its potential contribution in the search for extraterrestrial life, *Geochimica et Cosmochimica Acta*, 68(11), Supplement (14th Annual Goldschmidt Conference 5 to 11 June 2004, Copenhagen, Denmark), A808, abstract 6.7.32 (Oral).
7. Schröder, C., and G. Klingelhöfer (2004), Das Mössbauer-Spektrometer der NASA Mars Exploration Rover, 6. Internationale Wissenschaftliche Konferenz SATERRA, 11. -13. November 2004, Hochschule Mittweida (FH), Germany (Oral).
8. Schröder, C., G. Klingelhöfer, and the Athena Science Team (2005), Weathering of rocks in Gusev crater: Observational evidence from the MER Mössbauer spectrometer, Third Workshop of the Subgroup "Atmosphere and Surface Processes" of the DFG Priority Programme "Mars and the Terrestrial Planets", 10-11 March 2005, Darmstadt, Germany (Oral).
9. Schröder, C., G. Klingelhöfer, R.V. Morris, D.S. Rodionov, P.A. de Souza Jr., D.W. Ming, A.S. Yen, R. Gellert, J.F. Bell III, and the Athena Science Team (2005), Weathering of basaltic rocks from the Gusev plains up into the Columbia Hills from the perspective of the MER Mössbauer spectrometer, *Lunar and Planetary Science*, 36, 2309 (36th Lunar and Planetary Science Conference, Houston, Texas, USA) (Oral).
10. Schröder, C., G. Klingelhöfer, and J. Toporski (2005), Fe Mössbauer spectroscopy as a tool in astrobiology, *Geophysical Research Abstracts*, 7, Abstracts of the Contributions of the EGU General Assembly 2005, Vienna, Austria, 24-29 April, abstract EGU05-A-10288 (Poster).

11. Schröder, C., G. Klingelhöfer, P.A. de Souza Jr., D.W. Ming, R.V. Morris, D.S. Rodionov, and A.S. Yen (2005), Goethite identified by MER Spirit's Mössbauer spectrometer in the Columbia Hills, Gusev Crater, Mars, *Geophysical Research Abstracts*, 7, Abstracts of the Contributions of the EGU General Assembly 2005, Vienna, Austria, 24-29 April, abstract EGU05-A-10254 (Poster).
12. Klingelhöfer, G., C. Schröder, and W. Tremel (2005), Weathering of Iron-bearing Minerals on Mars, Kolloquium of the DFG Priority Programme "Mars and the Terrestrial Planets", August 29-30, 2005, Berlin, Germany (Oral).
13. Schröder, C., and G. Klingelhöfer (2005), Mössbauer Spectroscopy as a Tool in Astrobiology, International Conference on the Applications of the Mössbauer Effect (ICAME), September 5-9, 2005, Montpellier, France, abstract T4-P6 (Poster).
14. Schröder, C., G. Klingelhöfer, R.V. Morris, D.W. Ming, D. Rodionov, and P.A. de Souza Jr. (2005), Diversity of Rocks in the Columbia Hills, Gusev Crater, Mars, *Berichte der Deutschen Mineralogischen Gesellschaft*, Beiheft zum *European Journal of Mineralogy Vol. 17* (2005), No. 1, p. 123, DMG 2005 Tagung, Aachen 18.-21. September 2005 (Oral).
15. Schröder, C., D. Rodionov, I. Fleischer, M. Blumers, J. Girones, J.F. Sanchez, M. Hahn, and G. Klingelhöfer (2006), Neue Ergebnisse der MER Mössbauer-Spektrometer, *Verhandlungen der Deutschen Physikalischen Gesellschaft*, DPG Frühjahrstagung, Heidelberg, 13.-16.3. 2006, EP 21.1, p. 32 (Oral).
16. Schröder, C., G. Klingelhöfer, D.S. Rodionov, R.V. Morris, I. Fleischer, and A. Yen (2006), Mössbauer Spectroscopy with MIMOS II on Mars: A status report of data obtained so far, and how to work with them, Program and Abstracts, P-73, Sixth Seeheim Workshop on Mössbauer Spectroscopy, June 7-11, 2006, Seeheim, Germany (Poster).
17. Schröder, C., R. Gellert, B.L. Jolliff, G. Klingelhöfer, T.J. McCoy, R.V. Morris, D.S. Rodionov, P.A. de Souza Jr., A.S. Yen, J. Zipfel, and the Athena Science Team (2006), A stony meteorite discovered by the Mars Exploration Rover Opportunity on Meridiani Planum, Mars, *Meteoritics & Planetary Science*, 41, Supplement, A160, 69th Annual Meeting of the Meteoritical Society, 06-11 August 2006, Zürich, Switzerland, abstract 5285 (Oral).

18. Schröder, C., G. Klingelhöfer, R.V. Morris, D.S. Rodionov (2006), Correlations between primary and secondary Fe-bearing minerals identified in rocks in Gusev Crater by the MER Mössbauer spectrometer, European Planetary Science Congress 2006, 18.-22. September 2006 in Berlin, EPSC2006-A-00564 (Poster).

Selected abstracts, proceedings, etc.

1. De Souza Jr., P.A., G. Klingelhöfer, B. Bernhardt, C. Schröder, P. Gütlich, and T. Morimoto (2001), On-line and in-situ characterization of iron phases in particulate matter, Proceedings of the Air & Waste Management Association's 94th Annual Conference (Air & Waste Management Association's 94th Annual Conference and Exhibition, Orlando, FL, USA, June 24-28, 2001), (Air & Waste Management Association, Pittsburgh, PA, USA, 2001), 1-11.
2. Klingelhöfer, G., E. Evlanov, B. Zubkov, O. Prilutsky, V. Linkin, B. Bernhardt, D. Rodionov, and C. Schröder (2003), Miniaturized Mössbauer Spectrometer for an Analysis of the Iron Mineralogy on the Martian Surface, Russian Academy of Science, Space Research Institute, Pr-2081.
3. Rodionov, D., C. Schröder, G. Klingelhöfer, R.V. Morris, B. Bernhardt, P.A. de Souza Jr., A. Yen, F. Renz, T. Wdowiak, S.W. Squyres, and the Athena Science Team (2004), Mössbauer investigation of 'Bounce rock' at Meridiani Planum on Mars - indications for the first shergottite on Mars, *Meteoritics & Planetary Science*, 39, NR8, Supplement (67th Annual Meteoritical Society Meeting 2004), A91.
4. Bernhardt, B., D. Rodionov, G. Klingelhöfer, C. Schröder, S.N. Kane, F. Trolard, G. Bourrie, J.M. Genin, Automated Mössbauer Spectroscopy in the Field: Soil Monitoring and Bore Hole Investigations, ISIAE 2004, Program and Abstract Book, T8, P45, 4-8 October, 2004, Madrid, Spain.
5. Bailey, B.E., H. Staudigel, A. Templeton, B.M. Tebo, F. Ryerson, T. Plank, C. Schröder, and G. Klingelhöfer (2004), Biological Alteration of Basaltic Glass With Altered Composition and Oxidation States, *EOS Transactions AGU*, 85(47), Fall Meeting Supplement, Abstract B53C-1006.
6. Yen, A.S., D.W. Ming, R. Gellert, B.C. Clark, R.V. Morris, D. Rodionov, C. Schröder, G. Klingelhöfer, and the Athena Science Team

- (2005), Subsurface weathering of rocks and soils at Gusev Crater, *Lunar and Planetary Science*, *36*, 1571.
7. Morris, R.V., D.W. Ming, B.C. Clark, G. Klingelhöfer, R. Gellert, D. Rodionov, C. Schröder, P. de Souza, A. Yen, and the Athena Science Team (2005), Abundance and speciation of water and sulfate at Gusev Crater and Meridiani Planum, *Lunar and Planetary Science*, *36*, 2239.
 8. Schröder, C., G. Klingelhöfer, R.V. Morris, D.S. Rodionov, P.A. de Souza Jr., D.W. Ming, A.S. Yen, R. Gellert, J.F. Bell III, and the Athena Science Team (2005), Weathering of basaltic rocks from the Gusev plains up into the Columbia Hills from the perspective of the MER Mössbauer spectrometer, *Lunar and Planetary Science*, *36*, 2309.
 9. Des Marais, D.J., B.C. Clark, L.S. Crumpler, J.D. Farmer, J.P. Grotzinger, L.A. Haskin, A.H. Knoll, G.A. Landis, J. Moersch, C. Schröder, T. Wdowiak, A.S. Yen, S.W. Squyres, and the Athena Science Team (2005), Astrobiology and the basaltic plains in Gusev Crater, *Lunar and Planetary Science*, *36*, 2353.
 10. Rodionov, D.S., G. Klingelhoef, D.W. Ming, R.V. Morris, C. Schröder, P.A. de Souza, S.W. Squyres, and A.S. Yen (2005), An iron-nickel meteorite on Meridiani Planum: Observations by MER Opportunity's Moessbauer spectrometer, *Geophysical Research Abstracts*, *7*, Abstracts of the Contributions of the EGU General Assembly 2005, Vienna, Austria, 24-29 April 2005, abstract EGU05-A-10242.
 11. Yen, A.S., R. Gellert, J. Zipfel, T. Economou, S. McLennan, C. Schröder, and the Athena Science Team, Meteoritic contributions to the surface of Mars, *Geophysical Research Abstracts*, *7*, Abstracts of the Contributions of the EGU General Assembly 2005, Vienna, Austria, 24-29 April 2005, abstract EGU05-A-09861.
 12. Yen, A.S., J. Grotzinger, R. Gellert, B.C. Clark, S.M. McLennan, R.V. Morris, C. Schröder, G. Klingelhöfer, K.E. Herkenhoff, J.R. Johnson, and the Athena Science Team (2006), Evidence for Halite at Meridiani Planum, *Lunar and Planetary Science*, *37*, 2128.
 13. Jolliff, B.L., W.H. Farrand, J.R. Johnson, C. Schröder, C.M. Weitz, and the Athena Science Team (2006), Origin of Rocks and Cobbles on the Meridiani Plains as Seen by Opportunity, *Lunar and Planetary Science*, *37*, 2401.

14. Morris, R.V., G.A. McKay, D.W. Ming, G. Klingelhöfer, C. Schröder, D. Rodionov, and A. Yen (2006), Magnetite in Martian meteorite MIL 03346 and Gusev Adirondack Class basalt: Mössbauer evidence for variability in the oxidation state of Adirondack lavas, *Lunar and Planetary Science*, 37, 1594.
15. Schröder, C., R. Gellert, B.L. Jolliff, G. Klingelhöfer, T.J. McCoy, R.V. Morris, D.S. Rodionov, P.A. de Souza Jr., A.S. Yen, J. Zipfel, and the Athena Science Team (2006), A stony meteorite discovered by the Mars Exploration Rover Opportunity on Meridiani Planum, Mars, *Meteoritics & Planetary Science*, 41, Supplement, A160.
16. Schröder, C., G. Klingelhöfer, R.V. Morris, D.S. Rodionov (2006), Correlations between primary and secondary Fe-bearing minerals identified in rocks in Gusev Crater by the MER Mössbauer spectrometer, European Planetary Science Congress 2006, 18.-22. September 2006 in Berlin, EPSC2006-A-00564.

Education and public outreach

1. Online slide show "El Capitan and the Sweet Spots in Eagle Crater", available online at http://marsrovers.jpl.nasa.gov/spotlight/opportunity/opp_200404a_Sweet_Spot.html (last accessed: June 13, 2006).
2. Schröder, C. (2004), MER Anekdoten, Newsletter der Mars Society Deutschland, 12, April 2004, available online at <http://www.marssociety.de> (Downloads - Newsletter).

Awards

1. Selected participant for the "**5th Student Participation Programme for the 54th IAF Congress in Bremen**" of ESA, 29 September to 3 October 2003.
2. **NASA Group Achievement Award** (2004) for the Mars Exploration Rover Science/Science Support Team, "for outstanding efforts in the development of the science payload; support for operations and software testing; and characterization of the Martian environment, in preparation for MER science operations".
3. **NASA Group Achievement Award** (2004) for the Mars Exploration Rover Science Operations Team, "for outstanding planning and implementation of science operations for the Mars Exploration Rover Project, leading to data return that exceeded prelaunch expectations".

4. **NASA Group Achievement Award** (2005) for the Mars Exploration Rover First Extended Mission Team, "for excellence in operating the Mars Exploration Rovers during their first mission extension, resulting in an outstanding quantity of science data return, even with reduced staffing".
5. **NASA Group Achievement Award** (2005) for the Mars Exploration Rover Second Extended Mission Team, "for excellence in operating the Mars Exploration Rovers during their second mission extension, resulting in an outstanding level of science return with an exceptional operational efficiency".

Bibliography

Adams, J.B. (1968), Lunar and Martian surfaces: Petrologic significance of absorption bands in the near-infrared, *Science*, *159*, 1453-1455.

Advocat, T., J.L. Crovisier, E. Vernaz, G. Ehret, and H. Charpentier (1991), Hydrolysis of R7T7 nuclear waste glass in dilute media: Mechanisms and rate as a function of pH, *Mat. Res. Soc. Symp. Proc.*, *212*, 57-64.

Agresti, D.G., T.J. Wdowiak, and M.L. Wade (1994), Mössbauer spectroscopy as a tool in the search for evidence of past life on Mars, *Hyperfine Interactions*, *91*, 523-528.

Allen, C.C., L.W. Probst, B.E. Flood, T.G. Longazo, R.T. Schelble, and F. Westall (2004) Meridiani Planum hematite deposit and the search for evidence of life on Mars - iron mineralization of microorganisms in rock varnish, *Icarus*, *171*, 20-30.

Allwood, A.C., M.R. Walter, M.J. Van Kranendonk, and B.S. Kamber (2005a), 3.43 Ga Stromatolites, Rocky Shorelines and a Carbonate Platform: Strelley Pool Chert, Pilbara Craton, Western Australia, NASA Astrobiology Institute Biennial Meeting: *Astrobiology*, *5*(2), 184.

Allwood, A.C., M.R. Walter, and M.J. Van Kranendonk (2005b), Stromatolite facies of the 3.43 Ga Strelley Pool Chert: Pilbara Craton, Western Australia, NASA Astrobiology Institute Biennial Meeting: *Astrobiology*, *5*(2), 184.

Aramu, F., and V. Maxia (1970), Shift and broadening of Mössbauer peaks by lack of collimation, *Nuclear Instruments and Methods*, *80*, 35-39.

Arp, G. (1995), Lacustrine bioherms, spring mounds, and marginal carbonates of the Ries-impact-crater (Miocene, southern Germany),

Facies, 33, 35-90.

Arvidson, R.E., R.C. Anderson, P. Bartlett, J.F. Bell III, D. Blaney, P.R. Christensen, P. Chu, L. Crumpler, K. Davis, B.L. Ehlmann, R. Fergason, M.P. Golombek, S. Gorevan, J.A. Grant, R. Greeley, E.A. Guinness, A.F.C. Haldemann, K. Herkenhoff, J. Johnson, G. Landis, R. Li, R. Lindemann, H. McSween, D.W. Ming, T. Myrick, L. Richter, F.P. Seelos IV, S.W. Squyres, R.J. Sullivan, A. Wang, and J. Wilson (2004), Localization and Physical Properties Experiments Conducted by Spirit at Gusev Crater, *Science*, 305, 821-824.

Arvidson, R.E., S.W. Squyres, R.C. Anderson, J.F. Bell III, D. Blaney, J. Brückner, N.A. Cabrol, W.M. Calvin, M.H. Carr, P.R. Christensen, B.C. Clark, L. Crumpler, D.J. Des Marais, P.A. de Souza Jr., C. d'Uston, T. Economou, J. Farmer, W.H. Farrand, W. Folkner, M. Golombek, S. Gorevan, J.A. Grant, R. Greeley, J. Grotzinger, E. Guinness, B.C. Hahn, L. Haskin, K.E. Herkenhoff, J.A. Hurowitz, S. Hviid, J.R. Johnson, G. Klingelhöfer, A.H. Knoll, G. Landis, C. Leff, M. Lemmon, R. Li, M.B. Madsen, M.C. Malin, S.M. McLennan, H.Y. McSween, D.W. Ming, J. Moersch, R.V. Morris, T. Parker, J.W. Rice Jr., L. Richter, R. Rieder, D.S. Rodionov, C. Schröder, M. Sims, M. Smith, P. Smith, L.A. Soderblom, R. Sullivan, S.D. Thompson, N.J. Tosca, A. Wang, H. Wänke, J. Ward, T. Wdowiak, M. Wolff, and A. Yen (2006), Overview of the Spirit Mars Exploration Rover Mission to Gusev Crater: Landing site to Backstay Rock in the Columbia Hills, *Journal of Geophysical Research*, 111, E02S01, doi:10.1029/2005JE002499.

Bach, W., and K.J. Edwards (2003), Iron and Sulfide oxidation within the basaltic ocean crust: Implications for chemolithoautotrophic microbial biomass production, *Geochimica et Cosmochimica Acta*, 67(20), 3871-3887.

Bailey, B.E., H. Staudigel, A. Templeton, B.M. Tebo, F. Ryerson, T. Plank, C. Schröder, and G. Klingelhöfer (2004), Biological Alteration of Basaltic Glass With Altered Composition and Oxidation States, *EOS Transactions, AGU*, 85(47), Fall Meeting Supplement, Abstract B53C-1006.

Baker, L.L., D.J. Agenbroad, and S.A. Wood (2000), Experimental hydrothermal alteration of a Martian analog basalt: Implications for Martian meteorites, *Meteoritics and Planetary Science*, 35, 31-38.

- Bancroft, G.M. (1973), *Mössbauer Spectroscopy - An Introduction for Inorganic Chemists and Geochemists*, McGraw Hill, London, UK.
- Bandfield, J.L. (2002), Global mineral distributions on Mars, *Journal of Geophysical Research*, *107*(E6), 5042, doi:10.1029/2001JE001510.
- Banin, A. (2005), The Enigma of the Martian Soil, *Science*, *309*, 888-890, doi:10.1126/science.1112794.
- Banin, A., B.C. Clark, and H. Wänke (1992), Surface Chemistry and Mineralogy, in *Mars*, edited by H.H. Kieffer, B.M. Jakosky, C.W. Snyder, and M.S. Matthews, The University of Arizona Press, Tucson, pp. 594-625.
- Banin, A., F.X. Han, I. Kan, and A. Cicelsky (1997), Acidic volatiles and the Mars soil, *Journal of Geophysical Research*, *102*, 13341-13356.
- Battley, E.H. (1998), The development of direct and indirect methods for the study of the thermodynamics of microbial growth, *Thermochimica Acta*, *309*, 169-171.
- Bell, J. F., III, S.W. Squyres, K.E. Herkenhoff, J.N. Maki, H.M. Arneson, D. Brown, S.A. Collins, A. Dingizian, S.T. Elliot, E.C. Hagerott, A.G. Hayes, M.J. Johnson, J.R. Johnson, J. Joseph, K. Kinch, M.T. Lemmon, R.V. Morris, L. Scherr, M. Schwochert, M.K. Shepard, G.H. Smith, J.N. Sohl-Dickstein, R.J. Sullivan, W.T. Sullivan, and M. Wadsworth (2003), Mars Exploration Rover Athena Panoramic Camera (Pan-cam) investigation, *Journal of Geophysical Research*, *108*(E11), 8063, doi:10.1029/2003JE002070.
- Bernhardt, B. (1997), Güteuntersuchungen am Mößbauspektrometer MIMOS, Diplomarbeit, Technische Universität Darmstadt, Darmstadt, Germany.
- Bibring, J.-P., Y. Langevin, A. Gendrin, B. Gondet, F. Poulet, M. Berthé, A. Soufflot, R. Arvidson, N. Mangold, J. Mustard, P. Drossart, and the OMEGA team (2005), Mars Surface Diversity as Revealed by the OMEGA/Mars Express Observations, *Science*, *307*, 1576-1581, doi:10.1126/science.1108806.
- Bishop, J.L., and E. Murad (1996), Schwertmannite on Mars? Spectroscopic analyses of schwertmannite, its relationship to other ferric minerals,

and its possible presence in the surface material on Mars, in *Mineral Spectroscopy: A Tribute to Roger G. Burns*, edited by M. D. Dyar, C. McCammon, and M. W. Schaefer, Spec. Publ. Geochem. Soc., 5, 337-358.

Blackhurst, R.L., M.J. Genge, A.T. Kearsley, and M.M. Grady (2005), Cryptoendolithic alteration of Antarctic sandstones: Pioneers or opportunists?, *Journal of Geophysical Research*, 110, E12S24, doi:10.1029/2005JE002463.

Bland, W., and D. Rolls (1998), *Weathering: An introduction to the scientific principles*, Arnold, London, UK.

Bogard, D.D., and P. Johnson (1983), Martian gases in an Antarctic meteorite?, *Science*, 221, 651-654.

Borg, L.E., L.E. Nyquist, L.A. Taylor, H. Wiesmann, and C.-Y. Shih (1997), Constraints on Martian differentiation processes from Rb-Sr and Sm-Nd isotopic analyses of the basaltic shergottite QUE94201, *Geochimica et Cosmochimica Acta*, 61, 4915-4931.

Bowen, N.L. (1928), *The Evolution of the Igneous Rocks*, Princeton University Press, Princeton, New Jersey, USA.

Boynton, W.V., W.C. Feldman, S.W. Squyres, T.H. Prettyman, J. Brückner, L.G. Evans, R.C. Reedy, R. Starr, J.R. Arnold, D.M. Drake, P.A.J. Englert, A.E. Metzger, I. Mitrofanov, J.I. Trombka, C. d'Uston, H. Wänke, O. Gasnault, D.K. Hamara, D.M. Janes, R.L. Marcialis, S. Maurice, I. Mikheeva, G.J. Taylor, R. Tokar, and C. Shinohara (2002), Distribution of Hydrogen in the Near Surface of Mars: Evidence for Subsurface Ice Deposits, *Science*, 297, 81-85, doi:10.1126/science.1073722.

Brack, A., G. Horneck, and D. Wynn-Williams (2001), Exo/Astrobiology in Europe, *Origins of Life and Evolution of the Biosphere*, 31, 459-480.

Bridges, J.C., D.C. Catling, J.M. Saxton, T.D. Swindle, I.C. Lyon, and M.M. Grady (2001), Alteration assemblages in Martian meteorites: Implications for near-surface processes, *Space Science Reviews*, 96, 365-392.

Burns, R.G. (1991), Does Lafayette = Nakhla? Not necessarily so, based on 4.2 K Mössbauer spectra of all the SNC meteorites, *Lunar and Planetary Science*, 22, 157-158.

Burns, R.G. (1993a), Mössbauer Spectral Characterization of Iron in Planetary Surface Materials, in *Remote Geochemical Analysis: Elemental and Mineralogical Composition*, edited by C.M. Pieters and P.A.J. Englert, pp. 539-556, Cambridge University Press, Cambridge, UK.

Burns, R.G. (1993b), Rates and mechanisms of chemical weathering of ferromagnesian silicate minerals on Mars, *Geochimica et Cosmochimica Acta*, *57*, 4555-4574.

Burns, R.G. (1994), Mineral Mössbauer spectroscopy: Correlations between chemical shift and quadrupole splitting parameters, *Hyperfine Interactions*, *91*, 739-745.

Burns, R.G., and S.L. Martinez (1990), Mossbauer spectra of olivine-rich weathered achondrites: II. Brachina, Chassigny, ALHA 77005, and Nakhla, *Lunar and Planetary Science*, *21*, 91-92.

Burns, R. G., and T. C. Solberg (1990), 57Fe-bearing oxide, silicate, and aluminosilicate minerals: Crystal structure trends in Mössbauer spectra, in *Spectroscopic Characterization of Minerals and Their Surfaces*, ACS Symp. Ser., vol. 415, edited by L. M. Coyne, S. W. S. McKeever, and D. F. Blake, pp. 262-283, Am. Chem. Soc., Washington, D. C.

Byerly G.R., M.M. Walsh, and D.L. Lowe (1986), Stromatolites from the 3300-3500 Myr Swaziland Supergroup, Barberton Mountain Land, South Africa, *Nature*, *319*, 489-491.

Cabrol, N.A., E.A. Grin, M.H. Carr, B. Sutter, J.M. Moore, J.D. Farmer, R. Greeley, R.O. Kuzmin, D.J. Des Marais, M.G. Kramer, H. Newsom, C. Barber, I. Thorsos, K.L. Tanaka, N.G. Barlow, D.A. Fike, M.L. Urquhart, B. Grigsby, F.D. Grant, and O. de Goursac (2003), Exploring Gusev Crater with Spirit: Review of science objectives and testable hypotheses, *Journal of Geophysical Research*, *108*(E12), 8076, doi:10.1029/2003JE002026.

Cabrol, N.A., J.D. Farmer, E.A. Grin, L. Richter, L. Soderblom, R. Li, K. Herkenhoff, G.A. Landis, and R.E. Arvidson (2006), Aqueous processes at Gusev crater inferred from physical properties of rocks and soils along the Spirit traverse, *Journal of Geophysical Research*, *111*, E02S20, doi:10.1029/2005JE002490.

Carr, M.H. (1996), *Water on Mars*, Oxford University Press, New York,

USA.

Carroll, D. (1970), *Rock Weathering*, Monographs in Geoscience, edited by R.W. Fairbridge, Plenum Press, New York, USA.

Catling, D.C. (2004), On Earth, as it is on Mars?, *Nature*, *429*, 707-708.

Chapelle, F.H., K. O'Neill, P.M. Bradley, B.A. Methé, S.A. Ciuffo, L.L. Knobel, and D.R. Lovley (2002), A hydrogen-based subsurface microbial community dominated by methanogens, *Nature*, *415*, 312-315.

Christensen, P.R., J.L. Bandfield, R.N. Clark, K.S. Edgett, V.E. Hamilton, T. Hoefen, H.H. Kieffer, R.O. Kuzmin, M.D. Lane, M.C. Malin, R.V. Morris, J.C. Pearl, R. Pearson, T.L. Roush, S.W. Ruff, and M.D. Smith (2000), Detection of crystalline hematite mineralization on Mars by the Thermal Emission Spectrometer: Evidence for near-surface water, *Journal of Geophysical Research*, *105*, 9623-9642.

Christensen, P.R., R.V. Morris, M.D. Lane, J.L. Bandfield, and M.C. Malin (2001), Global mapping of Martian hematite deposits: Remnants of waterdriven processes on early Mars, *Journal of Geophysical Research*, *106*, 23873-23886.

Christensen, P.R., G.L. Mehall, S.H. Silverman, S. Anwar, G. Cannon, N. Gorelick, R. Kheen, T. Tourville, D. Bates, S. Ferry, T. Fortuna, J. Jeffryes, W. O'Donnell, R. Peralta, T. Wolverton, D. Blaney, R. Denise, J. Rademacher, R.V. Morris, and S.W. Squyres (2003), Miniature Thermal Emission Spectrometer for the Mars Exploration Rovers, *Journal of Geophysical Research*, *108*(E12), 8064, doi:10.1029/2003JE002117.

Christensen, P.R., M.B. Wyatt, T.D. Glotch, A.D. Rogers, S. Anwar, R.E. Arvidson, J.L. Bandfield, D.L. Blaney, C. Budney, W.M. Calvin, A. Fallacaro, R.L. Fergason, N. Gorelick, T.G. Graff, V.E. Hamilton, A.G. Hayes, J.R. Johnson, A.T. Knudson, H.Y. McSween Jr., G.L. Mehall, L.K. Mehall, J.E. Moersch, R.V. Morris, M.D. Smith, S.W. Squyres, S.W. Ruff, and M.J. Wolff (2004), Mineralogy et Meridiani Planum from the Mini-TES Experiment on the Opportunity Rover, *Science*, *306*, 1733-1739.

Clark, B.C., A.K. Baird, H.J. Rose, P. Toulmin III, K. Keil, A.J. Castro, W.C. Kelliher, C.D. Rowe, and P.H. Evans (1976), Inorganic analysis of Martian surface samples at the Viking landing sites, *Science*, *194*,

1283-1288.

Clark, B.C., R.V. Morris, S.M. McLennan, R. Gellert, B. Jolliff, A.H. Knoll, S.W. Squyres, T.K. Lowenstein, D.W. Ming, N.J. Tosca, A. Yen, P.R. Christensen, S. Gorevan, J. Brückner, W. Calvin, G. Dreibus, W. Farrand, G. Klingelhöfer, H. Wänke, J. Zipfel, J.F. Bell III, J. Grotzinger, H.Y. McSween, and R. Rieder (2005), Chemistry and mineralogy of outcrops at Meridiani Planum, *Earth and Planetary Science Letters*, *240*, 73-94, doi:10.1016/j.epsl.2005.09.040.

Cockell, C.S., Lee, P., Osinski, G., Horneck, G. and Broady, P. (2002), Impact-induced microbial endolithic habitats, *Meteoritics and Planetary Science*, *37*, 1287-1298.

Colman, S.M., and D.P. Dethier (eds.) (1986), *Rates of Chemical Weathering of Rocks and Minerals*, Academic Press, New York, USA.

Cornell, R.M., and U. Schwertmann (1996), *The Iron Oxides*, VCH Verlagsgesellschaft mbH, Weinheim, Germany.

Correns, C.W. (1968), *Einführung in die Mineralogie*, 2nd ed., Springer-Verlag, Berlin, Germany.

Daughney, C.J., J.P. Rioux, D. Fortin, and R. Pichler (2004), Laboratory investigation of the role of bacteria in the weathering of basalt near deep sea hydrothermal vents, *Geomicrobiology Journal*, *21*, 21-31.

De Grave, E., and A. Van Alboom (1991), Evaluation of Ferrous and Ferric Mössbauer Fractions, *Physics and Chemistry of Minerals*, *18*, 337-342.

De Ronde, C.E.J., M.J. de Wit, and E.T.C. Spooner (1994), Early Archaean (> 3.2 Ga) Fe-oxide-rich, hydrothermal discharge vents in the Barberton greenstone belt, South Africa, *Geological Society of America Bulletin*, *196*, 86-104.

Des Marais, D.J., and M.R. Walter (1999), Astrobiology: Exploring the Origins, Evolution, and Distribution of Life in the Universe, *Annual Review of Ecology and Systematics*, *30*, 397-420.

Des Marais, D.J., B.C. Clark, L.S. Crumpler, J.D. Farmer, J.P. Grotzinger, L.A. Haskin, A.H. Knoll, G.A. Landis, J. Moersch, C. Schröder,

T. Wdowiak, A.S. Yen, S.W. Squyres, and the Athena Science Team (2005), Astrobiology and the basaltic plains in Gusev Crater, *Lunar and Planetary Science*, 36, 2353.

De Souza Jr., P.A. (2004), Extraterrestrial and Terrestrial Outdoor Applications of Mössbauer Spectroscopy, dissertation, Johannes Gutenberg-Universität, Mainz, Germany.

De Souza Jr., P.A., G. Klingelhöfer, B. Bernhardt, C. Schröder, P. Gütlich, T. Morimoto (2001), On-line and in-situ characterization of iron phases in particulate matter, in Proceedings of the Air & Waste Management Association's 94th Annual Conference (Air & Waste Management Association's 94th Annual Conference and Exhibition, Orlando, Florida, USA, June 24-28, 2001), Air & Waste Management Association, Pittsburgh, PA, USA, pp. 1-11.

De Souza Jr., P.A., M.C.S. de Macedo, R.S. de Queiroz, G. Klingelhöfer (2002), Atmospheric Corrosion Investigation in Industrial, Marine and Rural Environments in South-East Brazil, *Hyperfine Interactions*, 139/140, 183-191.

De Souza Jr., P.A., B. Bernhardt, G. Klingelhöfer, P. Gütlich (2003), Surface Analysis in Archaeology Using the Miniaturized Mössbauer Spectrometer MIMOS II, *Hyperfine Interactions*, 151/152, 125-130.

De Wit, M.J., R. Hart, A. Martin, and P. Abbott (1982), Archaean abiogenic and probable biogenic structures associated with mineralised hydrothermal vent systems and regional metasomatism with implications for greenstone belt studies, *Economic Geology*, 77, 1783-1802.

Dorn, C. (1995), Aufbau und Test eines PIN-Dioden-Detektors für Mößbauerspektroskopie, Diplomarbeit, Technische Universität Darmstadt, Darmstadt, Germany.

Dreibus, G., and H. Wänke (1985), Mars, a volatile-rich planet, *Meteoritics*, 20, 367-381.

Drever, J.I. (Ed.) (2003), *Surface and Ground Water, Weathering, and Soils*, vol. 5, Treatise on Geochemistry, edited by H.D. Holland and K.K. Turekian, Elsevier-Pergamon, Oxford, UK.

Dyar, M.D. (2003), Ferric iron in SNC meteorites as determined by

Mössbauer spectroscopy: Implications for Martian landers and Martian oxygen fugacity, *Meteoritics & Planetary Science*, *38*(12), 1733-1752.

Dyar, M.D., A.V. McGuire, and R.D. Zeigler (1989), Redox equilibria and crystal chemistry of coexisting minerals from spinel lherzolite mantle xenoliths, *American Mineralogist*, *74*, 969-980.

Dyar, M.D., A.H. Treiman, C.M. Pieters, T. Hiroi, M.D. Lane, and V. O'Connor (2005), MIL03346, the most oxidized Martian meteorite: A first look at spectroscopy, petrography, and mineral chemistry, *Journal of Geophysical Research*, *110*, E09005, doi:10.1029/2005JE002426.

Edwards, H.G.M, M.C. Russell, and D.D. Wynn-Williams (1997), Fourier transform Raman spectroscopic and scanning electron microscopic study of cryptoendolithic lichens from Antarctica, *Journal of Raman Spectroscopy*, *30*, 685-690.

Edwards, H.G.M., D.D. Wynn-Williams, and S.E. Jorge Villar (2004), Biological modification of haematite in Antarctic cryptoendolithic communities, *Journal of Raman Spectroscopy*, *35*, 470-474.

Eeckhout, S.G., and E. De Grave (2003), Evaluation of ferrous and ferric Mössbauer fractions. Part II, *Physics and Chemistry of Minerals*, *30*, 142-146.

Eggleton, R.A. (1986), The Relation between Crystal Structure and Silicate Weathering Rates, in *Rates of chemical weathering of rocks and minerals*, edited by S.M. Colman and D.P. Dethier, Academic Press, London, pp. 21-40.

Feder, F., F. Trolard, G. Klingelhöfer, G. Bourrié (2005), In situ Mössbauer spectroscopy: Evidence for green rust (fougerite) in a gleysol and its mineralogical transformations with time and depth, *Geochimica et Cosmochimica Acta*, *69*(18), 4463-4483, doi:10.1016/j.gca.2005.03.042.

Fegley, B., K. Lodders, A.H. Treiman, and G. Klingelhöfer (1995), The Rate of Pyrite Decomposition on the Surface of Venus, *Icarus*, *115*, 159-180.

Fernández-Remolar, D., J. Gómez-Elvira, F. Gómez, E. Sebastian, J. Martíin, J.A. Manfredi, J. Torres, C. González Kesler, and R. Amils (2004), The Tinto River, an extreme acidic environment under control of

iron, as an analog of the Terra Meridiani hematite site of Mars, *Planetary and Space Science*, 52, 239-248, doi:10.1016/j.pss.2003.08.027.

Fernández-Remolar, D., R.V. Morris, J.E. Gruener, R. Amils, A.H. Knoll (2005), The Río Tinto Basin, Spain: Mineralogy, sedimentary geobiology, and implications for interpretation of outcrop rocks at Meridiani Planum, Mars, *Earth and Planetary Science Letters*, 240, 149-167, doi:10.1016/j.epsl.2005.09.043.

Fisk, M.R., S.J. Giovannoni, and I.H. Thorseth (1998), Alteration of Oceanic Volcanic Glass: Textural Evidence of Microbial Activity, *Science*, 281, 978-980.

Formisano, V., S. Atreya, T. Encrenaz, N. Ignatiev, and M. Giuranna (2004), Detection of Methane in the Atmosphere of Mars, *Science*, 306, 1758-1761.

Friedmann, E.I. (1982), Endolithic microorganisms in the Antarctic cold desert, *Science*, 215, 1045-1053.

Friedmann, E.I., M.S. Hua, and R. Ocampo-Friedmann (1988), Cryptoendolithic lichen and cyanobacterial communities of the Ross Desert, Antarctica, *Polarforschung*, 58, 251-259.

Fritz, R., and D. Schulze (1968), Neues Verfahren zur Geschwindigkeits-eichung von Mössbauerspektrometern, *Nuclear Instruments and Methods*, 62, 317-320.

Furnes, H., and H. Staudigel (1999), Biological mediation in ocean crust alteration: how deep is the deep biosphere?, *Earth and Planetary Science Letters*, 166, 97-103.

Furnes, H., I.H. Thorseth, O. Tumyr, T. Torsvik, and M.R. Fisk (1996), Microbial activity in the alteration of glass pillow lavas from Hole 896A, in *Proc. Ocean Drilling Prog., Sci. Results*, edited by J.C. Alt, H. Kinoshita, L.B. Stokking, and P.J. Michael, College Station, Texas, pp. 191-206.

Furnes, H., H. Staudigel, I.H. Thorseth, T. Torsvik, K. Muehlenbachs, and O. Tumyr (2001), Bioalteration of basaltic glass in the oceanic crust, *Geochemistry, Geophysics, Geosystems*, 2, Paperno. 2000GC000150.

Garrels, R.M., and C.L. Christ (1965), *Solutions, Minerals, and Equilibria*,

Harper and Row, New York, USA.

Gee, H, C. Surridge, and L. Allen (eds.) (2001), Nature Insight: Astrobiology, *Nature*, *409*, 1079-1122.

Gellert, R., R. Rieder, R.C. Anderson, J. Brückner, B.C. Clark, G. Deibus, T. Economou, G. Klingelhöfer, G.W. Lugmair, D.W. Ming, S.W. Squyres, C. d'Uston, H. Wänke, A. Yen, and J. Zipfel (2004), Chemistry of Rocks and Soils in Gusev Crater from the Alpha Particle X-ray Spectrometer, *Science*, *305*, 829-832.

Gellert, R., R. Rieder, J. Brückner, B.C. Clark, G. Deibus, G. Klingelhöfer, G.W. Lugmair, D.W. Ming, H. Wänke, A. Yen, J. Zipfel, and S.W. Squyres (2006), Alpha Particle X-Ray Spectrometer (APXS): Results from Gusev crater and calibration report, *Journal of Geophysical Research*, *111*, E02S05, doi:10.1029/2005JE002555.

Gilmour, I., and M.A. Sephton (eds.) (2003), *An Introduction to Astrobiology*, Cambridge University Press, Cambridge, UK.

Giovannoni, S.J., M.R. Fisk, T.D. Mullins, and H. Furnes (1996), Genetic evidence for endolithic microbial life colonizing basaltic glass/seawater interfaces, in *Proc. Ocean Drilling Prog., Sci. Results*, edited by J.J. Alt, H. Kinoshita, L.B. Stokking, and P. Michael, College Station, Texas, pp. 207-214.

Glazner, A.F. (1988), Stratigraphy, structure and potassic alteration of Miocene volcanic rocks in the Sleeping Beauty area, central Mojave Desert, California, *Geological Society of America Bulletin*, *100*, 424-435.

Goetz, W., P. Bertelsen, C.S. Binou, H.P. Gunnlaugsson, S.F. Hviid, K.M. Kinch, D.E. Madsen, M.B. Madsen, M. Olsen, R. Gellert, G. Klingelhöfer, D.W. Ming, R.V. Morris, R. Rieder, D.S. Rodionov, P.A. de Souza Jr., C. Schröder, S.W. Squyres, T. Wdowiak, and A. Yen (2005), Indication of drier periods on Mars from the chemistry and mineralogy of atmospheric dust, *Nature*, *436*, 62-65, doi:10.1038/nature03807.

Golden, D.C., D.W. Ming, R.V. Morris, and S.A. Mertzman (2005), Laboratory-simulated acid-sulfate weathering of basaltic materials: Implications for formation of sulfates at Meridiani Planum and Gusev crater, Mars, *Journal of Geophysical Research*, *110*, E12S07, doi:10.1029/2005JE002451.

Goldich, S.S. (1938), A study of rock weathering, *Journal of Geology*, *46*, 17-58.

Golombek, M.P., L.S. Crumpler, J.A. Grant, R. Greeley, N.A. Cabrol, T.J. Parker, J.W. Rice Jr., J.G. Ward, R.E. Arvidson, J.E. Moersch, R.L. Fergason, P.R. Christensen, A. Castaño, R. Castaño, A.F.C. Haldemann, R. Li, J.F. Bell III, and S.W. Squyres (2006), Geology of the Gusev cratered plains from the Spirit rover traverse, *Journal of Geophysical Research*, *111*, E02S07, doi:10.1029/2005JE002503.

Gonser, U. (ed.) (1975), *Mössbauer Spectroscopy*, Topics in Applied Physics, vol. 5, Springer-Verlag, New York - Heidelberg - Berlin.

González-Toril, E., E. Llobet-Brossa, E.O. Casamayor, R. Amann, and R. Amils (2003), Microbial Ecology of an Extreme Acidic Environment, the Tinto River, *Applied and Environmental Microbiology*, *69*(8), 4853-4865.

Gooding, J.L. (1978), Chemical Weathering on Mars: Thermodynamic Stabilities of Primary Minerals (and Their Alteration Products) from Mafic Igneous Rocks, *Icarus*, *33*, 483-513.

Gooding, J.L., R.E. Arvidson and M.Y. Zolotov (1992), Physical and Chemical Weathering, in *Mars*, edited by H.H. Kieffer, B.M. Jakosky, C.W. Snyder, M.S. Matthews, pp. 626-651, University of Arizona Press, Tucson, Arizona.

Gorevan, S.P., T. Myrick, K. Davis, J.J. Chau, P. Bartlett, S. Mukherjee, R. Anderson, S.W. Squyres, R.E. Arvidson, M.B. Madsen, P. Bertelsen, W. Goetz, C.S. Binou, and L. Richter (2003), Rock Abrasion Tool Mars Exploration Rover Mission, *Journal of Geophysical Research*, *108*(E12), 8068, doi:10.1029/2003JE002061.

Greenwood, N.N., and T.C. Gibb (1971), *Mössbauer Spectroscopy*, Chapman and Hall, New York, USA.

Gütlich, P., R. Link, and A. Trautwein (1978), *Mössbauer Spectroscopy and Transition Metal Chemistry*, Inorganic Chemistry Concepts, vol. 3, Springer-Verlag, Berlin - Heidelberg - New York.

Hartmann, W.K. (2003), *A Traveller's Guide to Mars - The Mysterious Landscapes of the Red Planet*, Workman Publishing, New York, USA.

Harvey, R.P., and H.Y. McSween Jr. (1991), New observations of Nakhla, Governador Valadares and Lafayette, and their bearing on petrogenesis, *Lunar and Planetary Science*, *22*, 527-528.

Haskin, L.A., A. Wang, B.L. Jolliff, H.Y. McSween, B.C. Clark, D.J. Des Marais, S.M. McLennan, N.J. Tosca, J.A. Hurowitz, J.D. Farmer, A. Yen, S.W. Squyres, R.E. Arvidson, G. Klingelhöfer, C. Schröder, P.A. de Souza Jr., D.W. Ming, R. Gellert, J. Zipfel, J. Brückner, J.F. Bell III, K. Herkenhoff, P.R. Christensen, S. Ruff, D. Blaney, S. Gorevan, N.A. Cabrol, L. Crumpler, J. Grant, and L. Soderblom (2005), Water alteration of rocks and soils on Mars at the Spirit rover site in Gusev crater, *Nature*, *436*, 66-69, doi:10.1038/nature03640.

Hawthorne, F.C. (1988), Mössbauer Spectroscopy, in *Spectroscopic Methods in Mineralogy and Geology*, Reviews in Mineralogy, vol. 18, edited by F.C. Hawthorne, pp. 255-340, Mineralogical Society of America, Washington, D.C., USA.

Heijnen, J.J., and J.P. Van Dijken (1992), In search of a thermodynamic description of biomass yields for the chemotrophic growth of microorganisms, *Biotechnology and Bioengineering*, *39*, 833-858.

Held, P. (1993), PIN-Photodioden als Detektoren für das Mößbauerspektrometer MIMOS zur Untersuchung der Marsoberfläche, Diplomarbeit, Technische Universität Darmstadt, Darmstadt, Germany.

Held, P. (1997), MIMOS II - Ein miniaturisiertes Mößbauerspektrometer in Rückstreugeometrie zur mineralogischen Analyse der Marsoberfläche, dissertation, Technische Universität Darmstadt, Darmstadt, Germany.

Held, P., R. Teucher, G. Klingelhöfer, J. Foh, H. Jäger, and E. Kankeleit (1993), Mössbauer spectrometer for the mineralogical analysis of the Mars surface: First temperature dependent tests of the detector and drive system, *Lunar and Planetary Science*, *34*, 633-634.

Herkenhoff, K., S.W. Squyres, J.F. Bell III, J.N. Maki, H.M. Arneson, P. Bertelsen, D.I. Brown, S.A. Collins, A. Dingizian, S.T. Elliott, W. Goetz, E.C. Hagerott, A.G. Hayes, M.J. Johnson, R.L. Kirk, S. McLennan, R.V. Morris, L.M. Scherr, M.A. Schwochert, L.R. Shiraishi, G.H. Smith, L.A. Soderblom, J.N. Sohl-Dickstein, and M.V. Wadsworth (2003), Athena Microscopic Imager investigation, *Journal of Geophysical Research*, *108*(E12), 8065, doi:10.1029/2003JE002076.

Hochella, M.F., and A.F. White (eds.) (1990), *Mineral-Water Interface Geochemistry*, vol. 23, Reviews in Mineralogy, Mineralogical Society of America, Washington, D.C., USA.

Hoefen, T.M., R.N. Clark, J.L. Bandfield, M.D. Smith, J.C. Pearl, P.R. Christensen (2003), Discovery of Olivine in the Nili Fossae Region of Mars, *Science*, 302, 627-630.

Hofmann, B.A. and J.D. Farmer (2000), Filamentous fabrics in low-temperature mineral assemblages: are they fossil biomarkers? Implications for the search for a subsurface fossil record on the early Earth and Mars, *Planetary and Space Science*, 48, 1077-1086.

Hofmann, B.A., M. Josset, and J.-L. Josset (2002), Imaging of Mars analogue materials using the Beagle2 camera system, Proceedings of the Second European Workshop on Exo/Astrobiology, Graz, Austria, 2002, ESA SP-518, 387-390.

Hofmann, H.J., K. Grey, A.H. Hickman, and R.I. Thorpe (1999), Origin of 3.45 Ga coniform stromatolites in Warrawoona Group, Western Australia, *Geological Society of America Bulletin*, 111(8), 1256-1262.

Hurowitz, J.A., S.M. McLennan, N.J. Tosca, R.E. Arvidson, J.R. Michalski, D.W. Ming, C. Schröder, and S.W. Squyres (2006), In situ and experimental evidence for acidic weathering of rocks and soils on Mars, *Journal of Geophysical Research*, 111, E02S19, doi:10.1029/2005JE002515.

Imkeller, U. (1990), Simulation und Analyse von Konversions-Elektronen-Mößbauerspektren, Einsatz von PIN-Dioden als Mößbauerdetektor, Diplomarbeit, Technische Universität Darmstadt, Darmstadt, Germany.

James, F. (2004), MINUIT Tutorial - Function Minimization, reprinted from the proceedings of the 1972 CERN Computing and Data Processing School, Pertisau, Austria, 10-24 September, 1972 (CERN 72-21), CERN, Geneva, Switzerland.

Kan, X., and J.M.D. Coey (1985), Mössbauer Spectra, Magnetic and Electrical Properties of Laihunite, a Mixed Valence Iron Olivine Mineral, *The American Mineralogist*, 70, 576-580.

Kankeleit, E. (1964), Velocity Spectrometer for Mössbauer Experiments,

The Review of Scientific Instruments, 35(2), 194-197.

Kargel, J.S. (2004), Proof for Water, Hints for Life?, *Science*, 306, 1689-1691.

Kerr, R.A. (2004), On Mars, a Second Chance for Life, *Science*, 306, 2010-2012.

Kieffer, H.H., B.M. Jakosky, C.W. Snyder, M.S. Matthews (eds.) (1992), *Mars*, The University of Arizona Press, Tucson, Arizona, USA.

Klingelhöfer, G., U. Imkeller, E. Kankeleit, and B. Stahl (1992), Remarks on depth selective CEMS-backscattering measurements, *Hyperfine Interactions*, 71, 1445-1448.

Klingelhöfer, G., P. Held, R. Teucher, F. Schlichting, J. Foh, and E. Kankeleit (1995), Mössbauer spectroscopy in space, *Hyperfine Interactions*, 95, 305-339.

Klingelhöfer, G., S.J. Campbell, G.M. Wang, P. Held, B. Stahl, E. Kankeleit (1998), Iron Ore Processing - In-Situ Monitoring, *Hyperfine Interactions*, 111, 335-339.

Klingelhöfer, G., F. Trolard, B. Bernhardt, G. Bourrie, F. Feder, J.-M.R. Genin (1999), The Monitoring of Iron Mineralogy and Oxidation States by Moessbauer Spectroscopy in the Field; the Green Rust Mineral in Hydromorphic Soils. In American Geophysical Union, Fall Meeting, San Francisco, 13-17 December 1999, Abstract H129-01.

Klingelhöfer, G., G.M. da Costa, A. Prous, B. Bernhardt (2002a), Rock Paintings from Minas Gerais, Brazil, Investigated by in situ Mössbauer Spectroscopy, *Hyperfine Interactions*, C5, 423.

Klingelhöfer, G., B. Bernhardt, J. Foh, U. Bonnes, D. Rodionov, P.A. de Souza Jr., C. Schröder, R. Gellert, S. Kane, P. Gütlich, E. Kankeleit (2002b), The Miniaturized Mössbauer Spectrometer MIMOS II for Extraterrestrial and Outdoor Applications: A Status Report. *Hyperfine Interactions*, 144/145, 371-379.

Klingelhöfer, G., R.V. Morris, B. Bernhardt, D. Rodionov, P.A. de Souza Jr., S.W. Squyres, J. Foh, E. Kankeleit, U. Bonnes, R. Gellert, C. Schröder, S. Linkin, E. Evlanov, B. Zubkov, and O. Prilutski (2003),

Athena MIMOS II Mössbauer spectrometer investigation, *Journal of Geophysical Research* 108(E12), 8067, doi:10.1029/2003JE002138.

Klingelhöfer, G., R.V. Morris, B. Bernhardt, C. Schröder, D.S. Rodionov, P.A. de Souza Jr., A. Yen, R. Gellert, E.N. Evlanov, B. Zubkov, J. Foh, U. Bonnes, E. Kankeleit, P. Gütlich, D.W. Ming, F. Renz, T. Wdowiak, S.W. Squyres, and R.E. Arvidson (2004), Jarosite and Hematite at Meridiani Planum from Opportunity's Mössbauer Spectrometer, *Science*, 306, 1740-1745.

Klingelhöfer, G., R.V. Morris, D. Rodionov, C. Schröder, P.A. de Souza Jr. (2005), In-situ Mössbauer Spectroscopy on Mars: Data Archiving and Availability, International Conference on the Applications of the Mössbauer Effect (ICAME), September 5-9, 2005, Montpellier, France, abstract T4-P1.

Knoll, A.H. (2003), *Life on a Young Planet - The First Three Billion Years of Evolution on Earth*, 4th ed. (1st paperback), Princeton University Press, Princeton, USA.

Knoll, A.H., M. Carr, B. Clark, D.J. Des Marais, J.D. Farmer, W.W. Fischer, J.P. Grotzinger, S.M. McLennan, M. Malin, C. Schröder, S. Squyres, N.J. Tosca, and T. Wdowiak (2005), An astrobiological perspective on Meridiani Planum, *Earth and Planetary Science Letters*, 240, 179-189, doi:10.1016/j.epsl.2005.09.045.

Knudsen, J.M. (1989), Mössbauer Spectroscopy of ^{57}Fe and the Evolution of the Solar System, *Hyperfine Interactions*, 47, 3-31.

Knudsen, J.M., S. Mørup, and J. Galazkha-Firedman (1990), Mössbauer Spectroscopy and the Iron on Mars, *Hyperfine Interactions*, 57, 2231-2236.

Knudsen, J.M., M.B. Madsen, M. Olsen, L. Vistisen, C.B. Koch, S. Mørup, E. Kankeleit, G. Klingelhöfer, E.N. Evlanov, V.N. Khromov, L.M. Mukhin, O.F. Prilutski, B. Zubkov, G.V. Smirnov, and J. Juchniewicz (1992), Mössbauer Spectroscopy on the Surface of Mars. Why?, *Hyperfine Interactions*, 68, 83-94.

Kondoh, S., M. Kitamura, and N. Morimoto (1985), Synthetic laihunite ($x\text{Fe}_2+2-3x\text{Fe}_3+2x\text{SiO}_4$), an oxidation product of olivine, *American Mineralogist*, 70(7-8), 737-746.

Langevin, Y., F. Poulet, J.-P. Bibring, B. Schmitt, S. Douté, and B. Gondet (2005), Summer Evolution of the North Polar Cap of Mars as Observed by OMEGA/Mars Express, *Science*, *307*, 1581-1584, doi:10.1126/science1109438.

Lee, D.-C., and A.N. Halliday (1997), Core formation on Mars and differentiated asteroids, *Nature*, *388*, 854-857.

Lemmon, M.T., M.J. Wolff, M.D. Smith, R.T. Clancy, D. Banfield, G.A. Landis, A. Ghosh, P.H. Smith, N. Spanovich, B. Whitney, P. Whelley, R. Greeley, S. Thompson, J.F. Bell III, and S.W. Squyres (2004), Atmospheric Imaging Results from the Mars Exploration Rovers: Spirit and Opportunity, *Science*, *306*, 1753-1756.

Lodders, K., and B. Fegley Jr. (1998), *The Planetary Scientist's Companion*, Oxford University Press, New York, USA.

Lugmair, G.W., and A. Shukolyukov (1998), Early solar system timescales according to ^{53}Mn - ^{53}Cr systematics, *Geochimica et Cosmochimica Acta*, *62*, 2863-2886.

Luhmann, J.G., C.T. Russell, L.H. Brace, and O.L. Vaisberg (1992), The intrinsic magnetic field and solar-wind interaction of Mars, in *Mars*, edited by H.H. Kieffer, B.M. Jakosky, C.W. Snyder, and M.S. Matthews, The University of Arizona Press, Tucson, pp. 1090-1134.

Madsen, M.B., P. Bertelsen, W. Goetz, C.S. Binou, M. Olsen, F. Folkmann, H.P. Gunnlaugsson, K.M. Kinch, J.M. Knudsen, J. Merrison, P. Nørnberg, S.W. Squyres, A.S. Yen, J.D. Rademacher, S. Gorevan, T. Myrick, and P. Bartlett (2003), Magnetic Properties Experiments on the Mars Exploration Rover mission, *Journal of Geophysical Research*, *108*(E12), 8069, doi:10.1029/2002JE002029.

Matthes, S. (2001), *Mineralogie - Eine Einführung in die spezielle Mineralogie, Petrologie und Lagerstättenkunde*, 6th ed., Springer-Verlag, Heidelberg, Germany.

McCammom, C. (1995), Mössbauer Spectroscopy of Minerals, in *Mineral Physics and Crystallography: A Handbook of Physical Constants*, AGU Reference Shelf, vol. 2, edited by T.J. Ahrens, pp. 332-347, AGU, Washington, D.C., USA.

McKay, D.S., E.K. Gibson Jr., K.L. Thomas-Keptra, H. Vali, C.S. Romanek, S.J. Clemett, X.D.F. Chillier, C.R. Maechling, and R.N. Zare (1996), Search for Past Life on Mars: Possible Relic Biogenic Activity in Martian Meteorite ALH84001, *Science*, *273*, 924-930.

McLennan, S.M., J.F. Bell III, W.M. Calvin, P.R. Christensen, B.C. Clark, P.A. de Souza Jr., J. Farmer, W.H. Farrand, D.A. Fike, R. Gellert, A. Ghosh, T.D. Glotch, J.P. Grotzinger, B. Hahn, K.E. Herkenhoff, J.A. Hurowitz, J.R. Johnson, S.S. Johnson, B. Jolliff, G. Klingelhöfer, A.H. Knoll, Z. Learner, M.C. Malin, H.Y. McSween Jr., J. Pockock, S.W. Ruff, L.A. Soderblom, S.W. Squyres, N.J. Tosca, W.A. Watters, M.B. Wyatt, and A. Yen (2005), Provenance and diagenesis of the evaporite-bearing Burns formation, Meridiani Planum, Mars, *Earth and Planetary Science Letters*, *240*, 95-121, doi:10.1016/j.epsl.2005.09.041.

McSween Jr., H.Y. (1994), What we have learned about Mars from SNC meteorites, *Meteoritics*, *29*, 757-779.

McSween, H.Y., R.E. Arvidson, J.F. Bell III, D. Blaney, N.A. Cabrol, P.R. Christensen, B.C. Clark, J.A. Crisp, L.S. Crumpler, D.J. Des Marais, J.D. Farmer, R. Gellert, A. Ghosh, S. Gorevan, T. Graff, J. Grant, L.A. Haskin, K.E. Herkenhoff, J.R. Johnson, B.L. Jolliff, G. Klingelhöfer, A.T. Knudson, S. McLennan, K.A. Milam, J.E. Moersch, R.V. Morris, R. Rieder, S.W. Ruff, P.A. de Souza Jr., S.W. Squyres, H. Wänke, A. Wang, M.B. Wyatt, A. Yen, and J. Zipfel (2004), Basaltic Rocks Analyzed by the Spirit Rover in Gusev Crater, *Science*, *305*, 842-845.

McSween, H.Y., M.B. Wyatt, R. Gellert, J.F. Bell III, R.V. Morris, K.E. Herkenhoff, L.S. Crumpler, K.A. Milam, K.R. Stockstill, L.L. Tornabene, R.E. Arvidson, P. Bartlett, D. Blaney, N.A. Cabrol, P.R. Christensen, B.C. Clark, J.A. Crisp, D.J. Des Marais, T. Economou, J.D. Farmer, W. Farrand, A. Ghosh, M. Golombek, S. Gorevan, R. Greeley, V.E. Hamilton, J.R. Johnson, B.L. Jolliff, G. Klingelhöfer, A.T. Knudson, S. McLennan, D. Ming, J.E. Moersch, R. Rieder, S.W. Ruff, C. Schröder, P.A. de Souza Jr., S.W. Squyres, H. Wänke, A. Wang, A. Yen, and J. Zipfel (2006), Characterization and petrologic interpretation of olivine-rich basalts at Gusev Crater, Mars, *Journal of Geophysical Research*, *111*, E02S10, doi:10.1029/2005JE002477.

Megonigal, J.P., M.E. Hines, and P.T. Visscher (2003) Anaerobic Metabolism: Linkages to Trace Gases and Aerobic Processes, in *Biogeo-*

chemistry, edited by W.H. Schlesinger, Treatise on Geochemistry (eds. H.D. Holland and K.K. Turekian), Vol. 8, Elsevier-Pergamon, Oxford, UK.

Melchiorre, E.B. and P.A. Williams (2001), Stable isotopic characterization of the thermal profile and subsurface biological activity during oxidation of the Great Australia Deposit, Cloncurry, Queensland, Australia, *Economic Geology*, *96*, 1685-1693.

Meyer, C. (2006), Mars Meteorite Compendium, Astromaterials Research & Exploration Science (ARES), Lyndon B. Johnson Space Center (JSC#27672 Revision B), Houston, Texas. Web access: <http://curator.jsc.nasa.gov/antmet/mmc/index.cfm> (last accessed August 2006).

Mikouchi, T., M. Miyamoto, and G.A. McKay (1998), Mineralogy of Antarctic basaltic shergottite Queen Alexandra Range 94201: Similarities to Elephant Moraine A79001 (Lithology B) Martian meteorite, *Meteoritics and Planetary Science*, *33*, 181-189.

Ming, D.W., D.W. Mittlefehldt, R.V. Morris, D.C. Golden, R. Gellert, A. Yen, B.C. Clark, S.W. Squyres, W.H. Farrand, S.W. Ruff, R.E. Arvidson, G. Klingelhöfer, H.Y. McSween, D.S. Rodionov, C. Schröder, P.A. de Souza Jr., and A. Wang (2006), Geochemical and mineralogical indicators for aqueous processes in the Columbia Hills of Gusev crater, Mars, *Journal of Geophysical Research*, *111*, E02S12, doi:10.1029/2005JE002560.

Mitra, S. (ed.) (1992), *Applied Mössbauer Spectroscopy - Theory and Practice for Geochemists and Archaeologists*, Pergamon Press, Oxford - New York - Seoul - Tokyo.

Moeller, F., and F. Fricke (1971), *Grundlagen der Elektrotechnik*, 14th ed., Teubner, Stuttgart, Germany.

Moore, J.G. (1966), Rate of palagonitization of submarine basalt adjacent to Hawaii, *U.S. Geol. Surv. Prof. Pap. HO-D*, 163-171.

Morris, R.V., D.G. Agresti, H.V. Lauer, Jr, J.A. Newcomb, T.D. Shelfer, and A.V. Murali (1989a), Evidence for pigmentary hematite on Mars based on optical, magnetic and Mössbauer studies of superparamagnetic (nanocrystalline) hematite, *Journal of Geophysical Research*, *94*, 2760-2778.

Morris, R.V., D.G. Agresti, T.D. Shelfer, and T.J. Wdowiak (1989b), Mossbauer backscatter spectrometer: A new approach for mineralogical analysis on planetary surfaces, *Lunar and Planetary Science*, 20, 723-724.

Morris, R.V., D.C. Golden, J.F. Bell III, H.V. Lauer Jr., and J.B. Adams (1993), Pigmenting agents in Martian soils: Inferences from spectral, Mössbauer, and magnetic properties of nanophase and other iron oxides in Hawaiian palagonitic soil PN-9, *Geochimica et Cosmochimica Acta*, 57, 4597-4609.

Morris, R.V., D.C. Golden, J.F. Bell III, and H.V. Lauer Jr. (1995), Hematite, pyroxene, and phyllosilicates on Mars: Implications from oxidized impact melt rocks from Manicouagan Crater Quebec, Canada, *Journal of Geophysical Research*, 100, 5319-5328.

Morris, R.V., D.W. Ming, D.C. Golden, and J.F. Bell III (1996), Occurrence of jarositic tephra on Mauna Kea, Hawaii: Implications for the ferric mineralogy of the Martian surface, in *Mineral Spectroscopy: A Tribute to Roger G. Burns*, edited by M.D. Dyar et al., Geochem. Soc. Spec. Publ., 5, pp. 327-336.

Morris R.V., D.C. Golden, and J.F. Bell III (1997), Low-temperature reflectivity spectra of red hematite and the color of Mars, *Journal of Geophysical Research*, 102, 9125-9133.

Morris, R.V., D.C. Golden, J.F. Bell III, T.D. Shelfer, A.C. Scheinost, N.W. Hinman, G. Furniss, S.A. Mertzman, J.L. Bishop, D.W. Ming, C.C. Allen, and D.T. Britt (2000), Mineralogy, composition, and alteration of Mars Pathfinder rocks and soils: Evidence from multispectral, elemental, and magnetic data on terrestrial analogue, SNC meteorite, and Pathfinder samples, *Journal of Geophysical Research*, 105(E1), 1757-1817.

Morris, R.V., D.C. Golden, D.W. Ming, T.D. Shelfer, L.C. Jørgensen, J.F. Bell III, T.G. Graff, and S.A. Mertzman (2001), Phyllosilicate-poor palagonite dust from Mauna Kea Volcano (Hawaii): A mineralogical analogue for magnetic Martian dust?, *Journal of Geophysical Research*, 106, 5057-5083.

Morris, R.V., G. Klingelhöfer, B. Bernhardt, C. Schröder, D.S. Rodionov, P.A. de Souza Jr., A. Yen, R. Gellert, E.N. Evlanov, J. Foh, E. Kankleit, P. Gütllich, D.W. Ming, F. Renz, T. Wdowiak, S.W. Squyres, and R.E. Arvidson (2004), Mineralogy at Gusev Crater from the Mössbauer

Spectrometer on the Spirit Rover, *Science*, *305*, 833-836.

Morris, R.V., D.W. Ming, B.C. Clark, G. Klingelhöfer, R. Gellert, D. Rodionov, C. Schröder; P. de Souza, A. Yen, and the Athena Science Team (2005), Abundance and speciation of water and sulfate at Gusev Crater and Meridiani Planum, *Lunar and Planetary Science*, *36*, 2239.

Morris, R.V., G. Klingelhöfer, C. Schröder, D.S. Rodionov, A. Yen, D.W. Ming, P.A. de Souza Jr., I. Fleischer, T. Wdowiak, R. Gellert, B. Bernhardt, E.N. Evlanov, B. Zubkov, J. Foh, U. Bonnes, E. Kankeleit, P. Gütlich, F. Renz, S.W. Squyres, and R.E. Arvidson (2006a), Mössbauer mineralogy of rock, soil, and dust at Gusev crater, Mars : Spirit's journey through weakly altered olivine basalt on the plains and pervasively altered basalt in the Columbia Hills, *Journal of Geophysical Research*, *111*, E02S13, doi:10.1029/2005JE002584.

Morris, R.V., G.A. McKay, D.W. Ming, G. Klingelhöfer, C. Schröder, D. Rodionov, and A. Yen (2006b), Magnetite in Martian meteorite MIL 03346 and Gusev Adirondack Class basalt: Mössbauer evidence for variability in the oxidation state of Adirondack lavas, *Lunar and Planetary Science*, *37*, 1594.

Morris, R.V., S.W. Ruff, D.W. Ming, G. Klingelhöfer, C. Schröder, and D. Rodionov (2006c), Clays or clay minerals at Gusev Crater, Mars: Evidence from the Mössbauer and Mini-TES instruments on the Mars Exploration Rover Spirit, 43rd Annual Meeting of the Clay Mineral Society, 3-7 June 2006, Ile d'Oléron, France.

Mössbauer, R.L. (1958a), Kernresonanzfluoreszenz von Gammastrahlung in Ir191, *Zeitschrift für Physik*, *151*, 124-143.

Mössbauer, R.L. (1958b), Kernresonanzfluoreszenz von Gammastrahlung in Ir191, *Naturwissenschaften*, *45*, 538-539.

Mössbauer, R.L. (2000), The discovery of the Mössbauer effect, *Hyperfine Interactions*, *126*, 1-12.

Muir Jr., A.H., K.J. Ando, and H.M. Coogan (eds.) (1967), Mössbauer Effect Data Index, Interscience Publishers, New York.

Murad, E. (1988), Properties and behavior of iron oxides as determined by Mössbauer spectroscopy, in *Iron in Soils and Clay Minerals*,

NATO ASI Series C: Mathematical and Physical Sciences, vol. 217, edited by J.W. Stucki et al., D. Reidel Publishing Company, Dordrecht/Boston/Lancaster/Tokyo.

Mustard, J.F., F. Poulet, A. Gendrin, J.-P. Bibring, Y. Langevin, B. Gondet, N. Mangold, G. Bellucci, F. Altieri (2005), Olivine and Pyroxene Diversity in the Crust of Mars, *Science*, 307, 1594-1597, doi:10.1126/science.1109098.

Neukum, G., R. Jaumann, H. Hoffmann, E. Hauber, J.W. Head, A.T. Basilevsky, B.A. Ivanov, S.C. Werner, S. van Gasselt, J.B. Murray, T. McCord, and the HRSC Co-Investigator Team (2004), Recent and episodic volcanic and glacial activity on Mars revealed by the High Resolution Stereo Camera, *Nature*, 432, 971-979, doi:10.1038/nature03231.

Nyquist, L.E., D.D. Bogard, C.-Y. Shih, A. Greshake, D. Stöffler, and O. Eugster (2001), Ages and geologic histories of Martian meteorites, *Space Science Reviews*, 96, 105-164.

Owen, T. (1992), The composition and early history of the atmosphere of Mars, in *Mars*, edited by H.H. Kieffer, B.M. Jakosky, C.W. Snyder, M.S. Matthews, pp. 523-554, University of Arizona Press, Tucson, Arizona.

Pache, M., J. Reitner, and G. Arp (2001), Geochemical evidence for the formation of a large Miocene "Travertine" mound at a sublacustrine spring in a soda lake (Wallerstein Castle Rock, Nördlinger Ries, Germany), *Facies*, 45, 211-230.

Pettijohn, F.J. (1941), Persistence of heavy minerals and geologic age, *Journal of Geology*, 49, 610-625.

Picardi, G., J.L. Plaut, D. Biccari, O. Bombaci, D. Calabrese, M. Cartacci, A. Cicchetti, S.M. Clifford, P. Edenhofer, W.M. Farrell, C. Federico, A. Frigeri, D.A. Gurnett, T. Hagfors, E. Heggy, A. Herique, R.L. Huff, A.B. Ivanov, W.T.K. Johnson, R.L. Jordan, D.L. Kirchner, W. Kofman, C.J. Leuschen, E. Nielsen, R. Orosei, E. Petinelli, R.J. Philips, D. Plettemeier, A. Safaeinili, R. Seu, E.R. Stofan, G. Vannaroni, T.R. Watters, and E. Zampolini (2005), Radar Soundings of the Subsurface of Mars, *Science*, 310, 1925-1928, doi:10.1126/science.1122165.

Pohl, J., D. Stöffler, H. Gall, and K. Ernstson (1977), The Ries Impact Crater, in *Impact and Explosion Cratering*, edited by D.J. Roddy et al,

Pergamon Press, pp. 343-404.

Press, F., and R. Siever (2000), *Understanding Earth*, 3rd ed., W.H. Freeman and Company, New York, USA.

Preston, R.S., S.S. Hanna, and J. Heberle (1962), Mössbauer Effect in Metallic Iron, *Physical Review*, *128*(5), 2207-2218.

Pullan, D., M.R. Sims, I.P. Wright, C.T. Pillinger, and R. Trautner (2003), Beagle 2, an Exobiological lander for the Mars Express mission. ESA SP-1240, December 2003.

Reid, A.M., and T.E. Bunch (1975), The nakhlites, part II. Where, when and how?, *Meteoritics*, *10*, 317-324.

Rieder, R., T. Economou, H. Wänke, A. Turkevich, J. Crisp, J. Brückner, G. Dreibus, and H.Y. McSween Jr. (1997), The Chemical Composition of Martian Soil and Rocks Returned by the Mobile Alpha Proton X-ray Spectrometer: Preliminary Results from the X-ray Mode, *Science*, *278*, 1771-1774.

Rieder, R., R. Gellert, J. Brückner, G. Klingelhöfer, G. Dreibus, A. Yen, and S.W. Squyres (2003), The new Athena alpha particle X-ray spectrometer for the Mars Exploration Rovers, *Journal of Geophysical Research*, *108*(E12), 8066, doi:10.1029/2003JE002150.

Rieder, R., R. Gellert, R.C. Anderson, J. Brückner, B.C. Clark, G. Dreibus, T. Economou, G. Klingelhöfer, G.W. Lugmair, D.W. Ming, S.W. Squyres, C. d'Uston, H. Wänke, A. Yen, and J. Zipfel (2004), Chemistry of Rocks and Soils at Meridiani Planum from the Alpha Particle X-ray Spectrometer, *Science*, *306*, 1746-1749.

Riesenman, R., J. Steger, and E. Kostiner (1969), Cosine effect in Mössbauer spectroscopy involving a source of non-zero radius, *Nuclear Instruments and Methods*, *72*, 109-110.

Robie, R.A., B.S. Hemingway, and J.R. Fisher (1978), Thermodynamic Properties of Minerals and Related Substances at 298.15 K and 1 Bar (105 Pascals) Pressure and at Higher Temperatures, *Geological Survey Bulletin*, *1452*, 1-456.

Rodionov, D., G. Klingelhöfer, B. Bernhardt, C. Schröder, M. Blumers,

S. Kane, F. Trolard, G. Bourrie, and J.M. Genin (2006), Automated Mössbauer Spectroscopy in the Field, *Hyperfine Interactions* (Proceedings of the International Conference on the Applications of the Mössbauer Effect (ICAME), September 5-9, 2005, Montpellier, France), in press.

Ross, K.A., and R.V. Fisher (1986), Biogenic grooving on glass shards, *Geology*, *14*, 571-573.

Rossman, G. R. (1980), Pyroxene spectroscopy, in *Pyroxenes*, Rev. Mineral., vol. 7, edited by C. T. Prewitt, pp. 93- 115, Mineral. Soc. of Am., Washington, D. C.

Rothschild, L.J., and R.L. Mancinelli (2001), Life in extreme environments, *Nature*, *409*, 1092-1101.

Sangameshwar, S.R. and Barnes, H.L. (1983) Supergene processes in zinc-lead-silver sulphide ores in carbonates. *Economic Geology*, *78*(7), 1379-1397.

Schaefer, M.W. (1983), Measurements of iron(III)-rich fayalites, *Nature*, *303*, 325-327.

Schlesinger, W.H. (Ed.) (2003), *Biogeochemistry*, vol. 8, Treatise on Geochemistry, edited by H.D. Holland and K.K. Turekian, Elsevier-Pergamon, Oxford, UK.

Schröder, C. (2001), Optimierung der Nachweiseigenschaften des miniaturisierten Mössbauer-Spektrometers MIMOS II und Messungen an Mars-Analog-Proben, Diplomarbeit, Johannes Gutenberg-Universität, Mainz, Germany.

Schröder, C. (2004), MER Anekdoten, Mars Society Newsletter, 12 (April 2004), 20-21, available online at <http://www.marsociety.de/>.

Schröder, C., G. Klingelhöfer, and W. Tremel (2004), Weathering of Fe-bearing minerals under Martian conditions, investigated by Mössbauer spectroscopy, *Planetary and Space Science*, *52*(11), 997-1010, doi:10.016/j.pss.2004.07.018.

Schröder, C., G. Klingelhöfer, R.V. Morris, D.S. Rodionov, P.A. de Souza Jr., D.W. Ming, A.S. Yen, R. Gellert, J.F. Bell III, and the Athena Science Team (2005), Weathering of basaltic rocks from the Gusev plains

up into the Columbia Hills from the perspective of the MER Mössbauer spectrometer, *Lunar and Planetary Science*, 36, 2309.

Schröder, C., B. Bailey, G. Klingelhöfer, H. Staudigel (2006), Fe Mössbauer spectroscopy as a tool in astrobiology, *Planetary and Space Science*, in press.

Sims, M.R., C.T. Pillinger, I.P. Wright, J. Dowson, S. Whitehead, A. Wells, J.E. Spragg, G. Fraser, L. Richter, H. Hamacher, A. Johnstone, N.P. Meredith, C. de la Nougerede, B. Hancock, R. Turner, S. Peskett, A. Brack, J. Hobbs, M. Newns, A. Senior, M. Humphries, H.U. Keller, N. Thomas, J.S. Lingard, J.C. Underwood, N.M. Sale, M.F. Neal, G. Klingelhöfer, and T.C. Ng (1999), Beagle 2: A proposed exobiology lander for ESA's 2003 Mars Express Mission, *Advances in Space Research*, 23(11), 1925-1928.

Sleep, N.H., A. Meibom, T. Fridriksson, R.G. Coleman, and D.K. Bird (2004), H₂-rich fluids from serpentinization: Geochemical and biotic Implications, *PNAS*, 101, 12818-12823.

Soderblom, L.A., R.C. Anderson, R.E. Arvidson, J.F. Bell III, N.A. Cabrol, W. Calvin, P.R. Christensen, B.C. Clark, T. Economou, B.L. Ehlmann, W.H. Farrand, D. Fike, R. Gellert, T.D. Glotch, M.P. Golombek, R. Greeley, J.P. Grotzinger, K.E. Herkenhoff, D.J. Jerolmack, J.R. Johnson, B. Joliff, G. Klingelhöfer, A.H. Knoll, Z.A. Learner, R. Li, M.C. Malin, S.M. McLennan, H.Y. McSween, D.W. Ming, R.V. Morris, J.W. Rice Jr., L. Richter, R. Rieder, D. Rodionov, C. Schröder, F.P. Seelos IV, J.M. Soderblom, S.W. Squyres, R. Sullivan, W.A. Watters, C.M. Weitz, M.B. Wyatt, A. Yen, and J. Zipfel (2004), Soils of Eagle Crater and Meridiani Planum at the Opportunity Rover Landing Site, *Science*, 306, 1723-1726.

Solberg, T.C., and R.G. Burns (1989), Iron Mossbauer spectral study of weathered Antarctic and SNC meteorites, Proceedings of the 19th Lunar and Planetary Science Conference, 313-322.

Squyres, S.W. (2005), *Roving Mars - Spirit, Opportunity, and the Exploration of the Red Planet*, Hyperion, New York.

Squyres, S.W., S.M. Clifford, R.O. Kuzmin, J.R. Zimbelman, and F.M. Costard (1992), Ice in the Martian regolith, in *Mars*, edited by H.H. Kieffer, B.M. Jakosky, C.W. Snyder, M.S. Matthews, pp. 523-554,

University of Arizona Press, Tucson, Arizona.

Squyres, S.W., R.E. Arvidson, E.T. Baumgartner, J.F. Bell III, P.R. Christensen, S. Gorevan, K.E. Herkenhoff, G. Klingelhöfer, M.B. Madsen, R.V. Morris, R. Rieder, and R.A. Romero (2003), Athena Mars rover science investigation, *Journal of Geophysical Research*, 108(E12), 8062, doi:10.1029/2003JE002121.

Squyres, S.W., R.E. Arvidson, J.F. Bell III, J. Brückner, N.A. Cabrol, W. Calvin, M.H. Carr, P.R. Christensen, B.C. Clark, L. Crumpler, D.J. Des Marais, C. d'Uston, T. Economou, J. Farmer, W. Farrand, W. Folkner, M. Golombek, S. Gorevan, J.A. Grant, R. Greeley, J. Grotzinger, L. Haskin, K.E. Herkenhoff, S. Hviid, J. Johnson, G. Klingelhöfer, A. Knoll, G. Landis, M. Lemmon, R. Li, M.B. Madsen, M.C. Malin, S.M. McLennan, H.Y. McSween, D.W. Ming, J. Moersch, R.V. Morris, T. Parker, J.W. Rice Jr., L. Richter, R. Rieder, M. Sims, M. Smith, L.A. Soderblom, R. Sullivan, H. Wänke, T. Wdowiak, M. Wolff, A. Yen (2004a), The Spirit Rover's Athena Science Investigation at Gusev Crater, Mars, *Science*, 305, 794-799.

Squyres, S.W., R.E. Arvidson, J.F. Bell III, J. Brückner, N.A. Cabrol, W. Calvin, M.H. Carr, P.R. Christensen, B.C. Clark, L. Crumpler, D.J. Des Marais, C. d'Uston, T. Economou, J. Farmer, W. Farrand, W. Folkner, M. Golombek, S. Gorevan, J.A. Grant, R. Greeley, J. Grotzinger, L. Haskin, K.E. Herkenhoff, S. Hviid, J. Johnson, G. Klingelhöfer, A. Knoll, G. Landis, M. Lemmon, R. Li, M.B. Madsen, M.C. Malin, S.M. McLennan, H.Y. McSween, D.W. Ming, J. Moersch, R.V. Morris, T. Parker, J.W. Rice Jr., L. Richter, R. Rieder, M. Sims, M. Smith, L.A. Soderblom, R. Sullivan, H. Wänke, T. Wdowiak, M. Wolff, and A. Yen (2004b), The Opportunity Rover's Athena Science Investigation at Meridiani Planum, Mars, *Science*, 306, 1689-1703.

Squyres, S.W., J.P. Grotzinger, R.E. Arvidson, J.F. Bell III, W. Calvin, P.R. Christensen, B.C. Clark, J.A. Crisp, W.H. Farrand, K.E. Herkenhoff, J.R. Johnson, G. Klingelhöfer, A.H. Knoll, S.M. McLennan, H.Y. McSween, R.V. Morris, J.W. Rice, R. Rieder, and L.A. Soderblom (2004c), In situ evidence for an ancient aqueous environment at Meridiani Planum, Mars, *Science*, 306, 1709-1714.

Squyres, S.W., R.E. Arvidson, D.L. Blaney, B.C. Clark, L. Crumpler, W.H. Farrand, S. Gorevan, K.E. Herkenhoff, J. Hurowitz, A. Kusack,

H.Y. McSween, D.W. Ming, R.V. Morris, S.W. Ruff, A. Wang, A. Yen (2006), The Rocks of the Columbia Hills, *Journal of Geophysical Research*, 111, E02S11, doi:10.1029/2005JE002562.

Staudigel, H., and S.R. Hart (1983), Alteration of basaltic glass: processes and significance for the oceanic crust-seawater budget, *Geochimica Cosmochimica Acta*, 47, 337-350.

Sun, H.J. and E.I. Friedmann (1999), Growth on geological time scales in the Antarctic cryptoendolithic microbial community, *Geomicrobiology Journal*, 16, 193-202.

Techer, I., J. Lancelot, N. Clauer, J.M. Liotard, and T. Advocat (2001), Alteration of a basaltic glass in an argillaceous medium: The Salagou dike of the Lodeve Permian Basin (France). Analogy with an underground nuclear waste repository, *Geochimica et Cosmochimica Acta*, 65(7), 1071-1086.

Teucher, R. (1994), Miniaturisierter Mößbauerantrieb, Diplomarbeit, Technische Universität Darmstadt, Darmstadt, Germany.

Thorseth, I.H., H. Furnes, and O. Tumyr (1991), A textural and chemical study of Icelandic palagonite of varied composition and its bearing on the mechanism of the glass-palagonite transformation, *Geochimica Cosmochimica Acta*, 55, 731-749.

Thorseth, I.H., H. Furnes, and M. Heldal (1992), The importance of microbiological activity in the alteration of natural basaltic glass, *Geochimica Cosmochimica Acta*, 56, 845-850.

Thorseth, I.H., H. Furnes, and O. Tumyr (1995), Textural and chemical effects of bacterial activity on basaltic glass: an experimental approach, *Chemical Geology*, 119, 139-160.

Tice, M., and D.R. Lowe (2004), Photosynthetic microbial mats in the 3,416-Myr-old ocean, *Nature*, 431, 549-552.

Titus, T.N., H.H. Kieffer, and P.R. Christensen (2003), Exposed Water Ice Discovered near the South Pole of Mars, *Science*, 299, 1048-1051, doi:10.1126/science.1080497.

Torsvik, T., H. Furnes, K. Muehlenbachs, I.H. Thorseth, and O. Tumyr

(1998), Evidence for Microbial Activity at the Glass-Alteration Interface in Oceanic Basalts, *Earth and Planetary Science Letters*, *162*, 165-176.

Tosca, N.J., S.M. McLennan, D.H. Lindsley, and M.A.A. Schoonen (2004), Acid-sulfate weathering of synthetic Martian basalt: The acid fog model revisited, *Journal of Geophysical Research*, *109*, E05003, doi:10.1029/2003JE002218.

Tosca, N.J., S.M. McLennan, B.C. Clark, J.P. Grotzinger, J.A. Hurowitz, A.H. Knoll, C. Schröder, and S.W. Squyres (2005), Geochemical modeling of evaporation processes on Mars: Insight from the sedimentary record at Meridiani Planum, *Earth and Planetary Science Letters*, *240*, 122-148, doi:10.1016/j.epsl.2005.09.042.

Toulmin III, P., A.K. Baird, B.C. Clark, K. Keil, H.J. Rose Jr., R.P. Christian, P.H. Evans, and W.C. Kelliher (1977), Geochemical and mineralogical interpretation of the Viking inorganic chemistry results, *Journal of Geophysical Research*, *84*, 4625-4634.

Treiman, A.H., J.D. Gleason, and D.D. Bogard (2000), The SNC meteorites are from Mars, *Planetary and Space Science*, *48*, 1213-1230.

Tull, R.G. (1966), The reflectivity spectrum of Mars in the near-infrared, *Icarus*, *5*, 505-514.

Vandenberghe, R.E., C.A. Barrero, G.M. da Costa, E. Van San, and E. De Grave (2000), Mössbauer characterization of iron oxides and (oxy)hydroxides: the present state of the art, *Hyperfine Interactions*, *126*, 247-259.

Vieira, V.W.A., T.V.V. Costa, H.G. Jensen, J.M. Knudsen, M. Olsen, and L. Vistisen (1990), Oxidation state of iron in SNC meteorites as studied by Mössbauer spectroscopy, *Physica Scripta*, *33*, 180-186.

Vistisen, L., N.O. Roy-Poulson, H.G. Jensen, J.M. Knudsen, M.B. Madsen, M. Olsen (1990), Mössbauer spectroscopy of pyroxens from the SNC meteorite Nakhla, *Meteoritics*, *25*, 417-418.

Wächtershäuser, G. (1988), Before Enzymes and Templates: Theory of Surface Metabolism, *Microbiological Reviews*, *52*(4), 452-484.

Wächtershäuser, G. (1992), Groundworks for an Evolutionary Biochem-

- istry: The Iron-Sulphur World, *Progress in Biophysics and Molecular Biology*, 58, 85-201.
- Wade, M.L., D.G. Agresti, T.J. Wdowiak, L.P. Armandarez, J.D. Farmer (1999), A Mössbauer investigation of iron-rich terrestrial hydrothermal vent systems: Lessons for Mars exploration, *Journal of Geophysical Research*, 104(E4), 8489-8507.
- Walker, J.C.G. (1979), The Early History of Oxygen and Ozone in the Atmosphere, *Pure and Applied Geophysics*, 117, 498-512.
- Walsh, M.M. (1992), Microfossils and possible microfossils from the Early Archean Onverwacht Group, Barberton Mountain Land, South Africa, *Precambrian Research*, 54, 271-293.
- Walsh, M.M. (2004), Evaluation of early Archean volcanoclastic and volcanic flow rocks as possible sites for carbonaceous fossil microbes, *Astrobiology*, 4, 429-437.
- Wang, A., L.A. Haskin, S.W. Squyres, B.L. Jolliff, L. Crumpler, R. Gellert, C. Schröder, K. Herkenhoff, J. Hurowitz, N.J. Tosca, W.H. Farrand, R. Anderson, and A.T. Knudson (2006), Sulfate deposition in subsurface regolith in Gusev crater, Mars, *Journal Geophysical Research*, 111, E02S17, doi:10.1029/2005JE002513.
- Wasklewicz, T.A. (1994), Importance of environment on the order of mineral weathering in olivine basalts, Hawaii, *Earth Surface Processes and Landforms*, 19, 715-734.
- Wdowiak, T.J., and D.G. Agresti (1984), Presence of a superparamagnetic component in the Orgueil meteorite, *Nature*, 311, 140-142.
- Wdowiak, T.J., L.P. Armandarez, D.G. Agresti, M.L. Wade, Y. Wdowiak, P. Claeys, and G. Izett (2001), Presence of an iron-rich nanophase material in the upper layer of the Cretaceous-Tertiary boundary clay, *Meteoritics and Planetary Science*, 36, 123-133.
- Wdowiak, T.J., G. Klingelhöfer, M.L. Wade, and J.I. Nuñez (2003), Extracting science from Mössbauer spectroscopy on Mars. *Journal of Geophysical Research*, 108(E12), 8097, doi:10.1029/2003JE002071.
- Wegener, H. (1965), *Der Mössbauer-Effekt und seine Anwendungen in*

Physik und Chemie, Bibliographisches Institut, Mannheim, Germany.

Weinheimer, C., M. Schrader, J. Bonn, T. Loeken, and H. Backe (1992), Measurement of energy resolution and dead layer thickness of LN₂-cooled PIN photodiodes, *Nuclear Instruments and Methods, Sect. A*, 311, 273-279.

Westall, F. (2005), Early Life on Earth and Analogies to Mars, in *Water on Mars and Life*, edited by T. Tokano, Adv. Astrobiol. Biogeophys., Springer, Berlin Heidelberg, pp. 45-64.

Westall, F. and G. Southam (2006), Early life on Earth, in *Archean Geodynamics and Environments*, edited by K. Benn et al., AGU Geophys. Monogr., 164, pp. 283-304.

Westall, F., A. Brack, B. Hofmann, G. Horneck, G. Kurat, J. Maxwell, G.G. Ori, C. Pillinger, F. Raulin, N. Thomas, B. Fitton, P. Clancy, D. Prieur, and D. Vassaux (2000), An ESA study for the search for life on Mars, *Planetary and Space Science*, 48, 181-202.

Westall, F., M.J. de Wit, J. Dann, S. van der Gaast, C.E.J. de Ronde, and D. Gerneke (2001), Early Archaean fossil bacteria and biofilms in hydrothermally-influenced sediments from the Barberton greenstone belt, South Africa, *Precambrian Research*, 106, 93-116.

White, A.F., and S.L. Brantley (eds.) (1995), *Chemical Weathering Rates of Silicate Minerals*, vol. 31, Reviews in Mineralogy, Mineralogical Society of America, Washington, D.C., USA.

Wierzchos, J., C. Ascaso, L.G. Sancho, and A. Green (2003), Iron-rich diagenetic minerals are biomarkers of microbial activity in Antarctic rocks, *Geomicrobiology Journal*, 20, 15-24.

Wilson, A. (ed.) (1999), *Exobiology in the Solar System & The Search for Life on Mars*, European Space Agency, SP-1231, October 1999.

Yen, A.S., R. Gellert, C. Schröder, R.V. Morris, J.F. Bell III, A.T. Knudson, B.C. Clark, D.W. Ming, J.A. Crisp, R.E. Arvidson, D. Blaney, J. Brückner, P.R. Christensen, D.J. DesMarais, P.A. de Souza Jr., T.E. Economou, A. Ghosh, B.C. Hahn, K.E. Herkenhoff, L.A. Haskin, J.A. Hurowitz, B.L. Joliff, J.R. Johnson, G. Klingelhöfer, M.B. Madsen, S.M. McLennan, H.Y. McSween, L. Richter, R. Rieder, D. Rodionov, L.

Soderblom, S.W. Squyres, N.J. Tosca, A. Wang, M. Wyatt, and J. Zipfel (2005a), An integrated view of the chemistry and mineralogy of Martian soils, *Nature*, *436*, 49-54, doi:10.1038/nature03637.

Yen, A.S., D.W. Ming, R. Gellert, B.C. Clark, R.V. Morris, D. Rodionov, C. Schröder, G. Klingelhöfer, and the Athena Science Team (2005b), Subsurface weathering of rocks and soils at Gusev Crater, *Lunar and Planetary Science*, *36*, 1571.

Zipfel, J. (2000), Sayh al Uhaymir 005/008 and its relationship to DAG 476/489, *Meteoritics and Planetary Science*, *35*, A178.

Zipfel, J., P. Scherer, B. Spettel, G. Dreibus, and L. Schultz (2000), Petrology and chemistry of the new shergottite Dar al Gani 476, *Meteoritics and Planetary Science*, *35*, 95-106.

Appendix A

Mars

Mars is the fourth planet from the Sun. Its diameter is about half of Earth's diameters (Table A.1). Gravity on the Martian surface is about 1/3 of the gravity on the surface of Earth. The surface area of Mars is comparable in size to all land surface on Earth. Among the many distinguishing features on the surface of Mars (Figure A.1) are its polar caps containing water ice and seasonal CO_2 ice, the Tharsis bulge including Olympus Mons, the Solar System's highest mountain; Valles Marineris, a canyon system that would span the entire USA from West coast to East coast; large impact craters such as Hellas Planitia; and the enigma of the Martian dichotomy, i.e. the old cratered terrain of the southern highlands and the low, uncratered plains of the north. Due to a currently almost identical tilt of Mars' rotational axis when compared to Earth's, the Red Planet experiences similar seasons. The atmosphere of Mars is thin - 6 mbars on average at the surface compared to 1013 mbar on Earth - and mainly composed of CO_2 (95 %). Surface temperatures can vary from $-120^\circ C$ to $+20^\circ C$. In today's climate water can

Table A.1: Comparison of selected properties of Earth and Mars [*Lodders and Fegley, 1998*].

Property	Earth	Mars
Mean distance to Sun (AU)	1.000	1.5236
Sidereal revolution period (d)	365.256	686.980
Sidereal rotational period (h)	23.9345	24.6230
Obliquity to orbit	23.45°	25.29°
Mass (10^{24} kg)	5.9736	0.6418
Mean radius (km)	6371.01	3389.92
Mean obs. density ($g\ cm^{-3}$)	5.515	3.934

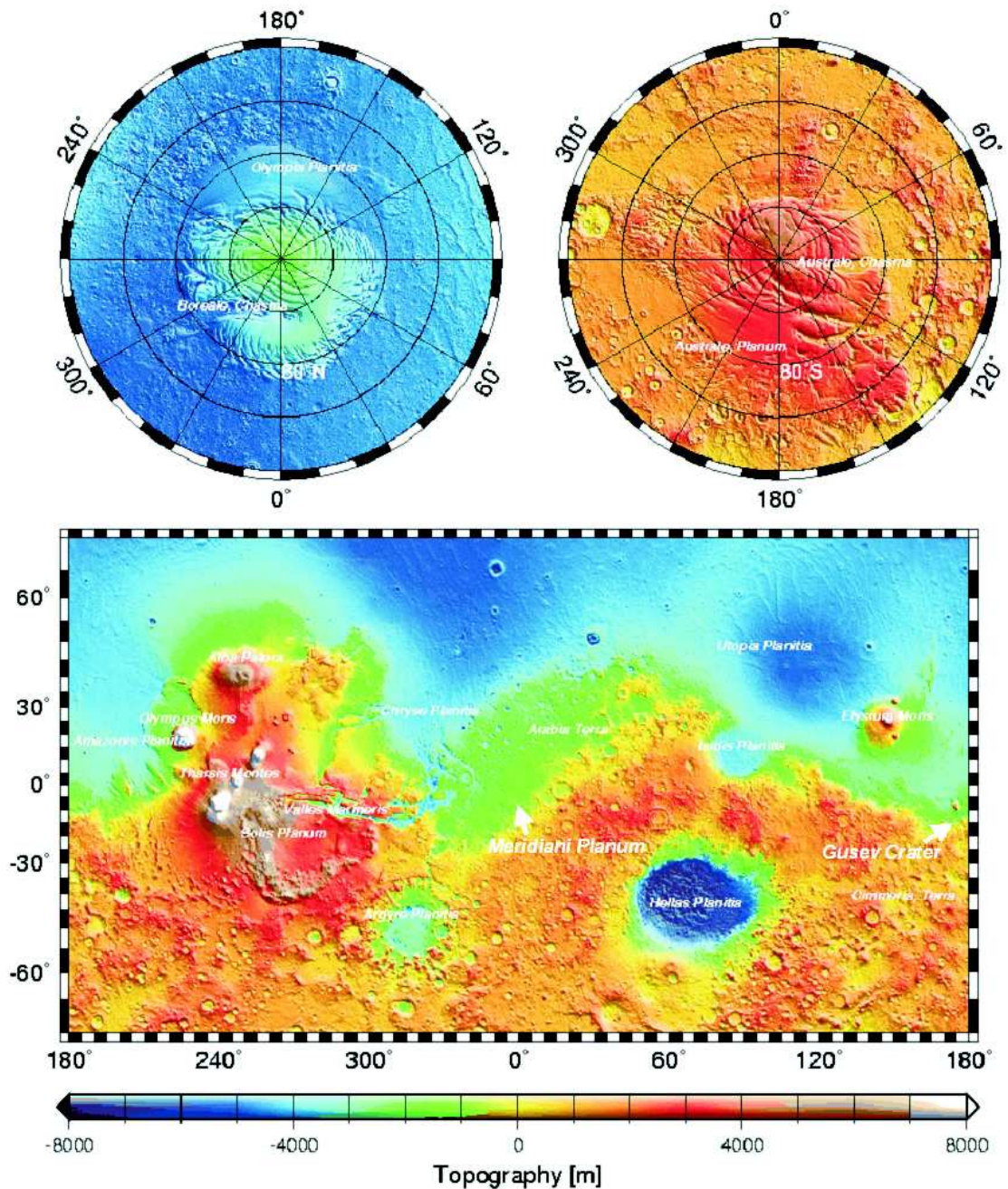


Figure A.1: The picture shows the Mars Orbital Laser Altimeter (MOLA) topographical map of the surface of Mars [e.g., Smith et al., 1999]. The landing sites of the NASA Mars Exploration Rovers Spirit and Opportunity - Gusev Crater and Meridiani Planum, respectively - are indicated by arrows (NASA, Mars Global Surveyor, MOLA team).

only exist as ice or vapor. However, many erosional features suggest that liquid water once ran over the Martian surface.

The Red Planet has inspired humanity for generations and a vast amount of literature is available on the subject, ranging from fact to fiction. A concise collection of reviews of the scientific literature before 1992 was assembled by *Kieffer et al.* [1992]. *Hartmann* [2003] wrote an entertaining but scientifically accurate description of the distinguishing features of Mars' surface. The many features attributed to the presence of liquid water on the surface of Mars in the past are summarized by *Carr* [1996].

Appendix B

Mars Exploration Rover

The NASA Mars Exploration Rover twins Spirit and Opportunity landed successfully on Mars in Gusev Crater on January 4, 2004, and at Meridiani Planum on January 24, 2004, respectively. They each carry the Athena instrument payload [Squyres *et al.*, 2003] (Figure B.1), including the Mössbauer spectrometer MIMOS II [Klingelhöfer *et al.*, 2003].

The intended mission duration of 90 sols (1 sol = 1 Martian day \sim 24 h 39 min) has been exceeded more than tenfold. By the time of writing, more than two and a half years after landing, both rovers are still operating. Most of the many scientific findings have been published as coordinated articles in dedicated journal issues, namely the Journal of Geophysical Research (volumes 108 [2003] and 111 [2006]), Science (volumes 305 and 306 [2004]), Nature (volume 436 [2005]), and Earth and Planetary Science Letters (volume 240 [2005]). The results were voted the scientific 'Breakthrough of the Year' 2004 by the journal Science [Kerr, 2004]. The daily progress of Spirit and Opportunity can be followed at <http://marsrovers.jpl.nasa.gov/>.

Serving as Payload Uplink Lead (PUL) and Payload Downlink Lead (PDL) for the Mössbauer spectrometers, and Science Theme Group (STG) member at the mission control center at NASA's Jet Propulsion Laboratory (JPL), California Institute of Technology in Pasadena/California was very intensive at the beginning of the mission, as the meeting schedule in Table B.1 shows. Working at mission control produced many memorable anecdotes [e.g., Schröder, 2004].

The journey of Spirit and Opportunity has also entered the public consciousness. The Principal Investigator (PI) of the mission, Steve Squyres, wrote a book describing the highs and lows from conceiving the mission until finally roving on Mars [Squyres, 2005]. Two documentaries were televised and the Disney company released an IMAX movie "Roving Mars" about the mission. A poem by John Updike captures the essence of the mission:

DUET ON MARS

Said Spirit to Opportunity,
"I'm feeling rather frail,
With too much in my memory,
Plus barrels of e-mail."

Responded Opportunity,
"My bounce was not so bad,
But now they send me out to see
These dreary rocks, bedad!"

"It's cold up here, and rather red,"
Sighed Spirit. "I feel faint."
Good Opportunity then said,
"Crawl on, without complaint!"

"This planet needs our shovels' bite
And treadmarks in the dust
To tell if life and hematite
Pervade its arid crust."

"There's life, by all the stars above,
On Mars - it's you and I!"
Blithe Spirit cried. "Let's rove, my love,
And meet before we die!"

With increasing experience this schedule was relaxed significantly (Table 2) and the mission was supported remotely from scientists' home institutions.

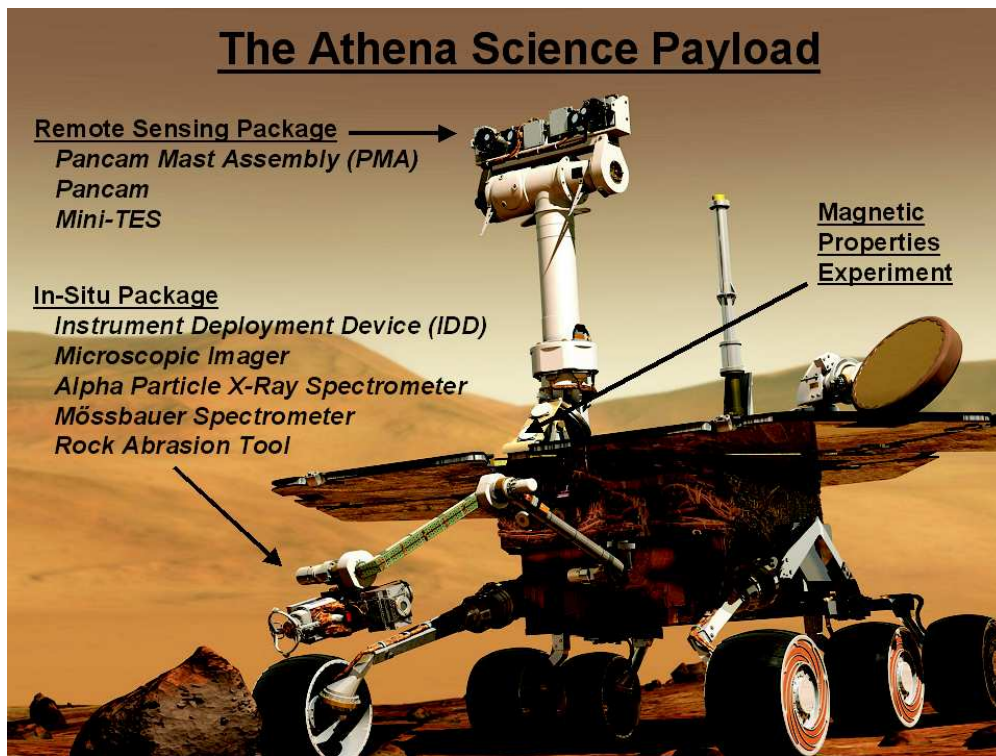


Figure B.1: An artist's impression of one of the Mars Exploration Rovers carrying the Athena science payload. The remote sensing package is supported by the Pancam Mast Assembly (PMA), which provides pointing capability for the Panoramic Camera (Pancam) and the Miniature Thermal Emission Spectrometer (Mini-TES). The in situ package is supported by the Instrument Deployment Device (IDD), which is a five degree-of-freedom manipulator for placement of the Microscopic Imager (MI), the Alpha Particle X-Ray Spectrometer (APXS), the Mössbauer Spectrometer (MB), and the Rock Abrasion Tool (RAT). A Magnetic Properties Experiment is enabled by magnets mounted near the base of the PMA and elsewhere on the rover [Squyres et al., 2003].

Table B.2: Planning schedule for Spirit in January 2006.

 SPIRIT Thursday (1/19/06 -- DOY = 019) Schedule (all times PST)

*** Note: We have just completed a single-sol planning session *** 1

Flight Director: Jones

01/18/2006 - 08:50 downlink <===== 47270 MRA_ODY_DOY018_3 ERT
 01/18/2006 16:50:00 (UTC) 256000 bps

01/18/2006 - 15:28 UPLINK =====> SOL 727 CONTINGENCY ONLY - YES,
 data management bundle needed

01/18/2006 - 21:55 downlink <===== 47273 MRA_ODY_DOY019_2 ERT
 01/19/2006 05:55:00 (UTC) 256000 bps

Flight Director: Eldeeb

01/19/2006 - 06:30 SOWG-MM-TUL-TDL Tag up (Meet me number :
 ###-###-####)

01/19/2006 - 07:00 MER-A -- Uplink kick off, Sol 728/729 (Meet me
 number: ###-###-####)

01/19/2006 - 07:30 POWER INCONS DUE for SOL 728

01/19/2006 - 08:00 MER-A -- Subsystem poll - current Sol 727
 data, issues, eng requests for sol 728/729

01/19/2006 - 10:00 MER-A -- Activity Plan Approval Meeting Sol
 728/729

01/19/2006 - 11:00 MER-A -- Master/Submaster walk through Sol
 728/729

01/19/2006 - 14:00 MER-A -- CAM Sol 728/729

01/19/2006 - 16:08 UPLINK ==> SOL 728/729 Nominal Bundles --
 YES, data management bundle needed

Curriculum Vitae

Christian Schröder

Geboren am 9. Juli 1975 in Wiesbaden.

Verheiratet.

Staatsangehörigkeit: Deutschland.

Ausbildung:

- 1981-1985 Johannes-Maaß-Schule in Wiesbaden
- 1985-1994 Diltheyschule in Wiesbaden
- 1994 Abitur
- 1994-2001 Johannes Gutenberg-Universität in Mainz (Physik - Diplom)
- 1998-1999 University of Edinburgh in Edinburgh, Schottland/GB (Astrophysik)
- 2001 Diplom in Physik, Johannes Gutenberg-Universität, Titel der Diplomarbeit: 'Optimierung der Nachweiseigenschaften des miniaturisierten Mössbauer-Spektrometers MIMOS II und Messungen an Mars-Analog-Proben'
- Seit Feb. 2002 Doktorand, Johannes Gutenberg-Universität in Mainz, Thema: 'Weathering of Fe-bearing Minerals Under Extraterrestrial Conditions, Investigated by Mössbauer Spectroscopy'
- Jan.-Mai 2004 Jet Propulsion Laboratory, California Institute of Technology, Pasadena, CA, USA, NASA Mars Exploration Rover Mission Operations Support

Beruflicher Werdegang:

- Seit Okt. 2001 Wissenschaftlicher Mitarbeiter am Institut für Anorganische und Analytische Chemie, Johannes Gutenberg-Universität in Mainz